

AUTOTHERMAL REFORMING OF PETROLEUM FRACTIONS

A THESIS SUBMITTED TO  
THE GRADUATE SCHOOL OF NATURAL AND APPLIED SCIENCES  
OF  
MIDDLE EAST TECHNICAL UNIVERSITY

BY

ARZU ARSLAN BOZDAĞ

IN PARTIAL FULFILLMENT OF THE REQUIREMENTS  
FOR  
THE DEGREE OF DOCTOR OF PHILOSOPHY  
IN  
CHEMICAL ENGINEERING

DECEMBER 2019



Approval of the thesis:

**AUTOTHERMAL REFORMING OF PETROLEUM FRACTIONS**

submitted by **ARZU ARSLAN BOZDAĞ** in partial fulfillment of the requirements for the degree of **Doctor of Philosophy in Chemical Engineering Department, Middle East Technical University** by,

Prof. Dr. Halil Kalıpçılar  
Dean, Graduate School of **Natural and Applied Sciences**

\_\_\_\_\_

Prof. Dr. Pınar Çalık  
Head of Department, **Chemical Engineering**

\_\_\_\_\_

Prof. Dr. Naime Aslı Sezgi  
Supervisor, **Chemical Engineering, METU**

\_\_\_\_\_

Prof. Dr. Timur Doğu  
Co-Supervisor, **Chemical Engineering, METU**

\_\_\_\_\_

**Examining Committee Members:**

Prof. Dr. Fatma Suna Balcı  
Chemical Engineering, Gazi University

\_\_\_\_\_

Prof. Dr. Naime Aslı Sezgi  
Chemical Engineering, METU

\_\_\_\_\_

Prof. Dr. Gürkan Karakaş  
Chemical Engineering, METU

\_\_\_\_\_

Prof. Dr. Sena Yaşyerli  
Chemical Engineering, Gazi University

\_\_\_\_\_

Assist. Prof. Dr. Bahar İpek Torun  
Chemical Engineering, METU

\_\_\_\_\_

Date: 30.12.2019

**I hereby declare that all information in this document has been obtained and presented in accordance with academic rules and ethical conduct. I also declare that, as required by these rules and conduct, I have fully cited and referenced all material and results that are not original to this work.**

Name, Surname: Arzu Arslan Bozdağ

Signature:

## ABSTRACT

### AUTOTHERMAL REFORMING OF PETROLEUM FRACTIONS

Arslan Bozdağ, Arzu  
Doctor of Philosophy, Chemical Engineering  
Supervisor: Prof. Dr. Naime Aslı Sezgi  
Co-Supervisor: Prof. Dr. Timur Doğu

December 2019, 263 pages

On site and on-demand hydrogen production through diesel autothermal (ATR) and steam reforming (DSR) reactions are attractive routes for both stationary and mobile auxiliary power unit applications (APUs). Maximization of H<sub>2</sub> production with coke minimization for cheap and active Ni/Al<sub>2</sub>O<sub>3</sub> catalysts was investigated with incorporation of different metals/metal oxides to Ni/Al<sub>2</sub>O<sub>3</sub> catalyst in DSR and ATR reactions. Two different synthesis techniques which are impregnation of metal/metal oxides to commercial Al<sub>2</sub>O<sub>3</sub> pellets and one-pot synthesis of metal/metal oxide incorporated Al<sub>2</sub>O<sub>3</sub> through surfactant aided evaporation induced self-assembly (EISA) approach, were applied. The effects of different metals/metal oxides such as Ru, W, CeO<sub>2</sub>, Mg, ZrO<sub>2</sub> and their different combinations such as Ru & CeO<sub>2</sub>, Mg, CeO<sub>2</sub> & ZrO<sub>2</sub>, W & CeO<sub>2</sub>, W & Mg on the hydrogen productivity and coke resistivity of Ni/Al<sub>2</sub>O<sub>3</sub> catalyst in DSR and ATR reactions were investigated. Performances of catalysts were investigated at the optimum operating conditions which were found to be 7500 h<sup>-1</sup> for GHSV, and 2.5 for H<sub>2</sub>O/C ratio in DSR reaction, 7500 h<sup>-1</sup> for GHSV, 2.5 for H<sub>2</sub>O/C ratio, and 0.5 for O<sub>2</sub>/C ratio in ATR reaction.

Catalyst investigations presented that among Ru and Ru-CeO<sub>2</sub> incorporated catalysts, 0.5 wt.% ruthenium loading results in the highest H<sub>2</sub> production in both DSR and ATR. Higher activity of this material was mostly due to its higher surface area and

easier reducibility of Ni on Ni@0.5Ru@Al<sub>2</sub>O<sub>3</sub> which also presented long term stability for 34 h. Superior activity in DSR was obtained with CeO<sub>2</sub> or CeO<sub>2</sub>/ZrO<sub>2</sub> incorporated (one-pot) Ni/Al<sub>2</sub>O<sub>3</sub>-EISA catalysts. However, instabilities in product composition of CeO<sub>2</sub>/ZrO<sub>2</sub> incorporated catalyst observed in DSR suggested that in the long term, incorporation of CeO<sub>2</sub> is more preferable. CeO<sub>2</sub> incorporated catalyst also presented higher hydrogen production in ATR reaction compared to CeO<sub>2</sub>/ZrO<sub>2</sub> incorporated catalyst. Long term DSR test performed with Ni@10CeO<sub>2</sub>-Al<sub>2</sub>O<sub>3</sub>-EISA lead to superior activity along with stability. Tests on Mg, W, W-CeO<sub>2</sub> and W-Mg incorporated (one-pot) mesoporous Al<sub>2</sub>O<sub>3</sub>-EISA supported nickel catalysts showed the most successful catalyst as Ni@10Mg-Al<sub>2</sub>O<sub>3</sub>-EISA in terms of hydrogen yield in DSR reaction. The stability and superior activity of Ni@10Mg-Al<sub>2</sub>O<sub>3</sub>-EISA catalyst was observed in long term DSR activity test. Higher success of this catalysts was due to formation of Ni<sup>0</sup> crystals whereas formation Ni<sub>4</sub>W crystals was observed along with lower surface area and higher acidity in W catalysts, leading to lower water gas shift and reforming reaction rates. However, significant coke minimization was achieved with W catalysts due to low solubility of carbon in Ni<sub>4</sub>W crystals and also due to WC crystal formation during reforming reactions.

The best performing catalysts in this study in terms of hydrogen production was Ni@10Mg-Al<sub>2</sub>O<sub>3</sub>-EISA, Ni@0.5Ru@Al<sub>2</sub>O<sub>3</sub> and Ni@10CeO<sub>2</sub>-Al<sub>2</sub>O<sub>3</sub>-EISA. Considering sustainability of the developed catalysts, it is suggested that Ni@10Mg-Al<sub>2</sub>O<sub>3</sub>-EISA catalyst can be used in commercial applications of DSR. The highest hydrogen production with low coke deposition in ATR reaction was obtained with Ni@10CeO<sub>2</sub>-Al<sub>2</sub>O<sub>3</sub>-EISA catalyst, which can be used in an APUs equipped with a reformer unit to produce hydrogen for solid oxide fuel cells.

Keywords: Hydrogen, Tungsten, Ceria/Zirconia, Diesel Reformer

## ÖZ

### PETROL FRAKSİYONLARININ OTOTERMAL REFORMLANMASI

Arslan Bozdağ, Arzu  
Doktora, Kimya Mühendisliği  
Tez Danışmanı: Prof. Dr. Naime Aslı Sezgi  
Ortak Tez Danışmanı: Prof. Dr. Timur Doğu

Aralık 2019, 263 sayfa

Dizelin ototermal (ATR) ve buharlı (DSR) reformlanma reaksiyonları için yerinde ve ihtiyaca bağlı hidrojen üretimi hem sabit hem de mobil yardımcı güç üniteleri (APUs) uygulamaları için ilgi çeken yöntemlerdir. Minimum kok ile maksimum H<sub>2</sub> üretimi sağlayacak ucuz ve aktif Ni/Al<sub>2</sub>O<sub>3</sub> katalizörleri, farklı metal/metal oksitlerin Ni/Al<sub>2</sub>O<sub>3</sub> katalizörlerine yüklenmesi ile DSR ve ATR reaksiyonlarında araştırılmıştır. Metal/metal oksitlerin ticari Al<sub>2</sub>O<sub>3</sub> peletlerine emdirilmesi ve metal/metal oksit yüklenmiş Al<sub>2</sub>O<sub>3</sub>'ün yüzey aktif madde kullanılan yaklaşımla (EISA) tek kapta sentezi şeklinde iki farklı sentez tekniği uygulanmıştır. Ru, W, CeO<sub>2</sub>, Mg, ZrO<sub>2</sub> gibi etkinleştiricilerin ve Ru & CeO<sub>2</sub>, Mg, CeO<sub>2</sub> & ZrO<sub>2</sub>, W & CeO<sub>2</sub>, W & Mg gibi bu metal/metal oksitlerin farklı kombinasyonlarının Ni/Al<sub>2</sub>O<sub>3</sub> katalizörünün hidrojen üretebilirliğindeki ve kok dayanımındaki etkileri DSR ve ATR reaksiyonlarında araştırılmıştır. Katalizör araştırmaları optimum çalışma koşullarında analiz edilmiştir. Katalizörlerin performansları, DSR reaksiyonunda, GHSV için 7500 sa<sup>-1</sup>, H<sub>2</sub>O / C oranı için 2,5 ve ATR reaksiyonunda, GHSV için 7500 sa<sup>-1</sup>, H<sub>2</sub>O / C oranı için 0,5 ve O<sub>2</sub> / C oranı için 0,5'in olduğu tespit edilen optimum çalışma koşullarında araştırıldı.

Katalizör araştırmalarına göre, Ru ve Ru-CeO<sub>2</sub> eklenmiş katalizörler arasında ağırlıklıca %0,5 Ru eklenmiş katalizör hem DSR hem de ATR'de en yüksek H<sub>2</sub> üretimi göstermiştir. Bu malzemenin daha yüksek aktivite vermesi yüksek yüzey alanı ve

Ni@0.5Ru@Al<sub>2</sub>O<sub>3</sub>'daki nikelin daha kolay indirgenebilmesi sayesinde. Ni@0.5Ru@Al<sub>2</sub>O<sub>3</sub> ayrıca uzun süreli stabilite göstermiştir. CeO<sub>2</sub> veya CeO<sub>2</sub>/ZrO<sub>2</sub> eklenmiş Ni/Al<sub>2</sub>O<sub>3</sub>-EISA katalizörleri ile üstün DSR aktivitesi elde edilmiştir. Fakat, CeO<sub>2</sub>/ZrO<sub>2</sub> eklenmiş katalizörün DSR reaksiyonunda elde edilen ürün dağılımdaki instabilitesi CeO<sub>2</sub>'nin uzun süreli kullanımda daha tercih edilebilir olduğunu önermektedir. CeO<sub>2</sub> eklenmiş katalizör CeO<sub>2</sub>/ZrO<sub>2</sub> eklenmiş katalizöre göre ayrıca ATR reaksiyonunda daha yüksek hidrojen üretimi göstermiştir. Ni@10CeO<sub>2</sub>-Al<sub>2</sub>O<sub>3</sub>-EISA ile gerçekleştirilen uzun süreli DSR testinde üstün aktivite ile birlikte stabilite elde edilmiştir. Mg, W, W-CeO<sub>2</sub> ve W-Mg eklenmiş mezogözenekli Al<sub>2</sub>O<sub>3</sub>-EISA destekli nikel katalizörleri ile gerçekleştirilen testler DSR reaksiyonunda hidrojen verimi açısından en başarılı katalizörü Ni@10Mg-Al<sub>2</sub>O<sub>3</sub>-EISA olarak göstermiştir, daha sonra uzun süreli DSR testi ile elde edilen üstün aktivite ve stabilite ile bu başarı kanıtlanmıştır. Bu malzemenin başarısının nedeni ise Ni<sup>0</sup> varlığıdır, W katalizörlerinde ise Ni<sub>4</sub>W kristallerinin oluşumu gözlenmiştir. W katalizörlerinde kristal fazı farkının yanı sıra daha düşük yüzey alanı ve yüksek asidite daha düşük su gazı reaksiyonu ve reformlanma aktivitesine sebep olmuştur. Fakat, karbonun Ni<sub>4</sub>W kristallerindeki düşük çözünürlüğü ve reformlanma reaksiyonu sırasında WC kristallerinin oluşumu nedeni ile dikkate değer kok minimizasyonu W katalizörleri ile elde edilmiştir.

Ni@10Mg-Al<sub>2</sub>O<sub>3</sub>-EISA, Ni@0.5Ru@Al<sub>2</sub>O<sub>3</sub> ve Ni@10CeO<sub>2</sub>-Al<sub>2</sub>O<sub>3</sub>-EISA katalizörleri ile bu çalışmada hidrojen üretimi açısından en başarılı performanslar elde edilmiştir. Geliştirilen katalizörlerin sürdürülebilirliği göz önüne alındığında ise Ni@10Mg-Al<sub>2</sub>O<sub>3</sub>-EISA katalizörü DSR reaksiyonunun ticari uygulamalarında kullanılabileceği önerilmektedir. ATR reaksiyonunda düşük kok birikimi ile en yüksek hidrojen üretiminin elde edildiği katalizör olan Ni@10CeO<sub>2</sub>-Al<sub>2</sub>O<sub>3</sub>-EISA ise katı yakıt pillerine hidrojen üretecek olan reformer ünitesi içeren APU'larda kullanılabilir.

Anahtar Kelimeler: Hidrojen, Tungsten, Seryum dioksit/Zirkonyum dioksit, Dizel Reformer

*To my beloved partner in life; Barış*

## ACKNOWLEDGEMENTS

Firstly, I would like to express my deepest gratitude to my supervisor Prof. Dr. Naime Aslı Sezgi, for her guidance, understanding, patience and encouragement throughout this research period. I also express my sincere gratitude and appreciation to my co-supervisor Prof. Dr. Timur Dođu for his guidance, support and very useful critiques. The support and guidance of my supervisors encouraged me and enabled me to finish this thesis.

Financial supports of Middle East Technical University Research Funds (DKT-304-2018-3719, GAP-304-2018-2855, BAP-07-02-2017-004-196, BAP-03-04-2017-005 and BAP-03-04-2016-002), Turkish Scientific and Technical Research Council (TUBITAK) through project number 213M027, TUBA support and Vestel Defence Industry are gratefully acknowledged.

I wish to thank to the Central Laboratory and Chemical Engineering Department of METU for the characterization analysis. Special thanks to Tüpraş R&D Center Laboratories for the analysis of liquid samples.

I would like to offer my sincere thanks to my close friend, my lab-mate and my colleague; İlker Şener for the help, motivation and support he gave me for the last five years. I wish to thank Merve Sarıyer for her kindness, friendship and companionship during our long experiments. Without the friendship of İlker and Merve, the time I spent in kinetic laboratory would not be so pleasant for the last five years. I would also like to thank my friend and my lab-mate Seda Sivri for her support. I would like to thank to all my past and present lab-mates; Pınar Değirmenciođlu, Sohrab Nikazad, Abdul Rehman Habib, Saeed Khan, Seval Gündüz and Gökhan Çelik for their valuable companionship. I would also like to thank all the Chemical Engineering Department personnel for their help.

I would like to express my sincerest thanks to my dearest friends; Zeynep Karakaş Helvacı, Veysi Helvacı, Hande Güneş Akıncıtürk, Tan Akıncıtürk, İklim Şahin and Gökhan Şahin for their everlasting support and encouragement, not only throughout this thesis, but also in all aspects of my life. I thank to Begüm Akcan, Ezgi Yavuzyılmaz, Merve Özkutlu, Fatma Şahin for their invaluable friendship and support. I would like to thank Eda Açık Çumkur, Cem Açıksarı, Cüneyt Karakaya and also all my friends and colleagues at Tüpraş R&D Center for their support.

I would like to express my special thanks to my family for their endless support. I know that their limitless faith in me will always be with me. I would like to offer my deepest gratitude to Barış Koray Bozdağ for his great support and motivation, invaluable contributions, endless patience, friendship and love. This accomplishment would not have been possible without him.

## TABLE OF CONTENTS

ABSTRACT .....	v
ÖZ .....	vii
ACKNOWLEDGEMENTS .....	x
TABLE OF CONTENTS .....	xii
LIST OF TABLES .....	xvi
LIST OF FIGURES.....	xviii
LIST OF ABBREVIATIONS .....	xxvi
CHAPTERS	
1. Introduction.....	1
1.1. The Importance of Hydrogen as an Energy Carrier .....	2
1.1.1. Hydrogen powered fuel cells .....	3
1.1.2. Market Research for Hydrogen & Fuel Cells .....	8
1.2. Reforming of diesel fuel .....	11
1.2.1. Operating conditions of diesel reforming reactions.....	16
1.2.2. Catalysts for diesel reforming reactions .....	18
1.2.3. Coke formation in diesel reforming reactions .....	29
1.3. Objectives .....	31
2. Chemical Equilibrium Analysis.....	37
2.1. Method.....	37
2.2. Equilibrium analysis results.....	39
3. Method .....	47
3.1. Catalyst Synthesis.....	48

3.2. Catalyst Characterization .....	53
3.3. Diesel Reforming Tests .....	55
3.3.1. Diesel Reforming Experimental Test Set-Up .....	55
3.3.2. Diesel Reforming Experimental Test Procedure .....	56
3.4. Liquid reaction sample analysis .....	58
4. The Effect of Operating Conditions of Diesel Steam and Autothermal Reforming Reactions .....	61
4.1. Diesel Steam Reforming Reaction .....	61
4.2. Diesel Autothermal Reforming Reaction .....	67
5. Development of Ceria and Tungsten Promoted Nickel/Alumina Catalysts for Steam And Autothermal Reforming of Diesel .....	71
5.1. Characterization Results .....	71
5.2. Catalyst Performance Test Results .....	83
5.2.1. Effect of Catalyst Composition on Hydrogen Production in Diesel Steam Reforming Reaction .....	83
5.2.2. Effect of Catalyst Composition on Hydrogen Production in Diesel Autothermal Reforming Reaction .....	88
6. Development of Ceria and Ruthenium Promoted Nickel/Alumina Catalysts for Steam and Autothermal Reforming of Diesel .....	91
6.1. Characterization Results .....	91
6.2. Catalyst Performance Test Results .....	102
6.2.1. Effect of Catalyst Composition on Hydrogen Production in the Diesel Steam Reforming Reaction .....	102
6.2.2. Effect of Catalyst Composition on Hydrogen Production in the Diesel Autothermal Reforming Reaction .....	105

6.2.3. Long Term Diesel Steam Reforming Reaction.....	107
7. Development of Mesoporous Ceria-Alumina and Ceria-Zirconia-Alumina Supported Nickel Catalysts for Steam and Autothermal Reforming of Diesel.....	111
7.1. Characterization Results .....	111
7.2. Catalytic Activity Test Results .....	126
7.2.1. The Effect of Catalyst Composition on Hydrogen Production in Diesel Steam Reforming Reaction .....	126
7.2.2. The effect of Catalyst Composition on Hydrogen Production in the Diesel Autothermal Reforming Reaction.....	132
7.2.3. Long Term Diesel Steam Reforming Test Results with Ni@10CeO <sub>2</sub> -Al <sub>2</sub> O <sub>3</sub> -EISA.....	133
8. Promotion Effect of Tungsten, Ceria and Magnesium on Nickel Alumina Catalysts Towards Diesel Steam and Autothermal Reforming Reactions.....	141
8.1. Characterization Results .....	141
8.2. Catalytic Activity Test Results .....	158
8.2.1. The Effect of Catalyst Composition on Hydrogen Production in Diesel Steam Reforming Reaction .....	158
8.2.2. The effect of Catalyst Composition on Hydrogen Production in the Diesel Autothermal Reforming Reaction.....	163
8.2.3. Long Term Diesel Steam Reforming Test Results with the Ni@10Mg-Al <sub>2</sub> O <sub>3</sub> -EISA Catalyst.....	166
9. Determination of the Best Catalyst Among the Synthesized Catalysts for the ATR and DSR .....	175
10. Conclusions and Recommendations .....	189
REFERENCES.....	195
APPENDICES.....	203

A. Applied Reactant Composition in Equilibrium Calculations .....	203
B. Diesel Steam and Autothermal Reforming Experimental Methods .....	205
C. Hexadecane Reforming Test Results.....	213
D. Liquid product analysis results .....	217
E. XRD Data .....	249
F. Crystal size calculation through Scherrer Equation.....	257
G. The effect of calcination temperature on Al <sub>2</sub> O <sub>3</sub> -EISA materials.....	259
CURRICULUM VITAE .....	261

## LIST OF TABLES

### TABLES

Table 1.1. The efficiency and energy consumption of hydrogen production methods	5
Table 1.2. Energy contents and carbon emissions of hydrogen and conventional and alternative fuels .....	6
Table 1.3. Specific fuel requirements of different fuel cell types .....	7
Table 1.4. The differences in cost and consumption values of heavy duty trucks with fuel cells and diesel engines. ....	10
Table 2.1. Range of chemical equilibrium parameters studied with Aspen HYSY....	38
Table 3.1 Catalysts synthesized for the scope of this work .....	49
Table 3.2. Properties of commercial Shell Diesel (analyzed at PAL, METU) .....	58
Table 4.1 Hydrogen yield, molar ratio of CO and CO <sub>2</sub> formation, produced side product amount and coke deposition results obtained from DSR optimization tests.	65
Table 4.2 Hydrogen yield, molar ratio of CO to CO <sub>2</sub> formation, and coke deposition results obtained in ATR optimization tests. ....	70
Table 5.1 Physical properties of catalysts .....	72
Table 5.2 Crystal sizes and number of acid sites of ceria and tungsten promoted nickel/alumina catalysts. ....	75
Table 5.3 Metal amounts in the synthesized catalysts. ....	82
Table 5.4 Catalyst activity test results in terms of average H <sub>2</sub> yield, coke deposition and average produced side product amount. ....	86
Table 5.5 Comparison of diesel steam and autothermal activity test results for Ni@10CeO <sub>2</sub> @Al <sub>2</sub> O <sub>3</sub> , Ni@Al <sub>2</sub> O <sub>3</sub> and Ni@20CeO <sub>2</sub> @Al <sub>2</sub> O <sub>3</sub> catalysts in terms of average gas product composition. ....	90
Table 6.1 Physical properties of Ru loaded catalysts.....	92
Table 6.2 Metal content of the synthesized catalysts obtained from EDX analysis.	101
Table 6.3 Activity test results of catalysts in DSR in terms of H <sub>2</sub> yield, the ratio of CO to CO <sub>2</sub> formation, average side product amount and coke deposition. ....	104

Table 6.4 Comparison of diesel steam and autothermal results for the Ni@0.5Ru@Al <sub>2</sub> O <sub>3</sub> , Ni@1.5Ru@Al <sub>2</sub> O <sub>3</sub> and Ni@1.5Ru@20CeO <sub>2</sub> @Al <sub>2</sub> O <sub>3</sub> catalysts in terms of average gas product composition.....	106
Table 7.1. Physical properties of the synthesized support materials and catalysts..	112
Table 7.2. Total acid capacity of the catalysts synthesized with EISA method.....	123
Table 7.3. Metal content of the synthesized catalysts according to EDX analysis..	125
Table 7.4. Activity test results of catalysts in DSR in terms of H <sub>2</sub> yield, the ratio of CO to CO <sub>2</sub> formation, average side product amount and coke deposition (GHSV= 7500 h <sup>-1</sup> , 800 °C, H <sub>2</sub> O/C=2.5).....	129
Table 8.1 Physical properties of catalysts .....	142
Table 8.2.Total acid capacity of the catalysts synthesized with EISA method.....	151
Table 8.3 Metal content of synthesized catalysts according to EDX analysis results. ....	157
Table 8.4 Activity test results of catalysts in DSR in terms of H <sub>2</sub> yield, the ratio of CO to CO <sub>2</sub> formation, produced average side product amount (in ppm), hydrogen formation rate per catalyst surface area and coke deposition (GHSV= 7500 h <sup>-1</sup> , 800 °C, H <sub>2</sub> O/C=2.5). ....	162

## LIST OF FIGURES

### FIGURES

Figure 1.1. Breakdown of energy usage in the transport sector globally in 2015.....	3
Figure 1.2. Thermal and electrical efficiencies of combined heat and power systems.. .....	4
Figure 1.3 Technological readiness level and opportunity for direct public engagement of fuel cell applications. ....	9
Figure 1.4. Cost of hydrogen production: current and projected .....	11
Figure 2.1. Effect of temperature on equilibrium product gas composition in the n- hexadecane steam reforming process ( $H_2O/C=2.5$ ). ....	40
Figure 2.2. Effect of $H_2O/C$ ratio on equilibrium product gas composition in the n- hexadecane steam reforming process ( $T=800\text{ }^\circ\text{C}$ ). ....	40
Figure 2.3. Effect of temperature on equilibrium product gas composition in the n- hexadecane autothermal reforming process ( $H_2O/C=0.5$ and $O_2/C=0.25$ ). ....	41
Figure 2.4. Effect of $H_2O/C$ ratio on equilibrium product gas composition in the n- hexadecane autothermal reforming process ( $T=800\text{ }^\circ\text{C}$ and $O_2/C=0.5$ ). ....	41
Figure 2.5. Effect of $O_2/C$ ratio on equilibrium product gas composition in the n- hexadecane autothermal reforming process ( $T=800\text{ }^\circ\text{C}$ and $H_2O/C=2.5$ ). ....	42
Figure 2.6. Effect of temperature on equilibrium product gas composition of diesel steam reforming process ( $H_2O/C=2.5$ ). ....	43
Figure 2.7. Effect of $H_2O/C$ ratio on equilibrium product gas composition of diesel steam reforming process ( $T=800\text{ }^\circ\text{C}$ and $O_2/C=0.1$ ) .....	43
Figure 2.8. Effect of temperature on equilibrium product gas composition of diesel autothermal reforming process ( $H_2O/C=2.5$ and $O_2/C=0.1$ ). ....	44
Figure 2.9. Effect of $H_2O/C$ ratio on equilibrium product gas composition of diesel autothermal reforming process ( $T=800\text{ }^\circ\text{C}$ and $O_2/C=0.1$ ) .....	44
Figure 2.10. Effect of $O_2/C$ ratio on equilibrium product gas composition of diesel autothermal reforming process ( $T=800\text{ }^\circ\text{C}$ and $H_2O/C=2.5$ ) .....	45

Figure 3.1 The selection of the promoter type, amount and the main reason for commercial Al <sub>2</sub> O <sub>3</sub> supported catalysts.....	50
Figure 3.2 The selection of the promoter type, amount and the main reason for EISA type catalysts.....	51
Figure 3.3 Schematic representation of laboratory scale ATR and DSR experimental test set-up. ....	55
Figure 4.1 The effect of A) GHSV(H <sub>2</sub> O/C=2.5), B) H <sub>2</sub> O/C molar ratio (GHSV=7500 h <sup>-1</sup> ) on average product compositions for the diesel steam reforming reaction over Ni@20CeO <sub>2</sub> @Al <sub>2</sub> O <sub>3</sub> catalyst at 800°C.....	64
Figure 4.2. Gas product compositions over the Ni@20CeO <sub>2</sub> @Al <sub>2</sub> O <sub>3</sub> catalyst with respect to time for the reproducibility of DSR experiments (800°C, GHSV=7500 h <sup>-1</sup> , H <sub>2</sub> O/C=2.5). ....	66
Figure 4.3. Average steady state gas product compositions over the Ni@20CeO <sub>2</sub> @Al <sub>2</sub> O <sub>3</sub> catalyst for the reproducibility of DSR experiments (800°C, GHSV=7500 h <sup>-1</sup> , H <sub>2</sub> O/C=2.5).....	66
Figure 4.4. The effect of GHSV on average product compositions over the Ni@20CeO <sub>2</sub> @Al <sub>2</sub> O <sub>3</sub> catalyst at 800 °C, H <sub>2</sub> O/C=2.5, O <sub>2</sub> /C=0.5. ....	69
Figure 4.5. The effect of H <sub>2</sub> O/C molar ratio on average product compositions over the Ni@20CeO <sub>2</sub> @Al <sub>2</sub> O <sub>3</sub> catalyst at 800 °C, GHSV=7500 h <sup>-1</sup> , O <sub>2</sub> /C=0.5. ....	69
Figure 4.6. The effect of O <sub>2</sub> /C molar ratio on average product compositions over the Ni@20CeO <sub>2</sub> @Al <sub>2</sub> O <sub>3</sub> catalyst at 800 °C, GHSV=7500 h <sup>-1</sup> , H <sub>2</sub> O/C =2.5. ....	70
Figure 5.1 N <sub>2</sub> adsorption/desorption isotherms (A) and pore size distributions (B) of the synthesized catalysts and Al <sub>2</sub> O <sub>3</sub> support. ....	73
Figure 5.2. X-Ray diffraction patterns of ceria and tungsten promoted nickel/alumina catalysts.....	75
Figure 5.3. DRIFTS spectra of the difference between pyridine adsorbed and fresh samples of the synthesized catalysts. ....	77
Figure 5.4. NH <sub>3</sub> -TPD desorption curves of the synthesized catalysts. ....	78
Figure 5.5. Temperature programmed reduction analysis results and H <sub>2</sub> consumption values of the synthesized catalysts (mmol/g <sub>cat</sub> ).....	81

Figure 5.6. SEM images of synthesized catalysts with electron (left) and backscattering electron (right) detector: A) Ni@20CeO <sub>2</sub> @Al <sub>2</sub> O <sub>3</sub> , B) Ni@10W-10CeO <sub>2</sub> @Al <sub>2</sub> O <sub>3</sub> , C) Ni@20W@Al <sub>2</sub> O <sub>3</sub> (Magnification: 50000, and the scale: 2 μm in all images).....	82
Figure 5.7. The effect of catalyst content on the average gas product composition for the DSR reaction (GHSV=7500, H <sub>2</sub> O/C=2.5, 800°C). .....	86
Figure 5.8. Change of hydrogen yield with respect to time for the Ni@Al <sub>2</sub> O <sub>3</sub> , Ni@10CeO <sub>2</sub> @Al <sub>2</sub> O <sub>3</sub> and Ni@10W-10CeO <sub>2</sub> @Al <sub>2</sub> O <sub>3</sub> (GHSV=7500, H <sub>2</sub> O/C=2.5, 800°C).....	88
Figure 5.9. The effect of catalyst content on the average gas product composition in the ATR reaction (GHSV=7500 h <sup>-1</sup> , H <sub>2</sub> O/C=2.5, O <sub>2</sub> /C=0.5, 800°C).....	89
Figure 6.1. N <sub>2</sub> adsorption/desorption isotherms (A) and pore size distributions (B) of Ru incorporated catalysts. ....	93
Figure 6.2. X-Ray diffraction patterns of the ceria and ruthenium promoted nickel/alumina catalysts. ....	94
Figure 6.3. TPR results of ruthenium loaded materials.....	96
Figure 6.4. TPR results of ruthenium and ceria loaded materials. ....	97
Figure 6.5. DRIFTS spectra of the difference between pyridine adsorbed and fresh samples of the ceria and ruthenium promoted nickel/alumina catalysts.....	98
Figure 6.6. Scanning electron detector images of A) 1.5Ru@10CeO <sub>2</sub> @Al <sub>2</sub> O <sub>3</sub> , B) 1.5Ru@20CeO <sub>2</sub> @Al <sub>2</sub> O <sub>3</sub> , and backscattering electron detector images of C) 1.5Ru@10CeO <sub>2</sub> @Al <sub>2</sub> O <sub>3</sub> , and D) 1.5Ru@20CeO <sub>2</sub> @Al <sub>2</sub> O <sub>3</sub> catalysts (Magnification: 100000 and the scale: 1 μm in all images).....	99
Figure 6.7. Scanning electron detector images of A) Ni@1.5Ru@10CeO <sub>2</sub> @Al <sub>2</sub> O <sub>3</sub> , B) Ni@1.5Ru@20CeO <sub>2</sub> @Al <sub>2</sub> O <sub>3</sub> , and backscattering electron detector images of C) Ni@1.5Ru@10CeO <sub>2</sub> @Al <sub>2</sub> O <sub>3</sub> , and D) Ni@1.5Ru@20CeO <sub>2</sub> @Al <sub>2</sub> O <sub>3</sub> catalysts.....	100
Figure 6.8. Scanning electron detector images of A) Ni@1.5Ru@Al <sub>2</sub> O <sub>3</sub> , B) Ni@1.0Ru@Al <sub>2</sub> O <sub>3</sub> , C) Ni@0.5Ru@Al <sub>2</sub> O <sub>3</sub> , and backscattering electron detector image of D) Ni@1.5Ru@Al <sub>2</sub> O <sub>3</sub> , E) Ni@1.0Ru@Al <sub>2</sub> O <sub>3</sub> , and F) Ni@0.5Ru@Al <sub>2</sub> O <sub>3</sub> catalysts (Magnification: 100000 and the scale: 1 μm in all images).....	101

Figure 6.9. The effect of catalyst content on the average product gas composition in the DSR reaction (GHSV=7500 h <sup>-1</sup> , H <sub>2</sub> O/C=2.5, 800°C).....	104
Figure 6.10. The effect of catalyst content on the average gas product composition in the ATR reaction (GHSV=7500 h <sup>-1</sup> , H <sub>2</sub> O/C=2.5, 800°C).....	106
Figure 6.11. Long term activity test of the Ni@0.5Ru@Al <sub>2</sub> O <sub>3</sub> catalyst in DSR (GHSV=7500 h <sup>-1</sup> , H <sub>2</sub> O/C=2.5, 800°C).....	108
Figure 6.12. TGA result of samples taken from two different parts of the used Ni@0.5Ru@Al <sub>2</sub> O <sub>3</sub> catalyst at the reaction time of thirty four hours. ....	108
Figure 6.13. Scanning electron detector images of Ni@0.5Ru@Al <sub>2</sub> O <sub>3</sub> catalyst A) after long-term activity test (34 h), B) after six hours activity test, and backscattering electron detector images of Ni@0.5Ru@Al <sub>2</sub> O <sub>3</sub> catalyst C) after long term activity test (34 h), and D) after six hours activity test.....	109
Figure 6.14. N <sub>2</sub> adsorption/desorption isotherms (A) and pore size distributions (B) of fresh and used Ni@0.5Ru@Al <sub>2</sub> O <sub>3</sub> catalyst in long term DSR reaction. ....	110
Figure 6.15. XRD patterns of fresh and used Ni@0.5Ru@Al <sub>2</sub> O <sub>3</sub> catalyst for long term DSR reaction. ....	110
Figure 7.1. N <sub>2</sub> adsorption/desorption isotherms (A) and pore size distributions (B) of the synthesized support materials .....	113
Figure 7.2. N <sub>2</sub> adsorption/desorption isotherms (A) and pore size distributions (B) of nickel impregnated catalysts. ....	114
Figure 7.3 X-Ray diffraction patterns of synthesized materials. ....	116
Figure 7.4. TPR results of synthesized EISA supports and nickel impregnated materials .....	118
Figure 7.5. DRIFTS spectra of the difference between pyridine adsorbed and fresh samples of the synthesized Al <sub>2</sub> O <sub>3</sub> -EISA, 10CeO <sub>2</sub> -Al <sub>2</sub> O <sub>3</sub> -EISA, 20CeO <sub>2</sub> -Al <sub>2</sub> O <sub>3</sub> -EISA, 20CeO <sub>2</sub> @Al <sub>2</sub> O <sub>3</sub> -EISA, and 8CeO <sub>2</sub> -2ZrO <sub>2</sub> @Al <sub>2</sub> O <sub>3</sub> -EISA support materials.....	120
Figure 7.6. DRIFTS spectra of the difference between pyridine adsorbed and fresh samples of the synthesized catalysts: A) Ni@Al <sub>2</sub> O <sub>3</sub> -EISA, B) Ni@10CeO <sub>2</sub> -Al <sub>2</sub> O <sub>3</sub> -EISA, C) Ni@8CeO <sub>2</sub> -2ZrO <sub>2</sub> @Al <sub>2</sub> O <sub>3</sub> -EISA, d) Ni@20CeO <sub>2</sub> -Al <sub>2</sub> O <sub>3</sub> -EISA, and E) Ni@20CeO <sub>2</sub> @Al <sub>2</sub> O <sub>3</sub> -EISA. ....	121

Figure 7.7. NH <sub>3</sub> -TPD results of synthesized materials: A) Ni@Al <sub>2</sub> O <sub>3</sub> -EISA, B) Ni@10CeO <sub>2</sub> -Al <sub>2</sub> O <sub>3</sub> -EISA, C) Ni@20CeO <sub>2</sub> -Al <sub>2</sub> O <sub>3</sub> -EISA, D) Ni@20CeO <sub>2</sub> @Al <sub>2</sub> O <sub>3</sub> -EISA, and E). Ni@8CeO <sub>2</sub> -2ZrO <sub>2</sub> @Al <sub>2</sub> O <sub>3</sub> -EISA. ....	122
Figure 7.8. Scanning electron detector images of A) 10CeO <sub>2</sub> -Al <sub>2</sub> O <sub>3</sub> -EISA and B) 8CeO <sub>2</sub> -2ZrO <sub>2</sub> @Al <sub>2</sub> O <sub>3</sub> -EISA (Magnification: 100000 and the scale: 1 μm in both images). ....	124
Figure 7.9. Scanning electron detector images of A) Ni@10CeO <sub>2</sub> -Al <sub>2</sub> O <sub>3</sub> -EISA, B) Ni@8CeO <sub>2</sub> -2ZrO <sub>2</sub> @Al <sub>2</sub> O <sub>3</sub> -EISA, and backscattering electron detector images of C) Ni@10CeO <sub>2</sub> -Al <sub>2</sub> O <sub>3</sub> -EISA and D) Ni@8CeO <sub>2</sub> -2ZrO <sub>2</sub> @Al <sub>2</sub> O <sub>3</sub> -EISA (Magnification: 100000 and the scale: 1 μm in all images). ....	124
Figure 7.10. Scanning electron detector images of A) Ni@Al <sub>2</sub> O <sub>3</sub> -EISA, B) Ni@20CeO <sub>2</sub> -Al <sub>2</sub> O <sub>3</sub> -EISA, and C) Ni@20CeO <sub>2</sub> @Al <sub>2</sub> O <sub>3</sub> -EISA (Magnification: 100000 and the scale: 1 μm for all images). ....	125
Figure 7.11. The effect of catalyst content on the average gas product composition in the DSR reaction (GHSV=7500 h <sup>-1</sup> , H <sub>2</sub> O/C=2.5, 800°C). ....	127
Figure 7.12. DSR activity test results of Ni@10CeO <sub>2</sub> -Al <sub>2</sub> O <sub>3</sub> -EISA (—) and Ni@8CeO <sub>2</sub> -2ZrO <sub>2</sub> -Al <sub>2</sub> O <sub>3</sub> -EISA (···) catalysts with respect to time (GHSV=7500 h <sup>-1</sup> , H <sub>2</sub> O/C=2.5, 800°C). ....	127
Figure 7.13. The effect of catalyst content on the average gas product composition obtained from DSR reaction at harsh reaction conditions (GHSV=17000 h <sup>-1</sup> , H <sub>2</sub> O/C=1.5, 800°C). ....	130
Figure 7.14 The effect of catalyst content on the side product formation and the ratio of CO to CO <sub>2</sub> obtained from the DSR reaction at harsh reaction conditions (GHSV=17000 h <sup>-1</sup> , H <sub>2</sub> O/C=1.5, 800°C). ....	131
Figure 7.15. Coke deposition in the DSR reaction at harsh reaction conditions (GHSV=17000 h <sup>-1</sup> , H <sub>2</sub> O/C=1.5, 800°C). ....	131
Figure 7.16. Comparison of gas average product composition obtained from the DSR reaction and the ATR reaction in the presence of Ni@10CeO <sub>2</sub> -Al <sub>2</sub> O <sub>3</sub> -EISA and Ni@8CeO <sub>2</sub> -2ZrO <sub>2</sub> @Al <sub>2</sub> O <sub>3</sub> -EISA catalysts (GHSV=7500 h <sup>-1</sup> , H <sub>2</sub> O/C=2.5, 800°C)	132

Figure 7.17. Long term Ni@10CeO <sub>2</sub> -Al <sub>2</sub> O <sub>3</sub> -EISA activity test result in the DSR reaction (GHSV=7500 h <sup>-1</sup> , H <sub>2</sub> O/C=2.5, 800°C).....	133
Figure 7.18 SEM images of used Ni@8CeO <sub>2</sub> -2ZrO <sub>2</sub> @Al <sub>2</sub> O <sub>3</sub> -EISA catalyst: A) scanning electron detector, B) backscattering electron detector (Size units are in μm, magnification: 100000 and the scale: 1 μm). .....	135
Figure 7.19. SEM images of used Ni@10CeO <sub>2</sub> -Al <sub>2</sub> O <sub>3</sub> -EISA catalyst: A) scanning electron detector, B) backscattering electron detector (Size units are in μm, magnification: 100000 and the scale: 1 μm). .....	135
Figure 7.20 SEM images of long term used Ni@10CeO <sub>2</sub> -Al <sub>2</sub> O <sub>3</sub> -EISA catalyst: A) scanning electron detector, B) backscattering electron detector (Size units are in μm, magnification: 100000 and the scale: 1 μm). .....	136
Figure 7.21. N <sub>2</sub> adsorption/desorption isotherms (A) and pore size distributions (B) of fresh and used in long term DSR activity test (Ni@10CeO <sub>2</sub> -Al <sub>2</sub> O <sub>3</sub> -EISA).....	138
Figure 7.22. TEM images of long term used Ni@10CeO <sub>2</sub> -Al <sub>2</sub> O <sub>3</sub> -EISA catalyst in DSR activity test (Size units are in nm). .....	139
Figure 7.23. XRD patterns of Ni@10CeO <sub>2</sub> -Al <sub>2</sub> O <sub>3</sub> -EISA catalyst; fresh and used in long term DSR activity test. ....	139
Figure 8.1. N <sub>2</sub> adsorption/desorption isotherms (A) and pore size distributions (B) of the synthesized support materials. ....	144
Figure 8.2. N <sub>2</sub> adsorption/desorption isotherms (A) and pore size distributions (B) of the synthesized nickel impregnated materials.....	145
Figure 8.3 X-Ray diffraction patterns of synthesized materials .....	146
Figure 8.4 The TPR results of the synthesized support materials and nickel impregnated catalysts with baseline correction and deconvolution of TPR spectra.	149
Figure 8.5 NH <sub>3</sub> -TPD results of synthesized materials: A) Ni@10Mg-Al <sub>2</sub> O <sub>3</sub> -EISA, B) Ni@10W-10Mg-Al <sub>2</sub> O <sub>3</sub> -EISA, C) Ni@10W-10CeO <sub>2</sub> -Al <sub>2</sub> O <sub>3</sub> -EISA, D) Ni@20W-Al <sub>2</sub> O <sub>3</sub> -EISA, and E) Ni@10W-Al <sub>2</sub> O <sub>3</sub> -EISA.....	151

Figure 8.6 DRIFTS spectra of the difference between pyridine adsorbed and fresh samples of the 10Mg-Al <sub>2</sub> O <sub>3</sub> -EISA, 10W-10CeO <sub>2</sub> -Al <sub>2</sub> O <sub>3</sub> -EISA, 10W-10Mg-Al <sub>2</sub> O <sub>3</sub> -EISA, 20W-Al <sub>2</sub> O <sub>3</sub> -EISA, and 10W-Al <sub>2</sub> O <sub>3</sub> -EISA supports.....	153
Figure 8.7 DRIFTS spectra of the difference between pyridine adsorbed and fresh samples of synthesized Ni@10Mg-Al <sub>2</sub> O <sub>3</sub> -EISA, Ni@10W-10CeO <sub>2</sub> -Al <sub>2</sub> O <sub>3</sub> -EISA, Ni@10W-10Mg-Al <sub>2</sub> O <sub>3</sub> -EISA, Ni@20W-Al <sub>2</sub> O <sub>3</sub> -EISA, and Ni@10W-Al <sub>2</sub> O <sub>3</sub> -EISA catalysts. ....	154
Figure 8.8 Scanning electron detector image of A) Ni@10Mg-Al <sub>2</sub> O <sub>3</sub> -EISA, B) Ni@10W-10Mg-Al <sub>2</sub> O <sub>3</sub> -EISA, C) Ni@10W-10CeO <sub>2</sub> -Al <sub>2</sub> O <sub>3</sub> -EISA, and backscattering electron detector image of D) Ni@10Mg-Al <sub>2</sub> O <sub>3</sub> -EISA, E) Ni@10W-10Mg-Al <sub>2</sub> O <sub>3</sub> -EISA and F) Ni@10W-10CeO <sub>2</sub> -Al <sub>2</sub> O <sub>3</sub> -EISA (Size units are in μm, magnification: 100000 and the scale: 1 μm in all images). ....	156
Figure 8.9 Scanning electron detector image of A) Ni@10W-Al <sub>2</sub> O <sub>3</sub> -EISA (Magnification: 50000 and the scale: 2 μm), B) Ni@20W-Al <sub>2</sub> O <sub>3</sub> -EISA (Magnification: 100000 and the scale: 1 μm), and backscattering electron detector image of D) Ni@10W-Al <sub>2</sub> O <sub>3</sub> -EISA, E) Ni@20W-Al <sub>2</sub> O <sub>3</sub> -EISA. ....	157
Figure 8.10. Effect of catalyst content on the average product gas composition during DSR experiments (GHSV=7500 h <sup>-1</sup> , H <sub>2</sub> O/C=2.5, 800°C). ....	159
Figure 8.11. X-Ray diffraction patterns of fresh and used Ni@10W-Al <sub>2</sub> O <sub>3</sub> -EISA catalyst (6 h DSR reaction, GHSV= 7500 h <sup>-1</sup> , 800 °C, H <sub>2</sub> O/C=2.5).....	163
Figure 8.12. Comparison of average gas product composition obtained from the DSR reaction and the ATR reaction in the presence of Ni@10Mg-Al <sub>2</sub> O <sub>3</sub> -EISA and Ni@10W-10CeO <sub>2</sub> @Al <sub>2</sub> O <sub>3</sub> -EISA catalysts (GHSV=7500 h <sup>-1</sup> , H <sub>2</sub> O/C=2.5, O <sub>2</sub> /C=0.5 (ATR), 800°C).....	165
Figure 8.13. Coke deposition comparison of Ni@10Mg-Al <sub>2</sub> O <sub>3</sub> -EISA catalyst after the DSR and ATR reactions. ....	165
Figure 8.14. Long term Ni@10Mg-Al <sub>2</sub> O <sub>3</sub> -EISA activity test result in the DSR reaction (GHSV=7500 h <sup>-1</sup> , H <sub>2</sub> O/C=2.5, 800°C).....	167
Figure 8.15. Long-term Ni@10Mg-Al <sub>2</sub> O <sub>3</sub> -EISA activity test result in the DSR reaction in terms of hydrogen yield and molar side product formation to diesel .....	167

Figure 8.16. Scanning electron detector images of used catalysts A, C) Ni@10Mg-Al <sub>2</sub> O <sub>3</sub> -EISA, D, E) Long Term Ni@10Mg-Al <sub>2</sub> O <sub>3</sub> -EISA, and backscattering electron detector image of B) Ni@10Mg-Al <sub>2</sub> O <sub>3</sub> -EISA, and F) Long Term Ni@10Mg-Al <sub>2</sub> O <sub>3</sub> -EISA (Magnification: 100000, and the scale: 1 μm). .....	169
Figure 8.17. SEM images of used Ni@10W-Al <sub>2</sub> O <sub>3</sub> -EISA catalyst: A) scanning electron detector, B) backscattering electron detector (Magnification: 100000, and the scale: 1 μm). .....	170
Figure 8.18. N <sub>2</sub> adsorption/desorption isotherms (A) and pore size distributions (B) of fresh and used in long term DSR activity test (Ni@10Mg-Al <sub>2</sub> O <sub>3</sub> -EISA). .....	171
Figure 8.19 XRD patterns of fresh and used Ni@10Mg-Al <sub>2</sub> O <sub>3</sub> -EISA catalyst in long term DSR activity test. ....	171
Figure 8.20. TEM images of long term used Ni@10Mg-Al <sub>2</sub> O <sub>3</sub> -EISA catalyst in DSR reaction. ....	173
Figure 9.1. Performance of synthesized catalysts in the DSR reaction (GHSV= 7500 h <sup>-1</sup> , .....	177
Figure 9.2. Performance of synthesized catalysts in the ATR reaction (GHSV= 7500 h <sup>-1</sup> , .....	178
Figure 9.3. Hydrogen formation rate and coke deposition results of synthesized commercial Al <sub>2</sub> O <sub>3</sub> supported W and/or CeO <sub>2</sub> incorporated catalysts in the DSR reaction: A) Hydrogen production rate per mass of catalyst (mmol/h.g <sub>catalyst</sub> ), B) Hydrogen production rate per surface area of catalyst (mmol/h.m <sup>2</sup> <sub>catalyst</sub> ), and C) Hydrogen production rate per acid capacity of catalyst (mmol/h.mmolacid sites), (GHSV= 7500 h <sup>-1</sup> , 800 °C, H <sub>2</sub> O/C=2.5). .....	180
Figure 9.4. Hydrogen formation rate and coke deposition results of synthesized commercial Al <sub>2</sub> O <sub>3</sub> supported Ru and/or CeO <sub>2</sub> incorporated catalysts in the DSR reaction. ....	182
Figure 9.5. Hydrogen formation rate and coke deposition results of synthesized tungsten, ceria, magnesium, zirconia incorporated EISA catalysts in the DSR reaction .....	184

## LIST OF ABBREVIATIONS

### ABBREVIATIONS

APUs	Auxilliary Power Units
ATR	Diesel Autothermal Reforming
CAPEX	Capital Expenditure
CNG	Compressed Natural Gas
DRIFTS	Pyridine Adsorbed Diffuse Reflectance Infrared Fourier Transform Spectroscopy
DS	Direct Synthesis
DSR	Diesel Steam Reforming
EDX	Energy Dispersed X-Ray
EISA	Evaporation Induced Self-Assembly
FC	Fuel Cell
GC	Gas Chromatography
GC-MC	Gas Chromatography-Mass Spectroscopy
GHSV	Gas Hourly Space Velocity
LNG	Liquified Natural Gas
MCFC	molten carbonate fuel cell
NH <sub>3</sub> -TPD	NH <sub>3</sub> Temperature Programmed Desorption
PAFC	Phosphoric acid fuel cell
PEMFC	proton-exchange membrane fuel cell
POX	Diesel Partial Oxidation
SEM	Scanning Electron Microscopy
SOFC	Solid oxide fuel cell
TCD	Thermal Conductivity Detector
TEM	Transmission Electron Microscopy
TGA	Termogravimetric Analysis
TPR	Temperature Programmed Reduction
TRL	Technology Readiness Level
WGSR	Water Gas Shift Reaction
WI	Wet Impregnation
XRD	X-Ray Diffraction

## **CHAPTER 1**

### **INTRODUCTION**

The motivation of this study was the application of combined reformer-fuel cell-auxillary power unit stationary system for electricity generation. Application of hydrogen powered fuel cells for stationary auxiliary power unit applications (APU) is an efficient and attractive technology in terms of providing the required power instead of running engines that generate high NO<sub>x</sub>, SO<sub>x</sub>, particulates emissions. Since fuel cells operate with hydrogen as the feed, Fuel Cell – APU systems should include either a large and pressurized hydrogen storage vessel or a process that converts a fuel into a gas with a high hydrogen content such as a reformer unit which is suggested in this study. For the application of in-situ hydrogen production through a reformer-fuel cell-APU combined technology in near future, hydrogen should be produced from practical fuels that already has an available distribution system such as diesel. Catalytic reforming process of diesel produces hydrogen rich gas, which can be directly fed to solid oxide fuel cells. The main drawbacks of diesel reformers are high reaction temperature requirement of diesel reforming reaction and catalyst deactivation. Moreover, there is no consensus in the literature about the optimum operating condition for the diesel reforming reaction. The main objective of this study was the development of diesel reforming catalyst that could withstand high reaction temperature, achieve high hydrogen production and preserve its high activity in a stable manner in a long term operation. Catalyst design studies included the investigation of different metal oxide incorporation to nickel/alumina catalyst to enhance the resistivity of the catalysts towards deactivation. The effect of the application of different synthesis methods for the synthesis of support materials was also investigated in order to obtain a catalyst with the highest hydrogen production capacity. Prior to catalyst investigation studies, the first goal was the determination of

optimum operating conditions of both reactions by analyzing the effects of feed composition and the contact time of the feed with the catalyst bed. Optimization of operating conditions as a first step enabled the determination of the optimum catalyst composition/synthesis method that would yield the highest hydrogen production.

### **1.1. The Importance of Hydrogen as an Energy Carrier**

The development of solutions for energy related problems is the main research area worldwide. As a result of industrial and technological developments in the world, low priced and clean energy is not just a commercial tool anymore, it directly affects the life quality of the population<sup>1</sup>. Technological developments shifted the energy sources from firewood and water mills towards hydroelectric energy, coal, oil, gas, nuclear energy, solar energy, wind energy, and others over the years. An increase in world population, technological developments and an increase in life standards are the biggest cause of the depletion of primary energy resources, which are the natural energy sources such as coal, petroleum, and natural gas<sup>1-3</sup>.

Studies of alternative energy are increasing due to economic and environmental concerns about the future of our world. Even though renewable energy resources such as wind and solar energies are promising, instability and non-storability of the produced energy limits the use of it. Among all alternatives, hydrogen is seen as an excellent energy carrier mainly due to its reducing effect on the environmental problems of fossil fuels and carbon footprint. Besides, the energy of hydrogen per unit mass is much higher compared to fossil fuels that are being used today, but hydrogen cannot be found in nature due to its high reactivity<sup>4</sup>. Other main advantages of hydrogen can be listed as<sup>5,6</sup>:

- ✓ It is a non-toxic and clean energy carrier.
- ✓ Hydrogen can be obtained using fossil fuels or renewable sources.
- ✓ Development in technology allows easy distribution of hydrogen according to the end user needs.
- ✓ Hydrogen can also be used in the production of valuable hydrocarbons.

- ✓ Hydrogen can be stored and then used for the production of electricity in fuel cells or directly used as fuel in automobiles.

### 1.1.1. Hydrogen powered fuel cells

A large proportion of total energy is spent in the transportation sector worldwide, and the major energy consumption occurs due to cars and motorbikes of road transport, as it can be seen in Figure 1.1. Even though the use of alternative technologies are growing, internal combustion engine is still mainly being used today for power generation. However, low thermal efficiency and high NO<sub>x</sub>, SO<sub>x</sub>, CO, and CO<sub>2</sub> emissions of internal combustion engines lead to advances in new technologies for transportation sector. Even though catalytic converters are being used to minimize emissions, they do not eliminate SO<sub>x</sub> and CO<sub>2</sub> emissions<sup>7</sup>. Hydrogen powered fuel cells becoming one of the most efficient technologies for converting chemical energy into electricity.

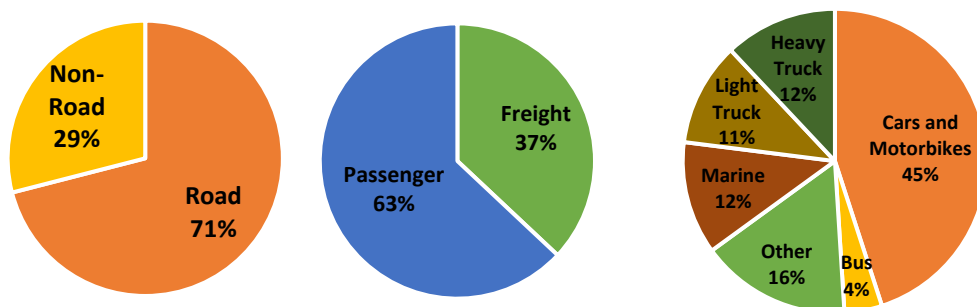


Figure 1.1. Breakdown of energy usage in the transport sector globally in 2015<sup>8</sup>.

The most important technology in terms of clean and alternative energy is the production of electricity through fuel cell technology. Fuel cells offer higher electrical efficiency compared to internal combustion engines or other combined heat and power systems, as it can be seen in Figure 1.2. Some of the other reasons for the importance of fuel cell technology are<sup>9,10</sup>:

- It provides clean energy as long as the production technique of hydrogen is clean.

- It increases the efficiency of energy distribution.
- It reduces environmentally pollutant substances and emissions of greenhouse gases.
- It reduces noise, considerably.

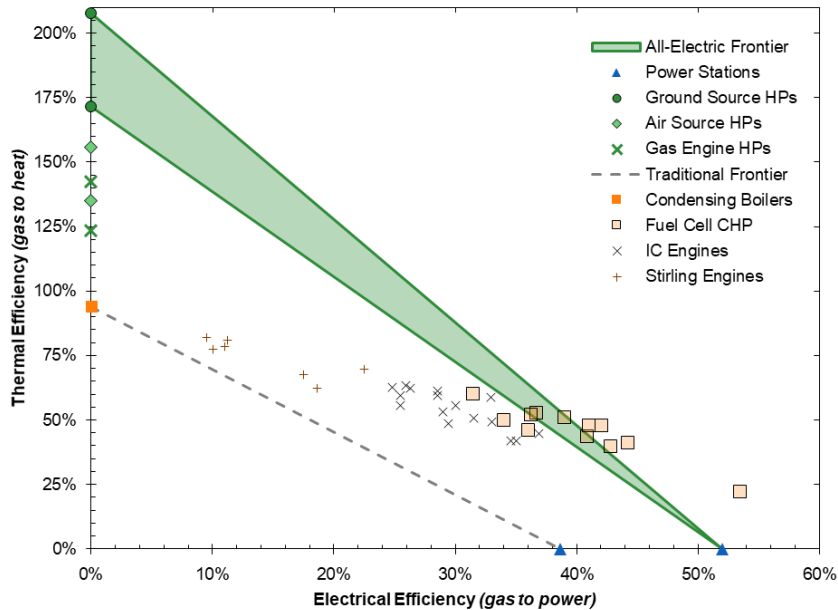


Figure 1.2. Thermal and electrical efficiencies of combined heat and power systems (Retrieved from: Staffel, 2015)<sup>11</sup>.

Nowadays, fuel cell powered vehicles are commercially available in which hydrogen is produced through mostly electrolysis process and stored at very high pressures. Automobile companies such as Toyota, Hyundai, and Honda are producing fuel cell electric passenger vehicles, and other major companies of the sector, such as Audi, Mercedes-Benz and others, are also developing their technologies<sup>8,12,13</sup>. Around 3000 electric vehicles powered by a fuel cell were sold until 2018 and commercial use of developed technology is becoming more widespread<sup>8</sup>. Use of fuel cells in the transport sector is not limited to only passenger vehicles, fuel cell applications are also started or planned for commercial buses, trucks, motorbikes, trains, ships, forklift trucks, and aircrafts.

To eliminate the high cost of electrolysis and usage of high pressured hydrogen tanks, studies are being conducted for the development of optimum hydrogen production, transportation, and storage technologies. Hydrogen can be produced from carbonaceous energy carriers: fossil fuels or renewable sources. Major production methods include steam reforming and gasification of liquid hydrocarbons, coal gasification and electrolysis (

Table 1.1). Gasification processes lead to low efficiency with a high energy requirement. Electrolysis attracts attention due to its renewable nature, but it is an extremely inefficient process that consumes significant amounts of electricity with the available technology. Among the major production methods, the highest efficiency and the lowest energy requirement can be obtained by using methane reforming as the hydrogen production route currently, according to

Table 1.1.

Table 1.1. The efficiency and energy consumption of hydrogen production methods<sup>8</sup>.

<b><i>Production Method</i></b>	<b><i>Efficiency % (lower heating value, LHV)</i></b>	<b><i>Energy Requirement (kWh/kgH<sub>2</sub>)</i></b>
<b><i>Methane Reforming</i></b>	65-75	44-51
<b><i>Electrolysis</i></b>	51-67	50-65
<b><i>Coal Gasification</i></b>	45-65	51-74
<b><i>Biomass Gasification</i></b>	44-48	69-76

Current fuel cell vehicles require stored hydrogen which is a costly solution. Hydrogen is required to be compressed and then filled in a tank. Liquid phase storage requires very low temperature and gas phase storage and transportation require special and expensive system that should not allow diffusion of hydrogen through the transportation material. Production and storage processes of hydrogen lead to fuel cell vehicles with high operational costs. In recent years, in-situ production of hydrogen

for fuel cells was proposed. Big automobile companies developed in-situ fuel reforming systems in the late 1990s by using light hydrocarbons such as methanol. Since then, researchers have been focused on in-situ systems and auxiliary power units (APUs)<sup>14,15</sup>. Costly storage problems of hydrogen can be eliminated by using conventional fuels such as gasoline, diesel or jet fuel, or alternative bio-fuels for on-site and on-demand hydrogen production. Besides, the use of these fuels for in-situ hydrogen production is more economical considering that they have more chemical energy in volume basis when compared to hydrogen (Table 1.2), and they already have the built-in transportation system worldwide<sup>14–19</sup>. Reforming system integrated fuel cells can be used in both stationary and mobile applications for power generation<sup>20</sup>. When the APUs with fuel cell systems that uses liquid fuel reforming products as feed, they can be used for on-board power generation in heavy-duty trucks or aircrafts. It was seen that net efficiency was much higher for this combined system compared to conventional technologies<sup>21</sup>.

Table 1.2. Energy contents and carbon emissions of hydrogen and conventional and alternative fuels<sup>16,22</sup>

Fuel Type	Energy		Specific carbon emission (kg C/kg fuel)
	(J/kg)	(J/m <sup>3</sup> )	
Liquid Hydrogen	141.90	10.10	0.00
Gaseous Hydrogen	141.90	0.013	0.00
Fuel Oil	45.50	38.65	0.84
Gasoline	47.40	34.85	0.90
Diesel	45.27	38.66	0.86
Jet Fuel	46.50	35.30	-
LPG	48.80	24.40	0.82
Methanol	22.30	18.10	0.50
Ethanol	29.90	23.60	0.50
Bio-diesel	37.00	33.00	0.50
Natural Gas	50.00	0.04	0.46
Charcoal	30.00	-	0.50

Among different types of fuel cells, solid oxide fuel cell is an ideal candidate to be used as an on-site electricity production device with its important properties. Generally, proton-exchange membrane fuel cell (PEMFC) type is being used in passenger vehicles that use platinum as a catalyst, and PEMFC is significantly affected by the impurities such as CO and H<sub>2</sub>S in fuel. Phosphoric acid fuel cells (PAFC) and molten carbonate fuel cells (MCFC) have a higher tolerance to impurities in fuel compared to PEMFC. Solid oxide fuel cells (SOFC) has more advantage in terms of H<sub>2</sub>S/S and CO presence in the fuel (Table 1.3). Another beneficial property of SOFC is the operating temperature which is in the range of 650°C and 800°C, because it allows direct supply of the reforming products (hydrogen rich gas), which are obtained in the same temperature range, without using any cooling process<sup>14,15</sup>.

Table 1.3. Specific fuel requirements of different fuel cell types<sup>8</sup>.

<i>Fuel Cell Type</i>	<i>Sulphur (S, H<sub>2</sub>S) in ppm</i>	<i>Carbon monoxide (CO)</i>	<i>Ammonia (NH<sub>3</sub>) %</i>
<i>PEMFC</i>	<0.1	<10-100 ppm	Poison
<i>PAFC</i>	<50	<0.5-1%	<4
<i>MCFC</i>	<1-10	Fuel	<1
<i>SOFC</i>	<1-2	Fuel	<0.5

In the long-term, use of bio-fuels for hydrogen production would be economical and sustainable. However, considering that gasoline and diesel will be the main fuels that will be used for long time, in the transition period towards alternative fuels these conventional liquid fuels (diesel, gasoline or jet-fuel) are considered as excellent candidates for the production of hydrogen with their readily available infrastructure and high energy density. Today, the most commonly used hydrogen production technique is steam reforming of natural gas, but centralized production of hydrogen leads to additional infrastructure and transportation costs. When on-board production of hydrogen from liquid fuels for auxiliary power units (APUs) is used in especially heavy duty vehicles, additional distribution and storage costs can be eliminated. For

these reasons, hydrogen production from liquid fuels (diesel, bio-diesel, methanol, ethanol etc.) is accepted as a promising approach for mid-term operations. Other than transportation systems, on-board hydrogen production system from diesel fuel can also be used in chemical industry such as hydrogenation or chemical synthesis reactions that require hydrogen<sup>7,10</sup>.

### **1.1.2. Market Research for Hydrogen & Fuel Cells**

Fuel cell market can be analyzed in two categories which are product category and application category. As product, different fuel cell types can be listed as PEMFC, PAFC, SOFC, MCFC and others. Application areas include stationary, transportation and portable applications. Market size of fuel cells is expected to increase five times the current volume and revenue in 2025. Fuel cells already became an alternative backup power option and the key factor in growing fuel cell market is seen as the increasing demand for unconventional energy sources<sup>23</sup>.

Market analysis shows that transportation sector will expand in a fast way due to increasing demand. PEMFC had the highest fuel cell market share (>65%) followed by PAFC, MCFC, SOFC and others, in 2015. PEMFC possess the largest share due to its ability to be used in a variety of applications such as forklifts, automobiles, telecommunications, data centers, primary systems and backup power systems. Projections show that SOFC will become the fastest growing fuel cell type with an 39% increase in market share due to economic reasons. SOFC operates at higher ratio values of the electricity produced to consumed hydrogen, than the rest of the fuel cell types and can be used in transportation and stationary applications. Another advantage of SOFC is that it operates at high temperatures (700-900 °C) which facilitates higher reaction kinetics and eliminates the need to use precious metals as catalysts. According to application areas of fuel cells, the highest market share belonged to stationary followed by portable and transportation applications in 2015. Stationary fuel cells are expected to have the largest application that will account for more than 70% of the market<sup>23</sup>.

Among transport applications, buses and cars have reached a high technological readiness level, while heavy duty trucks and trains are still developing as it can be seen from Figure 1.3. Among stationary applications, hydrogen injection to gas grids, residential combined heat and power systems and off-grid power reached a high technological readiness level. In terms of economic competitiveness, trains have the highest advantage. Buses, cars, port operations, power to hydrogen and residential combined heat and power technologies have developed a medium level of competitiveness<sup>24</sup>.

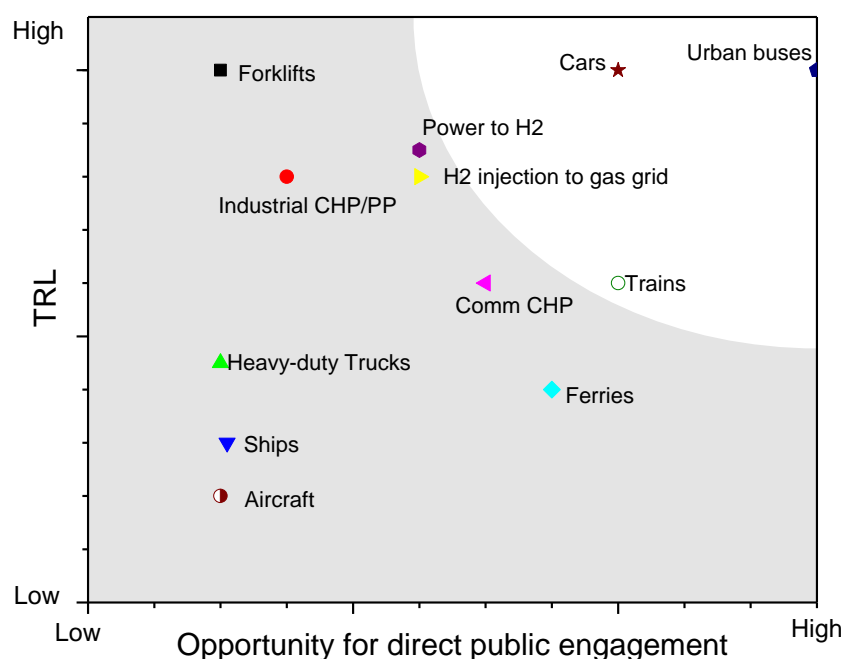


Figure 1.3 Technological readiness level and opportunity for direct public engagement of fuel cell applications<sup>25</sup>.

Development of large-scale fuel cell technology will lead to use of fuel cell modules in trains in the medium-term. Hydrogen-driven trains are expected to have the same availability as diesel trains. Moreover, the operation range of a fully fueled hydrogen-train (600-800 km) is expected to reach the range of a diesel train (1000 km). Other than technology, fuel cell trains are also expected to reach the same annualized total cost of ownership of diesel trains<sup>24,25</sup>. The capital expenditure (CAPEX) of fuel cell deployment in heavy duty trucks will projected to decrease to lower than its half value

until 2030, as it can be seen from Table 1.4. Other than CAPEX, power consumption and maintenance costs will also decrease and fuel cell driven heavy duty trucks will be competitive to diesel fuel cell trucks<sup>25</sup>. However, environmental concerns about the emissions caused by the use of diesel is expected to limit the use of diesel trucks. Even though diesel trucks are more economical, future emission regulations will eventually eliminate the widespread use of diesel trucks. This situation will accelerate the transition period from diesel trucks towards the fuel cell driven ones.

Table 1.4. The differences in cost and consumption values of heavy duty trucks with fuel cells and diesel engines<sup>25</sup>.

	<i>Year</i>	<i>Fuel Cell Truck</i>	<i>Diesel Truck</i>	<i>CNG/LNG Truck</i>
<i>CAPEX (€)</i>	2015	302000-334000	62000-68000	95000-105000
	2030	115000-127000	78000-86000	136000-150000
<i>Consumption (kWh/km)</i>	2015	1.91-2.11	2.27-2.51	2.53-2.79
	2030	1.64-1.82	1.80-1.98	2.03-2.25
<i>Maintenance (€/km)</i>	2015	0.48-0.53	0.15-0.16	0.17-0.19
	2030	0.11-0.12	0.15-0.16	0.15-0.16
<i>Range (distance)</i>		Medium-High	High	Medium-High

For stationary applications of fuel cells as off-grid solutions, they are generally compared with diesel generators. Even though the cost of fuel cells is significantly higher (3-4 times) than diesel generators, the electrical efficiency of a fuel cell is almost twice that of a diesel generator which also has a higher maintenance cost. Currently, high cost of fuel cells prevent their applications for off-grid solutions, but further performance improvements and reduction of costs will eventually lead to stationary fuel cell systems to become widespread over diesel generators. Moreover, CO<sub>2</sub> emissions due to off-grid solutions will significantly decrease during this

transition, even though the hydrogen is produced from fossil fuels. Eventually it will be eliminated by the use of green hydrogen<sup>24,25</sup>.

Currently, production of hydrogen can be performed by reforming of natural gas in the most economical way (<2 €/kgH<sub>2</sub>)<sup>25</sup>. The electrolysis process for hydrogen production has the highest cost (4-12 €/kgH<sub>2</sub>). Depending on the fuel prices and sustainability requirements, the cost of centralised electrolysis, decentralised gas reforming and centralised biomass pathways for hydrogen production is expected to decrease (Figure 1.4)<sup>25</sup>.

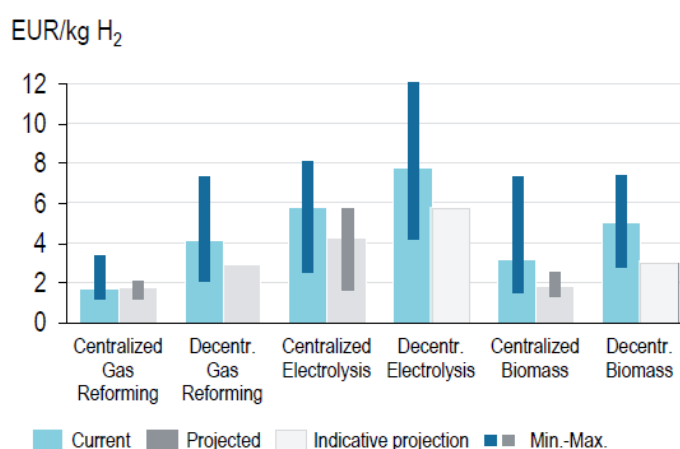


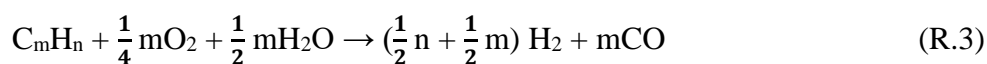
Figure 1.4. Cost of hydrogen production: current and projected<sup>25</sup> (retrieved from *Ruf et al.*, 2017).

## 1.2. Reforming of diesel fuel

Since the acceleration of hydrogen economy (1990s), hydrogen production through reforming was accepted as a transition technology for fuel cell systems towards on-board hydrogen supply. On-board reforming was even considered for modern internal combustion engines to increase their performance and after treatment units. Pure hydrogen produced from reforming can be a supplement to the main engine fuel that enables more efficient engine emission control<sup>26</sup>.

Hydrogen production from liquid fuels is generally carried out by using diesel, gasoline and jet fuel through reforming processes. Diesel and jet fuel are being used in aircrafts and ships and they are preferred as logistical fuels in military applications. The reason of the preferability of diesel in military applications is its high thermal efficiency and low flammability compared to gasoline. Diesel is also preferred due to its high power and hydrogen density and that it is an accepted fuel by public<sup>27</sup>. For these reasons, the use of diesel for hydrogen production through reforming processes attracts the attention of researchers. However, reforming system of diesel fuel can be problematic in terms of system design and operation. Application of the reforming reactions with diesel is challenging due to its wide range of hydrocarbons with different types of compounds. Diesel is a complex mixture of paraffins, olefins, cycloalkanes and aromatics and also includes sulphur and additive compounds. Different empirical formulas were reported in the literature for diesel and some of these formulas are; C<sub>12</sub>H<sub>20</sub><sup>28</sup>, C<sub>14.342</sub>H<sub>24.75</sub>O<sub>0.0495</sub><sup>29</sup>, C<sub>13.4</sub>H<sub>26.3</sub>, C<sub>13.57</sub>H<sub>27.14</sub><sup>30</sup>, C<sub>16.2</sub>H<sub>30.6</sub><sup>31</sup>, C<sub>13.3</sub>H<sub>24.7</sub><sup>10</sup>. High carbon content of diesel leads to coke formation on catalyst which causes deactivation and decreases catalytic activity. Other than coke formation, sulphur compounds that are present in diesel affect the catalyst activity and fuel cell electrolytes.

Conversion of diesel into hydrogen rich gas can be accomplished through three catalytic reactions which are partial oxidation reaction (POX, R.1), steam reforming reaction (DSR, R.2) and autothermal reforming reaction (ATR, R.3).



The most commonly studied process for hydrogen production from diesel is steam reforming reaction (DSR). It is an endothermic reaction and requires additional heat input. Through this reaction, very high hydrogen concentration and high efficiency can

be obtained. According to the literature, about 70-80% hydrogen by volume can be accomplished with SR reaction. Hydrogen production and coking rates can be adjusted by changing steam-to-carbon ratio. However, initiation time of this reaction is quite long, so it would be better to use this process in stationary fuel cell applications instead of mobile and portable fuel cell applications<sup>15,32</sup>.

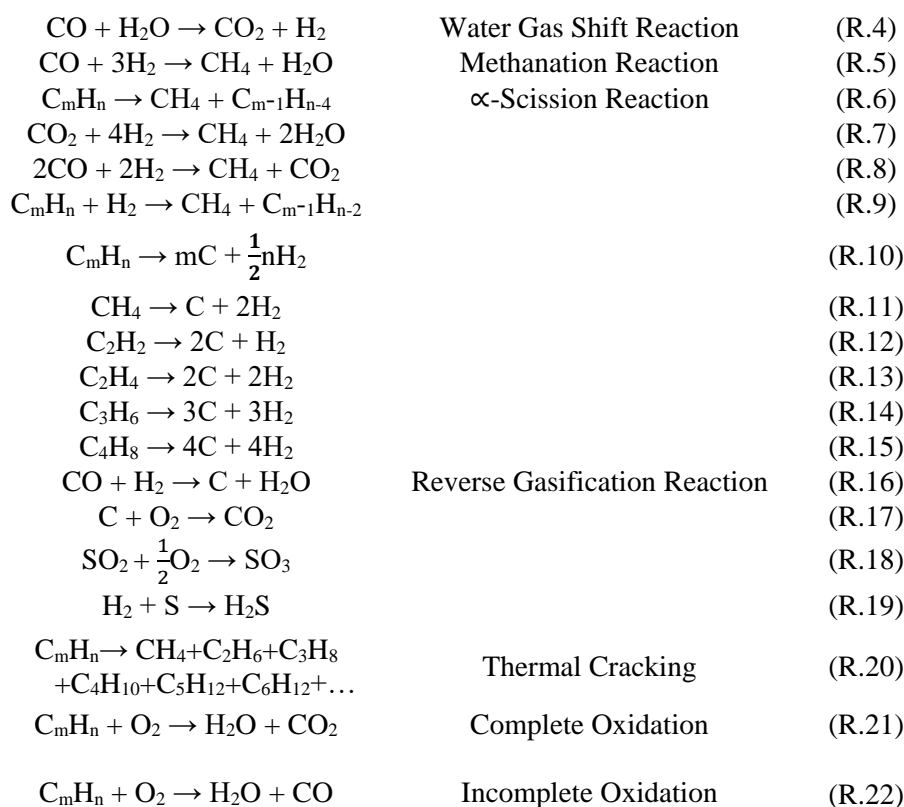
POX reaction is used for the production of synthesis gas. This reaction is quite exothermic and carried out at a temperature range of 1100°C-1200°C to avoid coke formation. Resulting hydrogen concentration in the product stream is very low compared to DSR reaction and it is about 35-40% by volume. Some advantages of POX compared to DSR are; POX reactor is more compact, has fast initiation time and fast response time to variations in process parameters such as flow rate and temperature. POX reaction can be carried out with or without a catalyst. Use of catalyst decreases the reaction temperature from 1200°C to 800-900°C. Sulphur in the feed stream is poisonous to the catalyst, for this reason catalysts with resistance to sulphur should be used<sup>15,32</sup>.

Autothermal reforming of diesel reaction is the combination of steam reforming and partial oxidation reactions. In ATR reaction, diesel reacts with both steam and oxygen that could be supplied from air. The energy generated from partial oxidation reaction supplies the energy requirement of the steam reforming reaction, which makes ATR an almost neutral reaction. For this reason, ATR reaction has better response to dynamic changes and easier control of reformer temperature and also less hot-spot formation along the reactor compared to DSR. Besides the energy requirement, oxygen present in the reaction environment reduces the formed coke on the catalyst. However, separation of nitrogen in the product gas becomes a problem when ATR reaction is carried out with air. Hydrogen concentration in the product gas is higher compared to POX reaction. Even though this reaction does not require an additional heat input during normal operation, a small energy input is required only at the initiation of oxidation reaction which does not occur at room temperature. Initiation stage of autothermal reaction is called "light-off". At this stage, 10% of diesel undergoes complete combustion reaction. This stage is characterized with light-off temperature

and affected from oxygen-to-carbon ratio, fuel and catalyst types. Autothermal reforming of diesel yields mostly hydrogen, carbon monoxide, carbon dioxide, methane and water vapor. Ethane and ethylene formation can also be observed due to decomposition reactions.

Theoretical or experimental investigations on catalytic reforming reaction of diesel are problematic due to the complex hydrocarbon content of diesel such as olefins, paraffin, cycloalkanes and aromatics. The aromatic content of diesel complicates dehydrogenation reaction which is necessary for reforming reaction<sup>27</sup>. The exact mechanism of diesel steam reforming reaction is still in discussion since reaction kinetics are highly dependent on the chemical nature of the reformed molecules<sup>28</sup>. It is accepted that steam reforming of hydrocarbons with high carbon numbers occurs by irreversible adsorption on catalyst surface yielding C1 compounds. Then surface reaction mechanism converts C1 compounds to CO which is then converted to CO<sub>2</sub> through water gas shift reaction<sup>10</sup>. For the autothermal reforming reaction, there is no generally accepted mechanism. Reaction mechanism, like every reaction, highly depends on the catalyst, fuel properties, reaction conditions. However, two mechanisms were described for aliphatic and/or aromatic hydrocarbon reforming reactions: combustion-reforming mechanism and pyrolysis-oxidation mechanism. Even though the mechanisms were not described in detail for the proposed mechanisms, the basic descriptions in the literature are given as follows. For the first one: it was stated that fuel firstly undergoes combustion with all available oxygen at the top portion of the catalyst bed leading to formation of CO<sub>2</sub> and H<sub>2</sub>O. Unconverted fuel reacts on the rest of the catalyst to form syngas or hydrogen rich gas. It was also found that for nickel catalysts, nickel in the inlet of the catalyst bed oxidizes by the oxygen in the feed leading to formation of NiO that promotes combustion reaction. The second pyrolysis-oxidation mechanism involves the formation of CO and H<sub>2</sub> through partial oxidation reaction. Similar to the mechanism described for DSR, hydrocarbon dissociatively adsorbs on catalyst surface for a first step and the catalyst takes part in scission of C-C bonds. The formed C1 species then reacts with adsorbed O<sub>2</sub> or steam and H<sub>2</sub> and CO form.

Even though the main aim is the production of hydrogen in hydrocarbon reforming reactions, methane formation is generally observed due to occurrence of side reactions. Carbon monoxide also forms through reverse methanation reaction (R. 5) and reverse methane dry reforming reaction (R. 8). Methane formation occurs if the catalyst zone of reforming system has temperature gradients and if there are inactive catalyst zones through R. 5, R. 7 and R. 8. Another formation route of methane is  $\alpha$ -scission reaction (R. 6)<sup>33,34</sup>. Another product of this reaction is  $C_{m-1}H_{n-4}$  which is then reformed and converted to  $H_2$ ,  $CO$ ,  $CO_2$  and other hydrocarbons. Experimental investigations were performed with hydrocarbons such as decalin, tetradecane, n-heptane, n-dodecane, n-hexadecane which are accepted as substitutes of diesel, since reaction mechanism cannot be found due to complex structure of diesel<sup>33,35</sup>. Other than the basic reactions given below and reactions which occur on catalyst surface, hundreds of gas phase reactions take place in diesel reforming system<sup>36</sup>.



### 1.2.1. Operating conditions of diesel reforming reactions

Gas hourly space velocity (GHSV) indicates the residence time of the reacting gases in catalyst bed. It correlates the reacting gas velocity with catalyst volume and has a significant impact on conversion and product distribution. Low contact time indicates large GHSV (50000-100000 h<sup>-1</sup>), when large GHSV is combined with low temperature, reaction yields mostly towards aldehydes, ketones, cracking products and dehydration products of aromatics. As the temperature and contact time increase, hydrogen and carbon monoxide yields enhance due to reforming of mid-products. According to Shigarov et al.<sup>33</sup>, the highest hydrogen yield can be obtained at a GHSV value of 2000-10000 h<sup>-1</sup> and at a temperature range of 840-880°C. Cheekatamarla and Lane<sup>20</sup> analyzed the effect of GHSV on product distribution by changing GHSV range of 9000 and 35000 h<sup>-1</sup>. When it increased from 9000 to 17000 h<sup>-1</sup> hydrogen yield increased only 3% and no significant change in product distribution was observed. Hydrogen yield was enhanced due to the decrease in mass transfer resistance. When GHSV value was increased to a higher value than 18000 h<sup>-1</sup>, a decrease in hydrogen concentration and an increase in carbon monoxide concentration in the product stream were observed. It was due to the increase of catalyst activity towards reverse water gas shift reaction and the optimum GHSV value was selected as 17000 h<sup>-1</sup>. Guggilla et al.<sup>9</sup> investigated the effect of GHSV change on the catalyst activity by changing the catalyst amount in autothermal reforming of n-dodecane. When it was changed between 48000 and 96000 h<sup>-1</sup>, hydrogen yield was seen to decrease with an increase in GHSV and become stable after 160000 h<sup>-1</sup>. It was stated that low GHSV values which mean high contact time with catalyst enhance yields of hydrogen and carbon dioxide and slightly lower carbon monoxide yield.

Diesel, oxygen and water concentrations in the feeding gas are important parameters for autothermal and steam reforming reactions of diesel. These concentrations have significant impact on formation of coke and hot spots though catalyst bed and hydrogen yield. Generally preferred water to carbon ratio in the feeding gas is between 1 and 3 and oxygen to carbon ratio range is 0.3 and 1<sup>15</sup>. It was

reported that a stoichiometric amount of water to carbon ratio is enough for steam reforming reaction, excess steam concentration provides water gas shift reaction. Significant change in product distribution was not observed when water to carbon ratio is changed between 1 and 3. Further increase in steam amount reduced coke formation in the catalyst zone, but also decreased thermal efficiency of the system mainly because increase in water amount reduced temperature of the system by increasing thermal load. Maximum hydrogen yield was obtained when oxygen to carbon ratio was between 0.7-1.2<sup>37</sup>. According to Shigarov et al.<sup>33</sup>, optimum water to carbon ratio is 1.5-1.7 and oxygen to carbon ratio is 0.5-0.6. Ibarreta et al.<sup>38</sup>, studied optimization through simulation and autothermal reforming of jet fuel A and reported that water and oxygen to carbon ratios and inlet temperature have an important effect on hydrogen yield. Low oxygen to carbon ratio does not allow exothermic oxidation reaction to supply the required heat for endothermic reforming reaction. Similarly, low water to carbon ratio does not activate steam reforming reaction enough. Researches showed that operating temperature depends on oxygen in the reaction environment and the highest temperature obtained on catalyst bed indicates the ending point of oxidation reaction and starting point of steam reforming reaction. This high temperature can be adjusted by changing oxygen to carbon ratio. Low temperature indicates low oxygen in the feeding gas leading to lower hydrogen yield due to lower rate steam reforming reaction. High temperature is also not desired because of the possibility of catalyst deactivation. Cheekatamarla and Lane<sup>39</sup> studied the effect of steam and oxygen to carbon ratio on diesel autothermal reforming reaction with a GHSV value of 17000 h<sup>-1</sup> over 1%Pt/Ceria catalyst. As oxygen to carbon ratio was increased, a decrease in hydrogen yield and increase in carbon dioxide concentration were observed. Hydrogen yield was 55% (Dry, without N<sub>2</sub>) when oxygen to carbon ratio was 0.5 and water to carbon ratio was 2.5. Creaser et al.<sup>40</sup> studied modelling of diesel autothermal reforming reaction and analyzed the effect of oxygen to carbon ratio by keeping water to carbon ratio at 2.3. Increasing oxygen amount enhanced both temperature and fuel conversion. It reduced water amount in the effluent stream by increasing reforming activity. They later analyzed steam to carbon ratio by increasing this value to 2.9: results showed

increased heat requirement for reforming reaction<sup>40</sup>. Pasel et al.<sup>41</sup> studied autothermal reforming of kerosene with oxygen to carbon ratio range of 0.43-0.47 and water to carbon ratio range of 1.7-1.9. When oxygen ratio was increased and water ratio decreased, reaction temperature increased as a result of fast kinetics of oxidation reaction. When water ratio was raised, hydrogen concentration in the product gas increased due to enhanced kinetics of water gas shift reaction with excess water vapor in the reaction zone. Low oxygen ratio enhanced hydrogen yield. Water to carbon ratio was found to have no impact on methane formation<sup>41</sup>. Guggilla et al.<sup>18</sup> analyzed the effect of water to carbon ratio on kinetics of steam reforming of n-dodecane by changing it between 1.5 and 3. It was seen that hydrogen and carbon dioxide yields increase and carbon monoxide yield decreases up to the ratio of 2.5. Feeding water above the necessary ratio increases the rate of endothermic steam reforming reaction, but leads to a drop in the catalyst temperature. This drop changed the equilibrium of water gas shift reaction and prevented carbon formation. Above the steam to carbon ratio value of 2.5, a drop in reactor system thermal efficiency was reported and optimum ratio range was found to be 2-2.5<sup>18</sup>. In another study, Guggilla et al.<sup>9</sup> analyzed the effect of water to carbon ratio on reforming of diesel, by changing it between 1.5 and 4 at an oxygen to carbon ratio of 0.35 and a GHSV value of 160000 h<sup>-1</sup>. Net positive effect on hydrogen yield was clearly observed when water to carbon ratio range is 1.5 and 2. Increasing water amount leads to increase in carbon dioxide yield and decrease in carbon monoxide yield as a result of enhanced water gas shift reaction kinetics. Besides, drop in methane formation indicates steam reforming of methane reaction kinetics with increasing water amount. When this ratio is 1.5, cracking reactions suppresses the reaction environment and coke formation deactivates the catalyst<sup>9</sup>.

### **1.2.2. Catalysts for diesel reforming reactions**

There are two critical issues about the hydrogen production through reforming of liquid fuels: high cost of the catalysts and the lack of precise knowledge of deactivation

pathways during reforming reactions<sup>42</sup>. These challenges lead to research on development of cheap, active, poison-resistant and renewable catalysts. A bifunctional catalyst is required in reforming reactions that consists of an active metal loaded catalyst with a moderate acidic property. Metal function is responsible from the dehydrogenation of paraffins and naphthenes, hydrogenation of olefins and aromatics and hydrogenolysis of paraffins which are demethylation and deethylation leading to the production of methane and ethane<sup>43</sup>. Besides the complex reaction kinetics, high reaction temperature (800-1000°C) causes thermal sintering, metal vaporization and poisoning of catalyst by sulphur and coke deposition. Especially low steam to carbon ratio and hydrocarbons with high molecular weight in diesel are main reason of coking problem in this reaction. Catalysts used in reforming of hydrocarbons with high carbon number have been investigated for years. Generally preferred catalysts for this type of reactions are noble (Pt, Pd, Ru and Rh) and transition (Fe, Ni and Co) metals loaded supports that are stable at high temperatures such as alumina, mixed metal oxides, ceria, zirconia and lanthanum. Noble metal based catalysts are very efficient with their stable and high activity and resistivity towards coking. However, their high cost limits their usage as main active catalyst component. Nickel based catalysts are cheap alternative for noble metals, but they lose their activity quickly due to sulphur and coke deposition<sup>35,42,44</sup>.

Other than high temperature stability, several other important physicochemical properties are required for catalyst support in diesel reforming reactions. Some of these are<sup>45</sup>:

- ✓ Support should provide high melting point with high thermal stability due to high reaction temperatures of gas phase reactions which are 700-800 °C. Surface reactions could occur even at higher temperatures (900-1100 °C).
- ✓ It should possess high surface area and mechanical strength.
- ✓ Support material should preserve its metal dispersion and should resist sintering and volatilization of active metals.
- ✓ It should have a role in catalytic activity and hydrogen generation capability, and removing deposited coke and sulphur from active sites of the catalyst.

- ✓ It should possess certain porosity in terms of pore size and shape distribution to provide easiness in impregnation and dispersion of active metals and catalytic activity in reforming reactions.

Supports serve as a substrate for the dispersion of active metal which makes them crucial for catalytic activity and stability. Besides their role in thermal stability, it was suggested that they also play an active role in reforming reactions. It has been found that deactivation of a catalyst is mainly depends on the support material and the acidity of the support materials promotes carbon formation by promoting dehydrogenation and cracking reactions. Metal oxides that are divided into two types as reducible and irreducible metal oxides are generally tested as support materials in heterogeneous catalysts. Irreducible metal oxides such as  $\text{Al}_2\text{O}_3$ ,  $\text{MgO}$  and  $\text{La}_2\text{O}_3$  are more traditional support materials due to their high thermal stability and low cost. Generally, alumina is used as heterogeneous catalyst support due to its high melting point ( $\sim 2000^\circ\text{C}$ ), high surface area and thermal stability<sup>46</sup>. Alumina can exist in different crystallographic forms, and generally gamma ( $150 \text{ m}^2/\text{g}$ ) and delta ( $100 \text{ m}^2/\text{g}$ ) alumina are being used as catalyst support in reforming reactions<sup>45</sup>. The acid sites in a support material are important and the most common surface acid sites are Lewis acid sites. They are believed to be active in stabilization of active metals in reaction to prevent coke deposition and sintering of metals<sup>47</sup>. Despite its high acidity amongst the mostly preferred support materials (in terms of acidity;  $\text{Al}_2\text{O}_3 > \text{ZrO}_2 > \text{TiO}_2 > \text{ZnO} > \text{SiO}_2 > \text{La}_2\text{O}_3 > \text{MgO}$ ), acidic character was also believed to decrease particle size of metals which improves activity and lowers coke deposition<sup>46</sup>.

In order to eliminate coking problem in reforming of hydrocarbons, studies focused on catalyst formulation and operating conditions of reactions. Coke deposition is observed on both catalyst bed and tubing before the catalyst bed due to high carbon number and aromatic composition of diesel. Besides increasing steam to carbon ratio in the feeding gas, this problem can also be solved by selecting catalysts with high coke resistance. In methane and ethanol steam reforming reactions, acidic properties and coke deposition was attempted to be reduced by the impregnation of alkaline earth oxides such as  $\text{MgO}$  or  $\text{CaO}$  on nickel based alumina supported catalysts. For nickel

to be active in steam reforming reactions, it should be in a metallic form instead of an oxide form, with small crystal size. Nickel catalysts are reduced at high temperatures with hydrogen before their application in reforming reactions. Addition of MgO and CaO to the catalyst reduced coke formation, but also reduced the activity of the catalyst towards reforming reaction by decreasing the reducibility of the catalyst<sup>48,49</sup>. Potassium compounds are generally used as promoters in catalysts to reduce coke formation in industry. Even though they reduce coke deposition, they also have many disadvantages such as: reducing catalyst activity, vaporization at high temperature and high vapor pressure and leading corrosion in reactor system. Borowiecki et al.<sup>50</sup> studied minimization of coke formation in steam reforming of n-butane using molybdenum and tungsten incorporated nickel-alumina catalysts. Compared to potassium addition, molybdenum addition enhanced catalyst activity tenfold. It was seen that molybdenum does not gasify the deposited coke, it prevents the formation of coke in the first place<sup>50</sup>.

In order to optimize catalyst activity, rare earth metal oxides are added to nickel based catalysts. Among rare earth metal oxides, ceria is seen as the best promoter. Ceria can modify structural and electronic properties of many catalysts of many reactions such as cracking of heavy oil, automotive exhaust gas conversion, methane reforming with CO<sub>2</sub> or steam and water gas shift reaction. It is preferred mainly because of its properties such as unique acid-base and redox behavior, high oxygen mobility, good hydrogen storage capacity, enhancing interaction between support and active metal on catalyst and changing crystal phase transformation. High oxygen storage capability of ceria is due to the high reducibility of Ce<sup>+4</sup>. Using ceria as the support material or promoter increases metal dispersion. Ceria also increases catalytic activity of nickel catalysts and it has high coke resistivity due to its good redox potential and interaction with nickel. It prevents diffusion and dissolution of carbon clusters on nickel crystals. Besides, it provides the environment for increasing steam adsorption on the surface of the catalyst which cleanses formed coke through rising active surface oxygen concentration. When zirconia is added to the structure of ceria, it improves thermal stability, reducibility and sulphur tolerance of ceria<sup>18,45,51</sup>. Since

ceria is an expensive material, researches are focused on the synthesis of ceria incorporated support materials with high surface areas instead of direct application of ceria as support material. Thormann et al.<sup>52</sup> stated that ceria promoted noble metal loaded alumina or silica supported catalysts are known as the best catalysts for steam reforming reactions. Other than reforming, these catalysts are also quite active for water gas shift reaction. Ceria plays an active role in steam reforming reactions in adsorbing steam and allowing surface diffusion of steam and oxygen. It was reported that at high temperatures (>600 °C) and in reducing atmospheres, CeO<sub>2</sub> and Al<sub>2</sub>O<sub>3</sub>, which were being used as support, react and form CeAlO<sub>3</sub> like species. The nucleation of CeAlO<sub>3</sub> takes place by diffusion of Al<sup>3+</sup> ions in partially reduced CeO<sub>2</sub> lattice. Since the size of Al<sup>3+</sup> is smaller compared to Ce<sup>3+</sup>, diffusion easily takes place at high temperatures. Ce<sup>3+</sup> ions could also incorporate into the vacant positions of alumina lattice<sup>53</sup>. It was also found that the presence of nickel promotes the transformation of CeO<sub>2</sub> and Al<sub>2</sub>O<sub>3</sub> into CeAlO<sub>3</sub>. Several authors stated that CeAlO<sub>3</sub> like species play a key role in removal of carbon residues<sup>54,55</sup>. Small amount of CeO<sub>2</sub> incorporation provides improvement in dispersion of active sites and enhancement in phase stability, shifting phase transformation temperature to higher temperatures of active  $\gamma$ -Al<sub>2</sub>O<sub>3</sub> to  $\alpha$ -Al<sub>2</sub>O<sub>3</sub> which has low surface area. According to Kim et al.<sup>55</sup>, formation of CeAlO<sub>3</sub> during autothermal reforming of methane with NiCe/Al catalysts resulted in acceleration of coke and CO oxidation. In the dry reforming of methane reaction, low ceria loading was found to be the most effective in enhancing thermal stability of alumina. The authors observed an improvement in dispersion of nickel and a reduction of NiAl<sub>2</sub>O<sub>4</sub> X-Ray Diffraction (XRD) peak intensities for ceria promoted alumina catalysts. These results suggest a diminished interaction between Ni and Al<sub>2</sub>O<sub>3</sub> by CeO<sub>2</sub><sup>56</sup>.

Tungsten compounds form active and stable catalysts for many chemical processes. Tungsten has been widely used in hydrocracking, hydrotreating, dehydrogenation and isomerization of petroleum compounds as catalyst component. In its early uses, when it was used with nickel, tungsten catalyst showed promising activity towards

hydrocracking of heavy bottoms of petroleum refining products which have high sulfur content. This catalyst showed high desulfurization activity and low coke formation. Tungsten incorporated nickel catalysts were tested for isomerization of normal paraffins in naphtha. According to results, tungsten incorporation enhanced the life time of the catalyst. Due to its ability to dehydrogenate naphthenes to aromatics and isomerize normal paraffins, tungsten was also considered for reforming reactions of naphtha. Compared to platinum catalysts, it is more resistant to impurities and poisons and do not require purified feedstock<sup>57</sup>.

Tungsten is known to react with proposed active metal components: Ni, Co and Ru which could lead to formation of  $\text{NiW}_2$ ,  $\text{NiW}$ ,  $\text{Ni}_4\text{W}$ ,  $\text{Co}_3\text{W}$ ,  $\text{Co}_7\text{W}_6$ ,  $\text{W}_3\text{Ru}_2$ <sup>58</sup>. Sheng and Fang<sup>59</sup> reported the enhancement effect of tungsten on the structure and sulfur tolerance of nano-nickel based catalysts for the hydrogenation of aromatic compounds. Poisoning mechanism of metals, as in the nickel case by sulfur compounds involves chemisorption of strong sulfur containing species on the sites of metal which leads to formation of stable and active metal-sulfur species. Metal-sulfur bond is strong for metals with high electron donor ability. Sulfur resistance of nickel catalysts can be increased by enhancing electron-deficient character of Ni sites. Sheng and Fang<sup>59</sup> reported the formation of  $\text{NiWO}_4$  species, reducing electron density of Ni atoms which decreased Ni-S bond. Tungsten was also proved to be an effective catalyst component for coke minimization in dry reforming of methane by Arbag et al.<sup>60</sup> due to redox ability of  $\text{WO}_x$ .

Studies showed that rhodium and ceria catalysts are quite active for steam reforming of hexadecane, but not active enough to bring water gas shift reaction to near equilibrium due to an increase in the ceria crystal size at high calcination temperature (800°C). Increase of crystal size leads to a change in the crystal structure of ceria and reduced its oxygen transfer capability<sup>52</sup>. Perovskite oxide catalysts have been developed and used as successful promoters. During the reductive conditions of steam reforming reaction, these materials disperse on catalysts as small crystals and become strong and stable oxides. It is proven that  $\text{LaCoO}_3$  is a successful promoter in

diesel steam reforming reaction. Reduction of  $\text{LaCoO}_3$  lead to formation of well dispersed Co crystals which has very high reforming activity and lanthanum oxides bring high stability and coke resistance to the catalyst. However this material has very low surface area which is the main disadvantage considering the low probability of interaction between active sites and reacting gases<sup>27,61</sup>. Kaila and Krause<sup>35</sup> studied zirconia supported rhodium and platinum catalysts and compared them with commercial  $\text{NiO}/\text{Al}_2\text{O}_3$  catalyst. Zirconia was preferred due to its high stability, bi-functional and amphoteric properties, and lower acidity compared to commercial alumina materials. Noble metals were preferred due to their resistivity towards coke and sulphur deposition. These catalysts were tested using n-dodecane and n-heptane blends instead of diesel. It was seen that main products were hydrogen and carbon oxides, side products were ethene and methane. While coke formation and catalyst deactivation were observed with  $\text{NiO}/\text{Al}_2\text{O}_3$  catalyst, noble metal loaded zirconia catalysts showed small amount of coke formation<sup>35</sup>. According to Kim et al.<sup>44</sup>, hydrotalcite type materials can be used in reforming, hydrogenation and polymerization reactions as catalysts. When calcined, they present high surface area, basic properties and form homogeneous mixture with oxides with small crystal sizes. Kim et al.<sup>44</sup> tested nickel and rhodium loaded hydrotalcite composed of magnesium and alumina in steam reforming of n-hexadecane as a diesel substitute. Rhodium loaded catalysts presented their long term activity, activity of nickel loaded catalysts dropped quickly after 45 h of reaction. Murata et al.<sup>62</sup> studied nickel based catalysts modified with alkaline earth metal and iron in steam reforming of methylcyclohexane and iso-octane. Results showed that  $\text{Fe}/\text{Mg}/\text{Al}_2\text{O}_3$  catalyst is quite active towards decomposition of methane in oxygen and carbon dioxide atmosphere. While this catalyst showed the formation of hydrogen, methane and carbon monoxide in reforming of iso-octane, addition of rhodium to this material lead to increase in formation of methane and C2 compounds. This catalyst also showed activity in steam reforming of methylcyclohexane. When  $\text{Ni}/\text{ZrO}_2$  and  $\text{Ni}/\text{Al}_2\text{O}_3$  catalysts were tested in the same reaction, zirconium supported catalyst showed more promising results. When alkaline metals were added to  $\text{Ni}/\text{ZrO}_2$  catalyst, higher activity was observed

with Na and K. When alkaline earth metals were loaded, activity enhancement was observed and hydrogen, methane carbon monoxide and carbon dioxide were obtained as gas products. When these promoters were compared, the most successful alkaline earth metal was strontium, then barium and calcium and lastly magnesium<sup>62</sup>. Wang et al.<sup>63</sup> analyzed autothermal reforming of gasoline and gasoline like fuels using Ni-Re/Al<sub>2</sub>O<sub>3</sub> catalyst. At low temperatures (~500°C), formation of methane and C<sub>2</sub> compounds were not observed. As the temperature increased, hydrogen formation decreased and carbon dioxide production increased. Compared to Ni/Al<sub>2</sub>O<sub>3</sub> catalyst, Ni-Re/Al<sub>2</sub>O<sub>3</sub> presented more stable and higher activity due to coke and sulphur resistance of Re<sup>63</sup>. Another metal that enhances coke resistivity of nickel is tungsten. It was seen that, unlike CaO or MgO, tungsten enhances coke resistivity without reducing catalytic activity of the catalyst due to its good redox potential<sup>64</sup>. Kratzas et al.<sup>45</sup> studied Rh loaded catalysts which was seen as optimum catalysts for autothermal reforming of diesel with its superior activity and resistance to coke and sulphur formation. They stated that the presence of both oxidative and reductive environments in diesel autothermal reforming reaction requires addition of oxidation metals to alloy with Rh to promote initial oxidation reactions. Pt was selected for this task and RhPt alloys were synthesized and tested in diesel reforming reaction. According to these results, RhPt catalyst showed high activity in autothermal reforming of diesel at low loading amounts. The most promising catalyst was selected to be RhPt/Ceria-Zirconia catalyst in terms of diesel conversion and hydrogen and ethylene selectivity. These catalysts were ordered in terms of diesel conversion as: RhPt/CeO<sub>2</sub>-ZrO<sub>2</sub> > RhPt/Al<sub>2</sub>O<sub>3</sub> > RhPt/TiO<sub>2</sub> > RhPt/SiO<sub>2</sub>.

Sulphur in diesel can poison the catalyst in diesel reforming reaction even though it is in trace amounts. The main sulphur compounds in logistic fuels are mercaptanes, sulphides, disulphides, thiophenes, benzothiophenes and dibenzothiophenes. Organic sulphur present in fossil fuels is converted to S<sup>2+</sup> in reforming conditions and reacts with active metals on the catalyst. Since the formed sulphides are not catalytically active, they block the active sites and prevent the adsorption of reacting gases on the catalyst<sup>32</sup>. Sulphur compounds that are expected after reforming reaction are mainly

H<sub>2</sub>S, SO<sub>2</sub> and rarely SO<sub>3</sub> and H<sub>2</sub>SO<sub>4</sub>. Formation of H<sub>2</sub>S and SO<sub>2</sub> generally leads to catalyst deactivation<sup>36</sup>. Researches showed that noble metal loaded catalysts present resistance towards sulphur compounds. Besides, it was stated that when a sulphur adsorbent material is used other than the active metal of the catalyst, this resistance rises. As the acidic properties of the support material rises, resistance to sulphur could be enhanced. For this reason, zirconium was seen as an ideal catalyst support for diesel reforming reaction<sup>65</sup>. Kaila et al.<sup>66</sup> studied Rh and Pt loaded catalysts in autothermal reforming of fuels which has similar properties as diesel and contain 10 ppm H<sub>2</sub>S. According to activity test results, the most active catalyst was bimetallic Pt-Rh loaded zirconia supported catalyst. Reforming of sulphur containing fuels leads to a decrease in activity with respect to time in all catalysts. Coke formation increased with Pt loading and the highest sulphur deposition was found on the Rh loaded catalyst. Reforming of sulphur containing fuels leads to smaller coke formation due to poisoning of active sites of the catalyst with sulphur. Experiments were performed with sulphur containing fuel, and then with the one that has no sulphur compounds in it by using same catalyst. The presence of sulphur decreased the performance of the catalyst. However, when the same catalyst was re-used in the experiment without any sulphur presence, its activity was the same as the activity of a fresh catalyst. It was concluded that presence of sulphur does not cause any permanent activity loss in catalyst due to reversibility of H<sub>2</sub>S adsorption. Gonzales et al.<sup>19</sup> stated the occurrence of sulphur adsorption on CeO<sub>2</sub>-ZrO<sub>2</sub> through formation of a stable sulfide at the temperature range of diesel autothermal reforming reaction, but under reducing conditions material also facilitates desorption of sulphur species as H<sub>2</sub>S which enhances catalyst resistivity.

Other than metal types used in the catalyst, synthesis route used for the preparation of the catalyst plays an important role in its activity. Properties such as total surface area, pore volume and metal distribution on catalyst surface have a huge impact on the catalytic activity of the material and significantly affected by the synthesis technique. Wet impregnation and co-precipitation methods are quite common and extensively used for nickel-alumina catalysts. Wet impregnation technique requires aqueous metal

solution at a desired weight loading to contact with the high surface area support material followed by drying and calcination. The metal precursor type whether it is nitrate, acetate, sulfide or chloride has impact on the nickel particle size since the precursor and support interaction defines the synergetic effect between metal and support material. Weak interaction between metal and support is caused by mainly larger metal particles with small interface with support material<sup>46</sup>. Co-precipitation method on the other hand is performed by precipitation of active metal precursor and support material by adjusting the temperature and pH of the mixture. Impregnation method generally results in higher surface area, larger pore volume and more homogeneous metal dispersion and weak active metal and support interaction compared to co-precipitation method. Stronger active metal and support interaction obtained using co-precipitation method can also lead to activity lost. It was observed that nickel-alumina catalysts prepared with co-precipitation method lost its activity with time in diesel reforming reaction and methane formation was enhanced. The catalyst prepared with impregnation method in the same study showed stable activity for 12 h and lower methane formation was observed<sup>42</sup>. Guggilla et al.<sup>18</sup> stated that one of the most important parts of synthesizing catalysts with high coke resistance is the synthesis method. Synthesis of metal oxides using solution-gelation (sol-gel) method allows obtaining materials with high surface area, unique textural and chemical properties. Ru-Ni-CeO<sub>2</sub>-Al<sub>2</sub>O<sub>3</sub> catalyst was synthesized using sol-gel method and tested in steam reforming of n-dodecane by the authors. In this study addition of ruthenium significantly enhanced its catalytic activity. Increase of nickel loading from 0% to 10% also enhanced its catalytic activity, but reduced hydrogen selectivity due to low homogeneous dispersion of metals on catalyst and higher crystal size of nickel. Success of the catalyst synthesized through this method was due to good metal dispersion, better reducibility of nickel, its high surface area and its alkaline properties. Same catalyst was also tested in autothermal reforming of n-dodecane and showed higher activity compared to the one that does not contain ruthenium. It was stated that ruthenium plays a role in breaking carbon hydrogen bond in nickel catalysts and is a promoter in hydrogen production. Characterization studies also presented enhanced

interaction between ceria-alumina and nickel in the presence of ruthenium<sup>9</sup>. Betancourt et al.<sup>67</sup> stated that activity of ruthenium supported catalysts show a strong dependence on metal dispersion. For ruthenium-alumina systems, ruthenium dispersion decreased as a result of increasing loading amount. Suzuki et al.<sup>68</sup> also used Ru/Al<sub>2</sub>O<sub>3</sub>-CeO<sub>2</sub> catalyst in reforming of kerosene and successful activity test results were obtained for 8000 h. It was stated that addition of ceria significantly enhanced the sulphur resistance of this catalyst. Mota et al.<sup>69</sup> also reported that an ruthenium incorporation into LaCoO<sub>3</sub> catalyst improved its catalytic activity and stability in oxidative steam reforming of diesel.

As a result of literature research on the catalysts for reforming of hydrocarbons, as the base catalyst of this study, Ni-Al<sub>2</sub>O<sub>3</sub> catalysts was selected. Nickel is selected as the main active metal component of the catalysts due to its low cost, availability, superior capability in the cleavage of C-C, C-H and O-H bonds. Quick deactivation due to coke formation and sulphur deposition is a main problem with nickel catalysts, but this issue will be tried to be solved by adjusting catalyst content with coke resistant metals. As mentioned before, several quite important properties such as high thermal stability, high surface area and resistance to coke and sulphur, are required in catalyst support used for reforming of diesel. Alumina is the mostly preferred catalyst and catalyst support in industry. Firstly, commercial alumina pellets were planned to be tested in this research. Besides, mesoporous alumina was planned to be synthesized using evaporation-induced self-assembly method (EISA) which attracted attention among other synthesis methods. Mesoporous alumina is preferred due to having high surface area and hence more active sites which brings easiness of diffusion of reactants through mesopores to these active sites. As the main focus of this study was the development of reforming catalyst with high hydrogen production capability and long term activity and stability, the properties and reforming activity and stability of Ni-Al<sub>2</sub>O<sub>3</sub> catalyst was decided to be improved by the incorporation of different promoters (Ru, Ce, Zr, W, Mg) and their different combinations (Ru-Ce, Ce-Zr, Ce-W, W-Mg).

### 1.2.3. Coke formation in diesel reforming reactions

Reforming reactions has the significant risk of carbon formation that could lead to operational problems. Carbon deposition may occur following different routes which affect the morphology of the carbonaceous deposits. Carbonaceous deposits generally referred as “coke”<sup>70,71</sup>. Baker et al.<sup>70</sup> stated that carbonaceous deposits can be divided into three main types: amorphous, filamentous and graphitic shell like structures. Nielsen<sup>71</sup> recognized the most common types in steam reforming reactions as whisker like carbon, encapsulating carbon and pyrolytic carbons.

Amorphous carbon is believed to be formed via condensation and polymerization reactions in thermal processes<sup>70</sup>. Formation of filamentous and graphitic carbons occurs on a catalyst. Adsorption and decomposition of carbon containing gas molecules may be followed by diffusion and precipitation of carbon atoms on the catalyst particles leading to formation of fibrous (whisker) structures<sup>70</sup>. Growing carbon structures may detach nickel crystals from catalyst resulting a significant catalyst deactivation<sup>71</sup>. Filamentous structures having different morphologies and degrees of crystallinity may form depending on the catalyst properties and reaction operating conditions. Graphitic type carbon also follows a similar formation route as the filamentous carbon. The formation route of these two carbon types differs in the involvement of the catalyst surfaces<sup>70</sup>. Nielsen<sup>71</sup> states that in reforming reactions that uses nickel catalyst; encapsulating carbon forms following a slow polymerization path of  $C_nH_m$  radicals on nickel surface leading to a formation of an graphitic encapsulating film causing progressive deactivation. According to Nielsen<sup>71</sup>, encapsulating carbon forms below  $\sim 500^\circ\text{C}$ , at low steam to carbon ratio and with aromatic feed. On the other hand, pyrolytic carbon formation occurs due to thermal cracking of hydrocarbons and depositon of carbon on catalysts. Pyrolytic carbon type also leads to encapsulation of catalyst particle which causes deactivation and pressure drop along catalyst bed. It requires temperatures above  $\sim 600^\circ\text{C}$ , low steam to carbon ratio and high activity of catalyst<sup>71</sup>.

Mechanism of deactivation of catalysts due to coke formation is different in noble and non-noble metals. Metallic nickel allows carbon diffusion and dissolution in nickel crystals and prone to formation of whisker type coke. Filamentous carbon forms through repeated process of carbon formation, diffusion and dissolution on nickel clusters<sup>71</sup>. These types of carbons form through reactions R.10, R.11, R.12, R.13, R.14, R.15, R.16 and Boudouard reaction (R. 23). As the coke deposition continues, catalyst dissolution causes disintegration of catalyst integrity until the loss of catalyst activity. Coking is a more serious problem in reforming of fuels with high carbon numbers such as diesel. Hydrocarbon and methane dissociation reactions generally take place at high temperatures. Coke formation through Boudouard and reverse gasification reactions occur at low temperatures. Amorphous carbon can be oxidized at temperatures lower than 400 °C, graphitic and whisker type carbon oxidation can be performed at temperatures higher than 400 °C<sup>36</sup>. Pyrolytic carbon can react with oxygen at above 400 °C.



Coke formation is affected from both active metal and support material of the catalysts. Coking could occur due to support acidity or it can be initiated due to large nickel crystal size for nickel catalysts<sup>42</sup>. Carbon dissolution is not generally observed on noble metals, but different deposition mechanisms can occur. Ruthenium added alumina catalysts are being used in reforming of hydrocarbons for their carbon resistive properties<sup>72</sup>. Catalysts generally lose their activity in reforming of diesel and diesel-like fuels within 100 h. This period could change according to the structure of the catalyst and flow rate of the reactants.

Catalyst deactivation cannot be understood just by analyzing the gas composition obtained during the reforming experiments. Activity can still be observed even if some parts of the catalyst is heavily deactivated. Aromatics, which are the least reactive compounds in liquid hydrocarbon fuels and need higher temperatures for its conversion to reforming products. They are accepted as the main coke precursors

causing severe coke formation and subsequent deactivation of the catalyst<sup>10</sup>. Lin et al.<sup>73</sup> stated that high reactant flow rates cause coke formation in autothermal steam reforming of diesel. During the experiments performed at different GHSV, initiation of coke deposition was observed at a GHSV value of 48500 h<sup>-1</sup>. The probable cause of this observation was probably the occurrence of only cracking reactions leading to coke formation at this limited space time which is not enough for reforming reactions to take place on the catalyst. Initiation of coking is observed through product gas which contains light hydrocarbons. Main precursors of coke formation were identified as ethylene, aromatics and naphthenes. Another research pointed out the initiation of coke formation of steam reforming of biodiesel reaction at a GHSV of 44000 h<sup>-1</sup><sup>74</sup>.

The reason behind the serious carbon deposition problem in diesel reforming reaction was the formation of ethylene. Ethylene was accepted as a serious carbon precursor leading to rapid coke formation during reforming reactions by Joensen and Rostrup-Nielsen<sup>75</sup>. Aromatic compounds in diesel promotes the formation of ethylene which is then transformed into carbon deposits. Performance loss of catalyst was observed following the increase in ethylene formation. According to Yoon et al.<sup>76</sup> ethylene was mostly generated in diesel autothermal reforming reactions through homogeneous gas phase reactions without even reaching to catalyst bed on which it was converted to coke. Thermal cracking reactions of higher hydrocarbons lead to formation of ethylene or other olefins which are then degraded to carbon either in the gas phase at high temperature or on catalyst surface at medium-high temperature<sup>77</sup>.

### 1.3. Objectives

This study focuses on catalyst development for diesel steam and autothermal reforming reactions. Multiple catalyst designs that include Rh<sup>35,44,45,66,78,52</sup>, Ru<sup>18,68,69,78</sup>, Pt<sup>35,66,78,45</sup>, Co<sup>27,61,69</sup>, Fe<sup>62</sup> and Ni<sup>9,18,42,44,55,56,62,79</sup> metals together with various transition metals supported on individual or mixed Zr-, Ce-, Gd-, La-, Mg-, Ti-, Si-, and Al-oxides were tested for reforming reactions of diesel or surrogate of diesel.

Catalysts were designed to achieve the highest activity, stability and the lowest deactivation due to coke formation and sintering of the supported metal particles at the high temperatures of diesel reforming processes. Some authors conducted their reforming studies by using diesel substitutes/surrogates such as hexadecane<sup>52,44</sup>, n-dodecane/n-heptane blends<sup>35</sup>, n-dodecane/n-heptane/methylcyclohexane/toluene blends<sup>66</sup>. Improvements in reforming activity results were achieved through the incorporation of secondary active metal addition such as Ni-Ru or Rh-Pt catalysts, or through the incorporation of promoters to the Al<sub>2</sub>O<sub>3</sub> support material such as La, Mg, Ce, Mg, Zr, Ce-Zr and Gd.

In this study, the main focus was the investigation of the effects of different promoters (Ru, Ce, W, Mg) and their different combinations (Ru-Ce, Ce-Zr, Ce-W, W-Mg) on the catalytic activity of Ni/Al<sub>2</sub>O<sub>3</sub> catalyst in diesel steam and autothermal reforming reactions. The success of the developed catalysts were tested by using diesel fuel acquired from a local gas station. The novelty of this study can be listed as;

- Even though Ru-CeO<sub>2</sub>-Al<sub>2</sub>O<sub>3</sub> catalysts was studied in reforming of kerosene<sup>68</sup> and Ni-Ru-CeO<sub>2</sub>-Al<sub>2</sub>O<sub>3</sub> catalyst was studied for steam reforming of n-dodecane which is a surrogate for jet fuels<sup>18</sup>, the authors did not test the developed catalyst for diesel reforming reactions which is a more complex process due to complex nature of diesel fuel. Moreover, the authors also did not investigate the effect of incorporation amount of CeO<sub>2</sub> and Ru. This study includes the investigation of Ru and CeO<sub>2</sub> incorporation to commercial Al<sub>2</sub>O<sub>3</sub> supports which are then impregnated with Ni (10 wt.%), for diesel steam and autothermal reforming reactions. Catalytic activities were investigated by changing the loading amount of CeO<sub>2</sub> (10 wt.% and 20 wt.%), by changing the loading amount of Ru (0.5 wt.%, 1.0 wt.% and 1.5 wt.%) and also by incorporating both Ru (1.5 wt.%) and CeO<sub>2</sub> (10 wt.% or 20 wt.%) to Ni/Al<sub>2</sub>O<sub>3</sub> catalyst.
- W incorporated catalysts are being used generally in hydrotreatment reactions<sup>80</sup>. They have also been tested for hydrogenation of aromatic

compounds<sup>59</sup> and methane reforming reactions<sup>60,81-83</sup>. In this study, the effect of tungsten incorporation to commercial Al<sub>2</sub>O<sub>3</sub> supported and also CeO<sub>2</sub> incorporated commercial Al<sub>2</sub>O<sub>3</sub> supported nickel catalyst was analyzed in diesel reforming reactions. In spite of the success of tungsten metal in methane reforming and hydrocarbon treating reactions, it was never been tested in reforming of large and complex hydrocarbons before this study.

- Incorporation of metals/metal oxides through impregnation technique is the more commonly used approach for catalyst synthesis. This study also focuses on promoter incorporation through direct/one pot synthesis of different promoters (Ce, Zr, W, Mg) and their different combinations (Ce-Zr, Ce-W, W-Mg) by following a similar synthesis technique developed for mesoporous Al<sub>2</sub>O<sub>3</sub> synthesis; evaporation induced self-assembly (EISA) method described by Gündüz et al.<sup>84</sup>. To our knowledge, Mg, Ca, Mn, Fe, Co, Ni, Cu and Ba were used in one-pot synthesis of mesoporous metal oxide-alumina materials, but CeO<sub>2</sub>, CeO<sub>2</sub>-ZrO<sub>2</sub>, W, CeO<sub>2</sub>-W and W-Mg added synthesis of alumina was tried in this work for the first time<sup>84,85</sup>.
  - Ceria incorporation to catalysts was investigated for reforming reactions of different components such as ethanol<sup>86</sup>, methane<sup>55,56</sup>, n-hexadecane<sup>78</sup>, and diesel<sup>19,78,79</sup>. In diesel reforming studies, for the catalyst synthesis either impregnation technique with commercial powders<sup>19,79</sup> were used or commercial catalyst supports were applied<sup>78</sup>. In this study, nickel impregnated ceria-alumina support materials that contain different ceria amounts (10 wt.% or 20 wt.%) synthesized through EISA method was investigated towards both diesel steam and autothermal reforming reactions. Similarly, the use of CeO<sub>2</sub> and ZrO<sub>2</sub> metal oxides together was previously applied for diesel autothermal reforming reaction in the form of a monolithic catalyst;

(Rh1.0Pt1.0Mg4.0Y5.0/CeO<sub>2</sub>-ZrO<sub>2</sub>) which was prepared by using an impregnation technique<sup>19</sup>, for n-hexadecane and diesel reforming reactions by applying commercial CeO<sub>2</sub>-ZrO<sub>2</sub> mixed oxides with Pt, Ru and Rh active metals<sup>78</sup>, and for diesel autothermal reforming reaction by commercial alumina impregnated with Rh, Pt, CeO<sub>2</sub> and ZrO<sub>2</sub><sup>45</sup>. In this study, the novelty in terms of CeO<sub>2</sub>-ZrO<sub>2</sub> application in reforming catalysts was the synthesis of CeO<sub>2</sub>-ZrO<sub>2</sub>-Al<sub>2</sub>O<sub>3</sub> support materials following the direct synthesis technique of EISA. Synthesized and nickel impregnated catalyst was tested towards both steam and autothermal reforming reactions of diesel, and the results were compared with the test results of CeO<sub>2</sub>-Al<sub>2</sub>O<sub>3</sub> supported nickel catalysts.

- The effect of W incorporation together with CeO<sub>2</sub> or Mg incorporation was analyzed by developing CeO<sub>2</sub>-W-Al<sub>2</sub>O<sub>3</sub> and Mg-W-Al<sub>2</sub>O<sub>3</sub> catalysts which were synthesized through EISA method for the first time in the literature and impregnated with nickel. These catalysts were tested in diesel reforming reactions and catalytic activity results were compared with the results of W-Al<sub>2</sub>O<sub>3</sub>, CeO<sub>2</sub>-Al<sub>2</sub>O<sub>3</sub>, Mg-Al<sub>2</sub>O<sub>3</sub> catalysts.
- After the evaluation of all synthesized catalysts in diesel steam reforming reaction, the best three catalysts was selected according to their hydrogen production capabilities and coke resistivities and their long-term activities were tested.

This study was also focused on parameter investigation for both diesel steam and autothermal reforming reactions. Even though literature suggest some results for the optimum parameters of diesel reforming reactions, there was no study that contain a detailed investigation for a parameter optimization for both reactions. The effects of GHSV and steam to carbon ratio in terms of hydrogen composition in the effluent gas

steam and also coke deposition of the catalyst was analyzed in diesel steam reforming reactions. Apart from GHSV and steam to carbon ratio, the effect of oxygen to carbon ratio was also analyzed for autothermal reforming reaction.

Considering the main focus of this study which is the catalyst investigation and the secondary focus, parameter investigation that is required to achieve the major focus, the beginning goal of this study was the design and construction of a laboratory scale diesel reforming test system that will enable me to test the operating conditions at lower and upper limits of both reactions.



## CHAPTER 2

### CHEMICAL EQUILIBRIUM ANALYSIS

Chemical equilibrium analysis was performed with Gibbs free energy minimization method in order to obtain the compositions of possible products and understand the limits in terms of product composition at different operating conditions (temperature and feed composition) for diesel steam and autothermal reforming reactions. Equilibrium composition analysis was also performed for n-hexadecane steam and autothermal reforming reactions for comparison of its results to results of diesel reforming reactions and observe the differences between these results. Analysis for these diesel and n-hexadecane steam reforming reactions were performed at a temperature range of 500-1000 °C and at a steam to carbon range of 1-3. Analysis for these diesel and n-hexadecane autothermal reforming reactions were performed at a temperature range of 500-1000 °C, at a steam to carbon range of 1-3 and at a oxygen to carbon range of 0.1-1.5. The most important results obtained from these analysis was the fact that hydrogen composition increases with increasing temperature and with increasing steam to carbon ratio for all reactions. For autothermal reforming reactions, hydrogen composition decreases and carbon dioxide composition increases with increasing oxygen to carbon ratio.

#### 2.1. Method

Diesel steam reforming reaction and autothermal reforming reaction chemical equilibrium compositions were analyzed with Aspen HYSY software and total Gibbs free energy minimization method. Gibbs free energy minimization method has been widely used for the simulation of reactions, since it enables to determine chemical equilibrium composition.

Simulation of thermodynamic equilibrium composition was performed for both n-hexadecane, which is accepted as a substitute of diesel, and diesel, according to the composition of diesel that was used in the experiments. The detailed composition used for the calculation of thermodynamic equilibrium composition for diesel is given in Appendix A.

Effects of temperature, H<sub>2</sub>O/C ratio and O<sub>2</sub>/C ratio were analyzed for both n-hexadecane and diesel steam & autothermal reforming reactions. Studied parameters and their range were given in detail in Table 2.1. In the chemical equilibrium analysis, the following assumptions were made:

- Isothermal reaction
- The PVT properties of the gas mixture were modelled by Peng Robinson equation of state
- Pressure is atmospheric
- Reacting gas is well mixed
- Carbon formation is negligible
- The following components were included in the reactant and product streams; H<sub>2</sub>O, H<sub>2</sub>, CO, CH<sub>4</sub>, CO<sub>2</sub>, C<sub>2</sub>H<sub>4</sub>, C<sub>2</sub>H<sub>6</sub>, C<sub>3</sub>H<sub>6</sub>, C<sub>4</sub>H<sub>10</sub>, C<sub>5</sub>H<sub>12</sub>, C<sub>6</sub>H<sub>14</sub>, C<sub>7</sub>H<sub>16</sub>, C<sub>8</sub>H<sub>18</sub>, C<sub>9</sub>H<sub>20</sub>, C<sub>10</sub>H<sub>22</sub>, C<sub>11</sub>H<sub>24</sub>, C<sub>12</sub>H<sub>26</sub>, C<sub>13</sub>H<sub>28</sub>, C<sub>14</sub>H<sub>30</sub>, C<sub>15</sub>H<sub>32</sub>, C<sub>16</sub>H<sub>34</sub>, C<sub>17</sub>H<sub>36</sub>, C<sub>18</sub>H<sub>38</sub>, C<sub>19</sub>H<sub>40</sub>.

Table 2.1. Range of chemical equilibrium parameters studied with Aspen HYSY.

Reactant	Reaction	T Range (°C)	H <sub>2</sub> O/C Ratio Range	O <sub>2</sub> /C Ratio Range
n-hexadecane	Steam Reforming	500-1000	1.0-3.0	-
	Autothermal Reforming	500-1000	0.25-3.0	0.1-1.5
Diesel (HC mixture according to PAL results)	Steam Reforming	500-1000	1-3	-
	Autothermal Reforming	500-1000	1-3	0.1-1.5

## 2.2. Equilibrium analysis results

Equilibrium analysis only showed the presence of H<sub>2</sub>, CO, CH<sub>4</sub> and CO<sub>2</sub> in the product results for n-hexadecane and diesel reforming reactions. An example of the used reactant composition and resulting product composition are given in Appendix A for diesel steam reforming reaction at a temperature of 800 °C and at a H<sub>2</sub>O/C ratio of 2.5.

Effects of temperature and H<sub>2</sub>O/C ratio on n-hexadecane steam reforming reaction were presented on Figure 2.1 and Figure 2.2, respectively. As it can be seen, increase of temperature enhances hydrogen composition until 800 °C. Compositions of carbon monoxide increases, carbon dioxide and methane decreases with increasing temperature probably as a result of steam reforming and dry reforming reactions of methane. H<sub>2</sub>O/C molar ratio increase enhances thermodynamics of hydrogen and carbon dioxide formation, as a result of enhanced water gas shift reaction and methane reforming reaction at equilibrium condition. For n-hexadecane autothermal reforming reaction, effect of temperature, H<sub>2</sub>O/C ratio and O<sub>2</sub>/C ratio were presented in Figure 2.3, Figure 2.4 and Figure 2.5, respectively. Effect of temperature on n-hexadecane autothermal reforming reaction is more distinguishable (Figure 2.3), since temperature analysis was performed by using ratio (H<sub>2</sub>O/C=0.5, O<sub>2</sub>/C=0.25). For both reactions, it could be said that high temperature enhances reforming of methane. Apparently, autothermal reforming reaction influences more from temperature as opposed to H<sub>2</sub>O/C ratio. Change in methane fraction was not observed with a change in H<sub>2</sub>O/C ratio as shown in Figure 2.4. Increase in steam content of the feed slightly increased composition of hydrogen and carbon monoxide, and decreased carbon monoxide fraction in the products indicating effect of water gas shift reaction. With an increase in oxygen supply (Figure 2.5), equilibrium compositions of hydrogen and carbon monoxide decreases indicating combustion reaction being more favorable compared to steam reforming reaction.

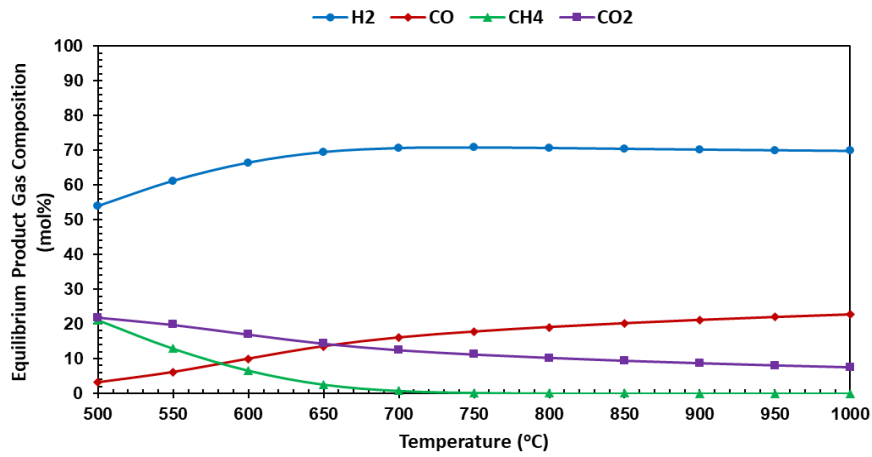


Figure 2.1. Effect of temperature on equilibrium product gas composition in the n-hexadecane steam reforming process ( $H_2O/C=2.5$ ).

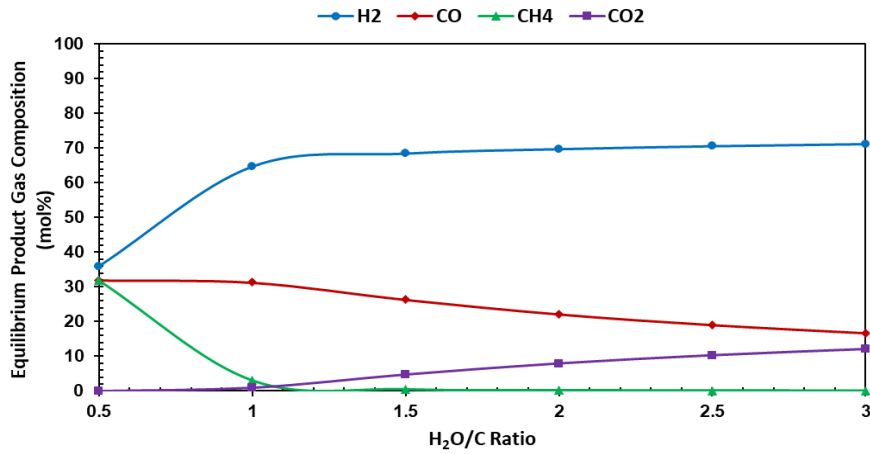


Figure 2.2. Effect of  $H_2O/C$  ratio on equilibrium product gas composition in the n-hexadecane steam reforming process ( $T=800\text{ }^\circ\text{C}$ )

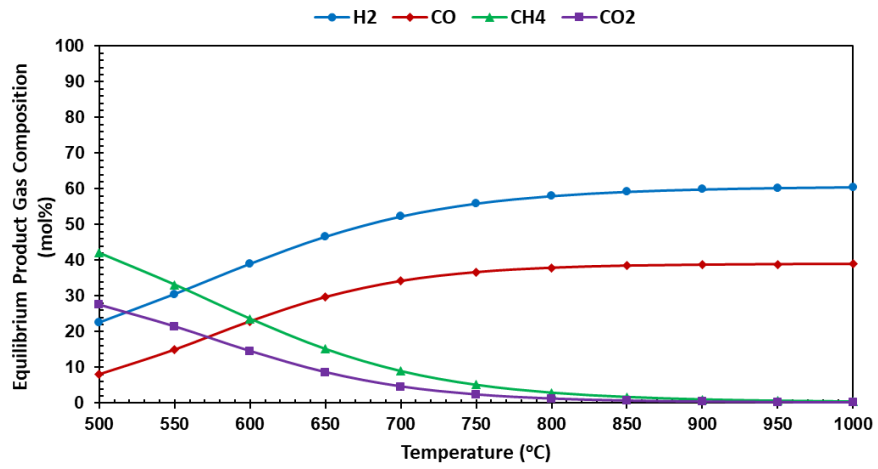


Figure 2.3. Effect of temperature on equilibrium product gas composition in the n-hexadecane autothermal reforming process ( $H_2O/C=0.5$  and  $O_2/C=0.25$ ).

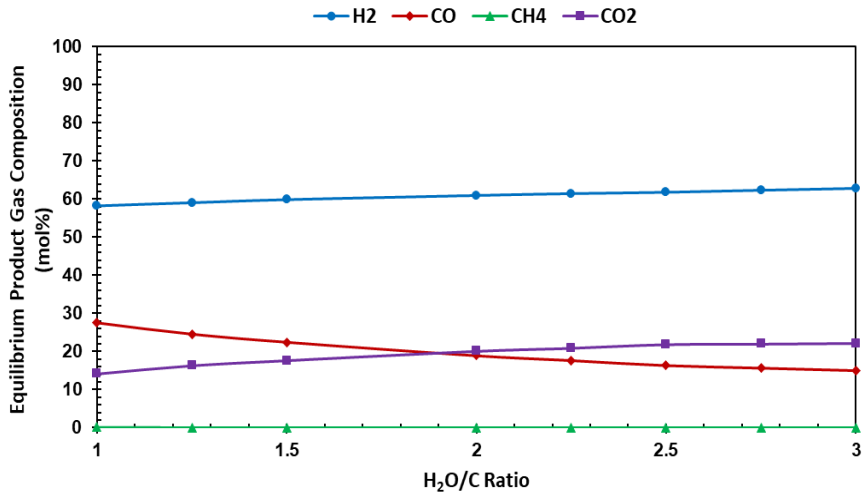


Figure 2.4. Effect of  $H_2O/C$  ratio on equilibrium product gas composition in the n-hexadecane autothermal reforming process ( $T=800$  °C and  $O_2/C=0.5$ ).

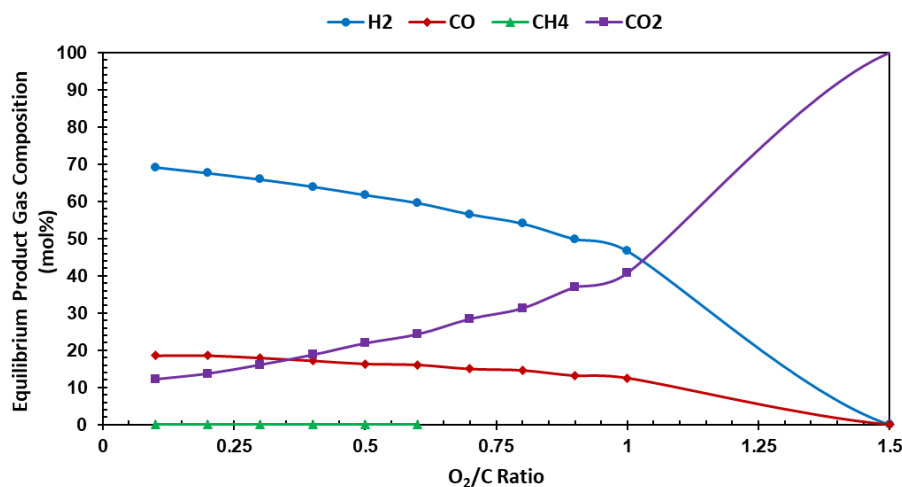


Figure 2.5. Effect of O<sub>2</sub>/C ratio on equilibrium product gas composition in the n-hexadecane autothermal reforming process (T=800 °C and H<sub>2</sub>O/C=2.5).

Equilibrium analysis results of diesel reforming reactions were similar to that of n-hexadecane reforming reactions. Figure 2.6 shows the effect of temperature on the product equilibrium composition during diesel steam reforming reaction. Similar to n-hexadecane steam reforming reaction conditions, raising temperature enhances the equilibrium composition of hydrogen and carbon monoxide and decreases the compositions of carbon dioxide and methane, probably due to methane steam and dry reforming reactions. The effect of H<sub>2</sub>O/C ratio on the equilibrium product composition is given in Figure 2.7. Thermodynamically, increase of H<sub>2</sub>O/C ratio enhanced hydrogen and carbon monoxide compositions and decreased carbon dioxide and methane compositions. Figure 2.8, Figure 2.9 and Figure 2.10 show the effects of temperature, H<sub>2</sub>O/C ratio and O<sub>2</sub>/C ratio on the equilibrium product composition for the diesel autothermal reforming reaction. Effect of temperature and H<sub>2</sub>O/C ratio was analyzed at a very low O<sub>2</sub>/C ratio (0.1), which is the reason of the similarity between the results of diesel autothermal reforming and diesel steam reforming reactions. Change of O<sub>2</sub>/C ratio significantly affected the equilibrium composition. Increase of oxygen supply enhanced combustion reaction and diminished reforming reactions.

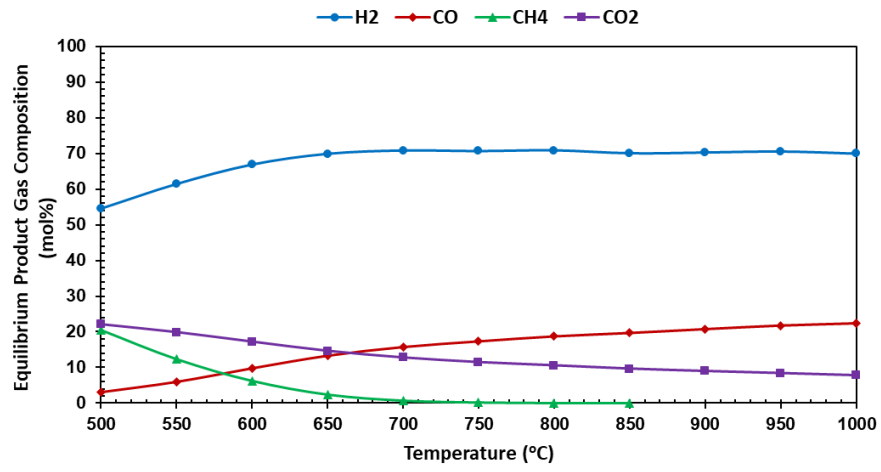


Figure 2.6. Effect of temperature on equilibrium product gas composition of diesel steam reforming process (H<sub>2</sub>O/C=2.5)

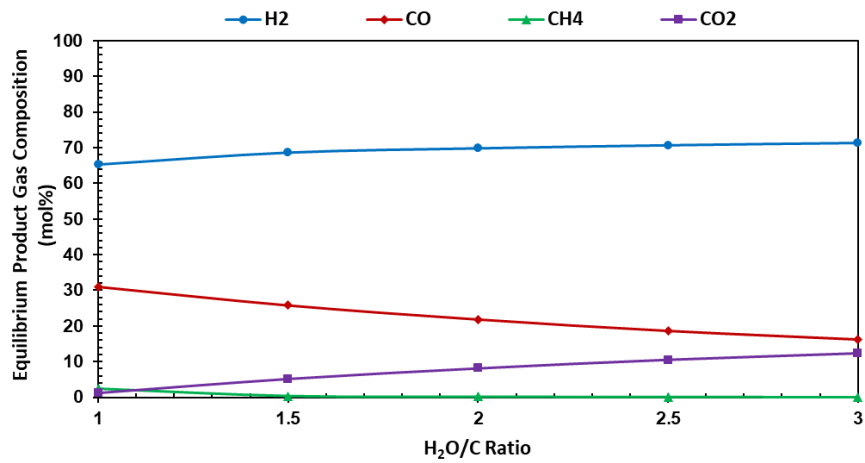


Figure 2.7. Effect of H<sub>2</sub>O/C ratio on equilibrium product gas composition of diesel steam reforming process (T=800 °C and O<sub>2</sub>/C=0.1)

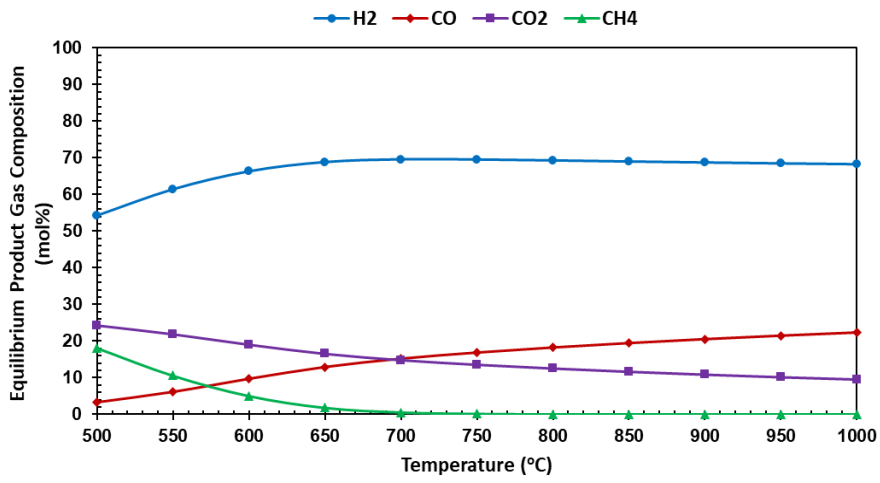


Figure 2.8. Effect of temperature on equilibrium product gas composition of diesel autothermal reforming process ( $H_2O/C=2.5$  and  $O_2/C=0.1$ ).

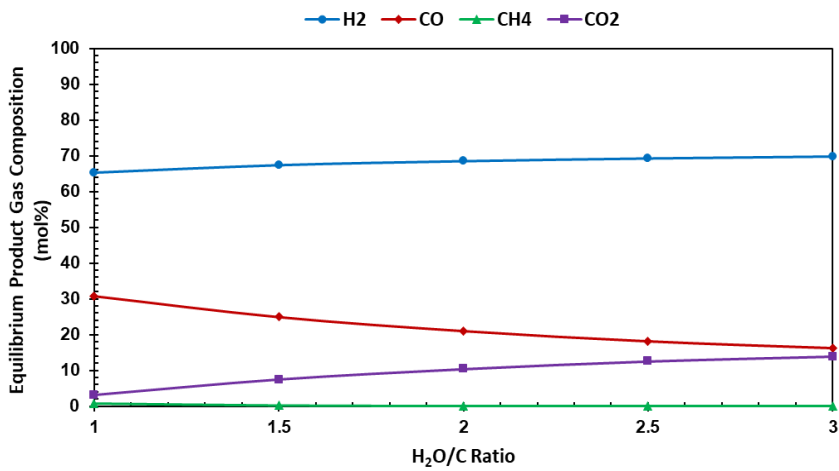


Figure 2.9. Effect of  $H_2O/C$  ratio on equilibrium product gas composition of diesel autothermal reforming process ( $T=800$  °C and  $O_2/C=0.1$ )

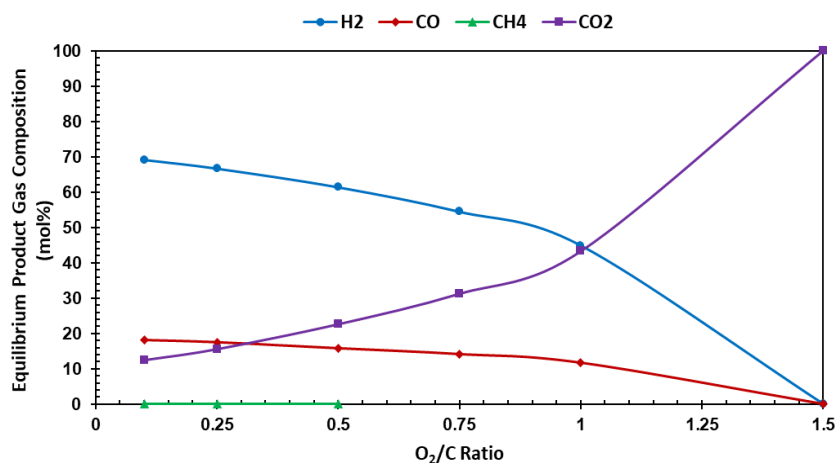


Figure 2.10. Effect of O<sub>2</sub>/C ratio on equilibrium product gas composition of diesel autothermal reforming process (T=800 °C and H<sub>2</sub>O/C=2.5)

In summary, results of chemical equilibrium analysis of hexadecane and diesel reforming reactions showed that hydrogen production is favorable at high temperature and high steam to carbon ratio of the feed. Results are in agreement with the findings in literature<sup>10</sup>. Kang and Bae<sup>87</sup> found the maximum hydrogen concentration at 750 °C for n-hexadecane autothermal reforming. Parmar et al.<sup>36</sup> analyzed the equilibrium compositions of diesel steam and autothermal reforming reaction through Gibbs free energy minimization and concluded that, similar to the results presented in this study, major species produced during reforming of diesel are H<sub>2</sub>, CO, CO<sub>2</sub>, CH<sub>4</sub> and carbon. According to the chemical equilibrium results, hydrogen maximization and methane minimization can be achieved above 750-800 °C. Operation at temperatures higher than 800 °C would make a minimum impact in terms of product composition. Increase of temperature from 800 °C to 1000 °C only increases hydrogen composition as 0.94 mol% and decreases methane composition as 0.07%. Considering these results and also the fact that the operation temperature of SOFC is about 800 °C, operating temperature for reforming reactions was selected as 800 °C in this study. Chemical equilibrium analysis results for the effect of steam to carbon ratio showed that steam to carbon ratio value of 1 is too low for hydrogen production. Since steam content of

the feed is too low, the occurrence of water gas shift reaction cannot be observed at this operating condition. For this reason, experiments will be performed at a steam to carbon ratio range of 1.5 and 3. Chemical equilibrium analysis was performed at an oxygen to carbon ratio range of 0.1 and 1.5 for autothermal reforming reactions of n-hexadecane and diesel. Equilibrium compositions at oxygen to carbon ratio values of 0.1 and 0.25 are very similar. Equilibrium composition at oxygen to carbon ratio value of 1.5 is very high to observe any hydrogen presence. For these reasons, autothermal reforming experiments will be performed at an oxygen to carbon ratio range of 0.25 and 1.

## CHAPTER 3

### METHOD

In this study, two different groups of nickel-alumina catalysts were synthesized. The first group of catalysts were synthesized following a consecutive wet impregnation technique with the assistance of an ultrasonic bath. The second group of catalysts were synthesized through a surfactant aided approach - “evaporation induced self assembly”, followed by the wet impregnation of nickel. Different promoters (Mg, Ru, Ce, Ce-Zr, W) with varying combinations and loading amounts were applied for both groups of catalysts. The selection criteria of the promoters and the route of the insertion of the selected metal/metal oxides were described in detail with the applied synthesis method. Catalyst characterization tools such as X-Ray Diffraction (XRD), N<sub>2</sub> Adsorption-Desorption, Transmission Electron Microscopy (TEM), Scanning Electron Microscopy (SEM), Energy Dispersed X-Ray Analysis (EDX), Temperature Programmed Reduction (TPR), NH<sub>3</sub> Temperature Programmed Desorption (NH<sub>3</sub>-TPD), pyridine adsorbed Diffuse Reflectance Infrared Fourier Transform Spectroscopy (DRIFTS), thermogravimetric analysis (TGA) were applied to understand the behavior of the synthesized catalysts in diesel reforming reactions. Diesel reforming test set-up designed, constructed and used for the activity tests towards both diesel steam and autothermal reforming reactions are presented together with the details of the constant operating conditions. The effluent streams of the designed test system consisted of two phases; gas and liquid. Gas phase was analyzed in an online manner with a gas chromatograph containing a thermal conductivity detector (TCD). Liquid stream on the other hand, was collected, stored and then analyzed by using GC and GC-MS devices.

### 3.1. Catalyst Synthesis

Two different synthesis routes were followed in this research for the synthesis of 22 materials of which the names and the synthesis routes were given on the following pages. The first set of catalyst group was synthesized using consecutive wet impregnation technique was named as Ni@X(M1)@Y(M2)@Al<sub>2</sub>O<sub>3</sub>. In this name, X represents the loading amount of first metal/metal oxide (M1) that was incorporated to the catalysts and Y represents the loading amount of second metal/metal oxide (M2) that was incorporated to the catalysts. The symbol “@” indicates that Ni, M1 and M2 were incorporated to the material through wet impregnation method consecutively. The symbol “-“ represent the two metal/metal oxides were impregnated to the support material at the same time. The details of the synthesis method is presented on the following pages.

Ten different catalysts that has either different promoter type or content were synthesized through evaporation induced self-assembly method (EISA). This set of catalyst group was named as Ni@Z(MO1)-W(MO2)(“@” or “-“)Al<sub>2</sub>O<sub>3</sub>-EISA. In this name, Z represents the loading amount of first metal/metal oxide (MO1) that was incorporated to the catalysts and W represents the loading amount of second metal/metal oxide (MO2) that was incorporated to the catalysts. The symbol “@” indicates that metal/metal oxides were incorporated by using wet impregnation method and the symbol “-“ indicates that the incorporation was performed by following one-pot (direct) synthesis method (EISA), of which the details were given on the following pages.

The list of all catalysts including their names, promoters used, loading amount of metals/metal oxides that were incorporated to them and the synthesis method used are given in in Table 3.1. The logic and reasons behind the selection criteria (e.g. increase of sulfur or coke resistance) of the promoter type and the loading amount for commercial Al<sub>2</sub>O<sub>3</sub> supported catalysts and EISA type catalysts are presented on Figure 3.1 and Figure 3.2, respectively.

Table 3.1 Catalysts synthesized for the scope of this work

Catalyst	1 <sup>st</sup> Promoter/ Incorporation Method/ Target (wt.%)	2 <sup>nd</sup> Promoter/ Incorporation Method/ Target (wt.%)	Incorporation Method/ Target Ni (wt.%)	
Ni@Al <sub>2</sub> O <sub>3</sub>	-	-	WI/10	Impregnation of commercial Al <sub>2</sub> O <sub>3</sub>
Ni@10CeO <sub>2</sub> @Al <sub>2</sub> O <sub>3</sub>	CeO <sub>2</sub> /WI*/10	-	WI/10	
Ni@20CeO <sub>2</sub> @Al <sub>2</sub> O <sub>3</sub>	CeO <sub>2</sub> /WI/20	-	WI/10	
Ni@10W-10CeO <sub>2</sub> @Al <sub>2</sub> O <sub>3</sub>	CeO <sub>2</sub> /WI/10	W/WI/10	WI/10	
Ni@20W@Al <sub>2</sub> O <sub>3</sub>	W/WI/20	-	WI/10	
Ni@1.5Ru@10CeO <sub>2</sub> @Al <sub>2</sub> O <sub>3</sub>	Ru/WI/1.5	CeO <sub>2</sub> /WI/10	WI/10	
Ni@1.5Ru@20CeO <sub>2</sub> @Al <sub>2</sub> O <sub>3</sub>	Ru/WI/1.5	CeO <sub>2</sub> /WI/20	WI/10	
Ni@1.5Ru@Al <sub>2</sub> O <sub>3</sub>	Ru/WI/1.5	-	WI/10	
Ni@1Ru@Al <sub>2</sub> O <sub>3</sub>	Ru/WI/1.0	-	WI/10	
Ni@0.5Ru@Al <sub>2</sub> O <sub>3</sub>	Ru/WI/0.5	-	WI/10	
1.5Ru@10CeO <sub>2</sub> @Al <sub>2</sub> O <sub>3</sub>	Ru/WI/1.5	CeO <sub>2</sub> /WI/10	0	
1.5Ru@20CeO <sub>2</sub> @Al <sub>2</sub> O <sub>3</sub>	Ru/WI/1.5	CeO <sub>2</sub> /WI/20	0	
Ni@Al <sub>2</sub> O <sub>3</sub> -EISA	-	-	WI/10	
Ni@10CeO <sub>2</sub> -Al <sub>2</sub> O <sub>3</sub> -EISA	CeO <sub>2</sub> /DS**/10	-	WI/10	
Ni@20CeO <sub>2</sub> -Al <sub>2</sub> O <sub>3</sub> -EISA	CeO <sub>2</sub> /DS/20	-	WI/10	
Ni@20CeO <sub>2</sub> @Al <sub>2</sub> O <sub>3</sub> -EISA	CeO <sub>2</sub> /WI/20	-	WI/10	
Ni@8CeO <sub>2</sub> -2ZrO <sub>2</sub> -Al <sub>2</sub> O <sub>3</sub> -EISA	ZrO <sub>2</sub> /DS/2	CeO <sub>2</sub> /DS/8	WI/10	
Ni@10W-10CeO <sub>2</sub> -Al <sub>2</sub> O <sub>3</sub> -EISA	W/DS/10	CeO <sub>2</sub> /DS/10	WI/10	
Ni@10W-Al <sub>2</sub> O <sub>3</sub> -EISA	W/DS/10		WI/10	
Ni@20W-Al <sub>2</sub> O <sub>3</sub> -EISA	W/DS/20		WI/10	
Ni@10W-10Mg-Al <sub>2</sub> O <sub>3</sub> -EISA	Mg/DS/10	W/DS/10	WI/10	
Ni@10Mg-Al <sub>2</sub> O <sub>3</sub> -EISA	Mg/DS/10	-	WI/10	

\*WI: Wet Impregnation

\*\*DS: Direct Synthesis

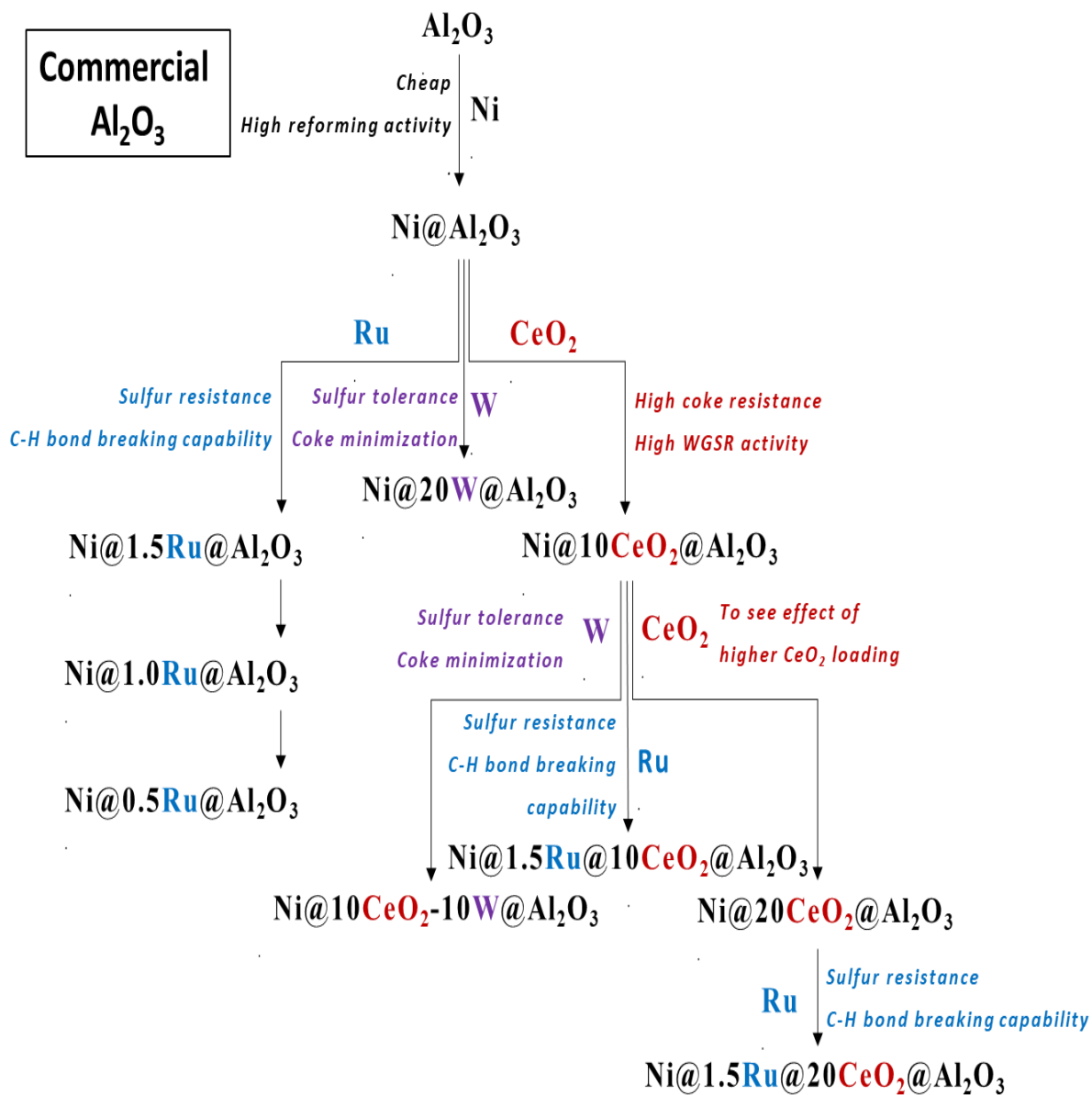


Figure 3.1 The selection of the promoter type, amount and the main reason for commercial  $\text{Al}_2\text{O}_3$  supported catalysts.

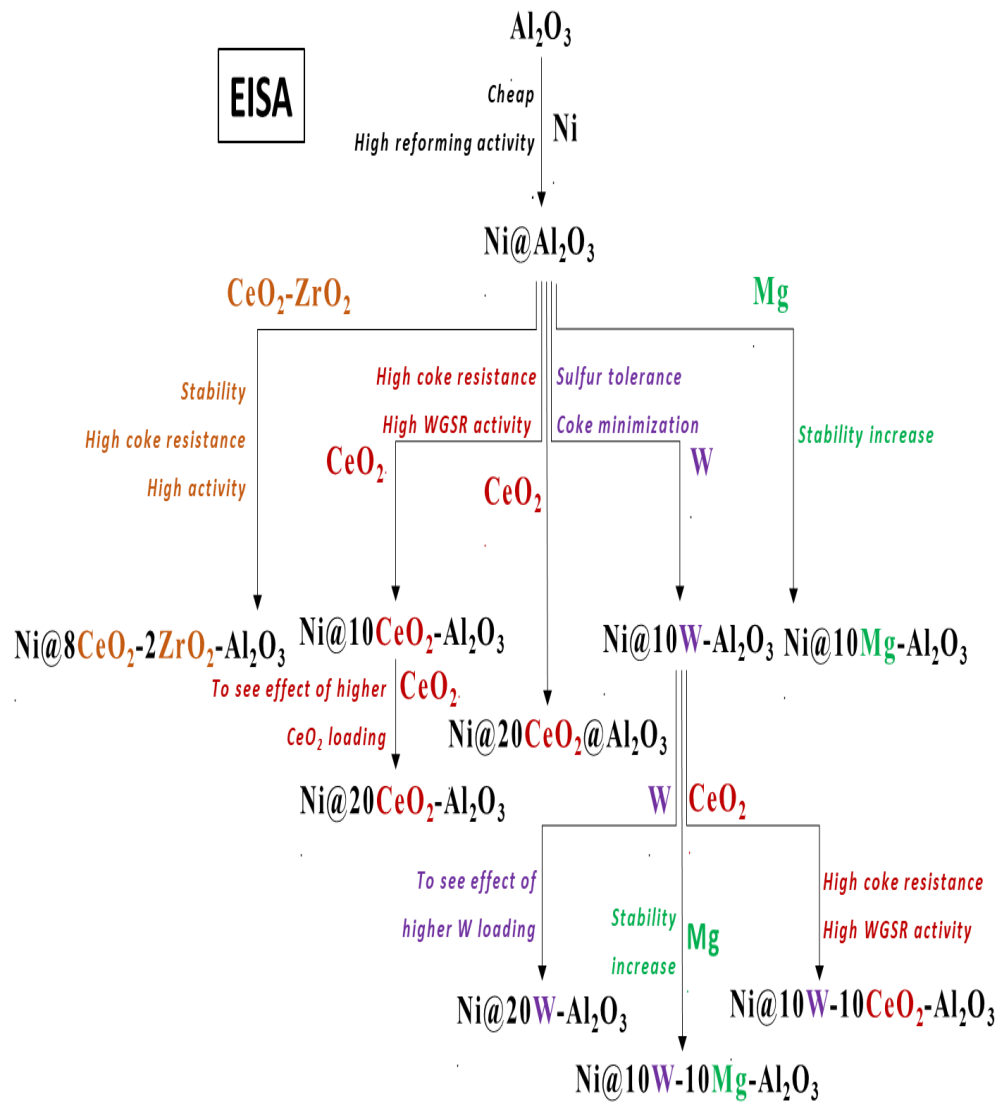


Figure 3.2 The selection of the promoter type, amount and the main reason for EISA type catalysts.

### **Synthesis of commercial Al<sub>2</sub>O<sub>3</sub> loaded catalysts:**

As support material, commercial cylindrical  $\gamma$ -Al<sub>2</sub>O<sub>3</sub> (Saint-Gobain NorPro, SA 6\*73) pellets were used. As nickel, ceria, ruthenium and tungsten precursors, Ni(NO<sub>3</sub>)<sub>2</sub>H<sub>2</sub>O (Acros Organics), Ce(NO<sub>3</sub>)<sub>3</sub>.6H<sub>2</sub>O (Aldrich Chemicals), Cl<sub>3</sub>Ru.xH<sub>2</sub>O (Acros Organics) and (NH<sub>4</sub>)<sub>6</sub>H<sub>2</sub>W<sub>12</sub>O<sub>40</sub>.xH<sub>2</sub>O (Aldrich) were used, respectively.

During the synthesis, cylindrical  $\gamma$ -Al<sub>2</sub>O<sub>3</sub> pellets which were previously calcined at 900°C, were used. Selection of the calcination temperature was based on conduction of reforming experiment at a temperature of 800°C and the calcination temperature of the catalysts was above this value; 900 °C. Materials were synthesized by consecutive wet impregnation using an ultrasonic bath. CeO<sub>2</sub> and/or W or CeO<sub>2</sub> and/or Ru impregnation was performed by adding metal precursor-deionized water solutions that contain targeted amount of metal precursors dropwise to the  $\gamma$ -Al<sub>2</sub>O<sub>3</sub>-deionized water mixture placed in an ultrasonic bath at a temperature range of 50 and 60 °C. After 6 hours of mixing in the ultrasonic bath, the resultant mixture was dried at 60°C, then calcined with dry air at 900°C, for 6 hours. After the calcination, the second metal/metal oxide impregnation was conducted in the same manner, if required. Al<sub>2</sub>O<sub>3</sub> and synthesized support materials then impregnated by nickel following the same impregnation method. After calcination at 900 °C, material was reduced with H<sub>2</sub> for 4 hours at 900°C.

### **Synthesis of “EISA” catalysts:**

Material synthesis was performed by the modification of the EISA synthesis technique described elsewhere<sup>84</sup>. During synthesis of EISA supports, Poly(ethylene glycol)–block–poly(propylene glycol)–block–poly(ethylene glycol) (Pluronic P123, Sigma Aldrich) as surfactant, aluminum isopropoxide (C<sub>9</sub>H<sub>21</sub>O<sub>3</sub>Al, Merck) as alumina precursor, nitric acid (HNO<sub>3</sub>, Merck) as acid source and ethanol (absolute, Sigma Aldrich) as solvent were used. As metal/metal oxide precursors; Ce(NO<sub>3</sub>)<sub>3</sub>.6H<sub>2</sub>O (Aldrich Chemicals), ZrO(NO<sub>3</sub>)<sub>2</sub>.xH<sub>2</sub>O, Mg(NO<sub>3</sub>)<sub>2</sub>.6H<sub>2</sub>O, (NH<sub>4</sub>)<sub>6</sub>H<sub>2</sub>W<sub>12</sub>O<sub>40</sub>.xH<sub>2</sub>O (Aldrich) and Cl<sub>3</sub>Ru.xH<sub>2</sub>O (Acros Organics) were used.

8 g Pluronic P123 was dissolved in 60 ml ethanol and solution was stirred until a clear solution was obtained. While P123 was dissolving, 12.8 ml of 65 wt.% nitric acid and 40 ml ethanol were mixed with 16 g aluminum isopropoxide and stirred until no solid particle remained. Later, second solution was added to the first one dropwise and resulting mixture was stirred for 18 h, then put into oven and left for aging at 60 °C for 48 h. Obtained yellow solid was calcined at 900 °C for 6 h with a heating ramp of 1 °C/min.

For the synthesis of Metal/Metal Oxide-Al<sub>2</sub>O<sub>3</sub>-EISA, a similar procedure to the synthesis of Al<sub>2</sub>O<sub>3</sub>-EISA material was followed. 8 g Pluronic P123 was dissolved in 60 ml ethanol and solution was stirred until a clear solution was obtained. While P123 was dissolving, 12.8 ml of 65 wt.% nitric acid, 40 ml ethanol and the required amounts of metal oxide precursors were mixed with 16 g aluminum isopropoxide and stirred until no solid particle remained. Later, second solution was added to the first one dropwise and resulting mixture was stirred for 18 h, then put into oven and left for aging at 60 °C for 48 h. Obtained yellow solid was calcined at 900 °C for 6 h with a heating ramp of 1 °C/min.

Lastly, nickel was impregnated to the synthesized materials following the wet impregnation method. After calcination at 900 °C, material was reduced with H<sub>2</sub> for 4 hours at 900°C.

### **3.2. Catalyst Characterization**

Synthesized materials were characterized using several techniques. XRD analysis of the synthesized materials was performed using Rigaku D/MAX2200 diffractometer with a CuK $\alpha$  radiation source. X-Ray was charged with 40 kV and 30 mA. The scanning range of 2 $\theta$  was set between 10° and 90° with a scanning speed of 1°/ min.

Physical properties of the synthesized materials such as surface area, average pore diameter, pore volume were measured by the N<sub>2</sub> adsorption technique using Micromeritics Tristar II 3020 apparatus. Analysis was carried out at 77K temperature

with different nitrogen relative pressure ranges. All samples were dried and degassed before the analysis at 200 °C for 4 hours at vacuum conditions. During the analysis, relative pressure range ( $P/P_0$ ) was taken between  $1 \times 10^{-5}$  and 0.99.

Morphology and elemental content determination of catalysts were performed with SEM and EDX analyses with QUANTO 400F Field Emission high resolution scanning electron microscopy with 20 kV beam voltage. Prior to analysis, samples were attached to carbon tape and coated with palladium and gold to minimize charging of the materials under electron beam.

DRIFTS analysis of the pyridine adsorbed samples were carried out using Perkin Elmer Spectrum One instrument. Prior to analysis all samples were dried at 110 °C, then placed in a desiccator with pyridine for one week. Fresh samples, which were also dried at 110 °C, and pyridine adsorbed samples were analyzed and differences of these spectra were used for acid site determination.

TPR and  $\text{NH}_3$ -TPD experiments were performed with Micromeritics Chemisorb 2720 Pulse Chemisorption System. For TPR analysis, samples each being 0.025 g were dried at 300 °C under argon flow prior to reduction analysis. TPR analysis was performed between room temperature and 900 °C with a heating rate of 3 °C/min under 30 ml/min flow of 5%  $\text{H}_2$ -Ar.  $\text{NH}_3$ -TPD experiments were performed after drying each sample (0.1 g) at 200 °C for 1 h. Samples were saturated with 50 ml/min flow of 5%  $\text{NH}_3$ -He for 1 h. After 15 minutes of argon flow, samples were analyzed with the following temperature program under 30 ml/min helium flow; temperature was firstly raised to 125 °C with a heating rate of 30 °C/min, and after 10 minutes, sample was heated to 900 °C with a heating rate of 10 °C/min. Samples were cooled down to room temperature.

Catalysts which were used in diesel steam reforming activity tests were also analyzed using thermogravimetric analysis (TGA) technique with Shimadzu TA-60 WS under dry air flow of 60 ml/min in the temperature range of 25–900 °C with a constant heating rate of 10 °C/min. Used catalysts were also analyzed with Transmission Electron Microscopy (TEM) analysis, by using JEOL 2100F HRTEM

equipment with 200 kV accelerating voltage. Suspension of powder sample in alcohol was dropped on the C-film grids and dried prior to analysis.

### 3.3. Diesel Reforming Tests

#### 3.3.1. Diesel Reforming Experimental Test Set-Up

Activity tests for diesel steam and autothermal reforming reactions were performed by using the experimental test set-up that was designed and constructed in the scope of this study. Schematic representation of the experimental system is presented in Figure 3.3.

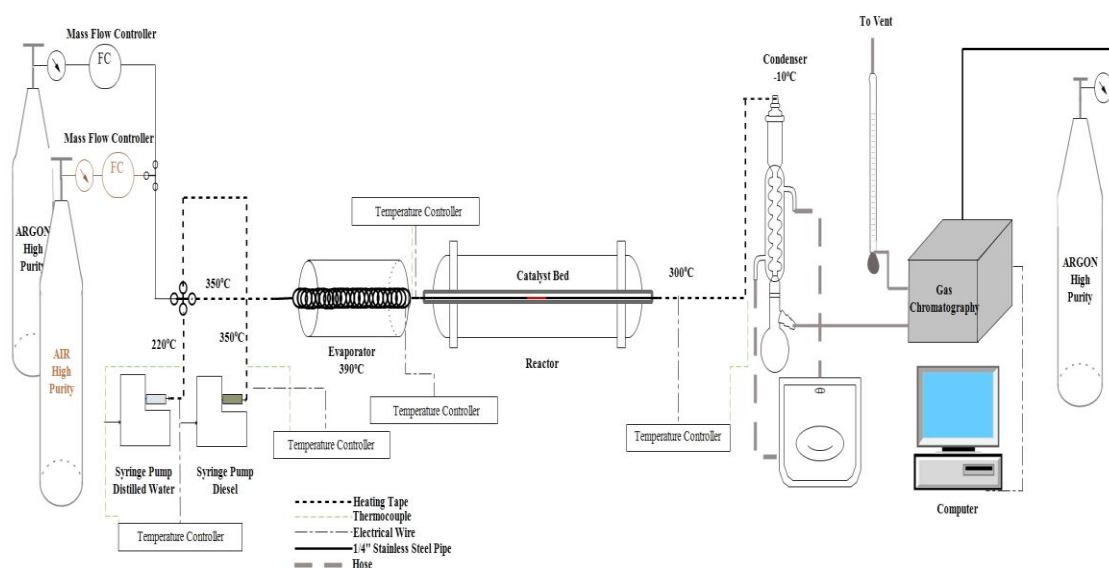


Figure 3.3 Schematic representation of laboratory scale ATR and DSR experimental test set-up.

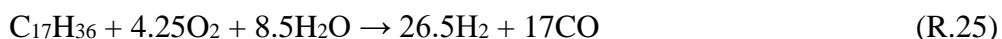
Diesel steam and autothermal reforming experiments were performed in a tubular flow quartz reactor having an inner diameter of 25 mm and containing 1.0 g pellet catalyst which was 3 mm in diameter. The height of the catalyst bed was approximately 4 mm. Argon, which was used as the carrier for liquid reactants constitutes of a 60% of the inlet gas stream volumetric flow rate at the entrance of the catalyst bed (800 °C). Diesel and water are fed to the system by using syringe pumps, separately. Diesel and

water pipes are heated with heating tapes to 350 °C and 220 °C, respectively. For diesel steam reforming reaction, diesel, water and argon are mixed and then sent to the evaporator which operates at 390 °C in order to completely vaporize the mixture. Mixture is then fed to the reactor after the evaporator. Reactants that pass through the catalyst zone is then sent to the condenser which operates at -10 °C by using a water bath, in order to condensate water and other condensable compounds that could be present in the product stream. Condensable compounds are collected as liquid and gas mixture is sent to the gas chromatograph (SRI 8610-C Multigas #1 gas chromatograph) equipped with a thermal conductivity detector and carbosphere packed column. For ATR experiments, a mass flow controller for air is connected to the system with a valve. During ATR experiments, air is sent through the mass flow controller and mixed with diesel, water and argon before the evaporator.

### **3.3.2. Diesel Reforming Experimental Test Procedure**

The diesel fuel was Shell FuelSave Diesel acquired from a local gas station and analyzed to determine the properties which were presented in Table 3.2. It had a sulfur content of 6.4 ppm. According to the analysis performed with a gas chromatograph, the average carbon number was found to be 17 (Table 3.2), detailed results are given in Appendix B. In parameter calculations of activity tests, the formula of diesel was assumed as  $C_{17}H_{36}$ , by neglecting the aromatics content of diesel fuel which would constitute a maximum value of 11% (molar) of diesel according to EN 590 standards. In reality, hydrogen number of diesel would be lower considering nature of aromatics. Calculations of the reactant flow rates were made according to the specified operating conditions (GHSV, which is calculated at 800 °C, steam to carbon ratio and oxygen to carbon ratio) and according to the DSR (R.24) and ATR (R.25) reactions given below. A sample calculation of the reactant and carrier gas flow rates is presented in Appendix B.





Diesel reforming experiments were performed at atmospheric pressure. Reactor was placed into a tubular furnace operating at 800 °C for all experiments. Duration of all experiments was 6 h, except for the long-term experiments. Experiments were performed firstly by cooling the water bath to the desired temperature and heating the system to the desired temperature under argon flow, after loading the catalyst pellets into reactor. After reaching the desired temperature for all lines, evaporator and reactor; diesel and water syringe pumps were turned on and feed was sent to the system. The first analysis of gas products were performed after 30 minutes of the starting time of the pumps. After the experiment is finished, firstly diesel and water pumps were turned off and then system heating was turned off. Argon feed was turned off after the system temperature dropping to near room temperature. Condensable compounds were then collected in a sample vial.

Parameter investigation experiments with different GHSV values were performed by keeping the catalyst amount constant and by just changing the inlet flow rate of diesel, water and the carrier gas argon mixture. ATR experiments were performed with a similar procedure to DSR experiments. At a same GHSV target, diesel and water flow rates were the same as in DSR experiments, but argon flow rate was decreased to a value of which the total flow rates of argon and air matched the flow rate of argon of DSR experiment. ATR experimental procedure also differs from DSR procedure regarding the starting and ending of air feeding. Air feeding was started at the same time with diesel and water in order to prevent oxidation of the catalyst prior to the experiment. Similarly, air feeding was stopped at the same time of stopping diesel and water feeding, to eliminate catalyst/coke oxidation.

Prior to all experiments, calibration analysis of gas chromatography was completed by using standard gas mixtures of all gases that could be in the reactor effluent stream. Calibration calculation method, the calibration factors used in the calculation of test results, sample calculation for conversion of GC results into molar composition of the

gas products and also the conditions used for gas analysis were presented in the appendices section (Appendix B).

Table 3.2. Properties of commercial Shell Diesel (analyzed at PAL, METU)

Weight average C number	17
Density @ 15 °C (kg/L)	0.83
Distillation – 95% (°C)	356.6

Following the determination of calibration factors and analysis of diesel, the first experiments were performed by using n-hexadecane ( $C_{16}H_{34}$ ) in order to confirm the calculations made for diesel reforming reactions and to check the operational problems in the built reactor system prior to introducing a complex mixture such as diesel. n-hexadecane has been used as a substitute for diesel and was tested towards both steam reforming and autothermal reforming reactions. The diesel reforming experimental methods was also confirmed by using an empty reactor with no catalyst in it, at diesel steam reforming operating conditions prior to catalytic activity tests in order to observe its limits. In order to observe the repeatability of the activity results of the synthesized catalysts and to calculate the experimental errors through standard deviation values, Ni@20CeO<sub>2</sub>@Al<sub>2</sub>O<sub>3</sub> catalyst was tested in DSR reaction for three times. Calculated standard deviation values are reported in the following chapter.

### 3.4. Liquid reaction sample analysis

Liquid samples collected after DSR and ATR experiments which were stored in vials contained both hydrocarbons which are in liquid phase at room temperature (>C<sub>5</sub>) and may have been produced during the experiments and also water phase. For the determination of hydrocarbon compounds in the liquid samples, water phase of the samples was required to be separated. The standard method which is called *EPA Method 1664, Revision B, n-Hexane Extractable Material (HEM; Oil and Grease)* was

partly followed for the separation of the water rich part of the sample from the hydrocarbon rich part. This method involves extraction of the dispersed and dissolved components from water with hexane which is used as the solvent and separation of solvent and water rich samples<sup>88</sup>.

Method of separation was performed by firstly measuring the collected sample volumes. Firstly, 2 ml of hexane was added to the sample and the mixture was shaken vigorously. Then, 2 ml of hexane was added to rinse the sample container so that its entire content was transferred to the extraction vessel. Liquid mixture rich in hexane phase was kept in the extraction vessel for a few minutes in order to obtain two phases. Water phase at the bottom portion of the vessel was taken from the vessel and put into a liquid sample holder. Phase at the upper portion which was hexane rich sample was taken into another liquid sample holder.

For the analysis of the hexane rich samples, two methods were applied by TÜPRAŞ R&D Center Laboratory. Firstly, all samples were analyzed with simulated-distillation analysis (SIM-DIS, ASTM D7169.23648) using a high temperature gas chromatography to determine the range of hydrocarbons present in the sample. This analysis showed presence of hydrocarbons qualitatively. According to the results of SIM-DIS analysis, some of the samples were further analyzed quantitatively with high-resolution gas chromatography (DHA, ASTM D6730-01), in detail. Both analyses were performed by following standard test methods. Details of these analysis and the conditions applied during the analysis is given in Appendix B.



## CHAPTER 4

### THE EFFECT OF OPERATING CONDITIONS OF DIESEL STEAM AND AUTOTHERMAL REFORMING REACTIONS

Parameter optimization studies were performed for both diesel steam and autothermal reforming reactions. The effects of GHSV, steam to carbon ratio and also oxygen to carbon ratio (for autothermal reforming reaction) on hydrogen production were investigated by using CeO<sub>2</sub> incorporated Ni-Al<sub>2</sub>O<sub>3</sub> catalyst (Ni@20CeO<sub>2</sub>@Al<sub>2</sub>O<sub>3</sub>) at a reaction temperature of 800 °C. Detailed characterization analysis results of Ni@20CeO<sub>2</sub>@Al<sub>2</sub>O<sub>3</sub> is presented on the following chapter.

In order to confirm the calculations made for diesel reforming reactions and to check the operational problems in the constructed reactor system prior to introducing diesel (C<sub>17</sub>H<sub>36</sub>), n-hexadecane (C<sub>16</sub>H<sub>34</sub>) which has been used as a substitute for diesel due to its similar carbon content, was tested for both n-hexadecane steam reforming (HSR) and n-hexadecane autothermal reforming (HAR) reactions. Results are given in the appendices section (Appendix C). HSR and HAR experiments showed that the calculations made for the determination of flow rates according to the selected operating conditions are correct.

#### 4.1. Diesel Steam Reforming Reaction

Hydrogen production through diesel steam reforming reaction using Ni@20CeO<sub>2</sub>@Al<sub>2</sub>O<sub>3</sub> catalyst at a reaction temperature of 800 °C was performed to optimize operating conditions which were gas hourly space velocity (GHSV) and steam to carbon (H<sub>2</sub>O/C) ratio of the feed. Calculation of the operating conditions were decided according to the molecular formula of diesel (Table 3.2). GHSV was chosen in the range of 5000 h<sup>-1</sup> - 25000 h<sup>-1</sup>, and H<sub>2</sub>O/C ratio was chosen in the range of 1.5 - 3.0. The gas analysis results of the reactor outlet showed the presence of H<sub>2</sub>, CO, CO<sub>2</sub>,

CH<sub>4</sub>, C<sub>2</sub>H<sub>4</sub> and C<sub>2</sub>H<sub>6</sub> gases. The liquid analysis of the reactor outlet was performed as described in Chapter 3.4, and the results were presented in Appendix D. Results showed that there was only a trace amount of hydrocarbons in the liquid samples collected after the steam reforming experiment. There was no indication of hydrocarbons with higher molecular weight. Only C<sub>5</sub>-C<sub>7</sub> group hydrocarbons were found in the liquid samples through the high resolution gas chromatography analysis. For the samples of diesel steam reforming operating condition optimization experiments, the total amount of hydrocarbons in the liquid sample was less than 0.1 mol % of the diesel feed, indicating complete conversion of diesel to products. Experiments for the optimization of GHSV values and H<sub>2</sub>O/C molar ratios were performed at 800°C using the Ni@20CeO<sub>2</sub>@Al<sub>2</sub>O<sub>3</sub> catalyst, of which the characterization results are presented in detail in Chapter 5.

Figure 4.1-A illustrates the average product gas composition obtained from the experiments performed at different GHSV values. According to these results, decrease of GHSV value from 25000 h<sup>-1</sup> to 7500 h<sup>-1</sup> enhanced diesel steam reforming reaction (R.24) which increased H<sub>2</sub>, CO and CO<sub>2</sub> formation, reduced CH<sub>4</sub>, C<sub>2</sub>H<sub>4</sub> and C<sub>2</sub>H<sub>6</sub> formation, and eliminated C<sub>3</sub>H<sub>6</sub> formation (Figure 4.1). CO<sub>2</sub> is accepted as the desired product since it forms through the WGSR (R.4), enhancing hydrogen production. CH<sub>4</sub>, C<sub>2</sub>H<sub>4</sub> and C<sub>2</sub>H<sub>6</sub>, and C<sub>3</sub>H<sub>6</sub> are accepted as side products in the DSR reaction forming through thermal cracking reaction (R.20). H<sub>2</sub> yield, which was defined as the molar amount of hydrogen produced to the molar amount of diesel feed, was enhanced (Table 4.1) with a decrease in GHSV. High side product formation at low contact times suggests that hydrocarbons with higher molecular weight are being cracked into C<sub>2</sub>-C<sub>3</sub> hydrocarbons and these hydrocarbons are then reformed into the desired products. It is possible that cracking of aromatic hydrocarbon compounds leads to the formation of large amounts of ethylene before reaching to the catalyst bed and reforming of produced ethylene leads to the production of hydrogen. At high contact times (GHSV=5000-7500 h<sup>-1</sup>), steam reforming of side products, especially methane, takes place, which enhances hydrogen formation. Further decrease of GHSV would not be

efficient considering the effect of insufficient mixing of reactants in the reactor used in this study, and it increases the catalyst bed height resulting in a possible pressure drop problem. Effect of GHSV on hydrogen yield, CO to CO<sub>2</sub> formation ratio and coke deposition can be seen from Table 4.1. Coke deposition amounts were calculated by using TGA results. At high GHSV values (17000, 25000 h<sup>-1</sup>) coke formation was very low since there was no time for further cracking of hydrocarbon compounds. Analysis results of liquid samples at GHSV values of 7500 h<sup>-1</sup> and 25000 h<sup>-1</sup> also proved the importance of residence time of diesel in the catalyst bed in terms of cracking and reforming reactions of hydrocarbons with high molecular weight. Analysis result of the liquid sample at GHSV of 7500 h<sup>-1</sup> and H<sub>2</sub>O/C ratio of 2.5 did not show any presence of hydrocarbon. The absence of hydrocarbon in the sample means that complete conversion was achieved at these operating conditions. However, the analysis of liquid sample at a GHSV value of 25000 h<sup>-1</sup> showed the presence of long-chained hydrocarbons that were ranging to C<sub>21</sub>. Majority of the alkanes that were present in the liquid sample which was separated from water phase by using hexane as solvent was composed of C<sub>10</sub>, C<sub>14</sub>, C<sub>17</sub>, C<sub>18</sub>, C<sub>20</sub> and C<sub>21</sub>, and their molar share was approximately 24%, 31%, 21%, 8%, 4%, and 11%, respectively. Total amount of hydrocarbons only corresponds to approximately 0.1% of the total diesel feed which would indicate achievement of almost complete conversion.

For results as mentioned above, an optimum GHSV value was selected as 7500 h<sup>-1</sup> for the H<sub>2</sub>O/C molar ratio and catalyst optimization. The effect of H<sub>2</sub>O/C on hydrogen production was investigated at a range of 1.5 - 3.0 (Figure 4.1-B). Increase of H<sub>2</sub>O/C ratio enhanced H<sub>2</sub> and CO<sub>2</sub> production and reduced CO formation indicating an increase in the WGS rate (Table 4.1). Side product formation was also reduced at higher steam feeding which showed further reforming of side products in an excess steam environment which could be seen as a decrease in the amount of side products in Table 4.1. Coke deposition amounts were compatible with these results showing a decreasing trend with increasing H<sub>2</sub>O/C ratio. Even though high H<sub>2</sub>O/C ratios are beneficial in terms of product distribution and catalyst lifetime which was proven

before by many authors<sup>76,79</sup>, the application of this reaction in APUs should be considered in terms of energy economy. Heating this excess steam would require extra energy. Thus an optimum H<sub>2</sub>O/C ratio should be applied and a coke resistive catalyst should be found at this optimum H<sub>2</sub>O/C ratio. For these reasons, H<sub>2</sub>O/C ratio was selected as 2.5 for catalyst investigation.

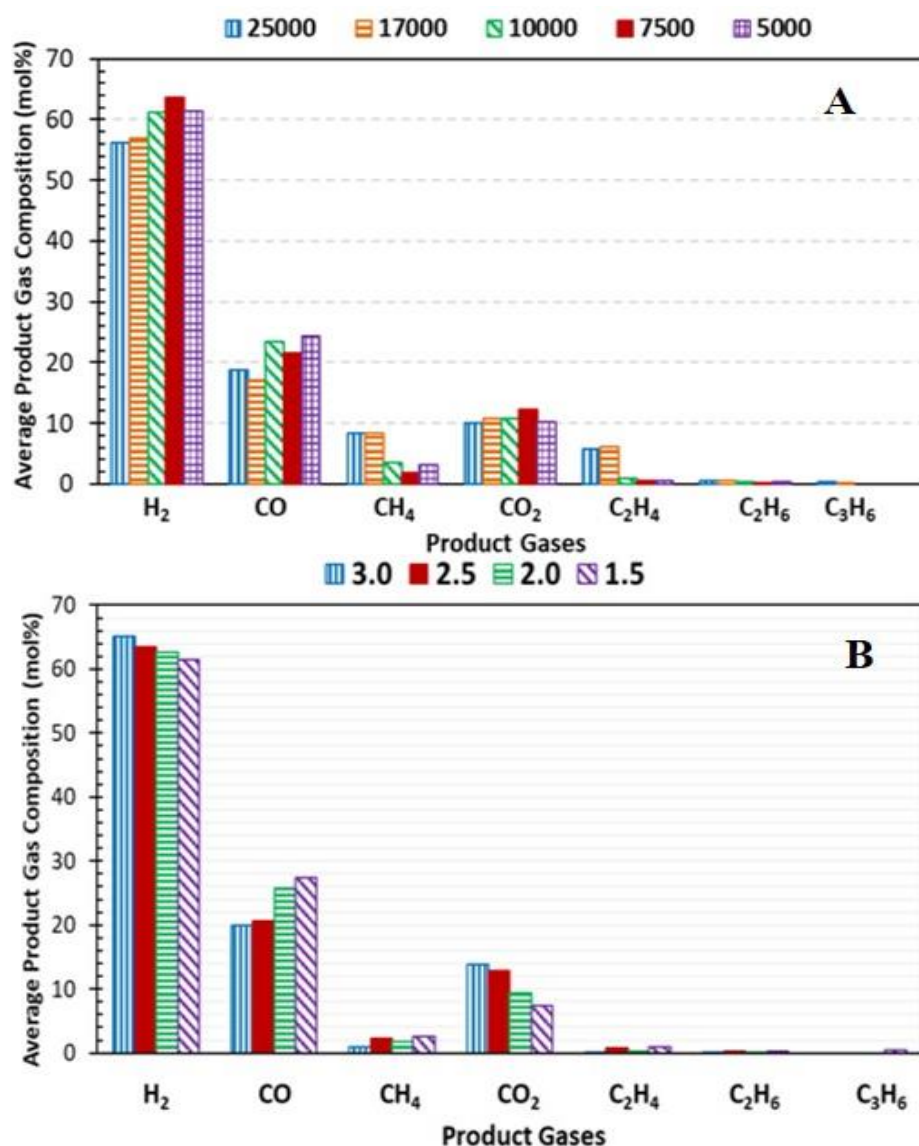


Figure 4.1 The effect of A) GHSV(H<sub>2</sub>O/C=2.5), B) H<sub>2</sub>O/C molar ratio (GHSV=7500 h<sup>-1</sup>) on average product compositions for the diesel steam reforming reaction over Ni@20CeO<sub>2</sub>@Al<sub>2</sub>O<sub>3</sub> catalyst at 800°C.

Table 4.1 Hydrogen yield, molar ratio of CO and CO<sub>2</sub> formation, produced side product amount and coke deposition results obtained from DSR optimization tests.

GHSV (h <sup>-1</sup> )	H <sub>2</sub> O/C	H <sub>2</sub> Yield (max <sup>theoretical</sup> =35)	$\frac{\dot{N}_{CO}}{\dot{N}_{CO_2}}$	Average Gas Product Composition of Side Products in ppm (molar)				Coke% (g <sub>coke</sub> / g <sub>spent</sub> catalyst)
				CH <sub>4</sub>	C <sub>2</sub> H <sub>4</sub>	C <sub>2</sub> H <sub>6</sub>	C <sub>3</sub> H <sub>6</sub>	
5000	2.5	26.6	2.4	3053	456	546	0	1.6
7500	2.5	29.1	1.7	1875	556	556	0	1.9
10000	2.5	26.1	2.2	3549	818	299	0	3.4
17000	2.5	19.6	1.6	8343	6123	595	216	1.7
25000	2.5	19.2	1.9	8300	5675	625	400	1.0
7500	1.5	25.4	3.7	2550	918	341	400	3.2
7500	2.0	28.3	2.8	1761	292	149	0	3.1
7500	3.0	31.7	1.4	844	104	35	0	1.4

The Ni@20CeO<sub>2</sub>@Al<sub>2</sub>O<sub>3</sub> catalyst was tested in the experimental set-up three times at a GHSV value of 7500 h<sup>-1</sup> and H<sub>2</sub>O/C ratio of 2.5, to check the reproducibility of the data and obtain the standard deviation values. Variation of gas product composition with respect to time was presented in Figure 4.2. Almost the same gas product composition values were observed. Standard deviation of mole fraction percent for each gas was found to be 0.21, 0.65, 0.33, 0.36, 0.18 and 0.06 for H<sub>2</sub>, CO, CH<sub>4</sub>, CO<sub>2</sub>, C<sub>2</sub>H<sub>4</sub> and C<sub>2</sub>H<sub>6</sub>, respectively. Standard deviation of hydrogen yield was found to be 0.35. In Figure 4.2, maximum theoretical composition of hydrogen was also given in three different lines; chemical equilibrium limit, DSR reaction limit and the combination of DSR and WGS limit. Hydrogen composition values in the gas product obtained from repeatability experiments were below the maximum possible hydrogen composition limits. Steady state average mol fraction of each component can also be seen from the column bar given on Figure 4.3. In other words, these results showed that the data and experiments are reproducible.

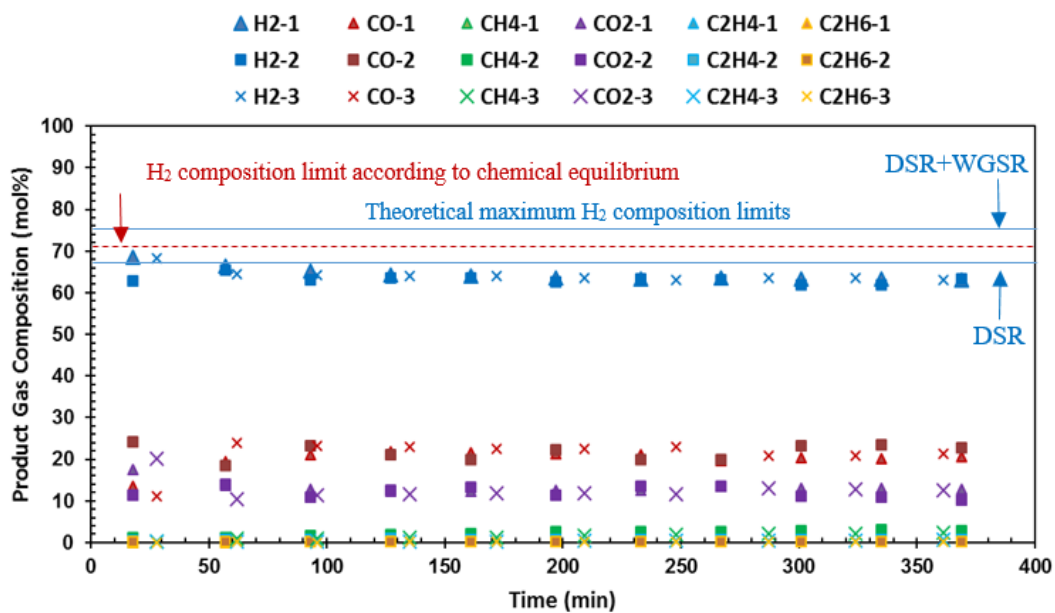


Figure 4.2. Gas product compositions over the Ni@20CeO<sub>2</sub>@Al<sub>2</sub>O<sub>3</sub> catalyst with respect to time for the reproducibility of DSR experiments (800°C, GHSV=7500 h<sup>-1</sup>, H<sub>2</sub>O/C=2.5).

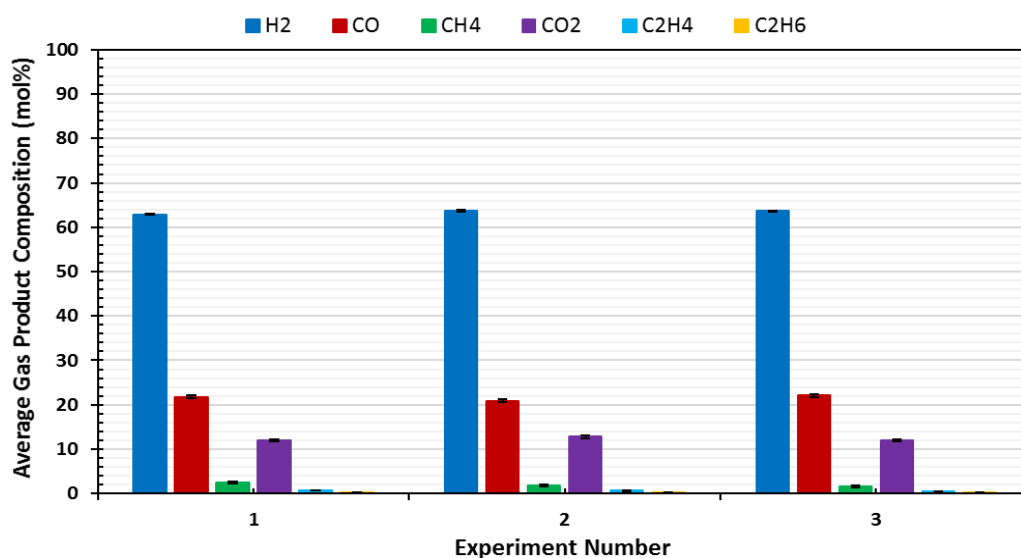


Figure 4.3. Average steady state gas product compositions over the Ni@20CeO<sub>2</sub>@Al<sub>2</sub>O<sub>3</sub> catalyst for the reproducibility of DSR experiments (800°C, GHSV=7500 h<sup>-1</sup>, H<sub>2</sub>O/C=2.5).

## 4.2. Diesel Autothermal Reforming Reaction

Hydrogen production through diesel autothermal reforming reaction using Ni@20CeO<sub>2</sub>@Al<sub>2</sub>O<sub>3</sub> catalyst at a reaction temperature of 800 °C was performed to optimize operating conditions which were gas hourly space velocity, steam to carbon molar ratio and oxygen to carbon molar ratio of the feed. Calculation of the operating conditions was performed according to the molecular formula of diesel (Table 3.2). GHSV was chosen in the range of 5000 h<sup>-1</sup> - 25000 h<sup>-1</sup>, the H<sub>2</sub>O/C ratio was chosen in the range of 1.5 - 3.0 and the O<sub>2</sub>/C ratio was chosen in the range of 0.25- 1.0. The gas analysis results of the reactor outlet showed the presence of H<sub>2</sub>, CO, CO<sub>2</sub>, CH<sub>4</sub>, C<sub>2</sub>H<sub>4</sub>, and C<sub>2</sub>H<sub>6</sub> gases. The liquid analysis of the reactor outlet was performed as described in Chapter 3.4, and these results were presented in Appendix D. Results showed that there was only a trace amount of hydrocarbons present in the liquid samples collected after the autothermal reforming experiments. There was no indication of hydrocarbons with high molecular weight. Only C5-C7 group hydrocarbons were found in the samples through high resolution gas chromatography analysis.

Average product gas compositions obtained through the GHSV optimization test performed at different GHSV values for the H<sub>2</sub>O/C molar ratio of 2.5, the O<sub>2</sub>/C molar ratio of 0.5 and at a temperature of 800 °C were presented in Figure 4.4. Similar results were obtained for the liquids and the liquids did not contain hydrocarbons at measureable amounts (Appendix D). For this reason, the complete conversion of diesel to products can be assumed for all autothermal reforming reactions and this suggests that hydrogen composition in the gas products determines the optimum operating conditions. The optimum GHSV value for the highest hydrogen production and minimum side product formation was found to be 7500 h<sup>-1</sup> (calculated at 800°C). An increase in the GHSV value results in a decrease in the catalyst activity in reforming, partial oxidation and water gas shift reactions. However, too much decrease in GHSV (below 7500 h<sup>-1</sup>) leads to loss of activity due to the coke formation amount (Table 4.2). Coke formation amount is almost zero in ATR reactions performed at GHSV values

of 10000 and 17000 h<sup>-1</sup>. However, the coke formation amounts in DSR reactions presented in section 4.1 was higher compared to ATR results. The difference in coke amounts in ATR and DSR is due to the presence of oxygen. At the GHSV value of 25000 h<sup>-1</sup>, side product formation, especially methane and ethylene, increases indicating the dominance of cracking reactions. As GHSV decreases, hydrogen formation increases due to reforming and partial oxidation reactions of cracking products; methane and ethylene. Table 4.2 also shows the effect of GHSV on hydrogen yield and the molar ratio of CO to CO<sub>2</sub> formation. Similar to H<sub>2</sub> composition in the product gas stream, the highest hydrogen yield was obtained with a GHSV value of 7500 h<sup>-1</sup> with the lowest CO to CO<sub>2</sub> molar ratio. The H<sub>2</sub>O/C ratio parameter was also investigated in the diesel autothermal reforming reaction at a GHSV value of 7500 h<sup>-1</sup>, O<sub>2</sub>/C molar ratio of 0.5 and at a temperature of 800 °C. The effect of the H<sub>2</sub>O/C ratio on average product gas compositions was presented in Figure 4.5 and coke deposition results were presented in Table 4.2. As can be seen from Figure 4.5, a decrease in water feed significantly decreases hydrogen and carbon dioxide production and enhances carbon monoxide and side product formation. This behavior suggests that the presence of excess steam enhances the reforming of mid-products and increases also the occurrence of the water gas shift reaction. According to these results, the highest hydrogen production was obtained with a H<sub>2</sub>O/C molar ratio of 3. However, since there is no significant difference between the ratio values of 2.5 and 3.0 considering the energy economy and additional heating requirement that is brought by excess water heating, an H<sub>2</sub>O/C molar ratio of 2.5 is selected as the optimum value. The effect of the O<sub>2</sub>/C molar ratio on hydrogen production was also investigated in the diesel autothermal reforming reaction at a GHSV value of 7500 h<sup>-1</sup>, H<sub>2</sub>O/C ratio of 2.5 and a temperature of 800 °C. The effect of O<sub>2</sub>/C molar ratio on the average product gas composition was presented in Figure 4.6 and coke deposition results along with the results of hydrogen yield and the ratio of CO to CO<sub>2</sub> formation were presented in Table 4.2. As can be seen from Figure 4.6, a decrease in oxygen feed increases hydrogen and decreases carbon dioxide production indicating that some of the diesel feed goes through a combustion reaction. The highest hydrogen production was observed at the

lowest O<sub>2</sub>/C molar ratio. However, to observe the effect of the synthesized catalysts in ATR besides DSR, the O<sub>2</sub>/C ratio was selected as 0.5.

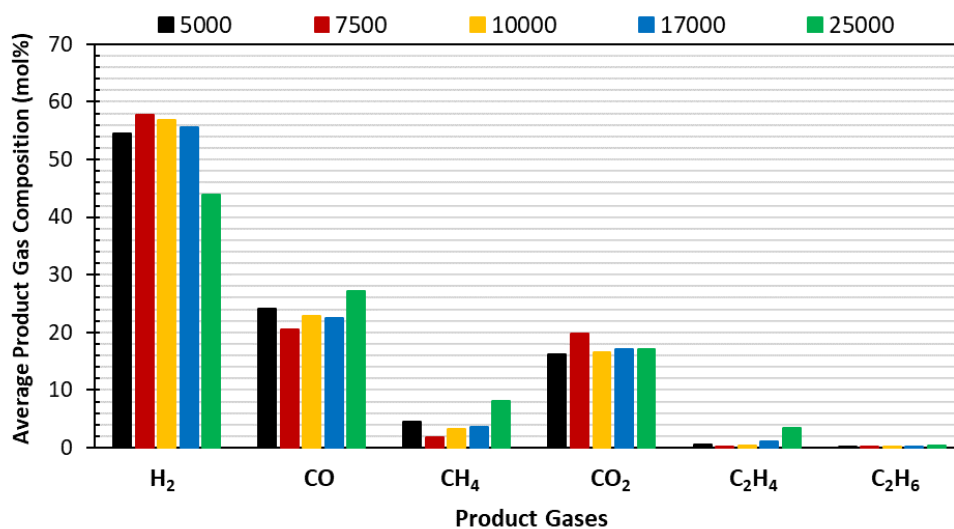


Figure 4.4. The effect of GHSV on average product compositions over the Ni@20CeO<sub>2</sub>@Al<sub>2</sub>O<sub>3</sub> catalyst at 800 °C, H<sub>2</sub>O/C=2.5, O<sub>2</sub>/C=0.5.

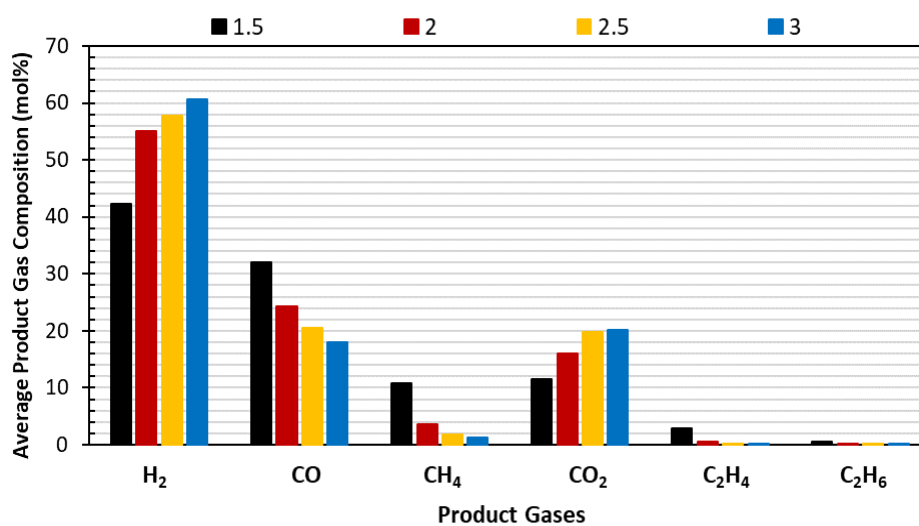


Figure 4.5. The effect of H<sub>2</sub>O/C molar ratio on average product compositions over the Ni@20CeO<sub>2</sub>@Al<sub>2</sub>O<sub>3</sub> catalyst at 800 °C, GHSV=7500 h<sup>-1</sup>, O<sub>2</sub>/C=0.5.

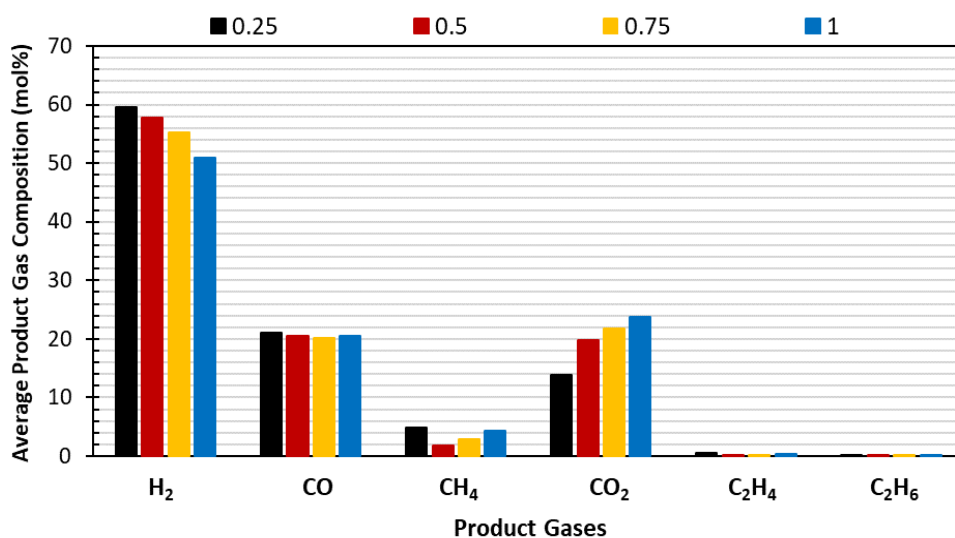


Figure 4.6. The effect of O<sub>2</sub>/C molar ratio on average product compositions over the Ni@20CeO<sub>2</sub>@Al<sub>2</sub>O<sub>3</sub> catalyst at 800 °C, GHSV=7500 h<sup>-1</sup>, H<sub>2</sub>O/C =2.5.

Table 4.2 Hydrogen yield, molar ratio of CO to CO<sub>2</sub> formation, and coke deposition results obtained in ATR optimization tests.

Operating Parameters			Performance Results					
GHSV (h <sup>-1</sup> )	H <sub>2</sub> O/C	O <sub>2</sub> /C	H <sub>2</sub> Yield (max <sub>theoretica</sub> <sub>i=26.5</sub> )	$\frac{\dot{N}_{CO}}{\dot{N}_{CO2}}$	Average Gas Product Composition of Side Products in ppm (molar)			Coke% (g <sub>coke</sub> /g <sub>used catalyst</sub> )
					CH <sub>4</sub>	C <sub>2</sub> H <sub>4</sub>	C <sub>2</sub> H <sub>6</sub>	
5000	2.5	0.5	20.1	1.5	4500	500	200	7.3
7500	2.5	0.5	23.2	1.0	1900	30	30	2.8
10000	2.5	0.5	22.2	1.4	3300	300	130	0.5
17000	2.5	0.5	20.7	1.3	3600	1000	220	0.7
25000	2.5	0.5	12.5	1.6	8100	3400	310	4.2
7500	1.5	0.5	11.8	2.8	10700	2900	500	2.0
7500	2.0	0.5	20.5	1.5	3700	600	200	3.5
7500	3.0	0.5	26.1	0.9	1200	100	20	1.1
7500	2.5	0	28.9	1.8	2000	600	200	1.9
7500	2.5	0.25	24.7	1.5	4800	500	200	3.2
7500	2.5	0.75	20.9	0.9	2800	100	0	2.3
7500	2.5	1.0	17.6	0.9	4300	300	100	0

## CHAPTER 5

### DEVELOPMENT OF CERIA AND TUNGSTEN PROMOTED NICKEL/ALUMINA CATALYSTS FOR STEAM AND AUTOTHERMAL REFORMING OF DIESEL

#### 5.1. Characterization Results

Characterization studies were performed on the  $\text{Al}_2\text{O}_3$  support,  $\text{Ni@10CeO}_2@\text{Al}_2\text{O}_3$ ,  $\text{Ni@20CeO}_2@\text{Al}_2\text{O}_3$ ,  $\text{Ni@10W-10CeO}_2@\text{Al}_2\text{O}_3$ , and  $\text{Ni@20W}@\text{Al}_2\text{O}_3$  catalysts which are calcined & reduced before analysis (except for TPR analysis). All catalysts possess 10 wt.% nickel. Characterization results were discussed throughout this section in terms of the effect of metal loading amount (10 or 20 wt.%) or the effect of the type of metal that was incorporated ( $\text{CeO}_2$  or W).

Physical properties of the commercial  $\text{Al}_2\text{O}_3$  support and metal incorporated and reduced catalysts containing ten weight percent nickel are presented in Table 5.1. Higher amounts of metal loading into alumina support lead to a decrease in BET surface area of the material. A decrease in surface area and pore volume values indicates pore blockage caused by metals and metal oxides loading. An increase in average pore diameter values despite the decrease in pore volume and surface area values, and decrease in microporosity percent after metal incorporation to  $\text{Al}_2\text{O}_3$  material suggest blockage of some micropores.

Table 5.1 Physical properties of catalysts

Material	Multi Point BET Surface Area (m <sup>2</sup> /g)	BJH Desorption Pore Volume (cm <sup>3</sup> /g)	BJH Desorption Average Pore Diameter (4V/A) (nm)	Microporosity (%)
Al <sub>2</sub> O <sub>3</sub>	142.0	0.55	7.1	8.3
Ni@Al <sub>2</sub> O <sub>3</sub>	113.0	0.49	8.1	7.4
Ni@10CeO <sub>2</sub> @Al <sub>2</sub> O <sub>3</sub>	91.3	0.42	8.9	7.3
Ni@20CeO <sub>2</sub> @Al <sub>2</sub> O <sub>3</sub>	83.0	0.39	9.4	7.7
Ni@10W-10CeO <sub>2</sub> @Al <sub>2</sub> O <sub>3</sub>	59.0	0.37	10.7	7.7
Ni@20W@Al <sub>2</sub> O <sub>3</sub>	77.4	0.44	11.3	7.1

Nitrogen adsorption/desorption isotherms of all materials are given in Figure 5.1-A, these materials can be classified as Type IV with H1 type hysteresis loop, according to IUPAC definition<sup>89,90</sup>. Type IV isotherm is a characteristic feature of mesoporous materials, and the H1 type hysteresis loop indicates the presence of narrow uniform pore size distribution. Sharp inflections on the adsorption and desorption branches were caused by the capillary condensation of nitrogen in the mesopores. Compared to the hysteresis loop observed for the Al<sub>2</sub>O<sub>3</sub> material, hysteresis loops of metal incorporated materials shifted to higher P/P<sub>0</sub> values, since metal incorporation lead to blockage of some pores. A decrease in pore volume and an increase in pore diameter due to pore blockage can be observed from Figure 5.1-B. The pore size distributions given in Figure 5.1-B also indicate a change in the pore structure of Al<sub>2</sub>O<sub>3</sub> support after metal loading from uniform to bi-modal pore size distribution for the Ni@10W-10CeO<sub>2</sub>@Al<sub>2</sub>O<sub>3</sub> and Ni@20W@Al<sub>2</sub>O<sub>3</sub> catalysts.

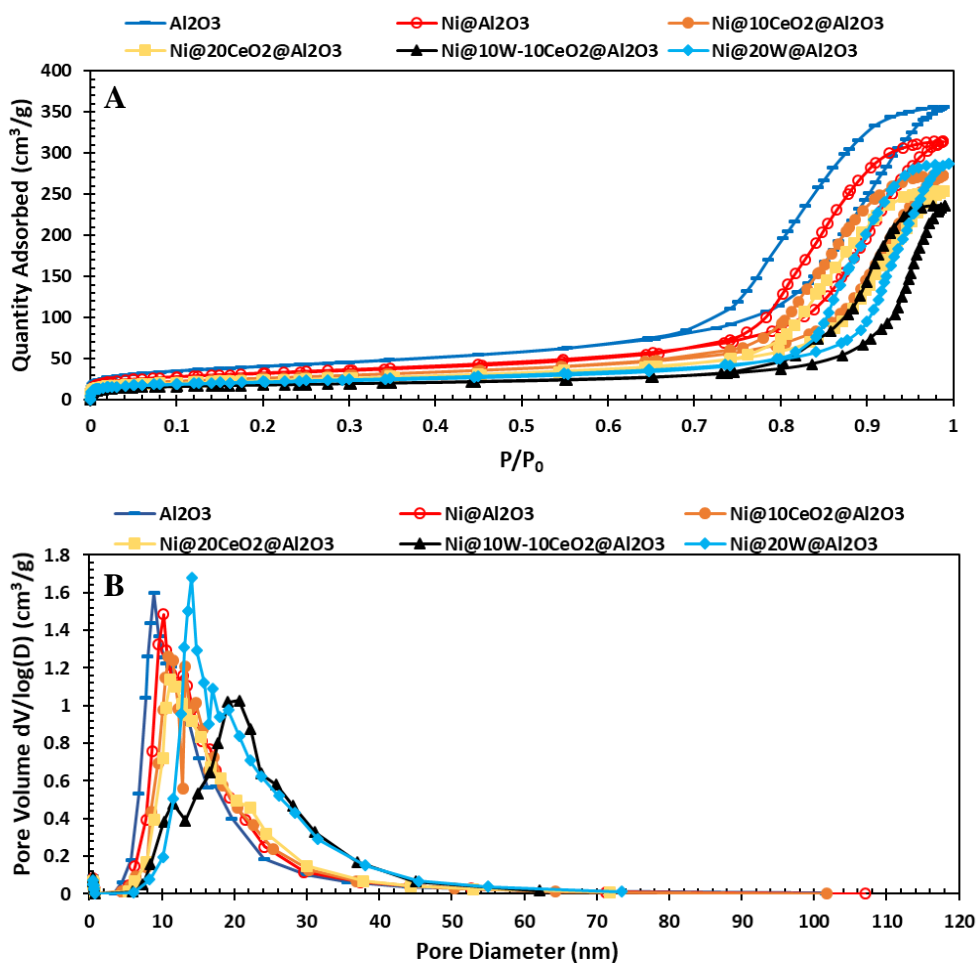


Figure 5.1 N<sub>2</sub> adsorption/desorption isotherms (A) and pore size distributions (B) of the synthesized catalysts and Al<sub>2</sub>O<sub>3</sub> support.

X-ray diffraction patterns of the synthesized catalysts are presented in Figure 5.2. XRD pattern of support material showed the characteristic peaks of  $\gamma$ -Al<sub>2</sub>O<sub>3</sub> (PDF card No. 01-074-4629) at  $2\theta$  values of 19.3°, 37.5°, 45.6°, 67.0° and 85.0°. XRD PDF data of all identified crystal phases are presented in Appendix E. However, observed  $\gamma$ -Al<sub>2</sub>O<sub>3</sub> peaks were wide and their intensities were quite low, which may suggest the possibility of the presence of other alumina phases. The XRD pattern of alumina shows the characteristic peaks of  $\gamma$ -Al<sub>2</sub>O<sub>3</sub>. However, its characteristic main peak ( $I/I_0=100$ ) location was close to that of  $\delta$ -Al<sub>2</sub>O<sub>3</sub> ( $\sim 67^\circ$ ) and  $\theta$ -Al<sub>2</sub>O<sub>3</sub> ( $\sim 67^\circ$ )<sup>91</sup> materials. Therefore,  $\gamma$ -Al<sub>2</sub>O<sub>3</sub>,  $\delta$ -Al<sub>2</sub>O<sub>3</sub> or  $\theta$ -Al<sub>2</sub>O<sub>3</sub> phases may be present in the material due to the instable nature of alumina. Partial transformation of  $\gamma$ -phase to other phases of alumina might

have occurred during the calcination.  $\gamma$ - $\text{Al}_2\text{O}_3$  generally transforms to  $\delta$ - $\text{Al}_2\text{O}_3$  at temperatures above  $\sim 850$  °C and these two phases can coexist together up to 950 °C. Beyond this temperature  $\theta$ - $\text{Al}_2\text{O}_3$  formation starts. Grain size, chemical composition and heating rate are the parameters that are accepted to affect phase transition temperatures<sup>92</sup>. In other words, the material may include  $\delta$ - $\text{Al}_2\text{O}_3$  phase in addition to  $\gamma$ - $\text{Al}_2\text{O}_3$ .

For nickel impregnated alumina support ( $\text{Ni@Al}_2\text{O}_3$ ), the presence of both cubic  $\text{Ni}^0$  (PDF card No. 01-071-4653) and  $\text{NiAl}_2\text{O}_4$  (PDF card No. 00-010-0339) was observed.  $\text{Ni}^0$  showed its peaks at  $2\theta$  values of  $44.2^\circ$ ,  $51.6^\circ$  and  $75.9^\circ$ .  $\text{NiAl}_2\text{O}_4$  peaks ( $37.5^\circ$ ,  $45.6^\circ$ ,  $61.0^\circ$  and  $67.0^\circ$ ) were observed at the same  $2\theta$  values with  $\gamma$ - $\text{Al}_2\text{O}_3$  peaks. XRD patterns of  $\text{Ni@10CeO}_2\text{@Al}_2\text{O}_3$  and  $\text{Ni@20CeO}_2\text{@Al}_2\text{O}_3$  showed the characteristic peaks of  $\text{Ni}^0$ ,  $\text{NiAl}_2\text{O}_4$ ,  $\gamma$ - $\text{Al}_2\text{O}_3$ , and  $\text{CeAlO}_3$  (PDF card No. 01-081-1185).  $\text{CeAlO}_3$  crystal forms at high temperatures in reducing atmosphere<sup>54</sup>. The presence of  $\text{CeAlO}_3$  was observed in XRD pattern of  $\text{Ni@20CeO}_2\text{@Al}_2\text{O}_3$  at  $2\theta$  values of  $23.6^\circ$ ,  $33.5^\circ$ ,  $33.6^\circ$ ,  $41.4^\circ$ ,  $48.3^\circ$ ,  $54.3^\circ$ ,  $60.0^\circ$ ,  $70.4^\circ$ , and  $80.5^\circ$ . XRD pattern of  $\text{Ni@10CeO}_2\text{@Al}_2\text{O}_3$  material showed only the major peak of  $\text{CeAlO}_3$  at a  $2\theta$  value of  $33.5^\circ$ . Pattern of  $\text{Ni@20CeO}_2\text{@Al}_2\text{O}_3$  showed the characteristic peaks of tetragonal  $\text{CeAlO}_3$  at  $2\theta$  values of  $23.6^\circ$ ,  $33.5^\circ$ ,  $41.3^\circ$ ,  $48.3^\circ$ ,  $54.4^\circ$ ,  $60.0^\circ$ ,  $70.4^\circ$  and  $80.5^\circ$ . Tungsten loaded materials ( $\text{Ni@10W-10CeO}_2\text{@Al}_2\text{O}_3$  and  $\text{Ni@20W@Al}_2\text{O}_3$ ) formed tetragonal  $\text{Ni}_4\text{W}$  (PDF card No. 01-072-2650) crystal with diffraction peaks located at  $2\theta$  values of  $21.9^\circ$ ,  $29.6^\circ$ ,  $31.2^\circ$ ,  $43.5^\circ$ ,  $44.7^\circ$ ,  $50.3^\circ$ ,  $51.4^\circ$ ,  $54.5^\circ$ ,  $56.5^\circ$ ,  $61.4^\circ$ ,  $64.1^\circ$ ,  $73.0^\circ$ ,  $73.9^\circ$ ,  $74.8^\circ$ , and  $89.9^\circ$ . Characteristic peaks of cubic tungsten crystal were also observed in the two patterns at  $40.3^\circ$ ,  $58.3^\circ$ ,  $73.2^\circ$ , and  $87.0^\circ$ . W (PDF card No. 01-089-3728) peak intensities observed in the pattern of  $\text{Ni@10W-10CeO}_2\text{@Al}_2\text{O}_3$  is higher compared to the intensities of the peaks located at the XRD pattern of  $\text{Ni@20W@Al}_2\text{O}_3$  despite its lower loading amount. The reason of the intensity difference in two patterns could be the effect of ceria and alumina interaction in the  $\text{Ni@10W-10CeO}_2\text{@Al}_2\text{O}_3$  catalyst. The presence of ceria-alumina interaction is believed to decrease the interaction of tungsten and alumina leading to the formation of larger tungsten crystals. The crystal size of tungsten was found to be 26 nm for

Ni@20W@Al<sub>2</sub>O<sub>3</sub> and 39 nm for Ni@10W-10CeO<sub>2</sub>@Al<sub>2</sub>O<sub>3</sub> catalyst (Table 5.2). Crystal sizes were calculated by using Scherrer equation as described in Appendix F. In the XRD pattern of the Ni@10W-10CeO<sub>2</sub>@Al<sub>2</sub>O<sub>3</sub> catalyst, Ni<sup>0</sup> peak intensities are higher than that of the Ni@20W@Al<sub>2</sub>O<sub>3</sub> catalyst indicating transformation of higher amounts of Ni<sup>0</sup> to Ni<sub>4</sub>W, probably due to its lower tungsten loading.

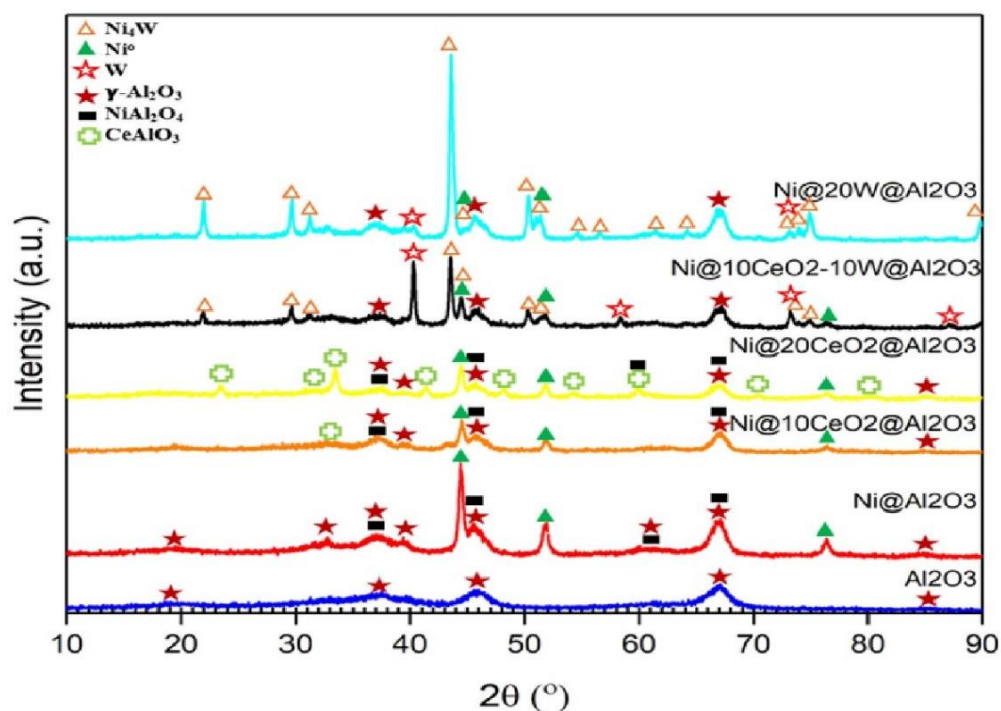


Figure 5.2. X-Ray diffraction patterns of ceria and tungsten promoted nickel/alumina catalysts.

Table 5.2 Crystal sizes and number of acid sites of ceria and tungsten promoted nickel/alumina catalysts.

Material	Crystal Size* (nm)				Total Acid Capacity** (mmol/g <sub>cat</sub> )
	Ni <sup>0</sup>	CeAlO <sub>3</sub>	Ni <sub>4</sub> W	W	
Ni@Al <sub>2</sub> O <sub>3</sub>	20	-	-		0.49
Ni@10CeO <sub>2</sub> @Al <sub>2</sub> O <sub>3</sub>	17	5	-		0.26
Ni@20CeO <sub>2</sub> @Al <sub>2</sub> O <sub>3</sub>	19	16	-		0.24
Ni@10W-10CeO <sub>2</sub> @Al <sub>2</sub> O <sub>3</sub>	-	10	39	43	0.33
Ni@20W@Al <sub>2</sub> O <sub>3</sub>	-	-	26	21	0.37

\*Crystal Size: Calculated by using XRD patterns and Scherrer equation

\*\*Total acid capacity: Calculated from NH<sub>3</sub>-TPD analysis

The nature of the acid sites of the catalysts was analyzed with DRIFTS of pyridine adsorbed samples. In the analysis, pyridine was used since it is a very strong base and gives information about strong Brønsted acid sites and strong Lewis acid sites. It can also form H-bonds with weak Brønsted acid sites. Figure 5.3 illustrates the DRIFTS spectra of the difference between pyridine adsorbed samples and fresh samples for the synthesized catalysts and Al<sub>2</sub>O<sub>3</sub> support. In the literature, it is stated that Lewis acid sites are identified from transmission bands located at about 1600-1630 cm<sup>-1</sup> and 1450 cm<sup>-1</sup> and Brønsted acid sites are identified from transmission bands located at about 1640 cm<sup>-1</sup> and 1545 cm<sup>-1</sup>. Transmission bands located at about 1580 cm<sup>-1</sup>, and 1590 cm<sup>-1</sup> are attributed to both weak Lewis acid sites and the hydrogen bond of weak Brønsted acid sites<sup>93</sup>. In Figure 5.3, for all materials, transmission bands were located at 1445 cm<sup>-1</sup>, 1575 cm<sup>-1</sup>, and 1614 cm<sup>-1</sup>, which indicate the presence of Lewis acid sites. The transmission band located at 1590 cm<sup>-1</sup> is assigned to hydrogen-bound pyridine originating from weak Brønsted acid sites. The transmission band located at 1485 cm<sup>-1</sup> is attributed to both weak Lewis and weak Brønsted acid sites.

The quantitative analysis of acid sites on the surfaces of catalysts was determined by stepwise temperature-programmed desorption of NH<sub>3</sub> (Figure 5.4 & Table 5.2). The strength of acidity on the material was distinguished with respect to the NH<sub>3</sub> desorption temperature of the catalysts given in Figure 5.4. Acid site strength was divided into three categories; desorption of NH<sub>3</sub> below 200 °C shows weak acidity, desorption at temperatures between 200 °C and 400 °C implies moderate acidity and desorption at temperatures above 400 °C indicates strong acidity<sup>94</sup>. All materials possess a certain degree of weak acidic sites as they can be seen in Figure 5.4. The total number of acid sites of the synthesized materials is presented in Table 5.2. According to these results, metal incorporation decreases the total number of number acid sites in these materials. A wide desorption peak was observed for Al<sub>2</sub>O<sub>3</sub> support indicating the presence of weak, moderate and strong acidity. The total number of acid sites is 0.66 mmol/g<sub>cat</sub> for Al<sub>2</sub>O<sub>3</sub> support. Nickel impregnation decreased the number of acid sites as can be seen from Table 5.2 to 0.49 mmol/g<sub>cat</sub>. The probable cause of the diminishing number of acid sites was the blockage of Al<sub>2</sub>O<sub>3</sub> acid sites with the incorporation of nickel, ceria

and tungsten. The incorporation of ceria and nickel led to blockage of acid sites by forming  $\text{CeAlO}_3$  and  $\text{NiAl}_2\text{O}_4$  crystals with  $\text{Al}_2\text{O}_3$ , respectively. The increase of Ce loading amount from 8 wt.% to 16wt.% caused a slight decrease of the total number of acid sites from 0.26 to 0.24  $\text{mmol/g}_{\text{cat}}$ . When ceria was incorporated together with tungsten, an increase in number of acid sites was observed. 20 wt.% incorporation of tungsten led to even higher number of acid sites (0.37  $\text{mmol/g}_{\text{cat}}$ ) compared to ceria loaded materials, but the value was still lower than the result obtained with  $\text{Ni@Al}_2\text{O}_3$  (0.49  $\text{mmol/g}_{\text{cat}}$ ) again suggesting the blockage of acid sites of  $\text{Al}_2\text{O}_3$  with the impregnation of W.

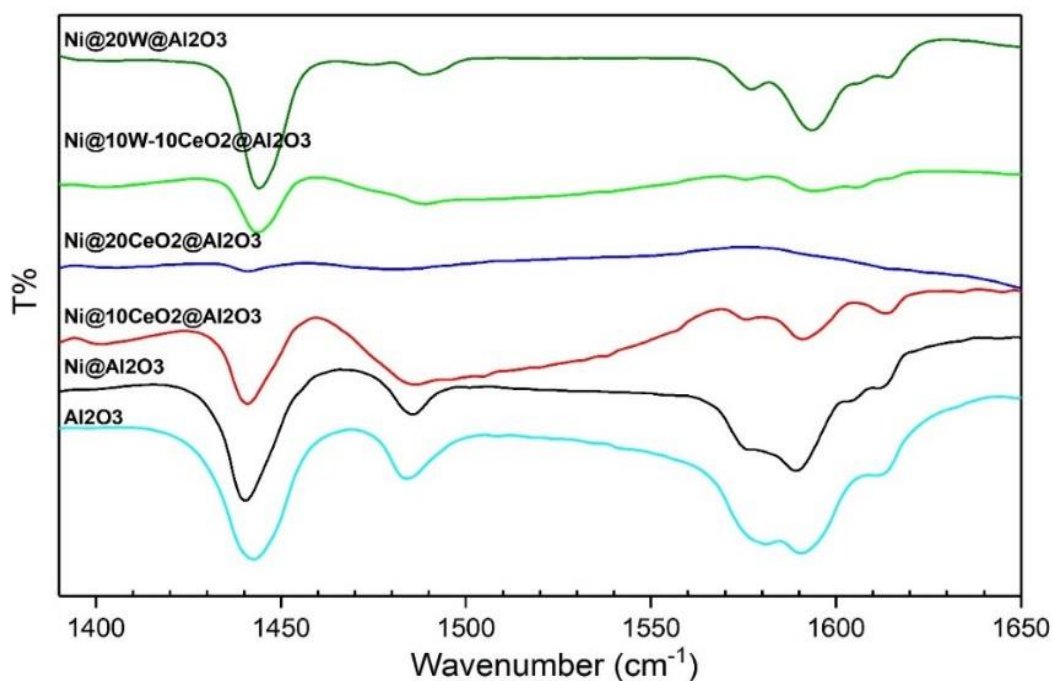


Figure 5.3. DRIFTS spectra of the difference between pyridine adsorbed and fresh samples of the synthesized catalysts.

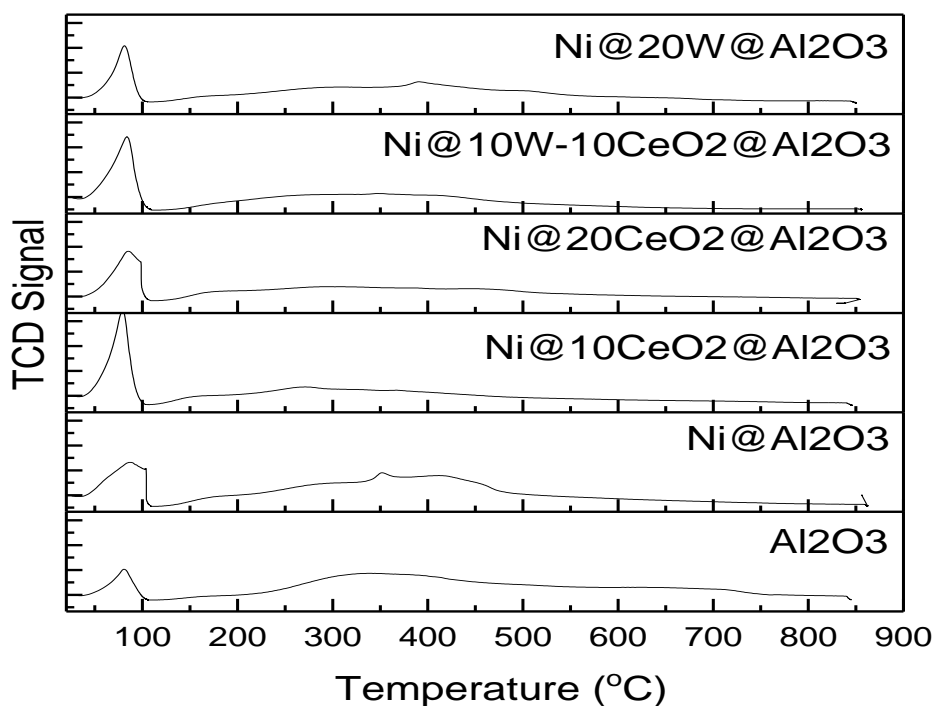


Figure 5.4.  $\text{NH}_3$ -TPD desorption curves of the synthesized catalysts.

TPR results of the catalysts given in Figure 5.5 present the reduction behavior of the metal oxides. Low temperature peak observed for  $\text{Ni@Al}_2\text{O}_3$  was associated with the reduction of surface  $\text{NiO}$  species which were in low concentration, and high temperature reduction peaks indicate the reduction of both non-stoichiometric surface  $\text{NiAl}_2\text{O}_4$  and stoichiometric  $\text{NiAl}_2\text{O}_4$ . Total  $\text{H}_2$  consumption for high temperature peak was approximately  $1.6 \text{ mmol/g}_{\text{cat}}$ . According to these results, the addition of 10 wt.%  $\text{CeO}_2$  did not change the reduction temperature of  $\text{NiAl}_2\text{O}_4$ . However, widening of the peak and increase of  $\text{H}_2$  uptake values compared to  $\text{Ni@Al}_2\text{O}_3$  ( $1.6 \text{ mmol/g}_{\text{cat}}$ ) obtained with the  $\text{Ni@10CeO}_2\text{@Al}_2\text{O}_3$  catalyst ( $2.5 \text{ mmol/g}_{\text{cat}}$ ) suggested the occurrence of the reduction of ceria materials at the same temperature range.  $20\text{CeO}_2\text{@Al}_2\text{O}_3$  material showed the two reduction peaks located at  $530 \text{ }^\circ\text{C}$  and  $692 \text{ }^\circ\text{C}$ , with hydrogen consumption values of  $0.05 \text{ mmol/g}_{\text{cat}}$  and  $0.07 \text{ mmol/g}_{\text{cat}}$ , respectively. Considering the 20 wt.% incorporation amount of  $\text{CeO}_2$ , hydrogen consumption value is quite low, suggesting that the reduction of  $\text{CeO}_2$  and formation of  $\text{CeAlO}_3$  occurred only at the surface of the material at this temperature during TPR analysis. During the reduction

of the catalysts which has a quite long duration (4 h) compared to TPR analysis, the formation of bulk  $\text{CeAlO}_3$  species, associated with the reduction of  $\text{Ce}^{4+}$  to  $\text{Ce}^{3+}$ , probably took place in the presence of nickel species since the characteristic peaks of  $\text{CeAlO}_3$  crystals were observed in the XRD patterns of nickel impregnated materials (Figure 5.2)<sup>95</sup>. One major reduction peak was observed for 20 wt.%  $\text{CeO}_2$  added  $\text{Ni}@20\text{CeO}_2@\text{Al}_2\text{O}_3$  material at 797 °C. Similar to the observations for the pattern of  $\text{Ni}@10\text{CeO}_2@\text{Al}_2\text{O}_3$  catalyst, this major peak was attributed to the reduction of non-stoichiometric surface  $\text{NiAl}_2\text{O}_4$ , stoichiometric  $\text{NiAl}_2\text{O}_4$ , and also the reduction of ceria materials to  $\text{CeAlO}_3$  crystals. The  $10\text{W}-10\text{CeO}_2@\text{Al}_2\text{O}_3$  material presented one major reduction peak (0.6 mmol/ $g_{\text{cat}}$ ) located at 860°C and  $\text{Ni}@10\text{W}-10\text{CeO}_2@\text{Al}_2\text{O}_3$  showed two major and one minor reduction peaks which occurred at 635 °C, 789°C and 860°C, respectively. XRD pattern of  $\text{Ni}@10\text{W}-10\text{CeO}_2@\text{Al}_2\text{O}_3$  catalyst showed the characteristic peaks of W and  $\text{Ni}_4\text{W}$  in Figure 5.2. The presence of tungsten oxide species was not observed since the XRD analysis was performed for the reduced catalyst. Without prior reduction, tungsten incorporation leads to the formation of  $\text{WO}_3$  crystals, which are reduced in a hydrogen atmosphere to  $\text{WO}_2$  and then W crystals<sup>96</sup>. The first peak of  $\text{Ni}@10\text{W}-10\text{CeO}_2@\text{Al}_2\text{O}_3$  has a hydrogen consumption amount of 0.8 mmol/ $g_{\text{cat}}$  and is probably due to the reduction of loosely bounded  $\text{WO}_3$  species on alumina and second wide peak which has a hydrogen consumption amount of 1.2 mmol/ $g_{\text{cat}}$  is assigned to the reduction of  $\text{WO}_3$  and formation of  $\text{Ni}_4\text{W}$  which takes places in three steps:  $\text{WO}_3$  to  $\text{WO}_2$ , and the further reduction of  $\text{WO}_2$  to tungsten metal and the formation of  $\text{Ni}_4\text{W}$ <sup>97</sup>. The peak located at around 860 °C for both  $10\text{W}-10\text{CeO}_2@\text{Al}_2\text{O}_3$  and  $\text{Ni}@10\text{W}-10\text{CeO}_2@\text{Al}_2\text{O}_3$  is probably due to the reduction of  $\text{WO}_3$  species that has a strong interaction with the alumina surface. The decrease of hydrogen consumption amount for this peak from 0.6 mmol/ $g_{\text{cat}}$  to 0.1 mmol/ $g_{\text{cat}}$  after nickel impregnation is due to the interaction of  $\text{WO}_3$  with incorporated nickel. TPR result of  $\text{Ni}@20\text{W}@\text{Al}_2\text{O}_3$  is similar to that of  $\text{Ni}@10\text{W}-10\text{CeO}_2@\text{Al}_2\text{O}_3$  except for the low temperature peak observed in the TPR of  $\text{Ni}@10\text{W}-10\text{CeO}_2@\text{Al}_2\text{O}_3$  which indicates that there is almost no loosely bounded  $\text{WO}_3$  species in the  $\text{Ni}@20\text{W}@\text{Al}_2\text{O}_3$  material (with a hydrogen consumption amount of 0.06 mmol/ $g_{\text{cat}}$ ) despite its higher

loading amount compared to Ni@10W-10CeO<sub>2</sub>@Al<sub>2</sub>O<sub>3</sub>. The absence of loosely bounded WO<sub>3</sub> species may indicate that the presence of ceria in Ni@10W-10CeO<sub>2</sub>@Al<sub>2</sub>O<sub>3</sub> decreases the interaction of tungsten and alumina. A decrease in the interaction of tungsten and alumina in Ni@10W-10CeO<sub>2</sub>@Al<sub>2</sub>O<sub>3</sub> may also be deduced from the major difference in the crystal sizes of tungsten species for the two materials, since the occurrence of sintering is easier if a metal/metal oxide has low interaction with the support. Crystal sizes of W are 43 nm and 21 nm (Table 5.2) for Ni@10W-10CeO<sub>2</sub>@Al<sub>2</sub>O<sub>3</sub> and Ni@20W@Al<sub>2</sub>O<sub>3</sub>, respectively.

SEM images of Ni@20CeO<sub>2</sub>@Al<sub>2</sub>O<sub>3</sub>, Ni@10W-10CeO<sub>2</sub>@Al<sub>2</sub>O<sub>3</sub> and Ni@20W@Al<sub>2</sub>O<sub>3</sub> catalysts are given in Figure 5.6. Images given on the left shows electron detector and images on the right shows backscattering electron detector images. Bright spots observed on the images of backscattering electron detector show metal particles with higher molecular weight. While Figure 5.6-A shows well dispersion of metals, probably Ni<sup>0</sup> and NiAl<sub>2</sub>O<sub>4</sub> species, in a non-uniform manner for the Ni@20CeO<sub>2</sub>@Al<sub>2</sub>O<sub>3</sub> catalyst, the presence of large particles was observed in Figure 5.6-B for the Ni@10W-10CeO<sub>2</sub>@Al<sub>2</sub>O<sub>3</sub> material. The backscattering image of Ni@20W@Al<sub>2</sub>O<sub>3</sub> given in Figure 5.6-C shows smaller particles compared to Figure 5.6-B also indicating the occurrence of sintering is more pronounced for Ni@10W-10CeO<sub>2</sub>@Al<sub>2</sub>O<sub>3</sub>. EDX analysis results showed that the targeted metal loading for all synthesized catalysts was mostly achieved (Table 5.3).

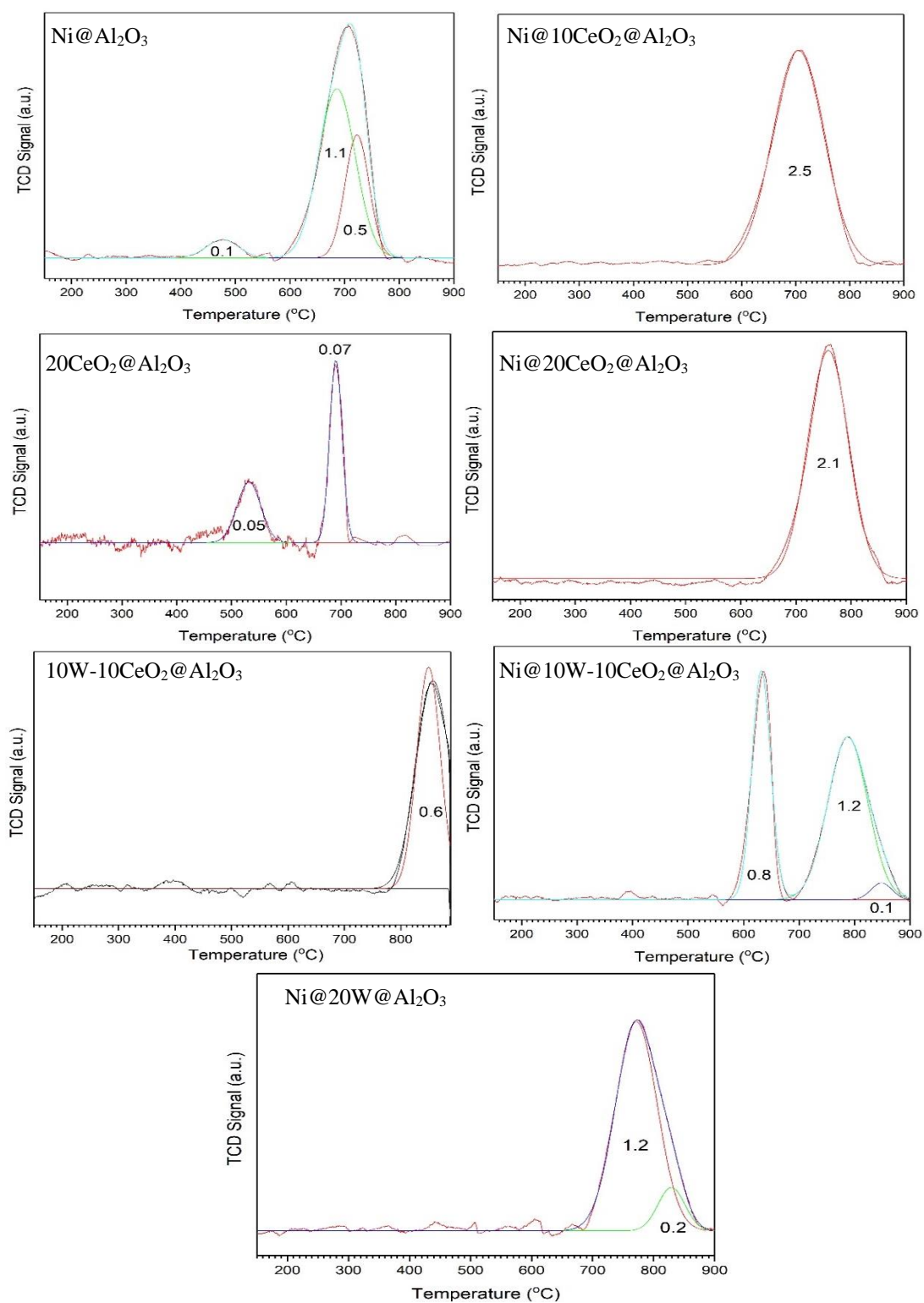


Figure 5.5. Temperature programmed reduction analysis results and H<sub>2</sub> consumption values of the synthesized catalysts (mmol/g<sub>cat</sub>).

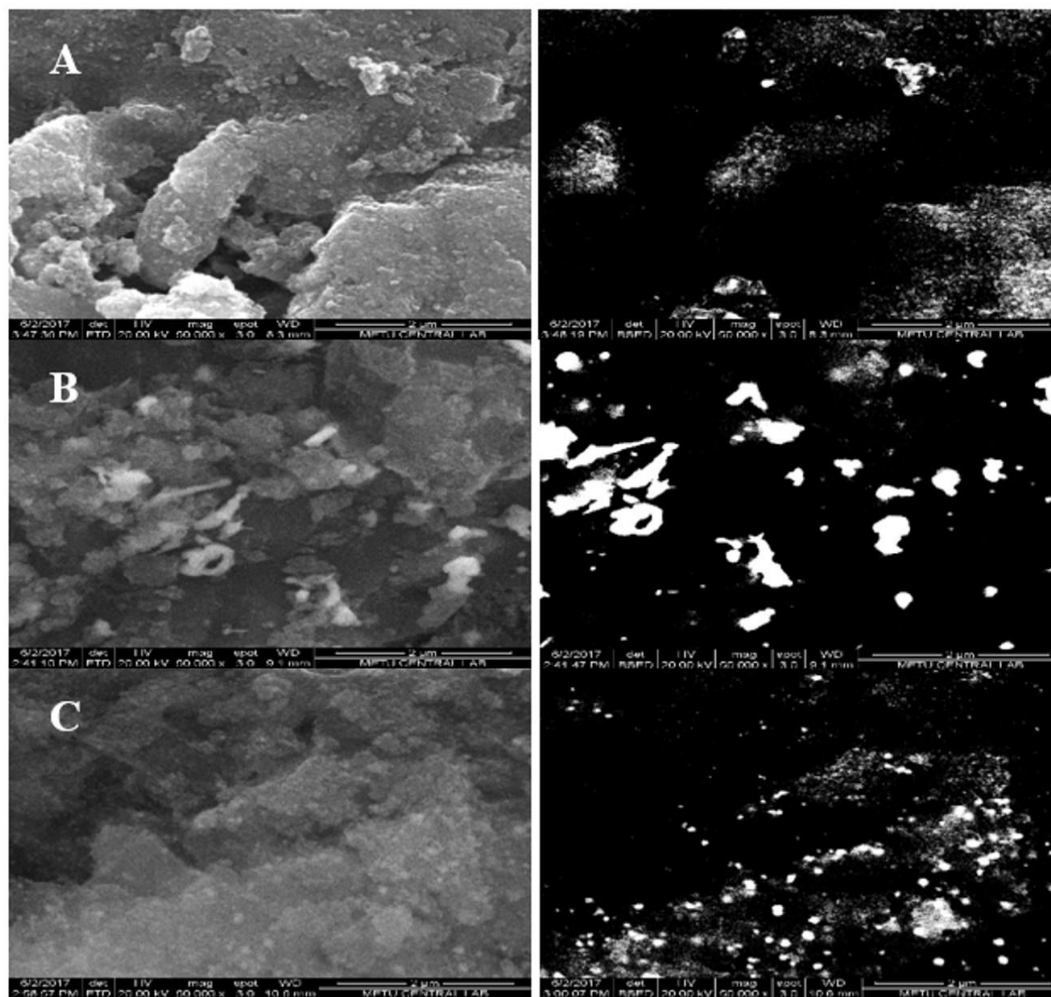


Figure 5.6. SEM images of synthesized catalysts with electron (left) and backscattering electron (right) detector: A) Ni@20CeO<sub>2</sub>@Al<sub>2</sub>O<sub>3</sub>, B) Ni@10W-10CeO<sub>2</sub>@Al<sub>2</sub>O<sub>3</sub>, C) Ni@20W@Al<sub>2</sub>O<sub>3</sub> (Magnification: 50000, and the scale: 2 μm in all images).

Table 5.3 Metal amounts in the synthesized catalysts.

Material	Metal Content (wt.%)					
	Ni		Ce		W	
	Target	EDX	Target	EDX	Target	EDX
Ni@Al <sub>2</sub> O <sub>3</sub>	10	9.2	-	-	-	-
Ni@10CeO <sub>2</sub> @Al <sub>2</sub> O <sub>3</sub>	10	10.8	8	6.6	-	-
Ni@20CeO <sub>2</sub> @Al <sub>2</sub> O <sub>3</sub>	10	7.5	16	14.4	-	-
Ni@10W-10CeO <sub>2</sub> @Al <sub>2</sub> O <sub>3</sub>	10	7.7	8	8.0	10	8.4
Ni@20W@Al <sub>2</sub> O <sub>3</sub>	10	10.4	-	-	20	22.1

## 5.2. Catalyst Performance Test Results

### 5.2.1. Effect of Catalyst Composition on Hydrogen Production in Diesel Steam Reforming Reaction

Performance tests of the Ni@Al<sub>2</sub>O<sub>3</sub>, Ni@10CeO<sub>2</sub>@Al<sub>2</sub>O<sub>3</sub>, Ni@20CeO<sub>2</sub>@Al<sub>2</sub>O<sub>3</sub>, Ni@20W@Al<sub>2</sub>O<sub>3</sub>, and Ni@10W-10CeO<sub>2</sub>@Al<sub>2</sub>O<sub>3</sub> catalysts in the DSR reaction were conducted at 800 °C and the selected operating conditions (GHSV=7500 h<sup>-1</sup> and H<sub>2</sub>O/C=2.5). The gas analysis of the reactor outlet showed the presence of H<sub>2</sub>, CO, CO<sub>2</sub>, CH<sub>4</sub>, C<sub>2</sub>H<sub>4</sub>, and C<sub>2</sub>H<sub>6</sub> gases and the results were presented and discussed throughout this section. The liquid analysis of the reactor outlet was performed as described in chapter 3, and the results were presented in detail in the appendix section (Appendix D). Results showed that there were only trace amounts of hydrocarbons present in the liquid samples. There was no indication of a hydrocarbons with higher molecular weight. Only C5-C7 group hydrocarbons were found in the liquid phase through high resolution gas chromatography analysis. For the experiments performed with the Ni@Al<sub>2</sub>O<sub>3</sub>, Ni@20CeO<sub>2</sub>@Al<sub>2</sub>O<sub>3</sub>, and Ni@20W@Al<sub>2</sub>O<sub>3</sub> catalysts, the total amount of hydrocarbons in the liquid phase was 0.01, 0 and 0.35 mol% of the diesel feed, respectively, indicating the complete conversion of diesel for all experiments. The synthesized catalysts were compared in terms of average gas product composition, coke deposition and hydrogen yield calculated using the average diesel formula (C<sub>17</sub>H<sub>36</sub>). Hydrogen yield was defined as the ratio of produced hydrogen moles to the moles of diesel fed to the reactor.

A DSR experiment was performed without a catalyst to observe the effect of a catalyst on hydrogen production at 800 °C and the selected optimum operating conditions. The DSR experiment without catalyst resulted in the production of a hydrogen composition (29.5% hydrogen in gas products, Figure 5.7) that is lower than the half of the value obtained with the Ni@20CeO<sub>2</sub>@Al<sub>2</sub>O<sub>3</sub> catalyst (62.8% hydrogen in gas products, Figure 5.7). Significant amounts of methane, ethylene, and ethane production were observed during this experiment showing that catalyst plays a

significant role in the hydrogen production and a small percent of the produced hydrogen was due to thermal cracking reactions.

According to the catalytic activity test results presented in Figure 5.7, tungsten incorporated Ni@20W@Al<sub>2</sub>O<sub>3</sub>, and Ni@10W-10CeO<sub>2</sub>@Al<sub>2</sub>O<sub>3</sub> catalysts showed lower H<sub>2</sub>, CO<sub>2</sub> and higher CO, CH<sub>4</sub>, and C<sub>2</sub>H<sub>4</sub> production. Average H<sub>2</sub> yield and CO/CO<sub>2</sub> ratio results are given in Table 5.4. As it can be seen from Table 5.4, the average H<sub>2</sub> yield values of Ni@20W@Al<sub>2</sub>O<sub>3</sub> and Ni@10W-10CeO<sub>2</sub>@Al<sub>2</sub>O<sub>3</sub> catalysts are lower compared to the Ni@Al<sub>2</sub>O<sub>3</sub>, Ni@10CeO<sub>2</sub>@Al<sub>2</sub>O<sub>3</sub>, and Ni@20CeO<sub>2</sub>@Al<sub>2</sub>O<sub>3</sub> catalysts. Comparison of average CO/CO<sub>2</sub> ratio together with average H<sub>2</sub> yield for the Ni@10CeO<sub>2</sub>@Al<sub>2</sub>O<sub>3</sub> and Ni@10W-10CeO<sub>2</sub>@Al<sub>2</sub>O<sub>3</sub> catalysts shows that tungsten incorporation decreased CO<sub>2</sub> and H<sub>2</sub> production, indicating low WGS rate for Ni@10W-10CeO<sub>2</sub>@Al<sub>2</sub>O<sub>3</sub>. Average H<sub>2</sub> yield and CO/CO<sub>2</sub> ratio results of Ni@20W@Al<sub>2</sub>O<sub>3</sub> catalyst which possesses a higher amount of tungsten, shows even lower WGS rate with lower CO<sub>2</sub> and H<sub>2</sub> production compared to Ni@10W-10CeO<sub>2</sub>@Al<sub>2</sub>O<sub>3</sub>.

Moreover, higher amounts of side product formation for Ni@20W@Al<sub>2</sub>O<sub>3</sub> and Ni@10W-10CeO<sub>2</sub>@Al<sub>2</sub>O<sub>3</sub> catalysts suggested slightly lower reforming reaction rate compared to ceria-alumina and alumina supported catalysts. The main reason of decreased reforming and WGS rate for the tungsten incorporated catalyst was the formation of Ni<sub>4</sub>W crystals (Figure 5.2), compared to ceria-alumina and alumina supported catalysts that showed the presence of Ni<sup>0</sup> and NiAl<sub>2</sub>O<sub>4</sub> crystals in their XRD patterns (Figure 5.2). XRD results (Figure 5.2) showed the presence of Ni<sup>0</sup> clearly for Ni@10W-10CeO<sub>2</sub>@Al<sub>2</sub>O<sub>3</sub>, whereas characteristic peak of Ni<sup>0</sup> was not sharp and clear for the Ni@20W@Al<sub>2</sub>O<sub>3</sub> catalyst which led to lower reforming reaction rate meaning lower hydrogen yield with the Ni@20W@Al<sub>2</sub>O<sub>3</sub> catalyst. The lower activity of the Ni@20W@Al<sub>2</sub>O<sub>3</sub> and Ni@10W-10CeO<sub>2</sub>@Al<sub>2</sub>O<sub>3</sub> catalysts may also be affected by their lower surface areas indicating lower number of active sites compared to other catalysts (Table 5.1). Even though tungsten-nickel structures reduced reforming reaction rate, it was also significantly minimized, even eliminated coke deposition

(Table 5.4). Minimization of coke deposition was surprising since the two materials had higher total number of acid sites compared to the ceria-alumina supported catalysts (Table 5.2). The promoting role of acid sites in coke deposition has been a known fact. However, the type of acid sites is also a key factor regarding the promotion of carbon deposition and Brønsted acid sites are believed to be mainly responsible for carbon deposition. Coking mainly originates from the role of Brønsted acid sites in cracking reactions. According to Figure 5.3, all materials possess Lewis type acid sites which are not directly linked with coke deposition. Another difference between synthesized catalysts in terms of their physical properties was that tungsten-alumina supported catalysts had higher pore diameter with bimodal pore size distribution than that of others. Lower coke deposition observed with the Ni@10W-10CeO<sub>2</sub>@Al<sub>2</sub>O<sub>3</sub> catalyst could be related to its higher pore diameter which could accelerate the transportation of reactant and products minimizing the time required for coking reactions to take place. The coke minimization effect of tungsten incorporation to nickel catalysts was previously reported in the dry reforming reaction of methane<sup>60</sup>. The main factor that resulted in the minimization of coke deposition is probably the presence of Ni<sub>4</sub>W crystals due to the low solubility of carbon in Ni<sub>4</sub>W crystals<sup>98</sup>. The coke minimization effect of W suggests that W incorporated catalysts can be used in long term DSR reaction without deactivation. Hydrogen production can be enhanced just by using a higher H<sub>2</sub>O/C molar ratio to improve not only WGSR but also coke deposition (Figure 5.7 and Table 5.4).

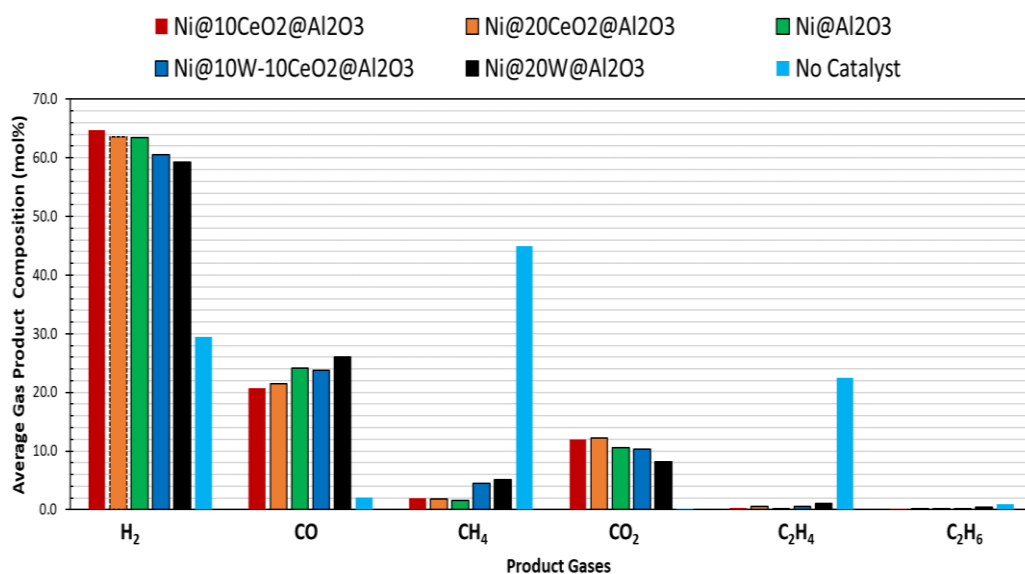


Figure 5.7. The effect of catalyst content on the average gas product composition for the DSR reaction (GHSV=7500, H<sub>2</sub>O/C=2.5, 800°C).

Table 5.4 Catalyst activity test results in terms of average H<sub>2</sub> yield, coke deposition and average produced side product amount.

Catalyst	Average H <sub>2</sub> Yield (max <sub>theoretical</sub> i=35)	$\frac{\dot{N}_{CO}}{\dot{N}_{CO_2}}$	Average Gas Side Product Composition (ppm, molar)				Coke% (g <sub>coke</sub> / g <sub>used</sub> catalyst)
			CH <sub>4</sub>	C <sub>2</sub> H <sub>4</sub>	C <sub>2</sub> H <sub>6</sub>	C <sub>3</sub> H <sub>6</sub>	
Ni@Al <sub>2</sub> O <sub>3</sub>	29.3	2.3	1500	200	70	0	3.1
Ni@10CeO <sub>2</sub> @Al <sub>2</sub> O <sub>3</sub>	30.8	1.7	1900	300	150	0	4.7
Ni@20CeO <sub>2</sub> @Al <sub>2</sub> O <sub>3</sub>	29.1	1.7	1900	550	200	0	1.9
Ni@10W-10CeO <sub>2</sub> @Al <sub>2</sub> O <sub>3</sub>	25.6	2.3	4500	600	200	0	0
Ni@20W@Al <sub>2</sub> O <sub>3</sub>	23.9	3.2	5000	1000	400	0	0.1

The highest H<sub>2</sub> yield and lowest CO/CO<sub>2</sub> formation ratio was obtained with the Ni@10CeO<sub>2</sub>@Al<sub>2</sub>O<sub>3</sub> catalyst, which also led to the highest coke deposition despite its stable activity (Figure 5.8 and Table 5.4). Thermogravimetric analysis of used Ni@10CeO<sub>2</sub>@Al<sub>2</sub>O<sub>3</sub> catalyst resulted in a weight loss at around 497°C, suggesting

filamentous carbon deposition. For the Ni@Al<sub>2</sub>O<sub>3</sub>, Ni@20CeO<sub>2</sub>@Al<sub>2</sub>O<sub>3</sub>, and Ni@10W-10CeO<sub>2</sub>@Al<sub>2</sub>O<sub>3</sub> catalysts, weight loss was observed at around 600 °C, 770 °C, and 700 °C, respectively. These temperature values indicated the presence of graphitic carbon, which is more stable and more difficult to remove from the catalyst surface. Higher activity of Ni@10CeO<sub>2</sub>@Al<sub>2</sub>O<sub>3</sub> over other catalysts is due to its higher catalytic success in WGSR (according to CO/CO<sub>2</sub> formation ratios given in Table 5.4). When 10 wt.% and 20 wt.% CeO<sub>2</sub> loaded catalysts were compared in terms of their properties, temperature programmed reduction pattern of 20 wt.% CeO<sub>2</sub> loaded catalyst showed higher reduction temperature, indicating stronger interaction of nickel with the support material (Figure 5.5). Higher CeO<sub>2</sub> loading and strong active metal-support interaction lead to a decrease in coke deposition (Table 5.4). 10 wt.% loaded one resulted in slightly higher acidity, much lower CeAlO<sub>3</sub> crystal size and slightly lower Ni<sup>0</sup> crystal size which could be the result of its higher reforming activity. Similar findings to the results obtained in this study were reported that at low incorporation amounts of CeO<sub>2</sub>, enhancement in dispersion of nickel and reduction in the intensities of NiAl<sub>2</sub>O<sub>4</sub> crystals were observed<sup>99</sup>. NiAl<sub>2</sub>O<sub>4</sub> crystal size cannot be calculated, since XRD characteristic peak location is same for NiAl<sub>2</sub>O<sub>4</sub> and  $\gamma$ -Al<sub>2</sub>O<sub>3</sub> phases. The second highest activity in diesel steam reforming reaction was obtained with Ni@Al<sub>2</sub>O<sub>3</sub> catalyst despite its higher Ni<sup>0</sup> crystal size. The reason of its success was believed to be due to its higher acidity (Figure 5.4). Higher number of acid sites of this catalyst lead to cracking of long-chained hydrocarbon compounds more easily.

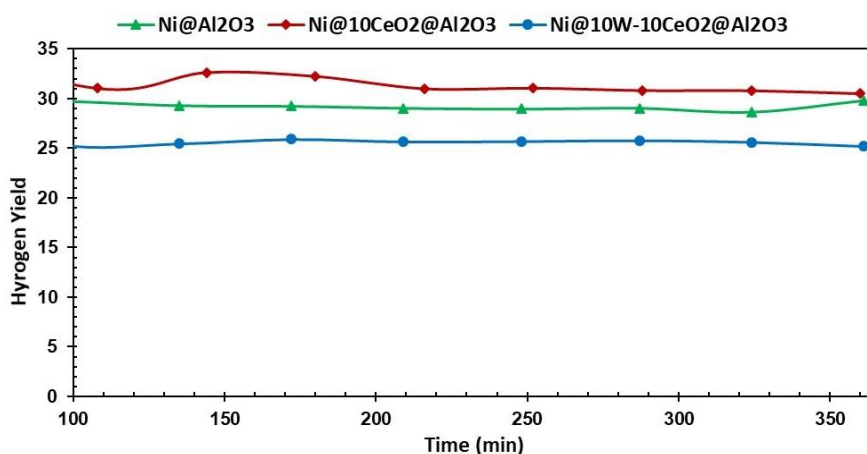


Figure 5.8. Change of hydrogen yield with respect to time for the Ni@Al<sub>2</sub>O<sub>3</sub>, Ni@10CeO<sub>2</sub>@Al<sub>2</sub>O<sub>3</sub> and Ni@10W-10CeO<sub>2</sub>@Al<sub>2</sub>O<sub>3</sub> (GHSV=7500, H<sub>2</sub>O/C=2.5, 800°C).

### 5.2.2. Effect of Catalyst Composition on Hydrogen Production in Diesel Autothermal Reforming Reaction

Performance test results of the catalysts analyzed in this chapter (Ni@10CeO<sub>2</sub>@Al<sub>2</sub>O<sub>3</sub>, Ni@20CeO<sub>2</sub>@Al<sub>2</sub>O<sub>3</sub>, Ni@Al<sub>2</sub>O<sub>3</sub>) in the diesel autothermal reforming reaction were presented in Figure 5.9. Comparison of these three catalysts showed that ceria incorporation are beneficial at low amounts for both steam and autothermal reforming reactions of diesel.

In the ATR reaction, the most successful catalyst among the catalysts presented in this section in terms of molar hydrogen concentration in the product gas stream is again Ni@10CeO<sub>2</sub>@Al<sub>2</sub>O<sub>3</sub> as can be seen from Figure 5.9. The comparison of the activities of the Ni@10CeO<sub>2</sub>@Al<sub>2</sub>O<sub>3</sub>, Ni@Al<sub>2</sub>O<sub>3</sub>, and Ni@20CeO<sub>2</sub>@Al<sub>2</sub>O<sub>3</sub> catalysts in both diesel steam and autothermal reforming reactions were presented in Table 5.5 in terms of average gas product composition. The lower composition of hydrogen in the gas products of ATR was expected considering the stoichiometry of the DSR and ATR reactions. 35 moles of hydrogen and 26.5 moles of hydrogen can be obtained from one mole of diesel (C<sub>17</sub>H<sub>36</sub>) in the steam and autothermal reforming reactions, respectively. The Ni@10CeO<sub>2</sub>@Al<sub>2</sub>O<sub>3</sub> catalyst, which showed the highest activity in the steam reforming reaction among ceria incorporated catalysts, presented the highest hydrogen

production capability in the diesel autothermal reforming reaction as it can be seen in Table 5.5. The Ni@Al<sub>2</sub>O<sub>3</sub> catalyst presented slightly better hydrogen production success in the diesel autothermal reforming reaction and slightly lower hydrogen production in the diesel steam reforming reaction compared to the Ni@20CeO<sub>2</sub>@Al<sub>2</sub>O<sub>3</sub> catalyst. For all catalysts, side product composition in the product gas is higher in the steam reforming reaction compared to the autothermal reforming reaction, showing that the oxygen in the reaction environment converts hydrocarbons into CO and CO<sub>2</sub>. The amount of CO<sub>2</sub> produced is much higher in the autothermal reforming reaction (Table 5.5) and the results given in Figure 5.9 also show that the hydrogen and methane concentration in the product gas are directly dependent on each other for the autothermal reforming reaction. In other words, under the oxygen atmosphere, mainly reforming of methane dominates the hydrogen production and CO and CO<sub>2</sub> production mainly indicates the occurrence of partial oxidation/combustion reactions. The higher CO<sub>2</sub> concentration suggests probable formation of combustion reactions before the catalyst bed.

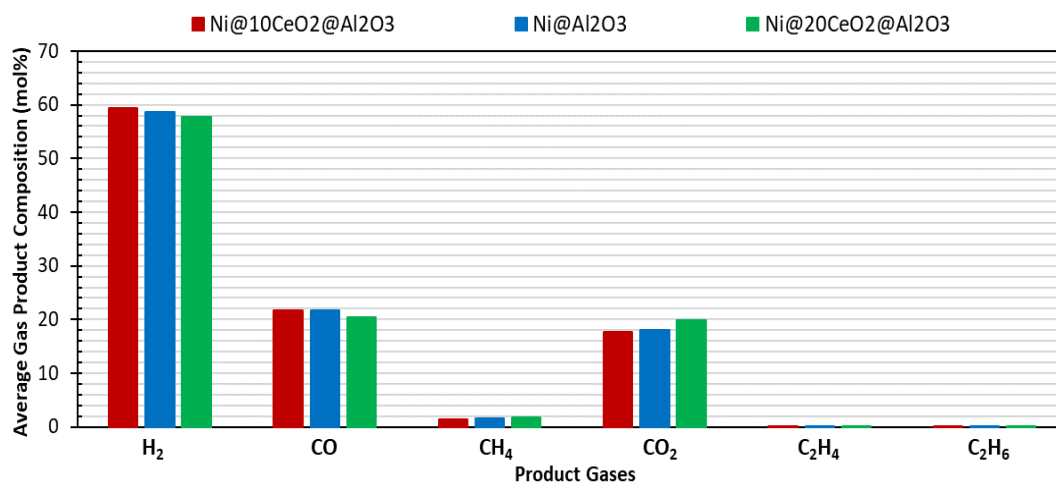


Figure 5.9. The effect of catalyst content on the average gas product composition in the ATR reaction (GHSV=7500 h<sup>-1</sup>, H<sub>2</sub>O/C=2.5, O<sub>2</sub>/C=0.5, 800°C).

Table 5.5 Comparison of diesel steam and autothermal activity test results for Ni@10CeO<sub>2</sub>@Al<sub>2</sub>O<sub>3</sub>, Ni@Al<sub>2</sub>O<sub>3</sub> and Ni@20CeO<sub>2</sub>@Al<sub>2</sub>O<sub>3</sub> catalysts in terms of average gas product composition.

Catalyst	RXN	Average Gas Product Composition (%)					
		H <sub>2</sub>	CO	CH <sub>4</sub>	CO <sub>2</sub>	C <sub>2</sub> H <sub>4</sub>	C <sub>2</sub> H <sub>6</sub>
Ni@10CeO <sub>2</sub> @Al <sub>2</sub> O <sub>3</sub>	<i>DSR</i>	64.8	20.7	1.9	12.0	0.4	0.2
	<i>ATR</i>	59.4	21.6	1.3	17.6	0	0
Ni@Al <sub>2</sub> O <sub>3</sub>	<i>DSR</i>	63.4	24.2	1.6	10.6	0.2	0.1
	<i>ATR</i>	58.6	21.8	1.6	18.0	0	0.1
Ni@20CeO <sub>2</sub> @Al <sub>2</sub> O <sub>3</sub>	<i>DSR</i>	63.6	21.5	1.9	12.3	0.6	0.2
	<i>ATR</i>	57.7	20.5	1.9	19.8	0.0	0.0

## CHAPTER 6

### DEVELOPMENT OF CERIA AND RUTHENIUM PROMOTED NICKEL/ALUMINA CATALYSTS FOR STEAM AND AUTOTHERMAL REFORMING OF DIESEL

#### 6.1. Characterization Results

Characterization studies were performed on  $\text{Al}_2\text{O}_3$  support,  $1.5\text{Ru}@10\text{CeO}_2@\text{Al}_2\text{O}_3$ ,  $1.5\text{Ru}@20\text{CeO}_2@\text{Al}_2\text{O}_3$ ,  $\text{Ni}@0.5\text{Ru}@Al_2O_3$ ,  $\text{Ni}@1.0\text{Ru}@Al_2O_3$ ,  $\text{Ni}@1.5\text{Ru}@Al_2O_3$ ,  $\text{Ni}@1.5\text{Ru}@10\text{CeO}_2@\text{Al}_2\text{O}_3$ , and  $\text{Ni}@1.5\text{Ru}@20\text{CeO}_2@\text{Al}_2\text{O}_3$  catalysts. All nickel impregnated catalysts (10 wt.% nickel) were reduced before the analysis (except for TPR analysis). Characterization results were discussed throughout this section in terms of the effect of metal loading amount (for Ru; 0.5 wt.%, 1.0 wt.% and 1.5 wt.% and for  $\text{CeO}_2$ ; 10 wt.% or 20 wt.%) or the effect of the type of metal that was incorporated ( $\text{CeO}_2$  and/or Ru) on the properties of the catalysts.

Physical properties of the catalytic materials are presented in Table 6.1. As it can be seen from these results, metal loading into alumina support decreases the BET surface area of the materials. Table 6.1 shows that metal incorporation decreases surface area when the results of  $\text{Al}_2\text{O}_3$  and metal impregnated materials are compared. A decrease in surface area and pore volume values indicates blockage of pores due to metal loading. An increase in pore diameter values suggests that the metal blockage occurred in some mesopores and micropores of the support. Table 6.1 also shows the results of microporosity percents of the metal incorporated materials are lower than that of  $\text{Al}_2\text{O}_3$ . All synthesized materials can be classified as mesoporous materials because their pore diameters are greater than 2 nm.

Nitrogen adsorption/desorption isotherms of all materials were given in Figure 6.1-A, these materials can be classified as Type IV with H1 type hysteresis loop, according to IUPAC definition<sup>89,90,100</sup>. Type IV isotherm and H1 type hysteresis loop indicate mesoporous material and the presence of narrow uniform pore size distribution. A decrease in pore volume and a shift in hysteresis loop to higher P/P<sub>0</sub> values can be observed as total metal loading increases (Table 6.1 and Figure 6.1-A, B). Figure 6.1-B shows the pore size distributions indicating mesoporosity accompanied by some microporosity, which was calculated by using the ratio of N<sub>2</sub> adsorbed volume at 0.02 P/P<sub>0</sub> to N<sub>2</sub> adsorbed volume at 0.95 P/P<sub>0</sub>. The lowest and highest average pore diameters are 8.5 and 12.9 nm, respectively. Pore size distribution of the catalysts also shows the dominance of mesoporosity.

Table 6.1 Physical properties of Ru loaded catalysts.

<b>Material</b>	<b>Multi Point BET Surface Area (m<sup>2</sup>/g)</b>	<b>BJH Desorption Pore Volume (cm<sup>3</sup>/g)</b>	<b>BJH Desorption Average Pore Diameter (nm)</b>	<b>Microporosity %</b>
Al <sub>2</sub> O <sub>3</sub>	142.0	0.55	8.5	8.3
Ni@0.5Ru@Al <sub>2</sub> O <sub>3</sub>	98.9	0.47	12.9	6.8
Ni@1.0Ru@Al <sub>2</sub> O <sub>3</sub>	100.4	0.48	11.8	6.9
Ni@1.5Ru@Al <sub>2</sub> O <sub>3</sub>	85.9	0.41	11.7	7.0
1.5Ru@10CeO <sub>2</sub> @Al <sub>2</sub> O <sub>3</sub>	109.7	0.48	11.1	7.5
1.5Ru@20CeO <sub>2</sub> @Al <sub>2</sub> O <sub>3</sub>	75.8	0.37	11.4	7.3
Ni@1.5Ru@10CeO <sub>2</sub> @Al <sub>2</sub> O <sub>3</sub>	81.7	0.39	12.9	7.7
Ni@1.5Ru@20CeO <sub>2</sub> @Al <sub>2</sub> O <sub>3</sub>	69.3	0.36	12.3	7.4

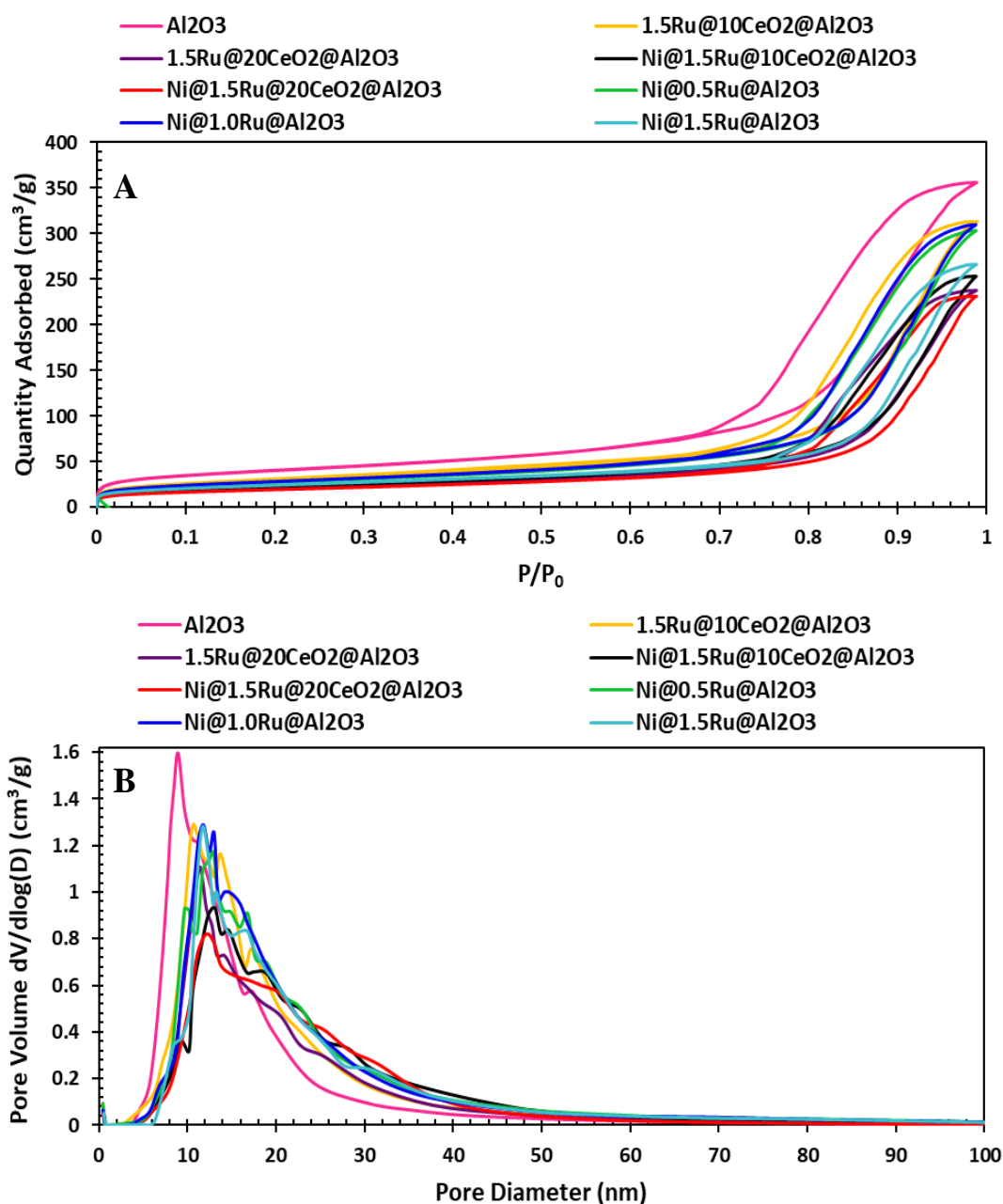


Figure 6.1.  $N_2$  adsorption/desorption isotherms (A) and pore size distributions (B) of Ru incorporated catalysts.

X-ray diffraction patterns of the synthesized catalysts are presented in Figure 6.2. XRD patterns of support materials showed the characteristic peaks of  $\gamma$ -Al<sub>2</sub>O<sub>3</sub> at  $2\theta$  values of 19.33°, 37.5°, 45.6°, 67.0° and 85.0°. XRD patterns of 1.5Ru@10CeO<sub>2</sub>@Al<sub>2</sub>O<sub>3</sub>, and 1.5Ru@20CeO<sub>2</sub>@Al<sub>2</sub>O<sub>3</sub> materials showed the

formation of  $\text{RuO}_2$  (PDF card No. 00-004-0593),  $\text{CeO}_2$  (PDF card No. 00-004-0593) and  $\gamma\text{-Al}_2\text{O}_3$  (PDF card No. 01-074-4629). After nickel impregnation, calcination and reduction of  $1.5\text{Ru}@10\text{CeO}_2@\text{Al}_2\text{O}_3$ , and  $1.5\text{Ru}@20\text{CeO}_2@\text{Al}_2\text{O}_3$ ,  $\text{CeAlO}_3$  (PDF card No. 01-081-1185),  $\text{NiAl}_2\text{O}_4$  (PDF card No. 00-010-0339),  $\text{Ni}^\circ$  (PDF card No. 01-071-4653) and  $\text{NiO}$  (PDF card No. 4-835) peaks appeared. The main characteristic peaks of  $\text{RuO}_2$  and  $\text{CeO}_2$  are at the same  $2\theta$  values. Therefore the peak at a  $2\theta$  value of  $28.1^\circ$  might correspond to  $\text{RuO}_2$  and  $\text{CeO}_2$ . X-Ray diffraction patterns of  $\text{Ni}@0.5\text{Ru}@Al_2O_3$ ,  $\text{Ni}@1.0\text{Ru}@Al_2O_3$ , and  $\text{Ni}@1.5\text{Ru}@Al_2O_3$  showed the formation of  $\text{Ni}^\circ$  (PDF card No. 01-071-4653),  $\text{NiAl}_2\text{O}_4$  (PDF card No. 00-010-0339),  $\text{Ru}$  (PDF card No. 01-071-4656) and  $\gamma\text{-Al}_2\text{O}_3$  (PDF card No. 01-074-4629). An increase in the intensities of  $\text{Ru}$  peaks in the  $\text{Ni}@0.5\text{Ru}@Al_2O_3$ ,  $\text{Ni}@1.0\text{Ru}@Al_2O_3$ , and  $\text{Ni}@1.5\text{Ru}@Al_2O_3$  catalysts were observed due to the increase in loading amount of  $\text{Ru}$  in the support.

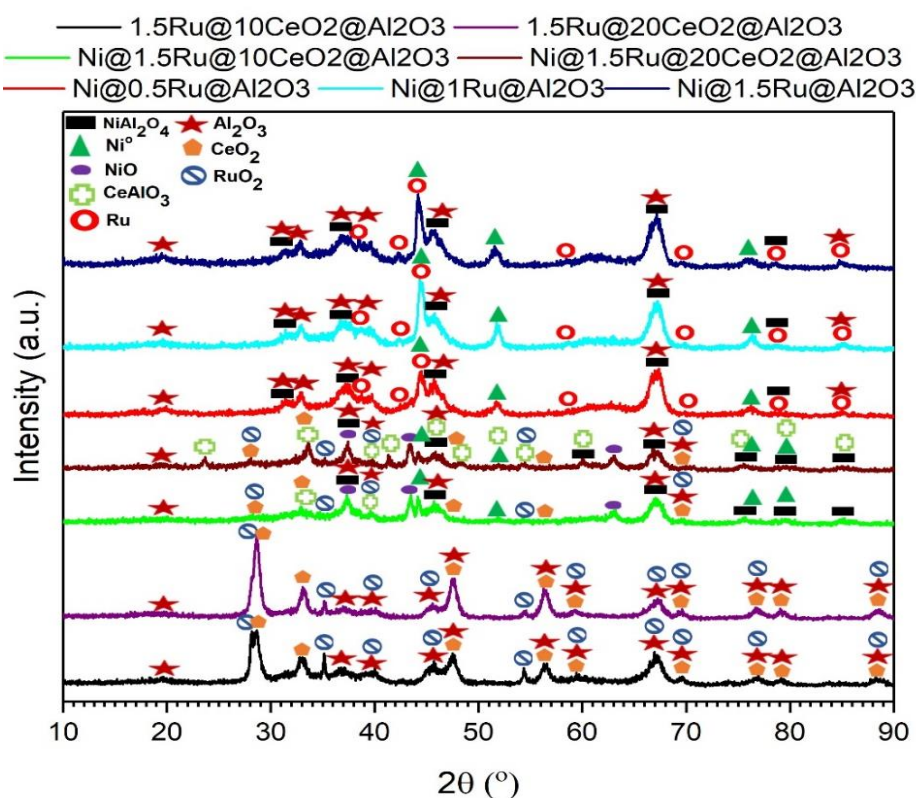


Figure 6.2. X-Ray diffraction patterns of the ceria and ruthenium promoted nickel/alumina catalysts.

The results of temperature programmed reduction analysis (TPR) of 1.5Ru@Al<sub>2</sub>O<sub>3</sub>, Ni@0.5Ru@Al<sub>2</sub>O<sub>3</sub>, Ni@1.0Ru@Al<sub>2</sub>O<sub>3</sub>, and Ni@1.5Ru@Al<sub>2</sub>O<sub>3</sub> materials are presented in Figure 6.3. For the 1.5Ru@Al<sub>2</sub>O<sub>3</sub> material, the presence of four reduction peaks was observed at 146 °C (0.20 mmol/g<sub>cat</sub>), 171 °C (0.64 mmol/g<sub>cat</sub>), 248 °C (1.25 mmol/g<sub>cat</sub>), and 352 °C (0.24 mmol/g<sub>cat</sub>). The first peak that is common in all nickel impregnated ruthenium loaded materials, can be assigned to the reduction of RuO<sub>2</sub>. Other three peaks are probably originating from the reduction of RuO<sub>x</sub> species that has different interaction with the alumina support<sup>67,101,102</sup>. Nickel impregnated catalysts, Ni@0.5Ru@Al<sub>2</sub>O<sub>3</sub>, Ni@1.5Ru@Al<sub>2</sub>O<sub>3</sub>, and Ni@1.5Ru@Al<sub>2</sub>O<sub>3</sub>, presented one high temperature peak that corresponds to the reduction of NiAl<sub>2</sub>O<sub>4</sub>. The reduction of both non-stoichiometric surface NiAl<sub>2</sub>O<sub>4</sub> and stoichiometric NiAl<sub>2</sub>O<sub>4</sub> at a temperature of 708 °C (1.93 mmol/g<sub>cat</sub>) for the Ni@Al<sub>2</sub>O<sub>3</sub> catalyst was presented in Chapter 5. Considering the TPR result of Ni@Al<sub>2</sub>O<sub>3</sub> catalyst, it was safe to assume that high temperature peak observed in the nickel impregnated materials was due to the reduction of both non-stoichiometric surface NiAl<sub>2</sub>O<sub>4</sub> and stoichiometric NiAl<sub>2</sub>O<sub>4</sub>. The reduction temperatures of NiAl<sub>2</sub>O<sub>4</sub> are close to each other in the Ni@0.5Ru@Al<sub>2</sub>O<sub>3</sub>, Ni@1.0Ru@Al<sub>2</sub>O<sub>3</sub>, and Ni@1.5Ru@Al<sub>2</sub>O<sub>3</sub> materials, and their H<sub>2</sub> uptake values were 1.74 mmol/g<sub>cat</sub>, 1.99 mmol/g<sub>cat</sub>, and 2.27 mmol/g<sub>cat</sub>, respectively. When the low temperature reduction peaks of Ni@0.5Ru@Al<sub>2</sub>O<sub>3</sub> and Ni@1.5Ru@Al<sub>2</sub>O<sub>3</sub> materials were compared, the total H<sub>2</sub> uptake values for the reduction of RuO<sub>2</sub> increased with increasing ruthenium content. However, the major change in the H<sub>2</sub> uptake after nickel impregnation into 1.5 wt.% Ru loaded support was due to the reduction peaks associated with ruthenium. Both this observation and also the high H<sub>2</sub> uptake value of the RuO<sub>2</sub> reduction peak of Ni@1.0Ru@Al<sub>2</sub>O<sub>3</sub> suggests that there may be a Ni-Ru alloy formation which changes the reduction behavior of the material. Figure 6.4 shows the TPR results of the 1.5Ru@10CeO<sub>2</sub>@Al<sub>2</sub>O<sub>3</sub>, 1.5Ru@20CeO<sub>2</sub>@Al<sub>2</sub>O<sub>3</sub>, Ni@1.5Ru@10CeO<sub>2</sub>@Al<sub>2</sub>O<sub>3</sub>, and Ni@1.5Ru@20CeO<sub>2</sub>@Al<sub>2</sub>O<sub>3</sub> materials. For the 1.5Ru@10CeO<sub>2</sub>@Al<sub>2</sub>O<sub>3</sub> and 1.5Ru@20CeO<sub>2</sub>@Al<sub>2</sub>O<sub>3</sub> materials, reduction peaks were observed at three different temperature ranges; < 250 °C, 250 °C-750 °C and >750 °C. The first range corresponds to the reduction of RuO<sub>2</sub> and RuO<sub>x</sub> species. The medium

temperature range shows the reduction of  $\text{CeO}_2$  crystals and the high temperature peaks are associated with the formation of  $\text{CeAlO}_3$  crystals. After nickel impregnation, two peaks were observed between 100 °C and 200 °C, which may indicate the effect of nickel on Ru- $\text{Al}_2\text{O}_3$  or Ru- $\text{CeO}_2$ - $\text{Al}_2\text{O}_3$  bond on the material surface. Major peak located between 700-800 °C corresponds to the reduction of both non-stoichiometric surface  $\text{NiAl}_2\text{O}_4$  and stoichiometric  $\text{NiAl}_2\text{O}_4$ , and the peak observed for  $\text{Ni}@1.5\text{Ru}@20\text{CeO}_2@\text{Al}_2\text{O}_3$  at 841 °C is due to the formation of  $\text{CeAlO}_3$  crystals.

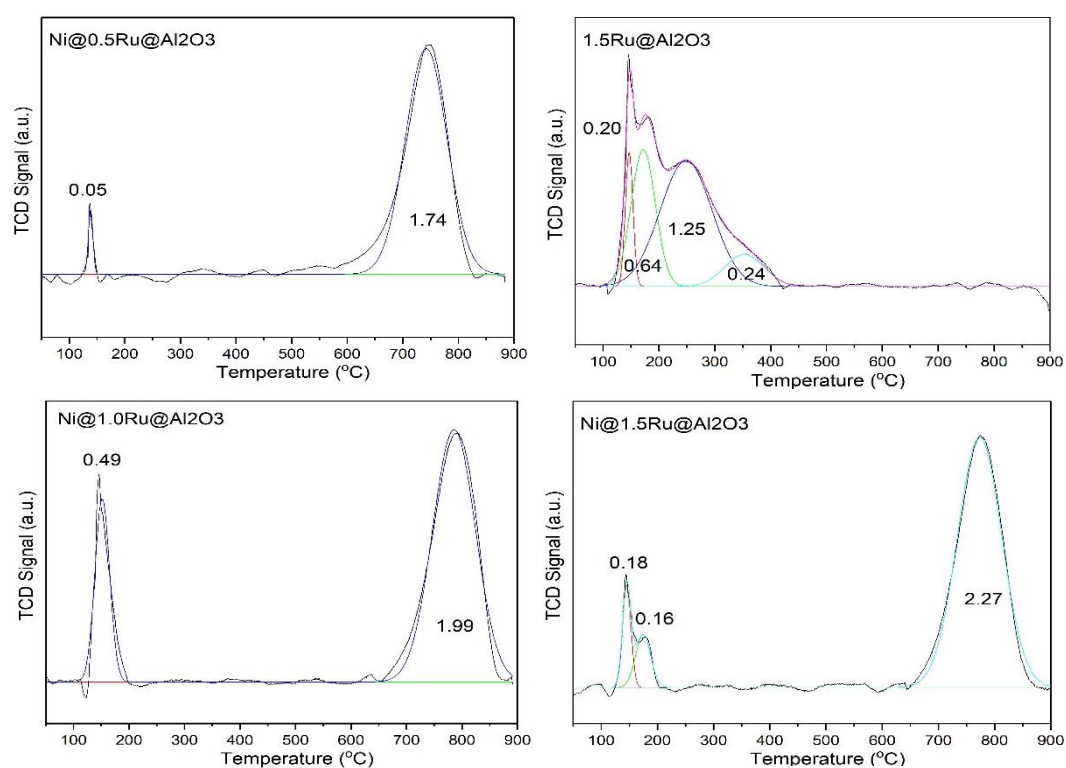


Figure 6.3. TPR results of ruthenium loaded materials.

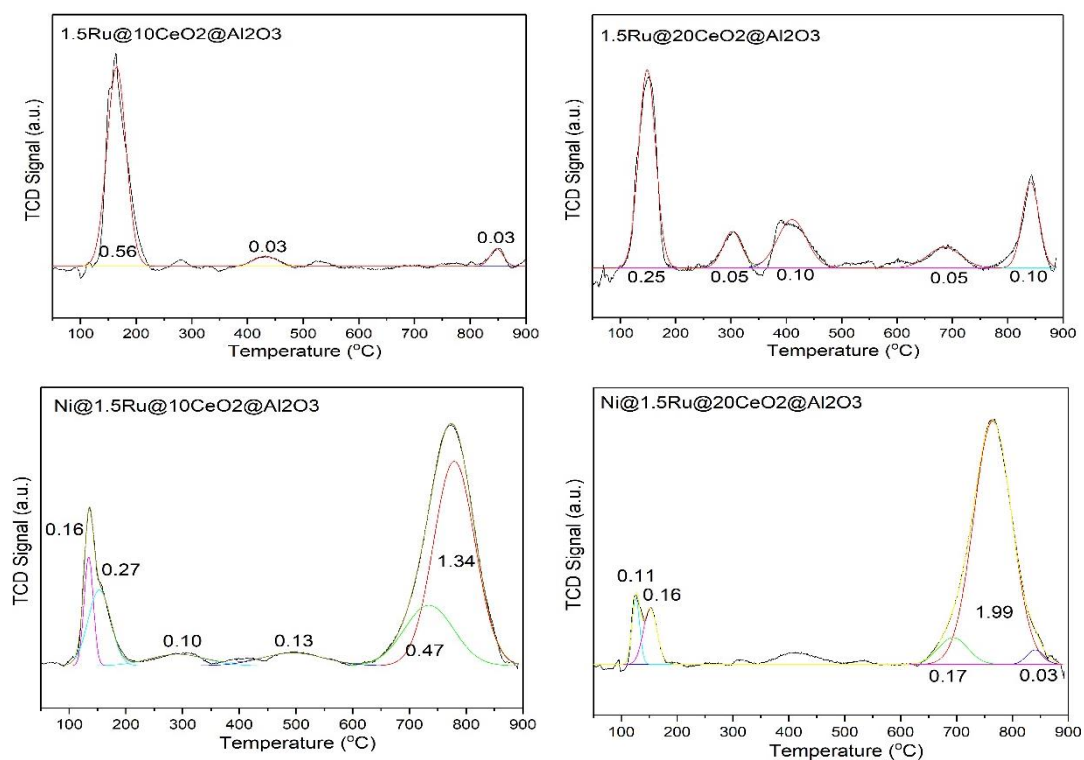


Figure 6.4. TPR results of ruthenium and ceria loaded materials.

Figure 6.5 illustrates the DRIFTS spectra of the difference between pyridine adsorbed and fresh samples for the synthesized materials. Peaks at  $1445\text{ cm}^{-1}$ ,  $1575\text{ cm}^{-1}$ , and  $1614\text{ cm}^{-1}$  were observed for all materials showed Lewis acid sites in the synthesized catalysts. Transmission band at  $1590\text{ cm}^{-1}$  is due to the presence of weak Brønsted acid site in the catalysts. The transmission band located at  $1485\text{ cm}^{-1}$  is attributed to both weak Lewis and weak Bronsted acid sites.

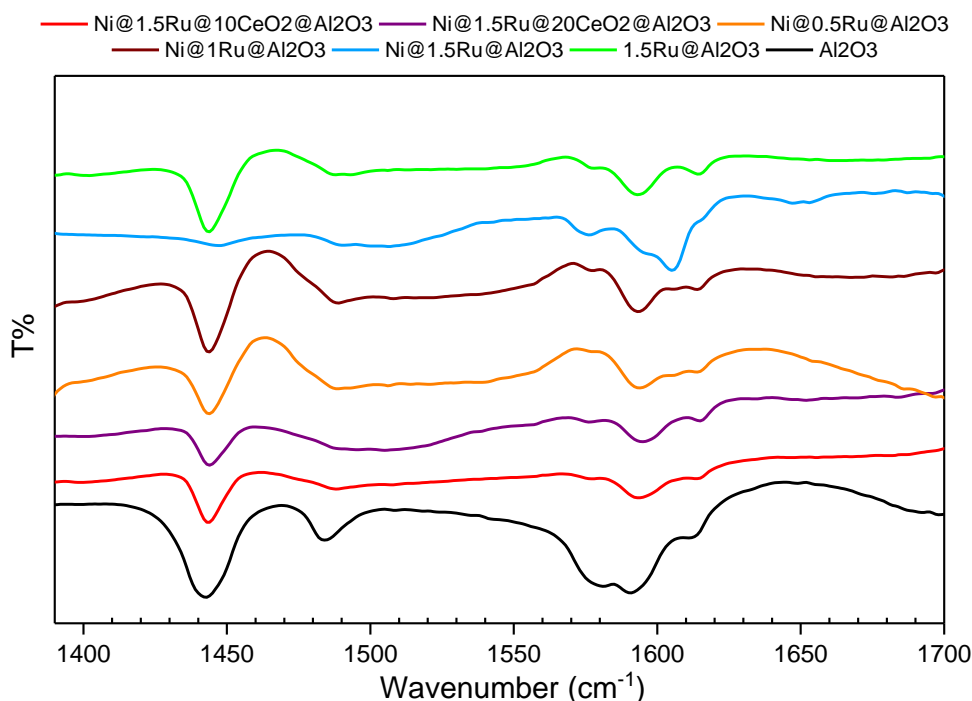


Figure 6.5. DRIFTS spectra of the difference between pyridine adsorbed and fresh samples of the ceria and ruthenium promoted nickel/alumina catalysts.

Scanning electron and backscattering electron detector images of the  $1.5\text{Ru}@10\text{CeO}_2@\text{Al}_2\text{O}_3$  and  $1.5\text{Ru}@20\text{CeO}_2@\text{Al}_2\text{O}_3$  materials are given in Figure 6.6, and the scanning electron and backscattering electron detector images of the  $\text{Ni}@1.5\text{Ru}@10\text{CeO}_2@\text{Al}_2\text{O}_3$  and  $\text{Ni}@1.5\text{Ru}@20\text{CeO}_2@\text{Al}_2\text{O}_3$  materials are given in Figure 6.7. Agglomerated ruthenium particles that have a size of  $1.28\ \mu\text{m}$  were observed in the images of  $1.5\text{Ru}@10\text{CeO}_2@\text{Al}_2\text{O}_3$  catalyst (Figure 6.6-A and C). Gathered ruthenium particles formed a cluster most probably due to the high temperature treatment of the synthesized materials. The bright areas seen in the SEM images are ruthenium clusters according to the EDX analysis results. The  $\text{Ni}@1.5\text{Ru}@10\text{CeO}_2@\text{Al}_2\text{O}_3$  (Figure 6.7-A and C) and  $\text{Ni}@1.5\text{Ru}@20\text{CeO}_2@\text{Al}_2\text{O}_3$  (Figure 6.7-B and D) materials also present ruthenium particles that have particles sizes of 100-230 nm. Scanning electron and backscattering electron detector images of  $\text{Ni}@0.5\text{Ru}@\text{Al}_2\text{O}_3$ ,  $\text{Ni}@1.0\text{Ru}@\text{Al}_2\text{O}_3$ , and  $\text{Ni}@1.5\text{Ru}@\text{Al}_2\text{O}_3$  materials are presented in Figure 6.8. Backscattering electron detector clearly shows agglomerated

particles that were identified as ruthenium using EDX analysis. This result indicates that ruthenium was not well dispersed on the support surface. EDX results revealed that the targeted metal loading was mostly achieved (Table 6.2). All EDX analysis showed somewhat the presence of larger amounts of Ru than the targeted values. The reason is probably due to the measurement limitations in the instrument.

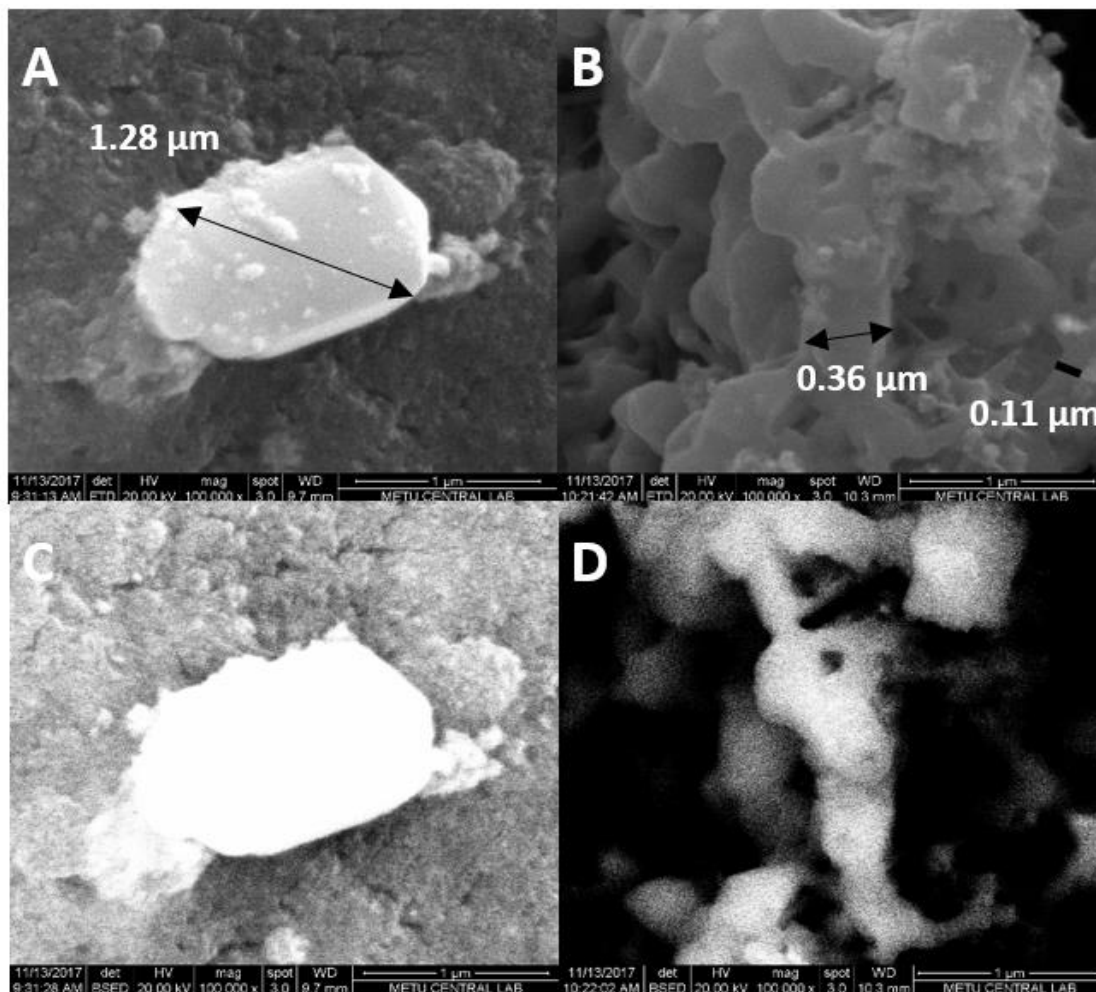


Figure 6.6. Scanning electron detector images of A) 1.5Ru@10CeO<sub>2</sub>@Al<sub>2</sub>O<sub>3</sub>, B) 1.5Ru@20CeO<sub>2</sub>@Al<sub>2</sub>O<sub>3</sub>, and backscattering electron detector images of C) 1.5Ru@10CeO<sub>2</sub>@Al<sub>2</sub>O<sub>3</sub>, and D) 1.5Ru@20CeO<sub>2</sub>@Al<sub>2</sub>O<sub>3</sub> catalysts (Magnification: 100000 and the scale: 1 μm in all images).

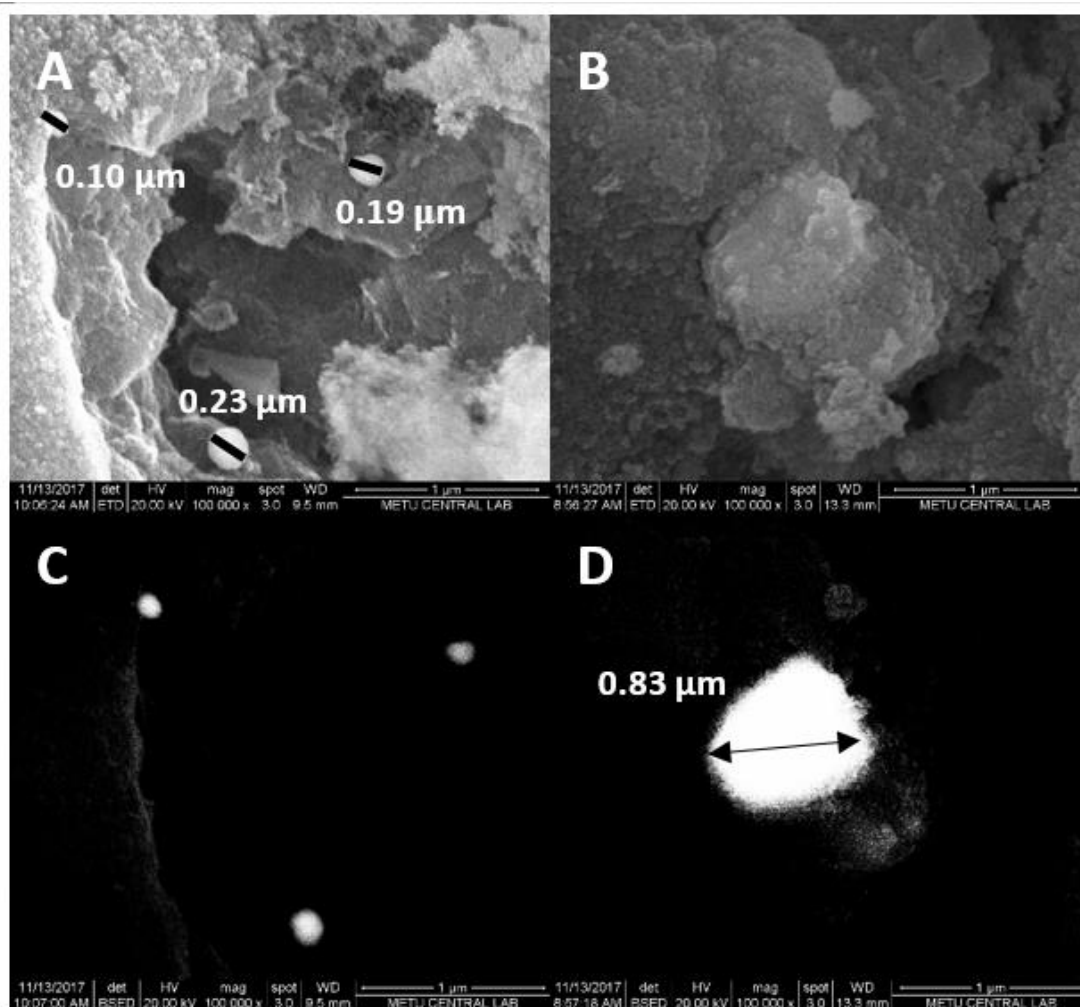


Figure 6.7. Scanning electron detector images of A) Ni@1.5Ru@10CeO<sub>2</sub>@Al<sub>2</sub>O<sub>3</sub>, B) Ni@1.5Ru@20CeO<sub>2</sub>@Al<sub>2</sub>O<sub>3</sub>, and backscattering electron detector images of C) Ni@1.5Ru@10CeO<sub>2</sub>@Al<sub>2</sub>O<sub>3</sub>, and D) Ni@1.5Ru@20CeO<sub>2</sub>@Al<sub>2</sub>O<sub>3</sub> catalysts (Magnification: 100000 and the scale: 1 μm in all images).

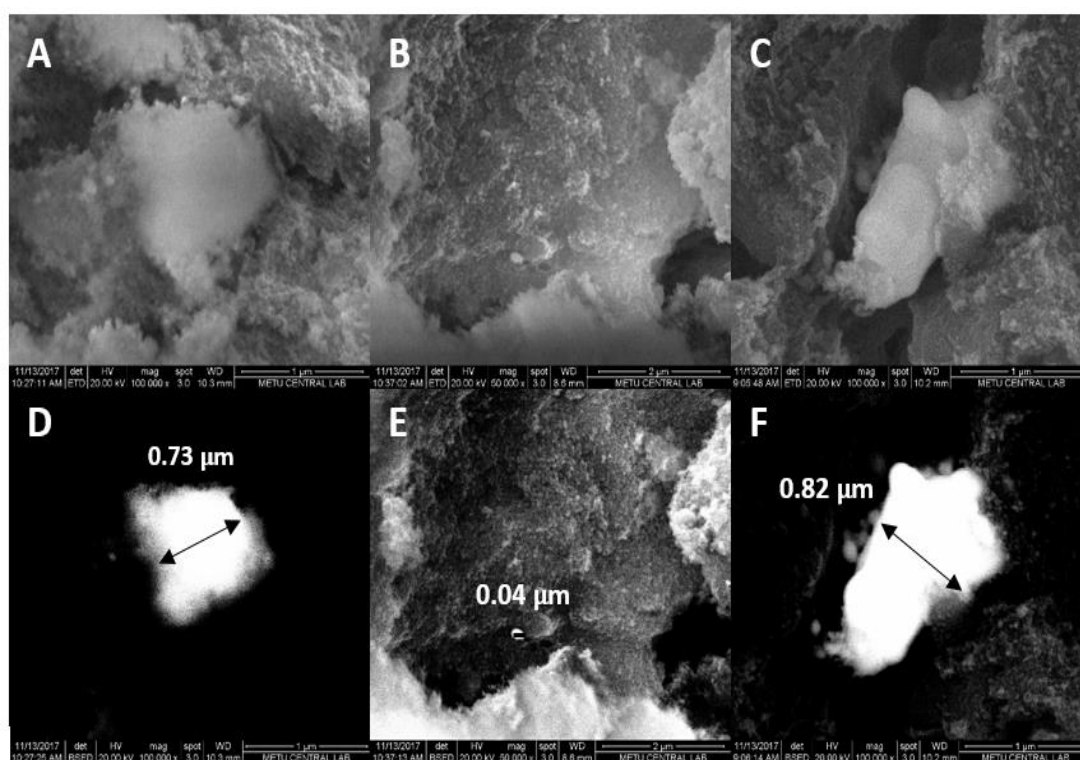


Figure 6.8. Scanning electron detector images of A) Ni@1.5Ru@Al<sub>2</sub>O<sub>3</sub>, B) Ni@1.0Ru@Al<sub>2</sub>O<sub>3</sub>, C) Ni@0.5Ru@Al<sub>2</sub>O<sub>3</sub>, and backscattering electron detector image of D) Ni@1.5Ru@Al<sub>2</sub>O<sub>3</sub>, E) Ni@1.0Ru@Al<sub>2</sub>O<sub>3</sub>, and F) Ni@0.5Ru@Al<sub>2</sub>O<sub>3</sub> catalysts (Magnification: 100000 and the scale: 1 μm in all images).

Table 6.2 Metal content of the synthesized catalysts obtained from EDX analysis.

Material	Metal Content (wt. %)					
	Ni		Ce		Ru	
	Target	EDX	Target	EDX	Target	EDX
Ni@1.5Ru@10CeO <sub>2</sub> @Al <sub>2</sub> O <sub>3</sub>	10	8.1	8	6.4	1.5	2.0
Ni@1.5Ru@20CeO <sub>2</sub> @Al <sub>2</sub> O <sub>3</sub>	10	17.5	16	16.8	1.5	3.2
Ni@0.5Ru@Al <sub>2</sub> O <sub>3</sub>	10	12.0		-	0.5	1.1
Ni@1.0Ru@Al <sub>2</sub> O <sub>3</sub>	10	10.2		-	1.0	1.5
Ni@1.5Ru@Al <sub>2</sub> O <sub>3</sub>	10	10.2		-	1.5	1.5

## 6.2. Catalyst Performance Test Results

### 6.2.1. Effect of Catalyst Composition on Hydrogen Production in the Diesel Steam Reforming Reaction

Performance results of  $1.5\text{Ru}@10\text{CeO}_2@\text{Al}_2\text{O}_3$ ,  $1.5\text{Ru}@20\text{CeO}_2@\text{Al}_2\text{O}_3$ ,  $\text{Ni}@1.5\text{Ru}@10\text{CeO}_2@\text{Al}_2\text{O}_3$ ,  $\text{Ni}@1.5\text{Ru}@20\text{CeO}_2@\text{Al}_2\text{O}_3$ ,  $\text{Ni}@1.5\text{Ru}@\text{Al}_2\text{O}_3$ ,  $\text{Ni}@1\text{Ru}@\text{Al}_2\text{O}_3$ , and  $\text{Ni}@0.5\text{Ru}@\text{Al}_2\text{O}_3$  catalysts in the diesel steam reforming reaction are presented in Figure 6.9 in terms of gas product composition. The analysis of gas products presented the formation of  $\text{H}_2$ ,  $\text{CO}$ ,  $\text{CH}_4$ ,  $\text{CO}_2$  and  $\text{C}_2\text{H}_4$  with an average standard deviation value of 0.4, as given in Chapter 4.1. The analysis results of the liquid samples showed that the samples did not contain any hydrocarbons that are higher in amount than ppm range and hence, the complete conversion of diesel was assumed for all experiments. Among these materials, 0.5 wt.% Ru incorporated catalyst ( $\text{Ni}@0.5\text{Ru}@\text{Al}_2\text{O}_3$ ) showed the production of the highest  $\text{H}_2$  and the lowest  $\text{CH}_4$  and  $\text{C}_2$  products. Hydrogen yield increased from 29.3 ( $\text{Ni}@\text{Al}_2\text{O}_3$ , Table 5.4) to 32.6 ( $\text{Ni}@0.5\text{Ru}@\text{Al}_2\text{O}_3$ , Table 6.3) with the incorporation of 0.5 wt.% ruthenium into the  $\text{Ni}@\text{Al}_2\text{O}_3$  catalyst. Apparently, the presence of ruthenium enhanced the reforming activity of the catalyst, by promoting reforming of side products. A decrease in the molar ratio of  $\text{CO}$  to  $\text{CO}_2$  after ruthenium incorporation was also observed, which indicates increase of hydrogen production with the water gas shift reaction. Besides the higher hydrogen production capability of 0.5 wt.% ruthenium loaded material, it also reduced coke deposition (2.4 wt.%, Table 5.4), compared to the  $\text{Ni}@\text{Al}_2\text{O}_3$  catalyst (3.1 wt.%) as can be seen from Table 6.3. The success of this catalyst was not just due to the presence of ruthenium as an active metal in reforming reactions, but also due to slightly enhanced interaction of nickel with the support surface according to TPR results (Figure 6.3).

The activity of  $1.5\text{Ru}@20\text{CeO}_2@\text{Al}_2\text{O}_3$ , and  $\text{Ni}@1.5\text{Ru}@20\text{CeO}_2@\text{Al}_2\text{O}_3$  materials in DSR showed the active role of nickel in the steam reforming reaction. Higher side product formation was observed with the catalysts that have no nickel

incorporation (Figure 6.9). The production of higher amounts of side products with  $1.5\text{Ru}@20\text{CeO}_2@\text{Al}_2\text{O}_3$  confirms the bond breaking capability of nickel. Activity results of the catalysts in DSR in terms of average  $\text{H}_2$  yield, the molar ratio of produced CO to  $\text{CO}_2$  and lastly coke deposition obtained during the six hours of reaction time (Table 6.3) also show the poor activity of  $1.5\text{Ru}@20\text{CeO}_2@\text{Al}_2\text{O}_3$ . The low average molar ratio of CO to  $\text{CO}_2$  could be an indication of higher WGS rate for ruthenium when nickel is not present. Nickel on the other hand is clearly more active than ruthenium towards reforming reactions. The reason of such a high coke deposition might be correlated with the presence of ethylene, since besides high coke deposition high amounts of ethylene formation was observed with  $1.5\text{Ru}@20\text{CeO}_2@\text{Al}_2\text{O}_3$  catalyst and ethylene is known as a strong coke promoter<sup>76</sup>. According to the coke deposition results given in Table 6.3 for the  $\text{Ni}@1.5\text{Ru}@\text{Al}_2\text{O}_3$  and  $\text{Ni}@1.5\text{Ru}@20\text{CeO}_2@\text{Al}_2\text{O}_3$  catalysts, the presence of ceria together with ruthenium also reduced coke deposition.

The success of  $\text{Ni}@0.5\text{Ru}@\text{Al}_2\text{O}_3$  catalysts over the catalysts with higher ruthenium loading ( $\text{Ni}@1.5\text{Ru}@\text{Al}_2\text{O}_3$  and  $\text{Ni}@1.0\text{Ru}@\text{Al}_2\text{O}_3$ ) suggests the promoting effect of ruthenium can be obtained at low loading amount. According to the TPR results of  $\text{Ni}@\text{Ru}@\text{Al}_2\text{O}_3$  materials (Figure 6.3), the lowest  $\text{NiAl}_2\text{O}_4$  reduction temperature was observed with the  $\text{Ni}@0.5\text{Ru}@\text{Al}_2\text{O}_3$  catalyst. Easier reducibility of nickel on this material together with a possible better dispersion coming from the lower loading amount of Ru could be the reason of its higher success. The higher success of the  $\text{Ni}@0.5\text{Ru}@\text{Al}_2\text{O}_3$  catalysts over the ceria incorporated ones ( $\text{Ni}@1.5\text{Ru}@10\text{CeO}_2@\text{Al}_2\text{O}_3$  and  $\text{Ni}@1.5\text{Ru}@20\text{CeO}_2@\text{Al}_2\text{O}_3$ ) could be due to its higher surface area and pore volume (Table 6.1).

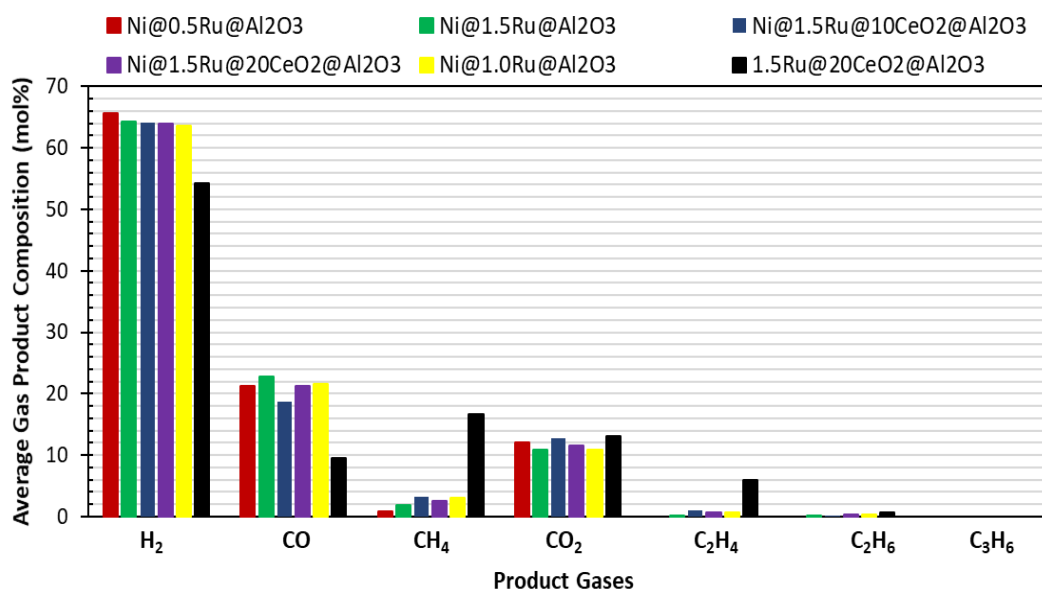


Figure 6.9. The effect of catalyst content on the average product gas composition in the DSR reaction (GHSV=7500 h<sup>-1</sup>, H<sub>2</sub>O/C=2.5, 800°C).

Table 6.3 Activity test results of catalysts in DSR in terms of H<sub>2</sub> yield, the ratio of CO to CO<sub>2</sub> formation, average side product amount and coke deposition.

Catalyst	Average H <sub>2</sub> Yield ( $\frac{\text{max}^{\text{theoretical}}}{=35}$ )	$\frac{\dot{N}_{\text{CO}}}{\dot{N}_{\text{CO}_2}}$	Average Gas Side Product Composition (ppm)				Coke % ( $\frac{\text{g}_{\text{coke}}}{\text{g}_{\text{used catalyst}}}$ )
			CH <sub>4</sub>	C <sub>2</sub> H <sub>4</sub>	C <sub>2</sub> H <sub>6</sub>	C <sub>3</sub> H <sub>6</sub>	
Ni@0.5Ru@Al <sub>2</sub> O <sub>3</sub>	32.6	1.8	9000	0	0	0	2.4
Ni@1.0Ru@Al <sub>2</sub> O <sub>3</sub>	29.0	2.0	30000	6000	3000	0	7.1
Ni@1.5Ru@Al <sub>2</sub> O <sub>3</sub>	30.2	2.1	19000	2000	1000	0	4.5
1.5Ru@20CeO <sub>2</sub> @Al <sub>2</sub> O <sub>3</sub>	17.7	0.7	166000	59000	6000	0	9.4
Ni@1.5Ru@10CeO <sub>2</sub> @Al <sub>2</sub> O <sub>3</sub>	29.4	1.5	32000	10000	2000	0	2.2
Ni@1.5Ru@20CeO <sub>2</sub> @Al <sub>2</sub> O <sub>3</sub>	29.4	1.8	25000	6000	3000	0	2.7

### 6.2.2. Effect of Catalyst Composition on Hydrogen Production in the Diesel Autothermal Reforming Reaction

Performance results of the Ni@0.5Ru@Al<sub>2</sub>O<sub>3</sub>, Ni@1.5Ru@Al<sub>2</sub>O<sub>3</sub>, and Ni@1.5Ru@20CeO<sub>2</sub>@Al<sub>2</sub>O<sub>3</sub> catalysts in the diesel autothermal reforming reaction are presented in Figure 6.10. In the ATR reaction, the most successful catalyst in terms of molar hydrogen concentration in the gas product stream is again the Ni@0.5Ru@Al<sub>2</sub>O<sub>3</sub> catalyst among the synthesized catalysts as can be seen from Figure 6.10. The comparison of the activities of Ni@0.5Ru@Al<sub>2</sub>O<sub>3</sub>, Ni@1.5Ru@Al<sub>2</sub>O<sub>3</sub>, and Ni@1.5Ru@20CeO<sub>2</sub>@Al<sub>2</sub>O<sub>3</sub> catalysts in both diesel steam and autothermal reforming reactions were presented in Table 6.4 in terms of average gas product composition. The lower composition of hydrogen in the ATR gas product was expected considering the stoichiometry of the DSR and ATR reactions. 35 moles of hydrogen and 26.5 moles of hydrogen can be obtained from one mole of diesel (C<sub>17</sub>H<sub>36</sub>) in steam and autothermal reforming reactions, respectively.

Steam and autothermal reforming activity test results of catalysts show that Ni@0.5Ru@Al<sub>2</sub>O<sub>3</sub> (Table 6.3) is the most successful catalyst in both DSR and ATR reactions. Ni@Al<sub>2</sub>O<sub>3</sub> (Table 5.5) catalyst presented better hydrogen production success in the diesel autothermal reforming reaction and lower hydrogen production in the diesel steam reforming reaction compared to Ni@1.5Ru@Al<sub>2</sub>O<sub>3</sub> (Table 5.5). For Ni@0.5Ru@Al<sub>2</sub>O<sub>3</sub> and Ni@1.5Ru@20CeO<sub>2</sub>@Al<sub>2</sub>O<sub>3</sub> catalysts, total amount of side product composition in the gas product is higher in the steam reforming reaction compared to the autothermal reforming reaction showing that the oxygen in the reaction environment converts hydrocarbons into CO and CO<sub>2</sub>. The amount of CO<sub>2</sub> produced is much higher in autothermal reforming reaction (Table 6.3). Hydrogen and methane mole fraction percent of the gas products (Figure 6.10) shows a dependency with each other in ATR. In other words, under the oxygen atmosphere of ATR, mainly reforming reaction of methane dominates the hydrogen production. Mole fraction results of CO and CO<sub>2</sub> in the gas products mainly suggest the occurrence of partial

oxidation/combustion reactions. The higher CO<sub>2</sub> concentration implies probable formation of combustion reactions before the catalyst bed.

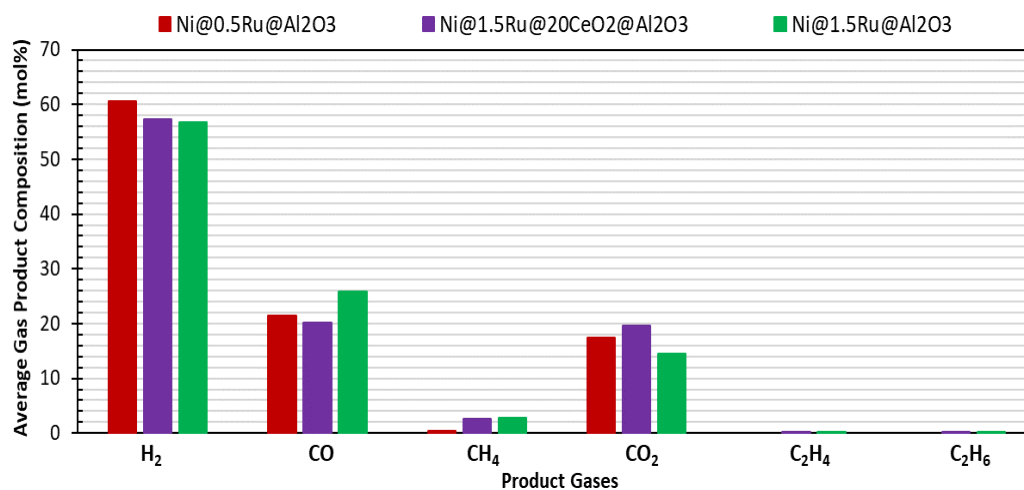


Figure 6.10. The effect of catalyst content on the average gas product composition in the ATR reaction (GHSV=7500 h<sup>-1</sup>, H<sub>2</sub>O/C=2.5, 800°C).

Table 6.4 Comparison of diesel steam and autothermal results for the Ni@0.5Ru@Al<sub>2</sub>O<sub>3</sub>, Ni@1.5Ru@Al<sub>2</sub>O<sub>3</sub> and Ni@1.5Ru@20CeO<sub>2</sub>@Al<sub>2</sub>O<sub>3</sub> catalysts in terms of average gas product composition.

Catalyst	RXN	Average Gas Product Composition (%)					
		H <sub>2</sub>	CO	CH <sub>4</sub>	CO <sub>2</sub>	C <sub>2</sub> H <sub>4</sub>	C <sub>2</sub> H <sub>6</sub>
Ni@0.5Ru@Al <sub>2</sub> O <sub>3</sub>	DSR	65.7	21.3	0.9	12.1	0	0
	ATR	60.6	21.5	0.5	17.4	0	0
Ni@1.5Ru@Al <sub>2</sub> O <sub>3</sub>	DSR	64.2	22.8	1.9	10.8	0.2	0.1
	ATR	56.7	25.8	2.8	14.4	0.1	0.2
Ni@1.5Ru@20CeO <sub>2</sub> @Al <sub>2</sub> O <sub>3</sub>	DSR	64.0	21.2	2.5	11.5	0.6	0.3
	ATR	57.3	20.1	2.6	19.6	0.2	0.2

### 6.2.3. Long Term Diesel Steam Reforming Reaction

Since for both diesel steam and autothermal reforming reactions, the best catalytic performance was obtained with the Ni@0.5Ru@Al<sub>2</sub>O<sub>3</sub> catalyst, further investigation of catalyst stability and long term activity test extending up to 34 h was performed. As it can be seen from Figure 6.11, very stable performance with a very little fluctuation was obtained with the Ni@0.5Ru@Al<sub>2</sub>O<sub>3</sub> catalyst.

Figure 6.12 shows the thermogravimetric analysis of the used Ni@0.5Ru@Al<sub>2</sub>O<sub>3</sub> catalyst which was performed twice to observe the distribution of coke deposition in the used catalyst. Weight percentages of coke deposition in two different parts of the used catalyst were 5.5 and 6.8, which indicate the homogeneous distribution of coke on the catalyst. On the average, 6.15% coke deposition in the DSR reaction was observed after thirty four hours, whereas 2.4% coke deposition was seen after six hours (Table 6.3). Even though coke deposition increased with an increase in reaction time, there was no indication of a stability loss through thirty four hours of experiment. Thermogravimetric analysis results also showed the presence of both filamentous carbon oxidized below 550 °C and graphitic carbon that was oxidized above 550 °C for the material used in the long term experiment, but the presence of mostly graphitic carbon was observed on the catalysts after six hours of experiment.

Used catalyst after the long term experiment was also analyzed with SEM technique and the images are presented in Figure 6.13 along with the fresh catalyst for comparison. According to these results, the sizes of ruthenium clusters in the used catalysts (6 h and 34 h) are quite close to each other, indicating that there was no physical change on the material surface. EDX analysis was also applied to the used catalyst revealing that there was no sulphur deposition observed after thirty four hours of reforming experiment. N<sub>2</sub> adsorption/desorption results give in Figure 6.14 presents a slight decrease in pore volume of the used catalyst due to blockage of its pore with coke. XRD pattern of the used catalyst (Figure 6.15) also showed coke deposition with a characteristic peak at a 2θ value of 26.2°. Other than the presence of carbon peak,

XRD patterns of fresh and used catalyst have other differences such as increase in peak intensities of NiO which is probably due to Ni<sup>0</sup> oxidation after the completion of reaction test during the cool-down period of the reactor.

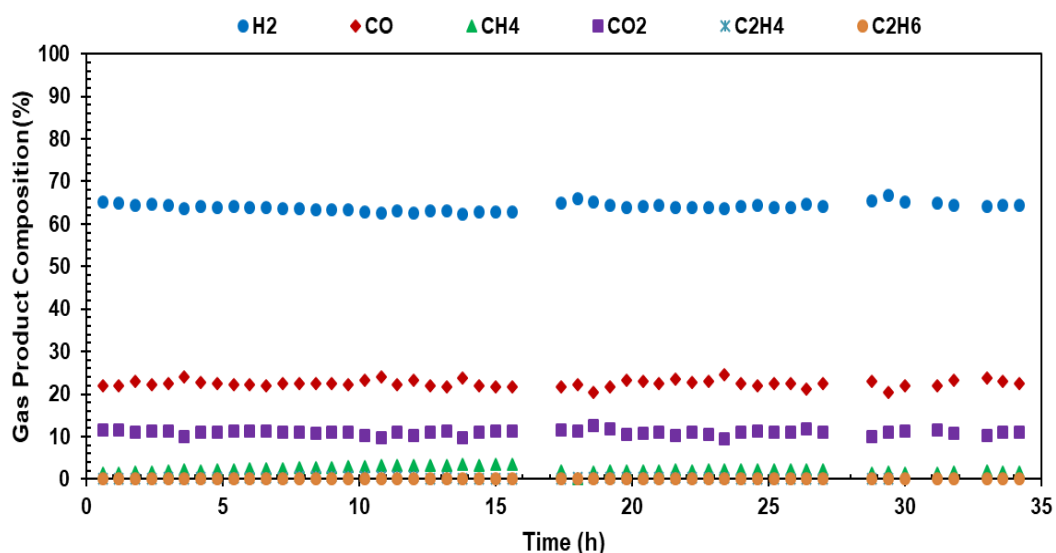


Figure 6.11. Long term activity test of the Ni@0.5Ru@Al<sub>2</sub>O<sub>3</sub> catalyst in DSR (GHSV=7500 h<sup>-1</sup>, H<sub>2</sub>O/C=2.5, 800°C).

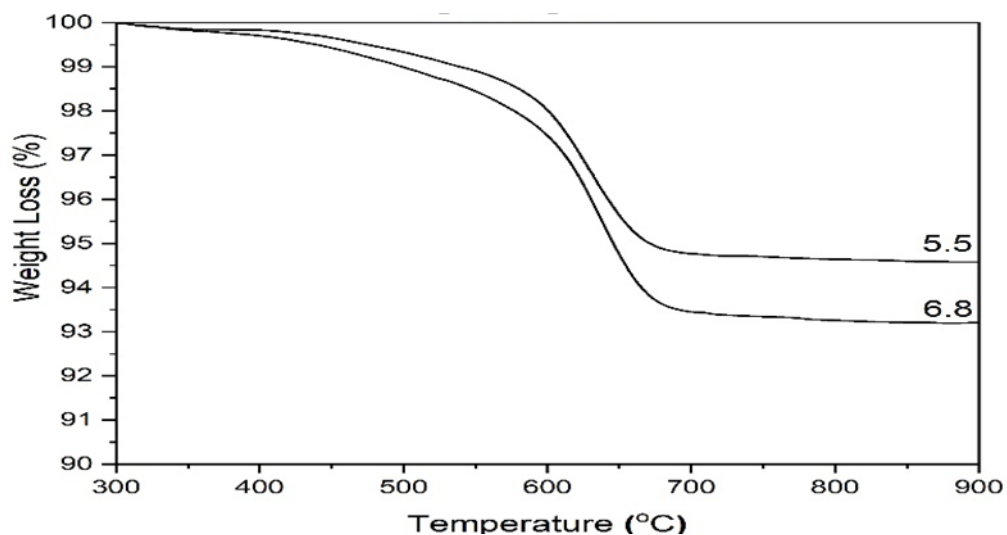


Figure 6.12. TGA result of samples taken from two different parts of the used Ni@0.5Ru@Al<sub>2</sub>O<sub>3</sub> catalyst at the reaction time of thirty four hours.

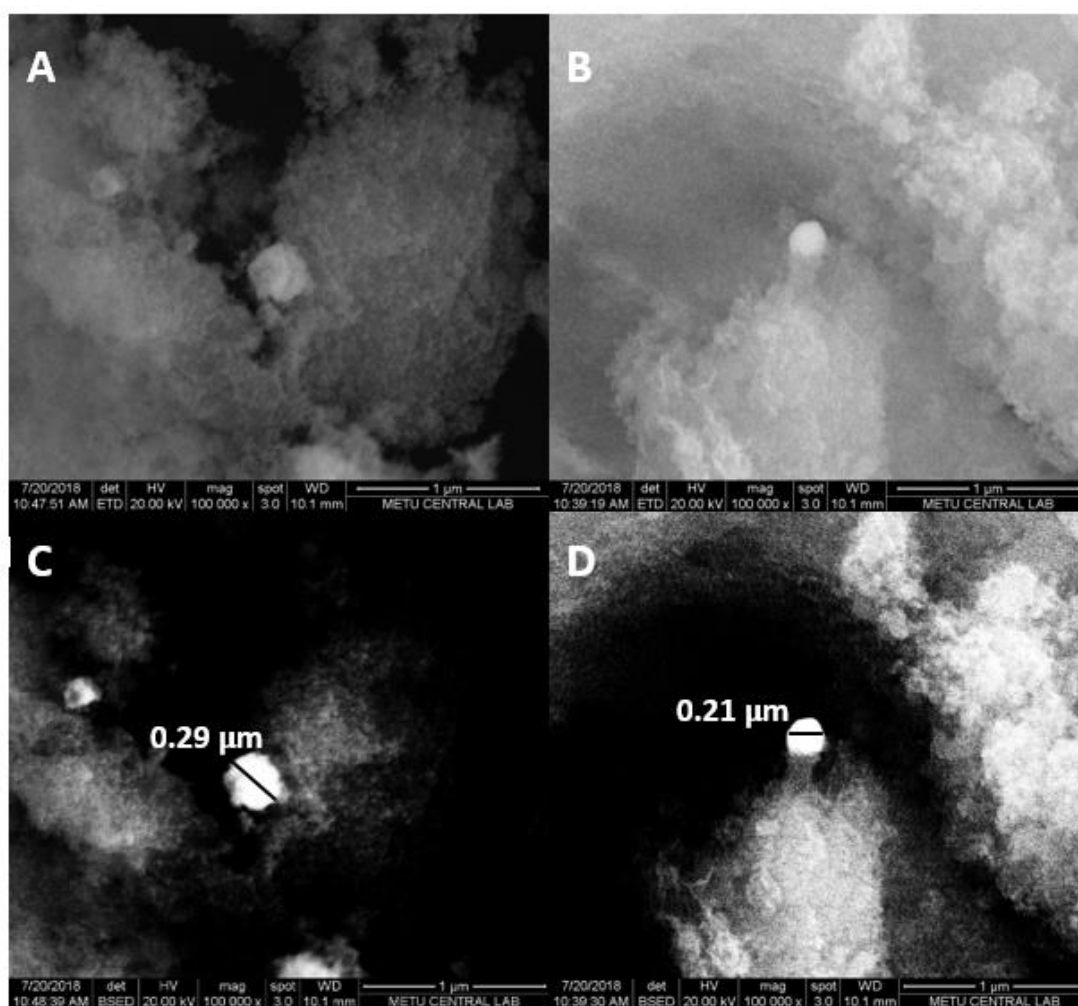


Figure 6.13. Scanning electron detector images of Ni@0.5Ru@Al<sub>2</sub>O<sub>3</sub> catalyst A) after long-term activity test (34 h), B) after six hours activity test, and backscattering electron detector images of Ni@0.5Ru@Al<sub>2</sub>O<sub>3</sub> catalyst C) after long term activity test (34 h), and D) after six hours activity test.

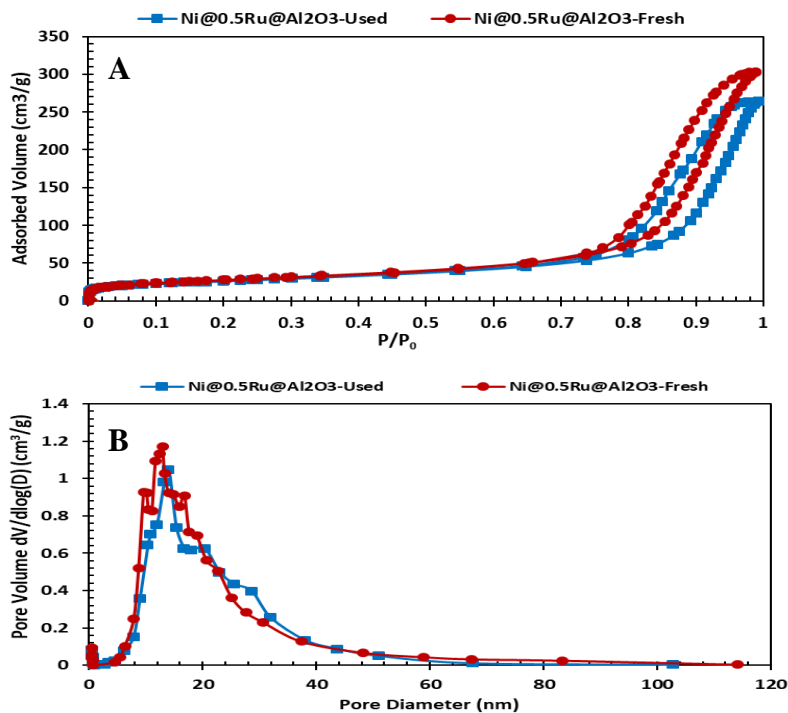


Figure 6.14. N<sub>2</sub> adsorption/desorption isotherms (A) and pore size distributions (B) of fresh and used Ni@0.5Ru@Al<sub>2</sub>O<sub>3</sub> catalyst in long term DSR reaction.

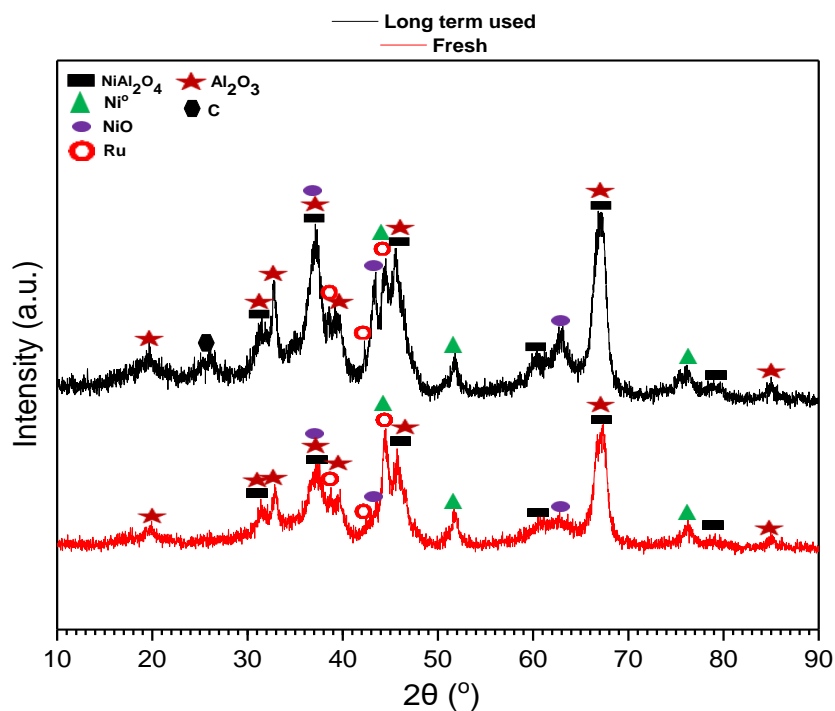


Figure 6.15. XRD patterns of fresh and used Ni@0.5Ru@Al<sub>2</sub>O<sub>3</sub> catalyst for long term DSR reaction.

## CHAPTER 7

### DEVELOPMENT OF MESOPOROUS CERIA-ALUMINA AND CERIA-ZIRCONIA-ALUMINA SUPPORTED NICKEL CATALYSTS FOR STEAM AND AUTOTHERMAL REFORMING OF DIESEL

#### 7.1. Characterization Results

Characterization studies were performed on the synthesized  $\text{Al}_2\text{O}_3$ -EISA support, metal incorporated support materials, and nickel impregnated catalysts (10 wt.% nickel). Nickel impregnated catalysts were reduced before the analysis (except for TPR analysis). Characterization results were discussed throughout this section in terms of the effect of the type of metal that was incorporated (10 wt.%  $\text{CeO}_2$  or 10 wt.%  $\text{CeO}_2$ - $\text{ZrO}_2$ ), the effect of metal incorporation amount (for  $\text{CeO}_2$ ; 10 wt.% or 20 wt.%) or the effect of the incorporation method of  $\text{CeO}_2$  (one-pot or impregnation).

Physical properties of the catalytic materials are presented in Table 7.1. As it can be seen from these results, synthesized  $\text{Al}_2\text{O}_3$ -EISA gave a quite high surface area with a pore diameter that fits in the mesoporous diameter range of materials. Nickel impregnation caused a decrease in surface area and pore volume values due to blockage of some of the pores with nickel metal. The synthesis of  $\text{Al}_2\text{O}_3$ -EISA together with  $\text{CeO}_2$ , and  $\text{CeO}_2/\text{ZrO}_2$  resulted in the formation of support materials that possess lower surface area, pore volume and percent microporosity values and significantly higher average pore diameter values, indicating a difference between the pore structures of  $\text{Al}_2\text{O}_3$ -EISA and these materials. Moreover, larger pore diameter values observed for the  $\text{CeO}_2$ - $\text{Al}_2\text{O}_3$ -EISA and  $\text{CeO}_2$ - $\text{ZrO}_2$ - $\text{Al}_2\text{O}_3$ -EISA materials indicate that the mesoporous structure of these materials contains larger non-uniform mesopores according to pore size distribution results given in Figure 7.1.-B. For the  $10\text{CeO}_2$ - $\text{Al}_2\text{O}_3$ -EISA and  $8\text{CeO}_2$ - $2\text{ZrO}_2$ - $\text{Al}_2\text{O}_3$ -EISA materials, nickel impregnation

followed by reduction lead to an increase in the microporosity of the material, suggesting some of the loaded nickel is located in some of the mesopores which are converted to micropores. Nickel impregnation to 20CeO<sub>2</sub>@Al<sub>2</sub>O<sub>3</sub>-EISA material caused a significant decrease in the microporosity of the material along with its surface area.

Table 7.1. Physical properties of the synthesized support materials and catalysts.

Material	Multi Point BET Surface Area (m <sup>2</sup> /g)	BJH Desorption Pore Volume (cm <sup>3</sup> /g)	BJH Desorption Average Pore Diameter (nm)	Microporosity %
Al <sub>2</sub> O <sub>3</sub> -EISA	188.2	0.52	9.5	10.6
<b>Ni@Al<sub>2</sub>O<sub>3</sub>-EISA</b>	<b>135.3</b>	<b>0.40</b>	<b>8.8</b>	<b>10.7</b>
10CeO <sub>2</sub> -Al <sub>2</sub> O <sub>3</sub> -EISA	76.9	0.45	21.8	5.9
<b>Ni@10CeO<sub>2</sub>-Al<sub>2</sub>O<sub>3</sub>-EISA</b>	<b>52.8</b>	<b>0.35</b>	<b>20.4</b>	<b>8.8</b>
20CeO <sub>2</sub> -Al <sub>2</sub> O <sub>3</sub> -EISA	72.1	0.48	28.8	9.2
<b>Ni@20CeO<sub>2</sub>-Al<sub>2</sub>O<sub>3</sub>-EISA</b>	<b>44.2</b>	<b>0.31</b>	<b>25.8</b>	<b>9.1</b>
20CeO <sub>2</sub> @Al <sub>2</sub> O <sub>3</sub> -EISA	128.5	0.37	7.7	16.2
<b>Ni@20CeO<sub>2</sub>@Al<sub>2</sub>O<sub>3</sub>-EISA</b>	<b>49.9</b>	<b>0.25</b>	<b>23.5</b>	<b>8.5</b>
8CeO <sub>2</sub> -2ZrO <sub>2</sub> -Al <sub>2</sub> O <sub>3</sub> -EISA	97.4	0.48	29.7	6.3
<b>Ni@8CeO<sub>2</sub>-2ZrO<sub>2</sub>-Al<sub>2</sub>O<sub>3</sub>-EISA</b>	<b>36.7</b>	<b>0.26</b>	<b>33.0</b>	<b>10.1</b>

Nitrogen adsorption/desorption isotherms of all support materials are given in Figure 7.1.-A, and all nickel impregnated catalysts are presented in Figure 7.2-A. These materials can be classified as Type IV with H1 type hysteresis loop, according to IUPAC classification. Type IV isotherm and H1 type hysteresis loop indicate the presence of narrow and uniform pore size distribution. Hysteresis loops of the 10CeO<sub>2</sub>-Al<sub>2</sub>O<sub>3</sub>-EISA, 20CeO<sub>2</sub>-Al<sub>2</sub>O<sub>3</sub>-EISA, and 8CeO<sub>2</sub>-2ZrO<sub>2</sub>-Al<sub>2</sub>O<sub>3</sub>-EISA materials were located at higher P/P<sub>0</sub> values compared to the Al<sub>2</sub>O<sub>3</sub>-EISA and 20 wt.% CeO<sub>2</sub> impregnated Al<sub>2</sub>O<sub>3</sub>-EISA materials. The difference in hysteresis loop formation suggests formation of different pore structures for the Al<sub>2</sub>O<sub>3</sub>-EISA support and Al<sub>2</sub>O<sub>3</sub>-EISA support synthesized through metal incorporation by one-pot synthesis method. Difference in pore structures between the two group of materials was also observed from their pore size distributions presented in Figure 7.1.-B. Hysteresis loop of

Ni@Al<sub>2</sub>O<sub>3</sub>-EISA was located at a lower P/P<sub>0</sub> value compared to other catalysts. Pore structures of nickel impregnated Al<sub>2</sub>O<sub>3</sub>-EISA and nickel impregnated metal incorporated Al<sub>2</sub>O<sub>3</sub>-EISA supports are different which was also observed on the isotherms of the support materials. Pore size distributions of nickel impregnated catalysts presented in Figure 7.2-B show that the pore size distributions are not uniform, suggesting the presence of a large range of pore sizes, especially for the Ni@8CeO<sub>2</sub>-2ZrO<sub>2</sub>-Al<sub>2</sub>O<sub>3</sub>-EISA material.

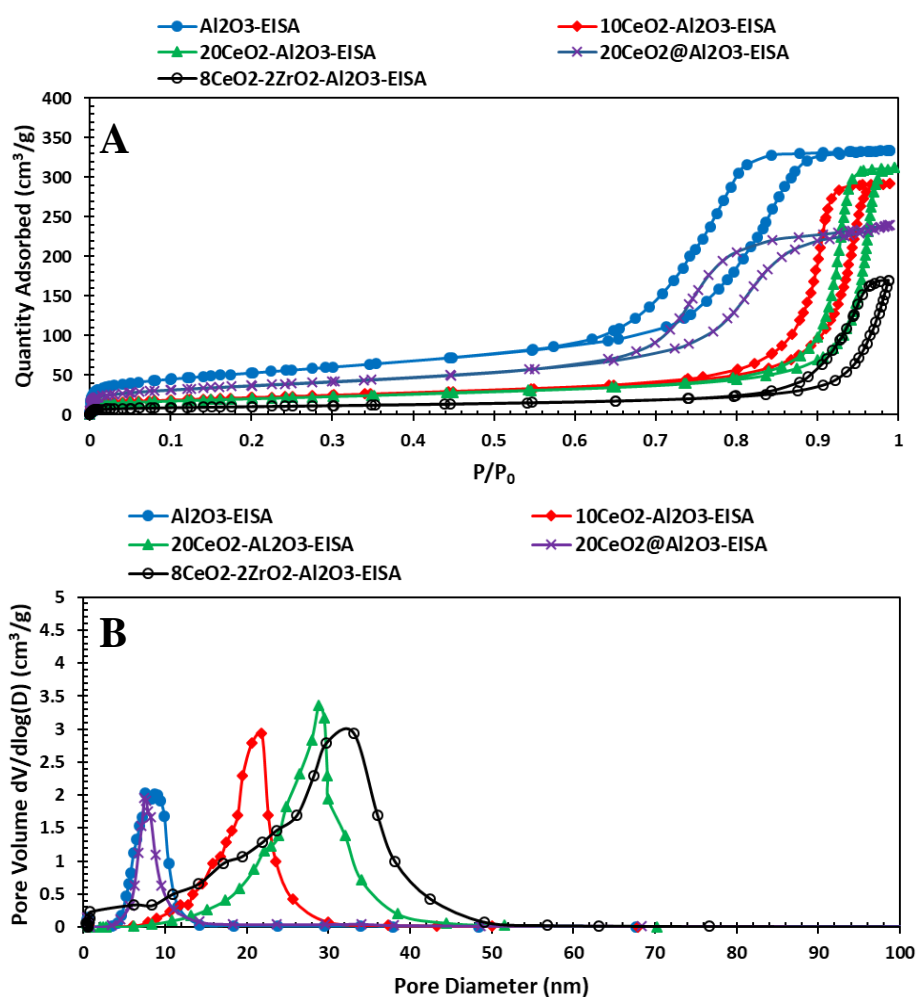


Figure 7.1. N<sub>2</sub> adsorption/desorption isotherms (A) and pore size distributions (B) of the synthesized support materials

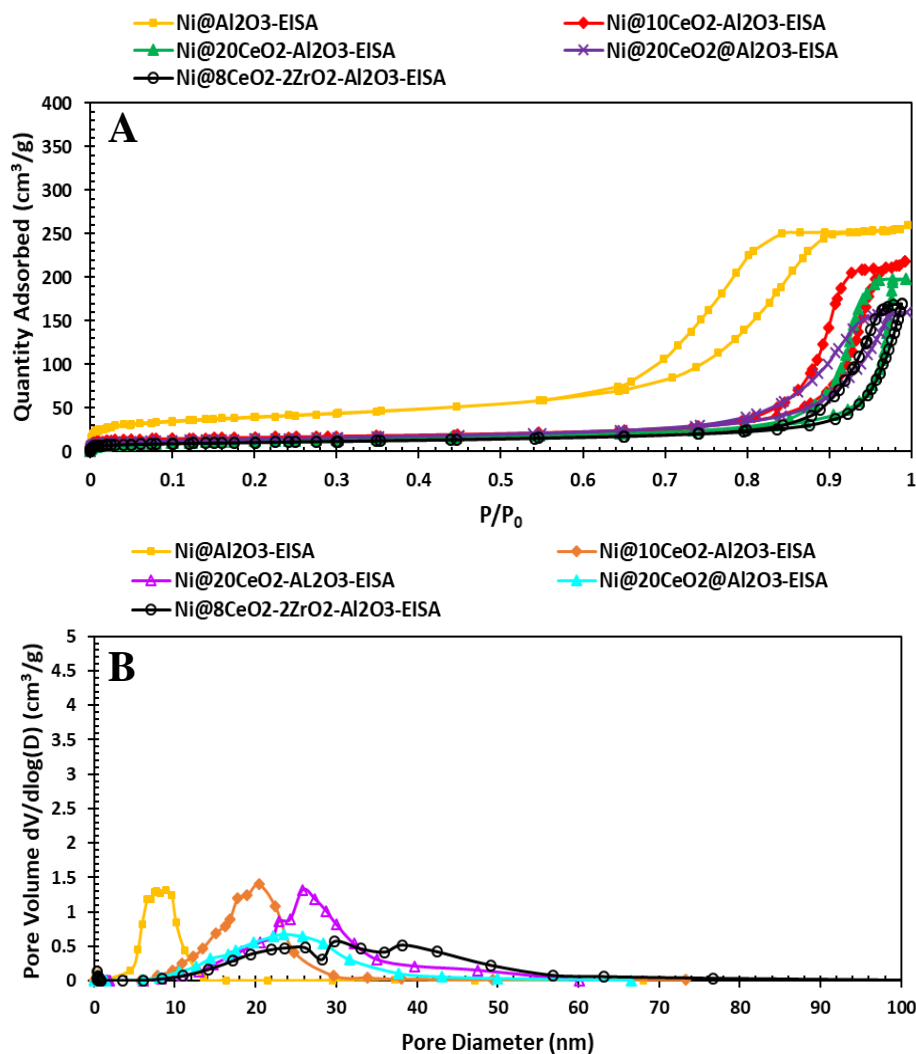


Figure 7.2. N<sub>2</sub> adsorption/desorption isotherms (A) and pore size distributions (B) of nickel impregnated catalysts.

X-ray diffraction patterns of the synthesized catalysts are presented in Figure 7.3. XRD pattern of Al<sub>2</sub>O<sub>3</sub>-EISA showed only the characteristic peaks of  $\gamma$ -Al<sub>2</sub>O<sub>3</sub> (PDF card No. 00-004-0875). The calcination temperature has a large impact on the crystallinity of the material. It was observed that with increasing calcination temperature, XRD peaks become sharper. Calcination at 700°C results in the formation of an amorphous structure which converts into crystalline phase after calcination at

800 °C. XRD results of the calcination temperature analysis is presented in Appendix G.

When only nickel was impregnated to Al<sub>2</sub>O<sub>3</sub>-EISA, the presence of the characteristic peaks of Ni<sup>0</sup> (PDF card No. 01-071-4653), NiAl<sub>2</sub>O<sub>4</sub> (PDF card No. 00-010-0339), and NiO (PDF card No. 4-835) were observed. It is not surprising to observe the presence of NiAl<sub>2</sub>O<sub>4</sub>, considering the high calcination (900 °C) temperature, which favors the reaction between nickel and alumina. Nickel ions can overcome the surface barrier of alumina and integrate into alumina lattice in a form of a spinel structure<sup>28,103</sup>.

XRD patterns of CeO<sub>2</sub> incorporated catalysts presented the characteristic peaks of CeAlO<sub>3</sub> crystals (PDF card No. 01-081-1185). There is no significant difference in the patterns of the Ni@10CeO<sub>2</sub>-Al<sub>2</sub>O<sub>3</sub>-EISA, and Ni@20CeO<sub>2</sub>-Al<sub>2</sub>O<sub>3</sub>-EISA catalysts. Formation of Ni<sup>0</sup>, NiAl<sub>2</sub>O<sub>4</sub>, CeAlO<sub>3</sub>, and  $\gamma$ -Al<sub>2</sub>O<sub>3</sub> was observed in the XRD pattern of Ni@8CeO<sub>2</sub>-2ZrO<sub>2</sub>-Al<sub>2</sub>O<sub>3</sub>-EISA similar to the pattern of the Ni@10CeO<sub>2</sub>-Al<sub>2</sub>O<sub>3</sub>-EISA catalyst. Differently than the Ni@10CeO<sub>2</sub>-Al<sub>2</sub>O<sub>3</sub>-EISA catalyst, the formation of NiO crystals and cubic CeO<sub>2</sub> crystals (PDF card No. 23-0394) were observed in the pattern of Ni@8CeO<sub>2</sub>-2ZrO<sub>2</sub>-Al<sub>2</sub>O<sub>3</sub>-EISA. The presence of CeO<sub>2</sub> crystals suggests that ZrO<sub>2</sub> incorporation prevented the complete reaction of CeO<sub>2</sub> present in the structure of the material with Al<sub>2</sub>O<sub>3</sub> in the presence of a reducing atmosphere, resulting in the formation of CeAlO<sub>3</sub> crystals. ZrO<sub>2</sub> crystal patterns were not observed probably due to low loading amount, or the formation of CeO<sub>2</sub>-ZrO<sub>2</sub> mixed oxide crystals which cause a slight shift in the XRD peak pattern positions of cubic CeO<sub>2</sub><sup>86</sup>.

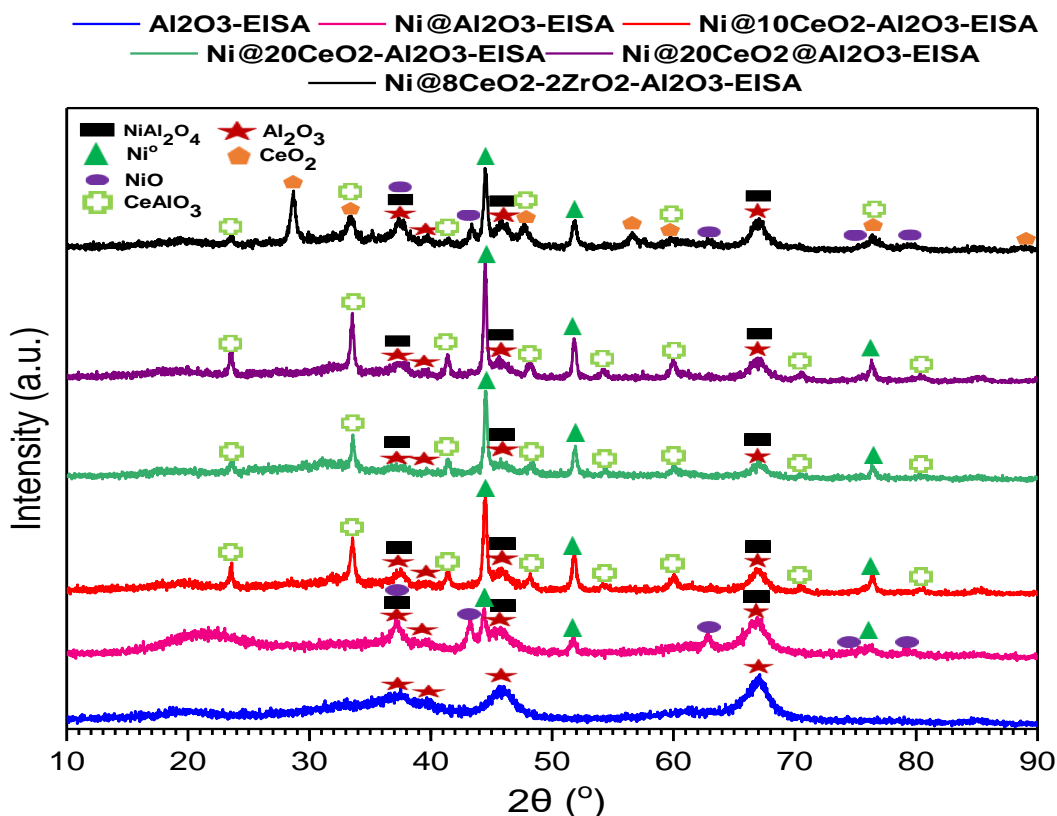


Figure 7.3 X-Ray diffraction patterns of synthesized materials.

The results of temperature programmed reduction analysis (TPR) of the support materials and nickel impregnated catalysts are given in Figure 7.4. TPR results of Ni@Al<sub>2</sub>O<sub>3</sub>-EISA material presented four reduction peaks located at 380 °C (0.06 mmol/g<sub>cat</sub>), 487 °C (0.10 mmol/g<sub>cat</sub>), 785 °C (1.06 mmol/g<sub>cat</sub>) and 833 °C (0.44 mmol/g<sub>cat</sub>). The presence of two peaks that are located at 380 and 487 °C indicated reduction of NiO crystals having different interactions with alumina support<sup>104</sup>. High temperature peaks indicate the reduction of both non-stoichiometric surface NiAl<sub>2</sub>O<sub>4</sub> and stoichiometric NiAl<sub>2</sub>O<sub>4</sub>.

TPR results of 10CeO<sub>2</sub>-Al<sub>2</sub>O<sub>3</sub>-EISA, 20CeO<sub>2</sub>-Al<sub>2</sub>O<sub>3</sub>-EISA and 20CeO@Al<sub>2</sub>O<sub>3</sub>-EISA materials show the reduction peaks located at low temperatures (Figure 7.4). Low temperature peaks may originate from the reduction of small CeO<sub>2</sub> crystallites that has a weak interaction with Al<sub>2</sub>O<sub>3</sub> surface<sup>105</sup>. Reduction of CeO<sub>2</sub> may lead to the

formation of  $\text{CeO}_x$  phase. Peaks observed until 700 °C could be due to reduction of  $\text{CeO}_2$  that has a stronger interaction with the support surface. Lastly, high temperature peaks (>800) is mainly due to formation of  $\text{CeAlO}_3$  crystals<sup>106,107</sup>. Considering the TPR pattern of  $10\text{CeO}_2\text{-Al}_2\text{O}_3\text{-EISA}$ ,  $20\text{CeO}_2\text{-Al}_2\text{O}_3\text{-EISA}$ , and  $20\text{CeO}_2@\text{Al}_2\text{O}_3\text{-EISA}$  materials, the first peak observed on the TPR result of  $\text{CeO}_2\text{-ZrO}_2$  incorporated material is probably originating from the reduction of  $\text{CeO}_2$  and the second reduction peak is probably due to the reduction of  $\text{CeO}_2\text{-ZrO}_2$  that may have a strong interaction with  $\text{Al}_2\text{O}_3$  surface.

TPR results of  $\text{Ni}@10\text{CeO}_2\text{-Al}_2\text{O}_3\text{-EISA}$ , and  $\text{Ni}@20\text{CeO}_2\text{-Al}_2\text{O}_3\text{-EISA}$  catalysts presented multiple reduction peaks. Major reduction peaks were located between 700 °C and 900 °C due to the reduction of both non-stoichiometric surface  $\text{NiAl}_2\text{O}_4$  and stoichiometric  $\text{NiAl}_2\text{O}_4$ . One major reduction peak was observed for the  $\text{Ni}@20\text{CeO}_2@\text{Al}_2\text{O}_3\text{-EISA}$ , and  $\text{Ni}@8\text{CeO}_2\text{-}2\text{ZrO}_2\text{-Al}_2\text{O}_3\text{-EISA}$  catalysts which were located at 787 °C and 819 °C, respectively. When the deconvoluted peaks of the  $\text{Ni}@10\text{CeO}_2\text{-Al}_2\text{O}_3\text{-EISA}$ , and  $\text{Ni}@20\text{CeO}_2\text{-Al}_2\text{O}_3\text{-EISA}$  catalysts are analyzed, peaks that are located at higher temperatures than the major peaks were probably due to the formation of  $\text{CeAlO}_3$  crystals. Smaller peaks located at lower temperatures than the major peaks were mainly caused by the reduction of isolated  $\text{NiO}$  species that has a weak interaction with the support.

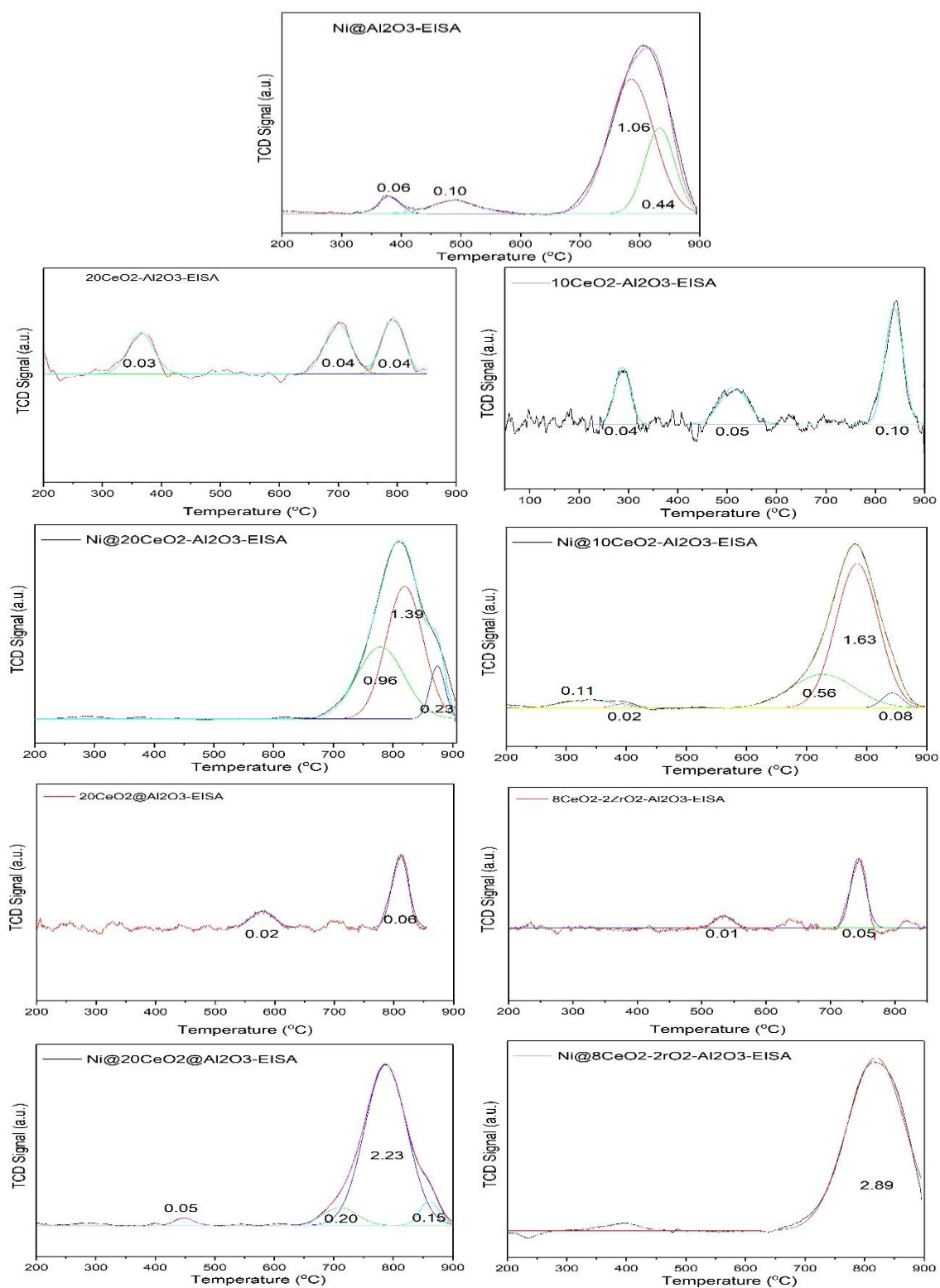


Figure 7.4. TPR results of synthesized EISA supports and nickel impregnated materials

The nature of the acid sites of the catalysts was analyzed with Diffuse Reflectance FT-IR Spectroscopy (DRIFTS) of pyridine adsorbed samples. Figure 7.5 illustrates the DRIFTS spectra of the difference between pyridine adsorbed samples and fresh samples for support materials synthesized through EISA method and nickel impregnated catalysts. As given in Figure 7.5, for the materials Al<sub>2</sub>O<sub>3</sub>-EISA, 10CeO<sub>2</sub>-Al<sub>2</sub>O<sub>3</sub>-EISA, and 20CeO<sub>2</sub>-Al<sub>2</sub>O<sub>3</sub>-EISA the transmission bands are located at 1445 cm<sup>-1</sup>, 1575 cm<sup>-1</sup>, 1485 cm<sup>-1</sup> and 1614 cm<sup>-1</sup>. While, the transmission bands located at 1445 cm<sup>-1</sup>, 1575 cm<sup>-1</sup> and 1614 cm<sup>-1</sup> indicate the presence of Lewis acid sites, transmission band located at 1485 cm<sup>-1</sup> is attributed to both weak Lewis and weak Brønsted acid sites. The transmission band located at 1590 cm<sup>-1</sup> is due to presence of H-bond that could be due to weak Brønsted acidity. For the 8CeO<sub>2</sub>-2ZrO<sub>2</sub>-Al<sub>2</sub>O<sub>3</sub>-EISA material (Figure 7.5) a weak transmission band was observed at 1445 cm<sup>-1</sup>. Lewis type acidity was also observed for nickel impregnated catalysts synthesized by the EISA method as can be seen in Figure 7.6. For all catalysts, the transmission bands were located at 1445 cm<sup>-1</sup>, 1485 cm<sup>-1</sup>, 1575 cm<sup>-1</sup> and 1614 cm<sup>-1</sup> indicating the presence of strong Lewis, weak Lewis and weak Brønsted acid sites similar to the results of support materials.

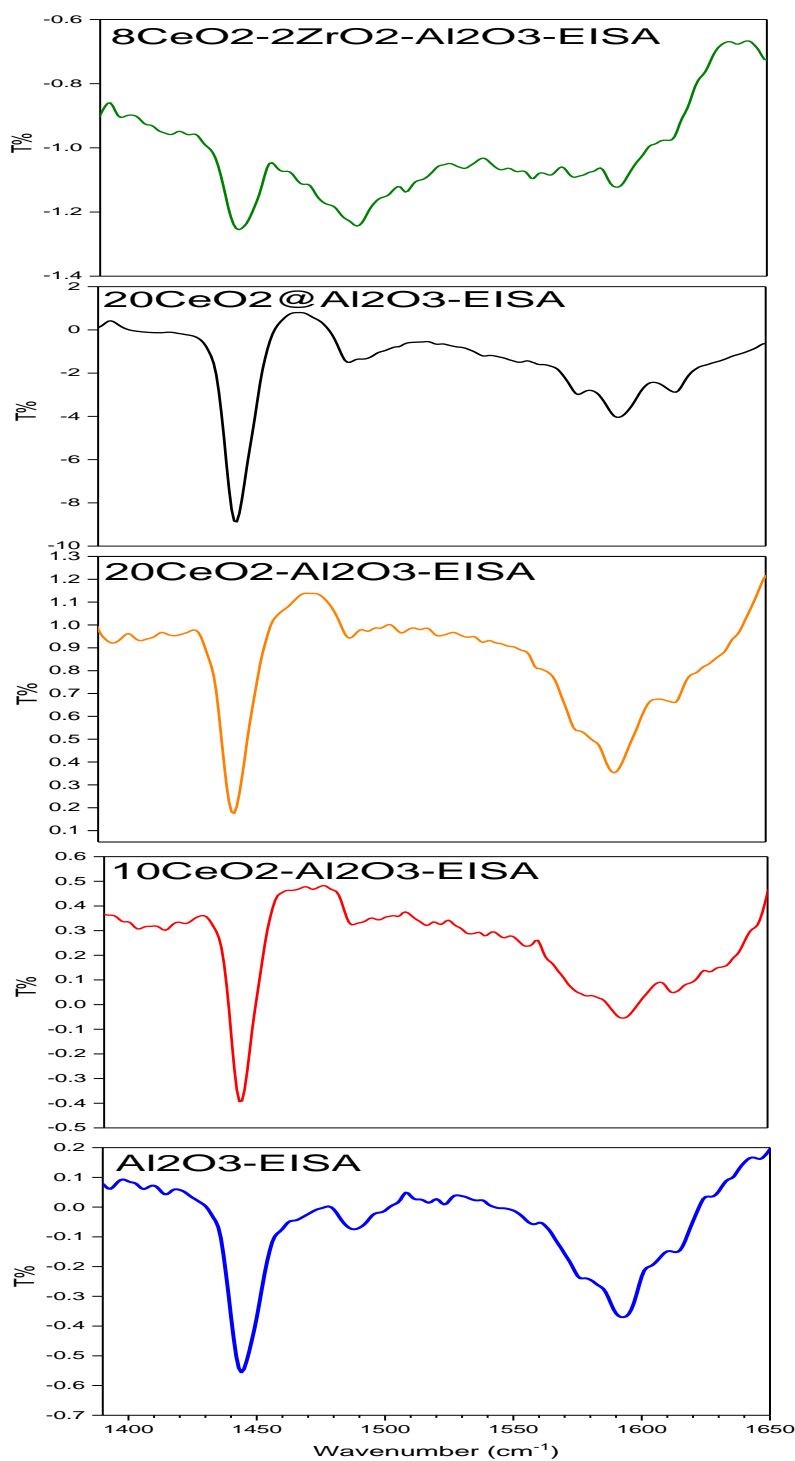


Figure 7.5. DRIFTS spectra of the difference between pyridine adsorbed and fresh samples of the synthesized Al<sub>2</sub>O<sub>3</sub>-EISA, 10CeO<sub>2</sub>-Al<sub>2</sub>O<sub>3</sub>-EISA, 20CeO<sub>2</sub>-Al<sub>2</sub>O<sub>3</sub>-EISA, 20CeO<sub>2</sub>@Al<sub>2</sub>O<sub>3</sub>-EISA, and 8CeO<sub>2</sub>-2ZrO<sub>2</sub>@Al<sub>2</sub>O<sub>3</sub>-EISA support materials.

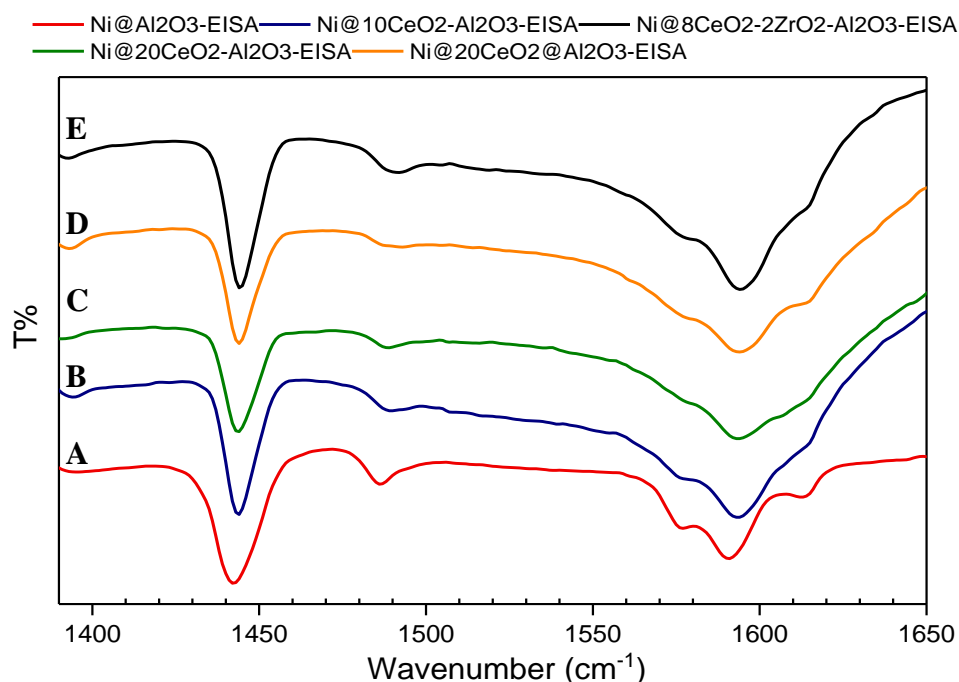


Figure 7.6. DRIFTS spectra of the difference between pyridine adsorbed and fresh samples of the synthesized catalysts: A) Ni@Al<sub>2</sub>O<sub>3</sub>-EISA, B) Ni@10CeO<sub>2</sub>-Al<sub>2</sub>O<sub>3</sub>-EISA, C) Ni@8CeO<sub>2</sub>-2ZrO<sub>2</sub>@Al<sub>2</sub>O<sub>3</sub>-EISA, d) Ni@20CeO<sub>2</sub>-Al<sub>2</sub>O<sub>3</sub>-EISA, and E) Ni@20CeO<sub>2</sub>@Al<sub>2</sub>O<sub>3</sub>-EISA.

Ammonia TPD results reported in Figure 7.7 gives information about the total acid capacity of the synthesized materials. The desorption temperature indicated the acid strength of catalysts. The higher temperature of desorption, the stronger is the acid strength of the catalysts. Weak acidity was attributed to temperatures below 200 °C, moderate acidity was observed between 200 °C and 400 °C and strong acidity can be observed at temperatures above 400 °C<sup>94</sup>. The synthesis of  $\gamma$ -Al<sub>2</sub>O<sub>3</sub> with CeO<sub>2</sub> eliminated the presence of some acid sites and decreased the total acidic capacity as can be seen in Table 7.2. According to these results, Ni@Al<sub>2</sub>O<sub>3</sub>-EISA (Figure 7.7-A) material possesses mostly moderate acid sites. The synthesis of Al<sub>2</sub>O<sub>3</sub> with 10 wt.% CeO<sub>2</sub> resulted in a higher number of strong acid sites that lead to desorption of NH<sub>3</sub> at around 420 °C with a sharp peak (Figure 7.7-B). Addition of 20 wt.% CeO<sub>2</sub> decreased the total acid capacity (Table 7.2), but did not cause a sharp desorption peak as shown in Figure 7.7-D as in the case of the Ni@10CeO<sub>2</sub>-Al<sub>2</sub>O<sub>3</sub>-EISA material (Figure 7.7-B).

A change in the acid capacities were observed with the change in the CeO<sub>2</sub> incorporation method. Impregnation method (Ni@20CeO<sub>2</sub>@Al<sub>2</sub>O<sub>3</sub>-EISA, 0.12 mmol/g<sub>cat</sub>) lead to smaller acid capacity compared to the catalysts synthesized with one-pot method (Ni@20CeO<sub>2</sub>-Al<sub>2</sub>O<sub>3</sub>-EISA, 0.27 mmol/g<sub>cat</sub>). The total acid capacities of the Ni@8CeO<sub>2</sub>-2ZrO<sub>2</sub>-Al<sub>2</sub>O<sub>3</sub>-EISA, and Ni@10CeO<sub>2</sub>-Al<sub>2</sub>O<sub>3</sub>-EISA materials are quite similar to that of Ni@Al<sub>2</sub>O<sub>3</sub>-EISA material (Table 7.2). Since DRIFTS spectra of the catalysts (Figure 7.6) showed the presence of weak Lewis and Brønsted acid sites together with strong Lewis acid sites, peaks obtained at temperatures above 400 °C in Figure 7.7 could be due to Lewis acid sites and peaks obtained at temperatures below 200 °C in Figure 7.7 could be originating from ammonia desorption from both weak Lewis and weak Brønsted acid sites.

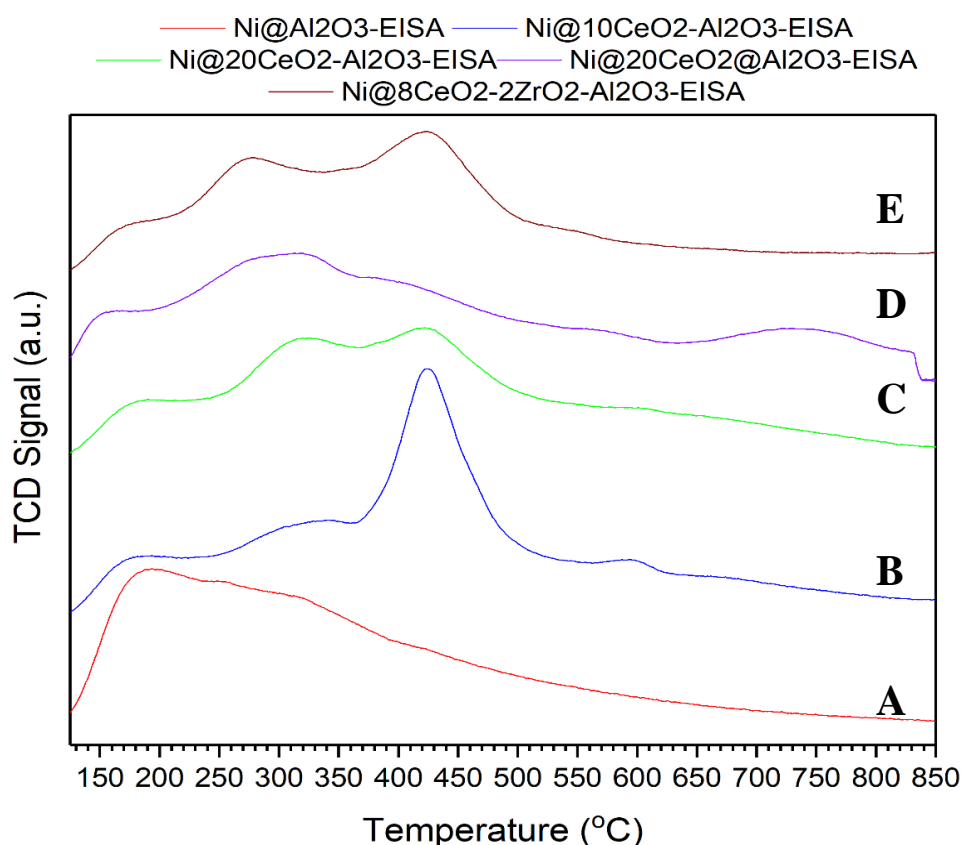


Figure 7.7. NH<sub>3</sub>-TPD results of synthesized materials: A) Ni@Al<sub>2</sub>O<sub>3</sub>-EISA, B) Ni@10CeO<sub>2</sub>-Al<sub>2</sub>O<sub>3</sub>-EISA, C) Ni@20CeO<sub>2</sub>-Al<sub>2</sub>O<sub>3</sub>-EISA, D) Ni@20CeO<sub>2</sub>@Al<sub>2</sub>O<sub>3</sub>-EISA, and E). Ni@8CeO<sub>2</sub>-2ZrO<sub>2</sub>@Al<sub>2</sub>O<sub>3</sub>-EISA.

Table 7.2. Total acid capacity of the catalysts synthesized with EISA method.

Catalyst Name	Acid Capacity (mmol/g <sub>cat</sub> )
Ni@Al <sub>2</sub> O <sub>3</sub> -EISA	0.35
Ni@10CeO <sub>2</sub> -Al <sub>2</sub> O <sub>3</sub> -EISA	0.34
Ni@20CeO <sub>2</sub> -Al <sub>2</sub> O <sub>3</sub> -EISA	0.27
Ni@20CeO <sub>2</sub> @Al <sub>2</sub> O <sub>3</sub> -EISA	0.12
Ni@8CeO <sub>2</sub> -2ZrO <sub>2</sub> -Al <sub>2</sub> O <sub>3</sub> -EISA	0.32

Scanning electron microscope images of the 10CeO<sub>2</sub>-Al<sub>2</sub>O<sub>3</sub>-EISA and 8CeO<sub>2</sub>-2ZrO<sub>2</sub>@Al<sub>2</sub>O<sub>3</sub>-EISA supports are presented in Figure 7.8. Ceria and ceria-zirconia incorporated support materials, 10CeO<sub>2</sub>-Al<sub>2</sub>O<sub>3</sub>-EISA and 8CeO<sub>2</sub>-2ZrO<sub>2</sub>@Al<sub>2</sub>O<sub>3</sub>-EISA, show different surface structures as can be seen from Figure 7.8-A and B. Scanning electron detector and backscattering electron detector images of the Ni@10CeO<sub>2</sub>-Al<sub>2</sub>O<sub>3</sub>-EISA and Ni@8CeO<sub>2</sub>-2ZrO<sub>2</sub>@Al<sub>2</sub>O<sub>3</sub>-EISA catalysts are presented in Figure 7.9. Both images contain different morphologies, which is not surprising considering both materials contain different crystal phases according to the XRD results presented in Figure 7.3. The Ni@10CeO<sub>2</sub>-Al<sub>2</sub>O<sub>3</sub>-EISA material contains Ni<sup>0</sup>, CeAlO<sub>3</sub>,  $\gamma$ -Al<sub>2</sub>O<sub>3</sub>, and NiAl<sub>2</sub>O<sub>4</sub> crystals and Ni@8CeO<sub>2</sub>-2ZrO<sub>2</sub>@Al<sub>2</sub>O<sub>3</sub>-EISA material showed the presence of Ni<sup>0</sup>, CeO<sub>2</sub>, CeAlO<sub>3</sub>,  $\gamma$ -Al<sub>2</sub>O<sub>3</sub>, and NiAl<sub>2</sub>O<sub>4</sub> crystals. Images of the Ni@10CeO<sub>2</sub>-Al<sub>2</sub>O<sub>3</sub>-EISA (Figure 7.9-A&C) material show the presence of nickel particles with a particle size range of 30-60 nm. Moreover, the presence of agglomerated particles were observed located on the ordered morphology with a particle size of 100 nm. Backscattering electron images of Ni@8CeO<sub>2</sub>-2ZrO<sub>2</sub>@Al<sub>2</sub>O<sub>3</sub>-EISA (Figure 7.9-D) shows the more dispersed nickel particles (bright dots indicates nickel particles) with sizes in the range of 60 and 70 nm compared to Ni@10CeO<sub>2</sub>-Al<sub>2</sub>O<sub>3</sub>-EISA (Figure 7.9-C). SEM image given in Figure 7.10-A of Ni@Al<sub>2</sub>O<sub>3</sub>-EISA material (A) shows the presence of a porous structure. SEM images of Ni@20CeO<sub>2</sub>@Al<sub>2</sub>O<sub>3</sub>-EISA and Ni@20CeO<sub>2</sub>-Al<sub>2</sub>O<sub>3</sub>-EISA materials given in Figure 7.10-B-C show different morphology with a cloudy surface compared to Ni@Al<sub>2</sub>O<sub>3</sub>-EISA (Figure 7.10-A).

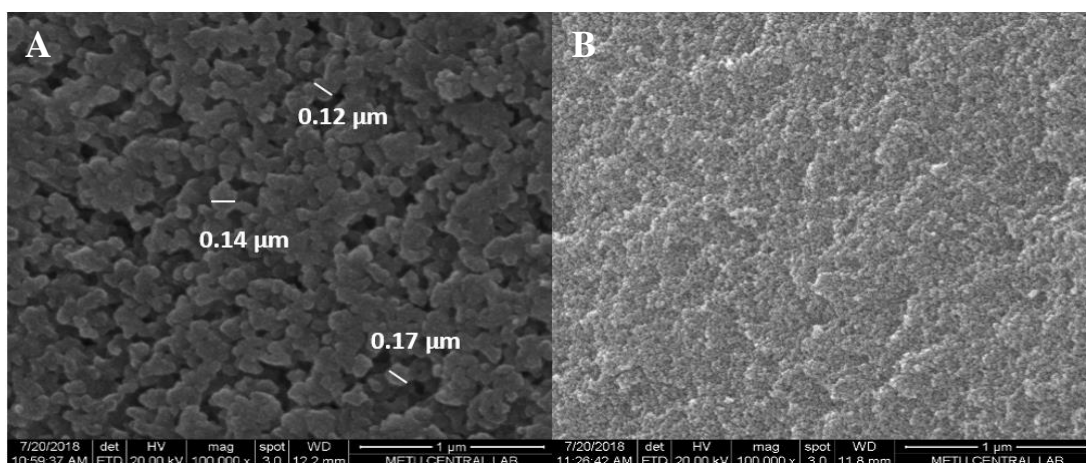


Figure 7.8. Scanning electron detector images of A)  $10\text{CeO}_2\text{-Al}_2\text{O}_3\text{-EISA}$  and B)  $8\text{CeO}_2\text{-2ZrO}_2\text{@Al}_2\text{O}_3\text{-EISA}$  (Magnification: 100000 and the scale:  $1\ \mu\text{m}$  in both images).

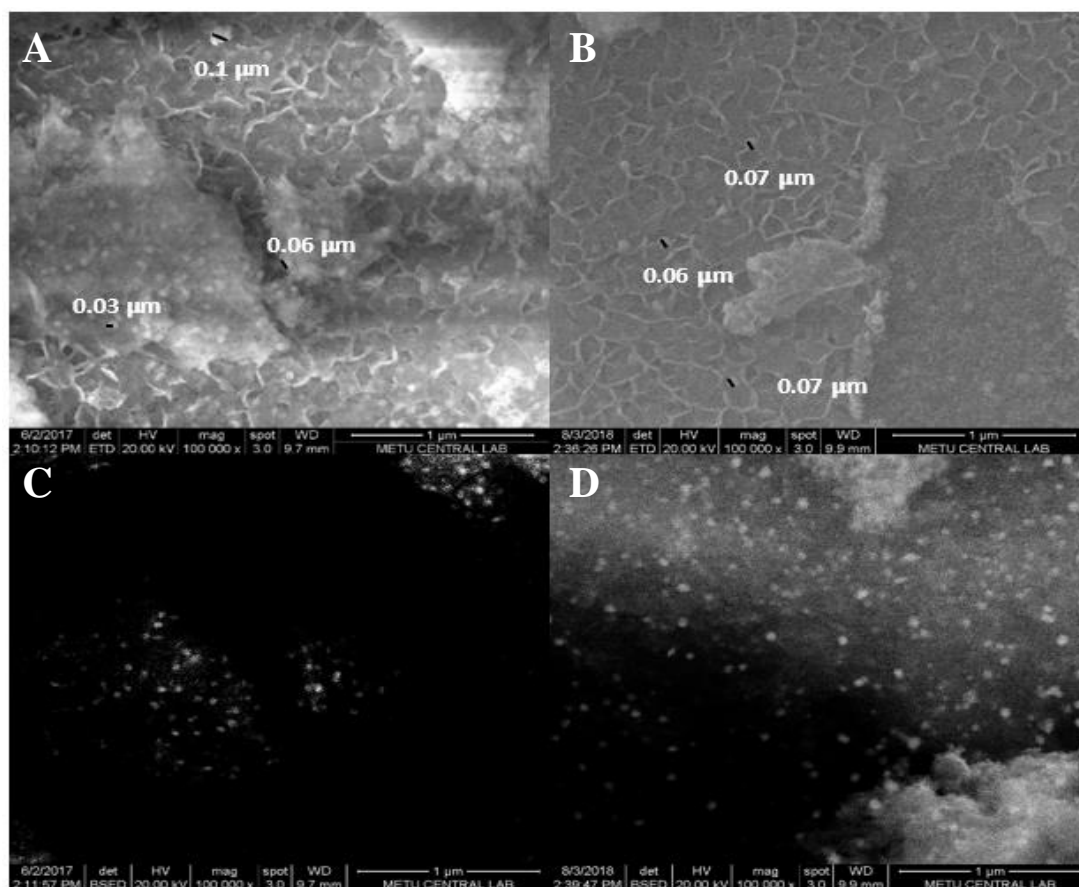


Figure 7.9. Scanning electron detector images of A)  $\text{Ni}@10\text{CeO}_2\text{-Al}_2\text{O}_3\text{-EISA}$ , B)  $\text{Ni}@8\text{CeO}_2\text{-2ZrO}_2\text{@Al}_2\text{O}_3\text{-EISA}$ , and backscattering electron detector images of C)  $\text{Ni}@10\text{CeO}_2\text{-Al}_2\text{O}_3\text{-EISA}$  and D)  $\text{Ni}@8\text{CeO}_2\text{-2ZrO}_2\text{@Al}_2\text{O}_3\text{-EISA}$  (Magnification: 100000 and the scale:  $1\ \mu\text{m}$  in all images).

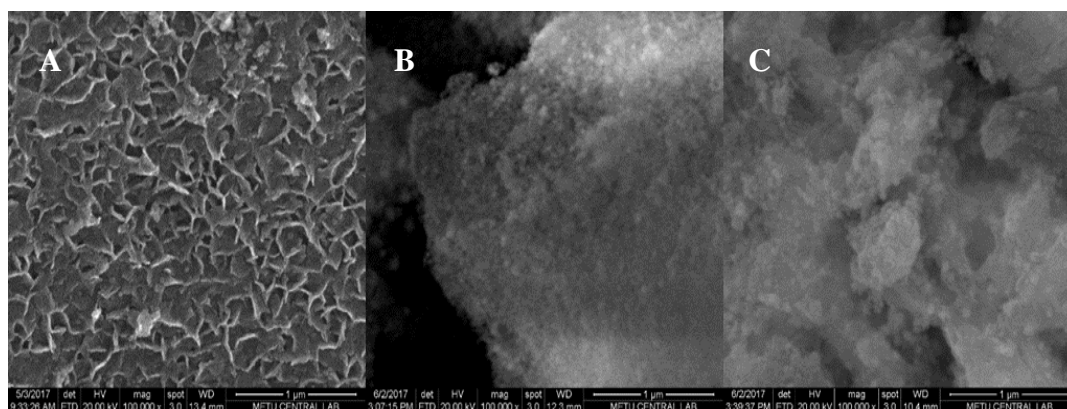


Figure 7.10. Scanning electron detector images of A) Ni@Al<sub>2</sub>O<sub>3</sub>-EISA, B) Ni@20CeO<sub>2</sub>-Al<sub>2</sub>O<sub>3</sub>-EISA, and C) Ni@20CeO<sub>2</sub>@Al<sub>2</sub>O<sub>3</sub>-EISA (Magnification: 100000 and the scale: 1 μm for all images).

EDX results given in Table 7.3 suggested that the targeted metal loading was mostly achieved. Differences in the EDX results from the targeted values was probably due to non-uniform metal/metal oxide distribution among the material.

Table 7.3. Metal content of the synthesized catalysts according to EDX analysis.

Material	Metal Content (wt. %)					
	Ni		Ce		Zr	
	Target	EDX	Target	EDX	Target	EDX
Ni@Al <sub>2</sub> O <sub>3</sub> -EISA	10.0	10.4	-	-	-	-
Ni@10CeO <sub>2</sub> -Al <sub>2</sub> O <sub>3</sub> -EISA	10.0	8.5	8	11.2	-	-
Ni@20CeO <sub>2</sub> -Al <sub>2</sub> O <sub>3</sub> -EISA	10.0	10.6	16	20.8	-	-
Ni@20CeO <sub>2</sub> @Al <sub>2</sub> O <sub>3</sub> -EISA	10.0	9.5	16	17.1	-	-
Ni@8CeO <sub>2</sub> -2ZrO <sub>2</sub> -Al <sub>2</sub> O <sub>3</sub> -EISA	10.0	14.4	6.4	8.3	1.5	1.8

## 7.2. Catalytic Activity Test Results

### 7.2.1. The Effect of Catalyst Composition on Hydrogen Production in Diesel Steam Reforming Reaction

Catalytic activity test results of the Ni@Al<sub>2</sub>O<sub>3</sub>-EISA, Ni@10CeO<sub>2</sub>-Al<sub>2</sub>O<sub>3</sub>-EISA, Ni@20CeO<sub>2</sub>-Al<sub>2</sub>O<sub>3</sub>-EISA, Ni@20CeO<sub>2</sub>@Al<sub>2</sub>O<sub>3</sub>-EISA, and Ni@8CeO<sub>2</sub>-2ZrO<sub>2</sub>@Al<sub>2</sub>O<sub>3</sub>-EISA catalysts towards the diesel steam reforming reaction is presented in Figure 7.11 in terms of average gas product compositions of the six hour reaction time. The analysis of liquid samples showed negligible amounts of hydrocarbon which is given in detail in Appendix D. For all samples, the total amount of hydrocarbons was less than 0.27 mole % of the diesel feed. Considering these results, the complete conversion assumption can be made for the DSR reaction.

According to Figure 7.11, hydrogen production for the Ni@8CeO<sub>2</sub>-2ZrO<sub>2</sub>@Al<sub>2</sub>O<sub>3</sub>-EISA and Ni@10CeO<sub>2</sub>-Al<sub>2</sub>O<sub>3</sub>-EISA catalysts was higher among the synthesized catalysts with also lower side product formation (CH<sub>4</sub>, C<sub>2</sub>H<sub>4</sub>, C<sub>2</sub>H<sub>6</sub>). Ni@8CeO<sub>2</sub>-2ZrO<sub>2</sub>@Al<sub>2</sub>O<sub>3</sub>-EISA resulted in slightly higher hydrogen production together with higher carbon dioxide and methane formation compared to the Ni@10CeO<sub>2</sub>-Al<sub>2</sub>O<sub>3</sub>-EISA catalyst. Production of higher amounts of carbon dioxide for zirconia incorporated catalyst suggests that the ability of Ni@8CeO<sub>2</sub>-2ZrO<sub>2</sub>@Al<sub>2</sub>O<sub>3</sub>-EISA catalyst towards the water gas shift reaction (WGSR), which is higher than Ni@10CeO<sub>2</sub>-Al<sub>2</sub>O<sub>3</sub>-EISA&Ni@Al<sub>2</sub>O<sub>3</sub>-EISA. In spite of higher methane formation which should limit hydrogen production observed with this catalyst, enhancement in the WGSR provided by Ni@8CeO<sub>2</sub>-2ZrO<sub>2</sub>@Al<sub>2</sub>O<sub>3</sub>-EISA was the leading effect for the best hydrogen production catalyst performance. The enhancement in the WGSR was probably provided by the different crystal structure of this material. In the Ni@8CeO<sub>2</sub>-2ZrO<sub>2</sub>@Al<sub>2</sub>O<sub>3</sub>-EISA catalyst, the incorporation of ZrO<sub>2</sub> diminished the reaction between CeO<sub>2</sub> and Al<sub>2</sub>O<sub>3</sub> leading to formation CeO<sub>2</sub> crystals besides CeAlO<sub>3</sub> crystal, according to the XRD results presented in Figure 7.3. Presence of cubic CeO<sub>2</sub> crystals instead of transformed CeAlO<sub>3</sub> crystals clearly had a positive effect on the hydrogen production capability of the material. Similar number of acid sites observed

for the Ni@10CeO<sub>2</sub>-Al<sub>2</sub>O<sub>3</sub>-EISA and Ni@8CeO<sub>2</sub>-2ZrO<sub>2</sub>@Al<sub>2</sub>O<sub>3</sub>-EISA combined with the enhancement provided by ceria was the key to achieving high hydrogen production. However, Figure 7.12 shows that although the Ni@8CeO<sub>2</sub>-2ZrO<sub>2</sub>@Al<sub>2</sub>O<sub>3</sub>-EISA catalyst provided higher hydrogen production, Ni@10CeO<sub>2</sub>-Al<sub>2</sub>O<sub>3</sub>-EISA catalyst provided higher hydrogen production, Ni@10CeO<sub>2</sub>-Al<sub>2</sub>O<sub>3</sub>-EISA possess a more stable activity in terms of gas product composition with respect to time.

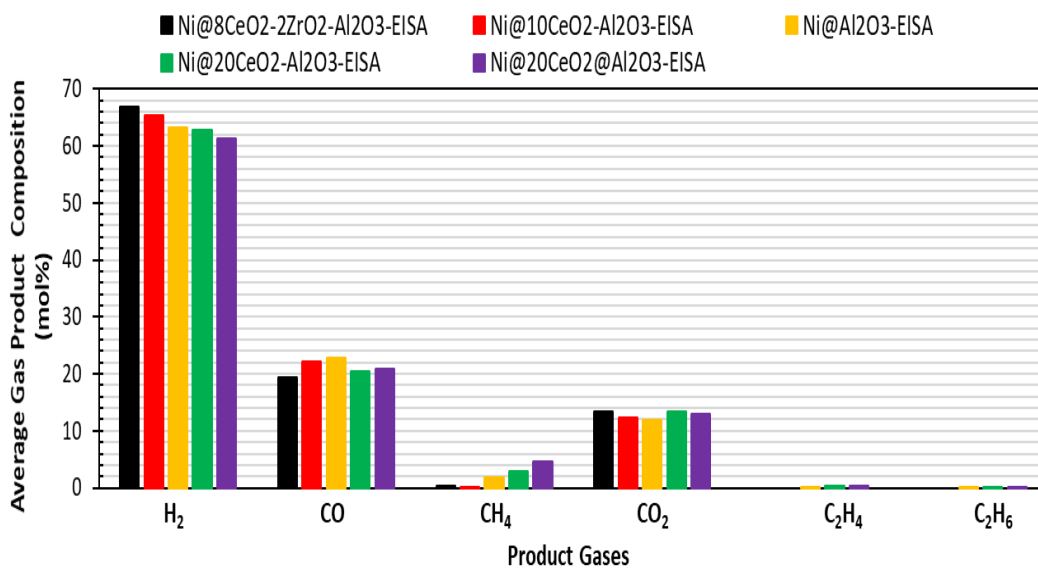


Figure 7.11. The effect of catalyst content on the average gas product composition in the DSR reaction (GHSV=7500 h<sup>-1</sup>, H<sub>2</sub>O/C=2.5, 800°C).

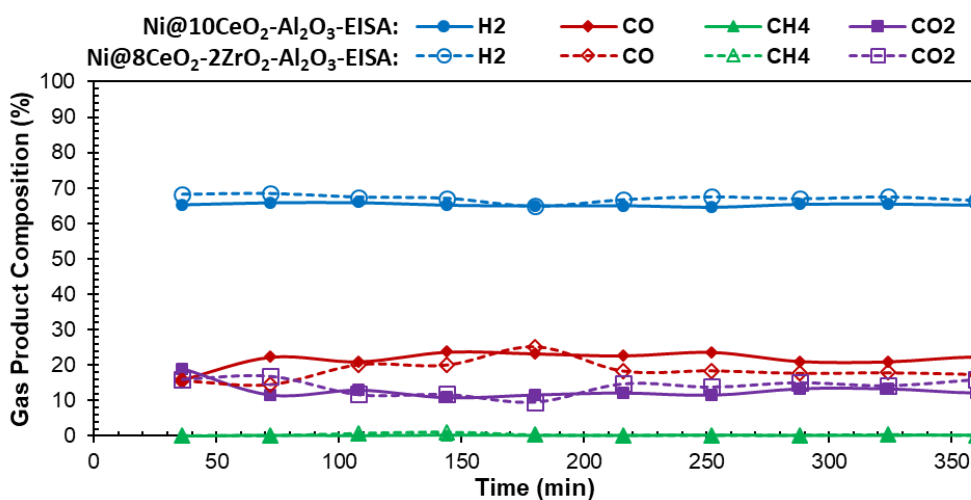


Figure 7.12. DSR activity test results of Ni@10CeO<sub>2</sub>-Al<sub>2</sub>O<sub>3</sub>-EISA (—) and Ni@8CeO<sub>2</sub>-2ZrO<sub>2</sub>-Al<sub>2</sub>O<sub>3</sub>-EISA (---) catalysts with respect to time (GHSV=7500 h<sup>-1</sup>, H<sub>2</sub>O/C=2.5, 800°C).

Hydrogen yield, the molar ratio of CO to CO<sub>2</sub> production, average gas composition of side products and coke deposition results given in Table 7.4 also showed the superior activity of Ni@10CeO<sub>2</sub>-Al<sub>2</sub>O<sub>3</sub>-EISA, and Ni@8CeO<sub>2</sub>-2ZrO<sub>2</sub>@Al<sub>2</sub>O<sub>3</sub>-EISA catalysts in the DSR reaction compared to others. Ni@8CeO<sub>2</sub>-2ZrO<sub>2</sub>@Al<sub>2</sub>O<sub>3</sub>-EISA catalyst showed no C<sub>2</sub>H<sub>4</sub> or C<sub>2</sub>H<sub>6</sub> formation and almost zero coke deposition (Table 7.4). The role of CeO<sub>2</sub> in terms of coke minimization in Ni@8CeO<sub>2</sub>-2ZrO<sub>2</sub>@Al<sub>2</sub>O<sub>3</sub>-EISA catalyst is believed to be due to its water adsorption and dissociation capability. CeO<sub>2</sub> increases water adsorption by oxygen vacant sites of CeO<sub>2</sub> and dissociates it and transfers produced oxygen to nickel<sup>108</sup>. Nickel provides reaction between carbon and oxygen leading to the production of CO or CO<sub>2</sub>. This process of water adsorption and oxygen transfer provides carbon free operation<sup>108</sup>. Similarly, Ni@10CeO<sub>2</sub>-Al<sub>2</sub>O<sub>3</sub>-EISA catalyst presented no C<sub>2</sub>H<sub>4</sub> or C<sub>2</sub>H<sub>6</sub> formation and low coke deposition (0.3 wt.%, Table 7.4). However, increase of ceria loading (Ni@20CeO<sub>2</sub>-Al<sub>2</sub>O<sub>3</sub>-EISA) enhanced side product formation along with carbon deposition as can be seen from Figure 7.11 and Table 7.4. The Ni@20CeO<sub>2</sub>@Al<sub>2</sub>O<sub>3</sub>-EISA material showed the lowest hydrogen production and resulted in the highest methane formation. The poor activity of the Ni@20CeO<sub>2</sub>@Al<sub>2</sub>O<sub>3</sub>-EISA catalysts showed that one-pot synthesis compared to impregnation of CeO<sub>2</sub> is slightly more effective in terms of hydrogen production and also is more effective in terms of increasing the coking resistance of the material (Table 7.4) in the diesel steam reforming reaction. Lower hydrogen production and coking resistance of Ni@20CeO<sub>2</sub>@Al<sub>2</sub>O<sub>3</sub>-EISA was believed to be due to low acid capacity of the material (Table 7.2) which might limit the occurrence of cracking reactions. The presence of higher amounts of side products such as CH<sub>4</sub>, C<sub>2</sub>H<sub>4</sub>, and C<sub>2</sub>H<sub>6</sub> apparently enhanced carbon deposition. Results presented in Chapter 4 suggested that this reaction occurs through cracking of longer chain hydrocarbons into C<sub>2</sub>-C<sub>3</sub> compounds which are then reformed into the desired products.

Higher activity was observed with the Ni@Al<sub>2</sub>O<sub>3</sub>-EISA material compared to the both 20 wt.% ceria incorporated catalysts despite the positive effect of the presence of ceria observed for the Ni@10CeO<sub>2</sub>-Al<sub>2</sub>O<sub>3</sub>-EISA catalyst. The cause of higher hydrogen production for the Ni@Al<sub>2</sub>O<sub>3</sub>-EISA catalyst is its higher surface area (135.3

m<sup>2</sup>/g) compared to the Ni@20CeO<sub>2</sub>-Al<sub>2</sub>O<sub>3</sub>-EISA (44.2 m<sup>2</sup>/g) and Ni@20CeO<sub>2</sub>@Al<sub>2</sub>O<sub>3</sub>-EISA (49.9 m<sup>2</sup>/g) catalysts. However, the highest CO/CO<sub>2</sub> ratio was observed with the Ni@Al<sub>2</sub>O<sub>3</sub>-EISA catalyst proves the enhancing effect of ceria in the WGSR. Moreover, when the average hydrogen formation rates were calculated by using Eq.1, the lower reforming activity of the Ni@Al<sub>2</sub>O<sub>3</sub>-EISA catalyst (with a hydrogen formation rate of 0.34 mmolH<sub>2</sub>/h.m<sup>2</sup>) became more prominent compared to the Ni@20CeO<sub>2</sub>-Al<sub>2</sub>O<sub>3</sub>-EISA (1.02 mmolH<sub>2</sub>/h.m<sup>2</sup>) and Ni@20CeO<sub>2</sub>@Al<sub>2</sub>O<sub>3</sub>-EISA (0.87 mmolH<sub>2</sub>/h.m<sup>2</sup>) catalysts.

$$R_{H_2} = \frac{\dot{N}_{H_2 \text{ Produced}}}{m_{\text{catalyst}} \times S_{\text{BET Surface Area}}} \frac{(\text{mmol})}{(\text{m}^2 \cdot \text{h})} \quad \text{Eq. 1}$$

Table 7.4. Activity test results of catalysts in DSR in terms of H<sub>2</sub> yield, the ratio of CO to CO<sub>2</sub> formation, average side product amount and coke deposition (GHSV= 7500 h<sup>-1</sup>, 800 °C, H<sub>2</sub>O/C=2.5).

Catalyst	Average H <sub>2</sub> Yield ( $\frac{\text{max}^{\text{theoretical}}}{=35}$ )	$\frac{\dot{N}_{\text{CO}}}{\dot{N}_{\text{CO}_2}}$	Average Side Product Composition (ppm)				Coke % ( $\frac{\text{g}_{\text{coke}}}{\text{g}_{\text{used catalyst}}}$ )
			CH <sub>4</sub>	C <sub>2</sub> H <sub>4</sub>	C <sub>2</sub> H <sub>6</sub>	C <sub>3</sub> H <sub>6</sub>	
Ni@10CeO <sub>2</sub> -Al <sub>2</sub> O <sub>3</sub> -EISA	32.0	1.8	1400	0	0	0	0.3
Ni@Al <sub>2</sub> O <sub>3</sub> -EISA	29.1	1.9	19000	1700	900	0	1.1
Ni@20CeO <sub>2</sub> -Al <sub>2</sub> O <sub>3</sub> -EISA	28.3	1.5	30000	3800	1200	0	1.9
Ni@20CeO <sub>2</sub> @Al <sub>2</sub> O <sub>3</sub> -EISA	26.6	1.6	46000	2400	1200	0	3.7
Ni@8CeO <sub>2</sub> -2ZrO <sub>2</sub> -Al <sub>2</sub> O <sub>3</sub> -EISA	34.2	1.4	4000	0	0	0	~0

### ***Diesel Steam Reforming Test Results at Harsh Operating Conditions***

The Ni@Al<sub>2</sub>O<sub>3</sub>-EISA and Ni@10CeO<sub>2</sub>-Al<sub>2</sub>O<sub>3</sub>-EISA catalysts were also tested at harsh operating conditions in the DSR reaction to observe their resistivity towards coke deposition. DSR tests with the Ni@10CeO<sub>2</sub>-Al<sub>2</sub>O<sub>3</sub>-EISA and Ni@Al<sub>2</sub>O<sub>3</sub>-EISA

catalysts were performed at higher GHSV and lower H<sub>2</sub>O/C ratio (GHSV=17000 h<sup>-1</sup>, H<sub>2</sub>O/C=1.5). Previous test conducted with optimum operating conditions with the Ni@10CeO<sub>2</sub>-Al<sub>2</sub>O<sub>3</sub>-EISA catalyst (Figure 7.11) did not show the formation of C<sub>2</sub>H<sub>4</sub> and C<sub>2</sub>H<sub>6</sub>. However, the results presented in Figure 7.13 show the formation of some C<sub>2</sub>H<sub>4</sub> and C<sub>2</sub>H<sub>6</sub> products with both catalysts. The total amount of hydrocarbons in the liquid sample was less than 0.01 mol% of the diesel feed for both catalysts.

According to these results, the Ni@10CeO<sub>2</sub>-Al<sub>2</sub>O<sub>3</sub>-EISA catalyst resulted in higher hydrogen and carbon dioxide production and lower carbon monoxide and side product formation. The difference in side product formation and produced CO/CO<sub>2</sub> molar ratio can be clearly seen from Figure 7.14. The most important difference was presented in Figure 7.15 with thermogravimetric analysis results of used Ni@10CeO<sub>2</sub>-Al<sub>2</sub>O<sub>3</sub>-EISA and Ni@Al<sub>2</sub>O<sub>3</sub>-EISA catalyst. Ni@10CeO<sub>2</sub>-Al<sub>2</sub>O<sub>3</sub>-EISA catalyst showed only 2.1 wt.% coke deposition. However, coke deposition observed in the Ni@Al<sub>2</sub>O<sub>3</sub>-EISA catalyst was 12.5 wt.%. These results clearly showed the importance of ceria incorporation in activity enhancement and coke resistivity.

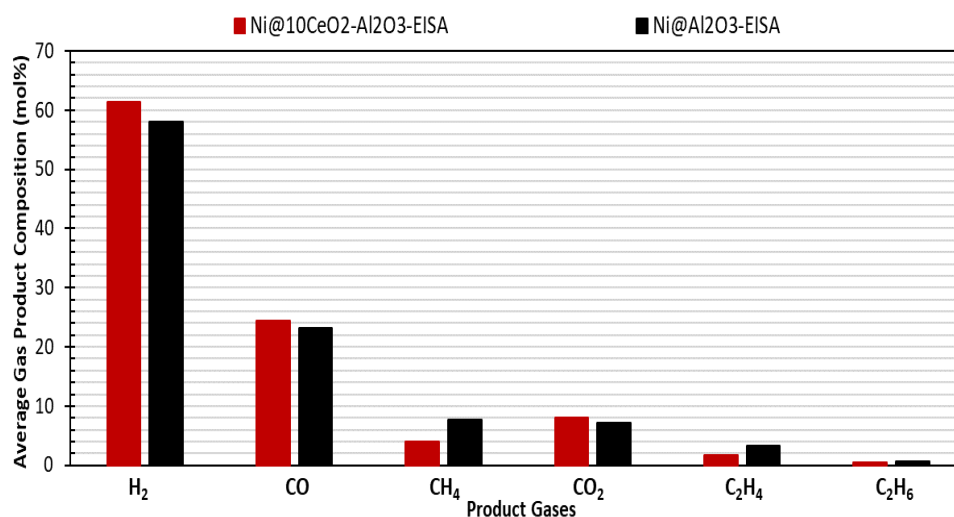


Figure 7.13. The effect of catalyst content on the average gas product composition obtained from DSR reaction at harsh reaction conditions (GHSV=17000 h<sup>-1</sup>, H<sub>2</sub>O/C=1.5, 800°C).

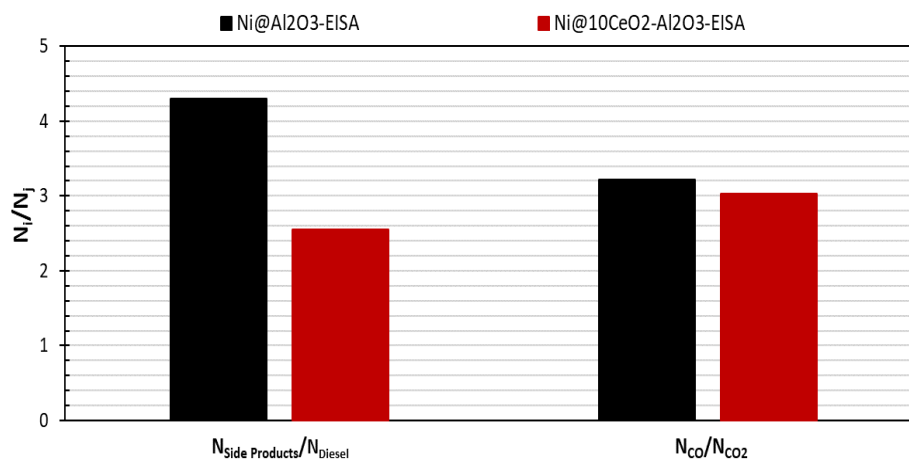


Figure 7.14 The effect of catalyst content on the side product formation and the ratio of CO to CO<sub>2</sub> obtained from the DSR reaction at harsh reaction conditions (GHSV=17000 h<sup>-1</sup>, H<sub>2</sub>O/C=1.5, 800°C).

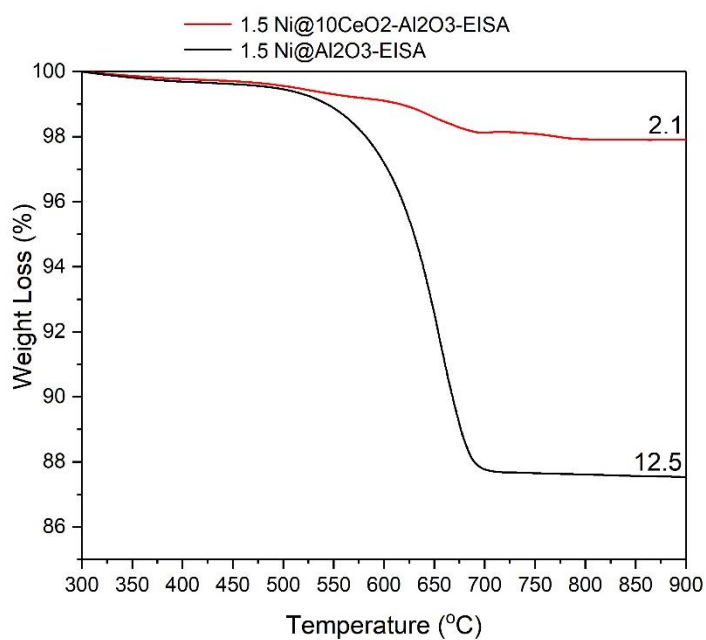


Figure 7.15. Coke deposition in the DSR reaction at harsh reaction conditions (GHSV=17000 h<sup>-1</sup>, H<sub>2</sub>O/C=1.5, 800°C).

### 7.2.2. The effect of Catalyst Composition on Hydrogen Production in the Diesel Autothermal Reforming Reaction

The most successful catalysts with the highest hydrogen yield (Ni@10CeO<sub>2</sub>-Al<sub>2</sub>O<sub>3</sub>-EISA and Ni@8CeO<sub>2</sub>-2ZrO<sub>2</sub>@Al<sub>2</sub>O<sub>3</sub>-EISA) in the DSR reaction were used in the autothermal reforming reaction. Average gas product composition of ATR and DSR results can be seen in Figure 7.16. In the ATR reaction, Ni@10CeO<sub>2</sub>-Al<sub>2</sub>O<sub>3</sub>-EISA catalyst presented the highest hydrogen production activity and the lowest coke deposition (0.4 wt.%). The coke deposition in the presence of Ni@8CeO<sub>2</sub>-2ZrO<sub>2</sub>@Al<sub>2</sub>O<sub>3</sub>-EISA catalyst was found to be 1.6 wt.% and also slightly higher methane formation was observed with the zirconia incorporated material.

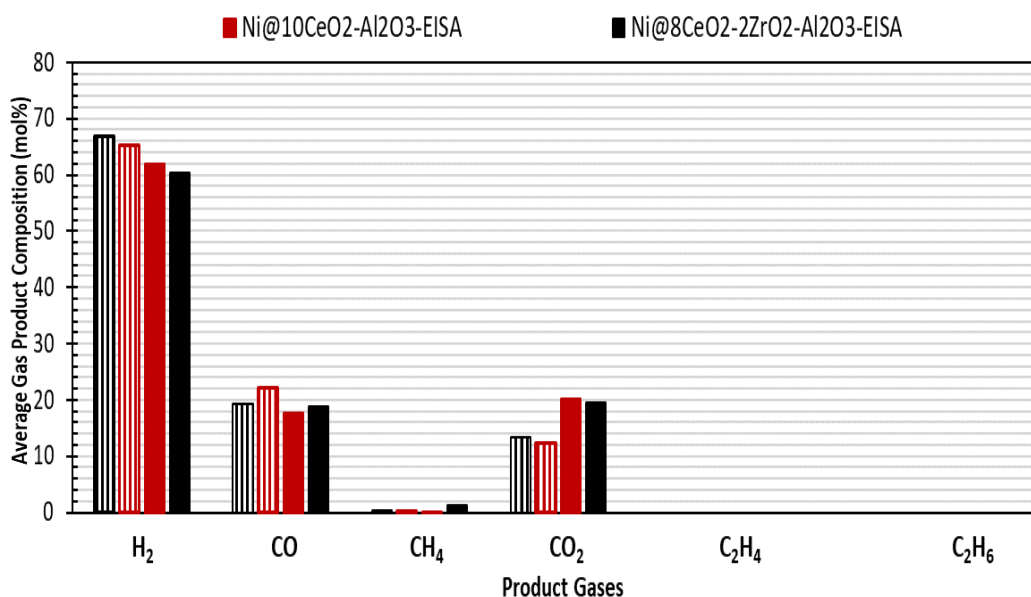


Figure 7.16. Comparison of gas average product composition obtained from the DSR reaction and the ATR reaction in the presence of Ni@10CeO<sub>2</sub>-Al<sub>2</sub>O<sub>3</sub>-EISA and Ni@8CeO<sub>2</sub>-2ZrO<sub>2</sub>@Al<sub>2</sub>O<sub>3</sub>-EISA catalysts (GHSV=7500 h<sup>-1</sup>, H<sub>2</sub>O/C=2.5, 800°C) (Striped bar: DSR, Filled bar: ATR).

### 7.2.3. Long Term Diesel Steam Reforming Test Results with Ni@10CeO<sub>2</sub>-Al<sub>2</sub>O<sub>3</sub>-EISA

All the experiments performed with ceria incorporated EISA catalysts showed good performance and among them the best catalyst was Ni@10CeO<sub>2</sub>-Al<sub>2</sub>O<sub>3</sub>-EISA. Coke resistance of this catalysts showed superiority especially in the DSR reaction conducted at harsh operating conditions. The stability of the catalyst was also determined with a long term DSR activity test that lasted for twenty six hours. The change in product gas composition depending on the reaction time is given in Figure 7.17. Termogravimetric analysis revealed 6.9 wt.% coke deposition in the Ni@10CeO<sub>2</sub>-Al<sub>2</sub>O<sub>3</sub>-EISA catalyst at the reaction time of twenty six hours. Loss of catalyst activity was not observed during the diesel steam reforming reaction experiment which shows long-term stability of this catalyst. Moreover, there was no indication of any hydrocarbon in the liquid sample. Considering these results, in addition to high hydrogen productivity and stability obtained with the Ni@10CeO<sub>2</sub>-Al<sub>2</sub>O<sub>3</sub>-EISA catalyst, the complete conversion of diesel was also achieved at the reaction time of 26 h.

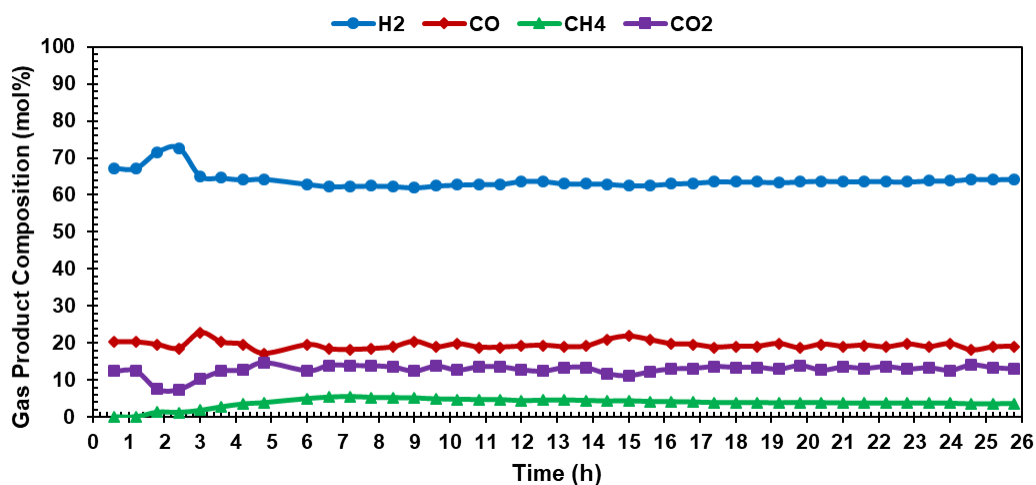


Figure 7.17. Long term Ni@10CeO<sub>2</sub>-Al<sub>2</sub>O<sub>3</sub>-EISA activity test result in the DSR reaction (GHSV=7500 h<sup>-1</sup>, H<sub>2</sub>O/C=2.5, 800°C).

### *Characterization results of used catalysts*

Scanning and backscattering electron microscope images of used catalysts Ni@8CeO<sub>2</sub>-2ZrO<sub>2</sub>@Al<sub>2</sub>O<sub>3</sub>-EISA, Ni@10CeO<sub>2</sub>-Al<sub>2</sub>O<sub>3</sub>-EISA, and long term Ni@10CeO<sub>2</sub>-Al<sub>2</sub>O<sub>3</sub>-EISA are presented in Figure 7.18-Figure 7.20. Scanning and backscattering electron detector images of Ni@8CeO<sub>2</sub>-2ZrO<sub>2</sub>@Al<sub>2</sub>O<sub>3</sub>-EISA catalyst show the presence of nickel particles with 50-70 nm sizes in Figure 7.19-A&B. SEM image of fresh catalyst did not show particles with these sizes (Figure 7.9-B&D), which indicated occurrence of agglomeration during the reforming reaction. The presence of 40 nm sized particles was observed on the SEM images of used Ni@10CeO<sub>2</sub>-Al<sub>2</sub>O<sub>3</sub>-EISA after the reaction time of 6 h (Figure 7.19-A&B). Similar to the SEM images of fresh Ni@10CeO<sub>2</sub>-Al<sub>2</sub>O<sub>3</sub>-EISA (Figure 7.9-B&D), different surface morphologies were observed suggesting the presence of a porous structure and dispersed crystals. After the long term reaction, the used Ni@10CeO<sub>2</sub>-Al<sub>2</sub>O<sub>3</sub>-EISA catalyst showed cloudy images with nickel particle on the porous structure which was also observed on the SEM image of the fresh catalyst (Figure 7.20-A&B). No significant deterioration of the surface was observed for the Ni@10CeO<sub>2</sub>-Al<sub>2</sub>O<sub>3</sub>-EISA catalyst after both six and twenty six hours of reaction times.

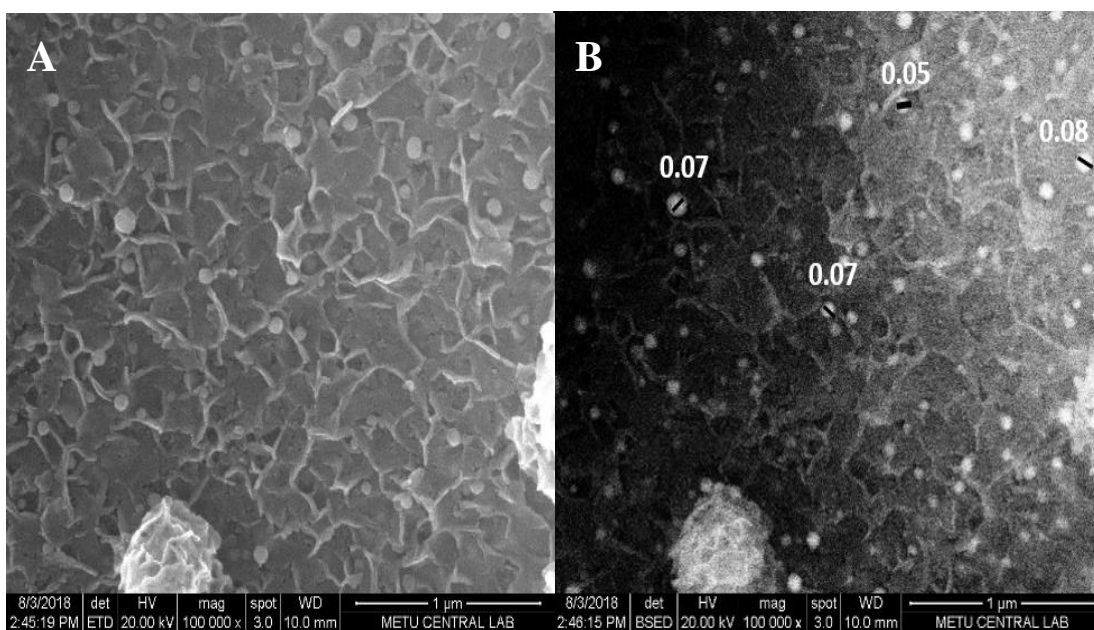


Figure 7.18 SEM images of used Ni@8CeO<sub>2</sub>-2ZrO<sub>2</sub>@Al<sub>2</sub>O<sub>3</sub>-EISA catalyst: A) scanning electron detector, B) backscattering electron detector (Size units are in μm, magnification: 100000 and the scale: 1 μm).

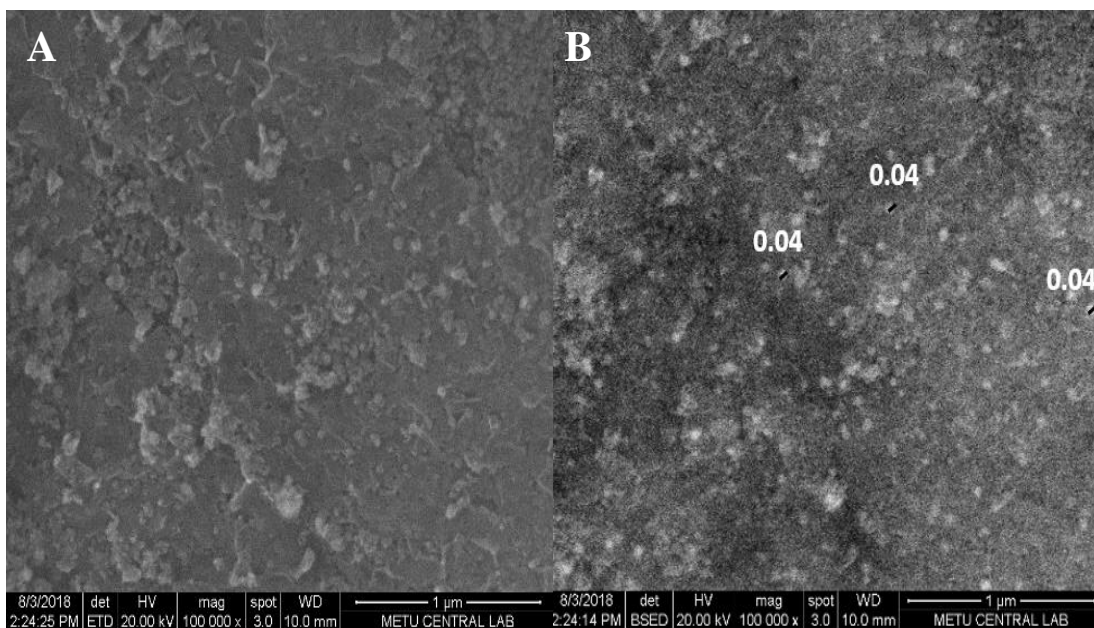


Figure 7.19. SEM images of used Ni@10CeO<sub>2</sub>-Al<sub>2</sub>O<sub>3</sub>-EISA catalyst: A) scanning electron detector, B) backscattering electron detector (Size units are in μm, magnification: 100000 and the scale: 1 μm).

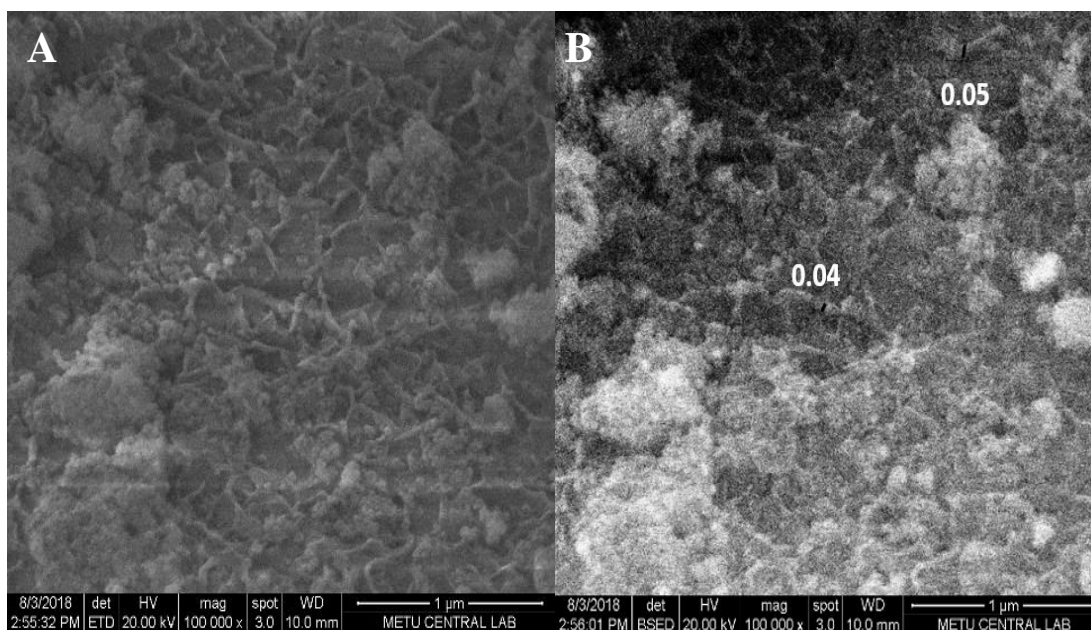


Figure 7.20 SEM images of long term used Ni@10CeO<sub>2</sub>-Al<sub>2</sub>O<sub>3</sub>-EISA catalyst: A) scanning electron detector, B) backscattering electron detector (Size units are in μm, magnification: 100000 and the scale: 1 μm).

The long term used Ni@10CeO<sub>2</sub>-Al<sub>2</sub>O<sub>3</sub>-EISA catalyst was characterized with N<sub>2</sub> adsorption/desorption analysis. N<sub>2</sub> adsorption/desorption isotherms and pore size distributions of the fresh and used catalysts are presented in Figure 7.21. After twenty six hours of test, BET surface area of the used material was 50.3 m<sup>2</sup>/g which was 52.8 m<sup>2</sup>/g for the fresh catalyst. However, a decrease in pore volume can be clearly seen from these graphs. BJH desorption average pore volume value was 0.35 cm<sup>3</sup>/g for fresh material, whereas it decreased to 0.19 cm<sup>3</sup>/g after long term activity test. Moreover, even though the pore size distribution result (Figure 7.21-B) of fresh and used material shows similar average pore diameter values, the presence of micropores can clearly be observed. Microporosity percent in the long term used Ni@10CeO<sub>2</sub>-Al<sub>2</sub>O<sub>3</sub>-EISA catalyst is 12.7, which was 8.8 for fresh catalyst. This indicates blockage of pores by coke deposition (6.9 wt.%) which resulted in an increase in the number of micropores which were mesopores before coke deposition. According to the results of microporosity percent increase after long term DSR reaction, it can be inferred that the

reactions leading to coke deposition including cracking and diesel steam reforming reactions take place in the mesopores of the Ni@10CeO<sub>2</sub>-Al<sub>2</sub>O<sub>3</sub>-EISA catalyst.

TEM images of Ni@10CeO<sub>2</sub>-Al<sub>2</sub>O<sub>3</sub>-EISA catalyst that was used in the long term DSR experiment is presented in Figure 7.22. Figure 7.22-A in which an image of the material with 100 nm scale is given, shows a variation in mass, density or thickness along the image. Darker spots indicates regions with higher mass or thickness. Figure 7.22-A also presents metal/metal oxide particle detachment from the surface through a carbon whisker. The diameter of carbon whisker is 14.3 nm which also seems to be covered with amorphous carbon. Detached particle might be nickel, considering the reported tip growth mechanism of carbon filaments over nickel crystals<sup>109</sup>. Figure 7.22-C suggests the formation of carbon with layered structure typical for graphene (shown with arrows) on the used catalyst. Figure 7.22-B&D shows the formation of either graphene sheets on top of each other or multiwall carbon nanotubes (MWNT) with a total thickness of of 5-7 nm. The distance between the carbon layers was measured as 0.4 nm which is consistent with graphene since the interlayer spacing in graphite is 0.34<sup>110</sup>. According to the long term activity test results given in Figure 7.17, the presence of carbon did not cause any activity loss. Other than the presence of characteristic peak of carbon, there was no indication of a change of material crystal structure according to the XRD pattern of the used catalyst given in Figure 7.23. Carbon formation was observed with a characteristic peak of carbon (PDF Card No: 00-026-1076) located at 26° indicating carbon deposition.

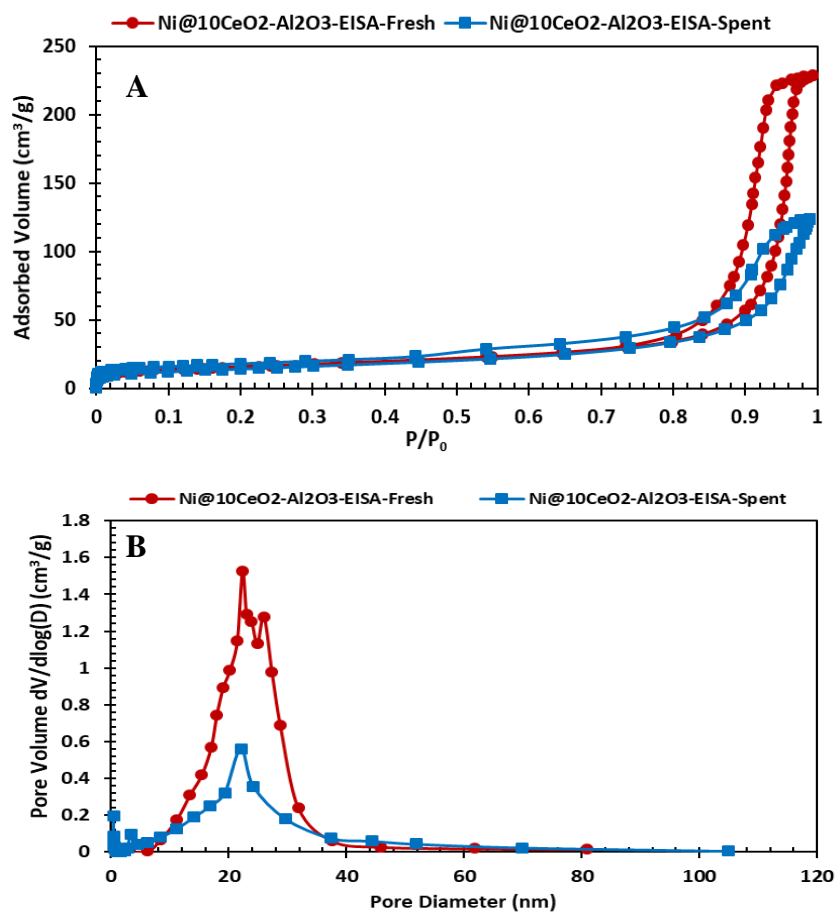


Figure 7.21. N<sub>2</sub> adsorption/desorption isotherms (A) and pore size distributions (B) of fresh and used in long term DSR activity test (Ni@10CeO<sub>2</sub>-Al<sub>2</sub>O<sub>3</sub>-EISA).

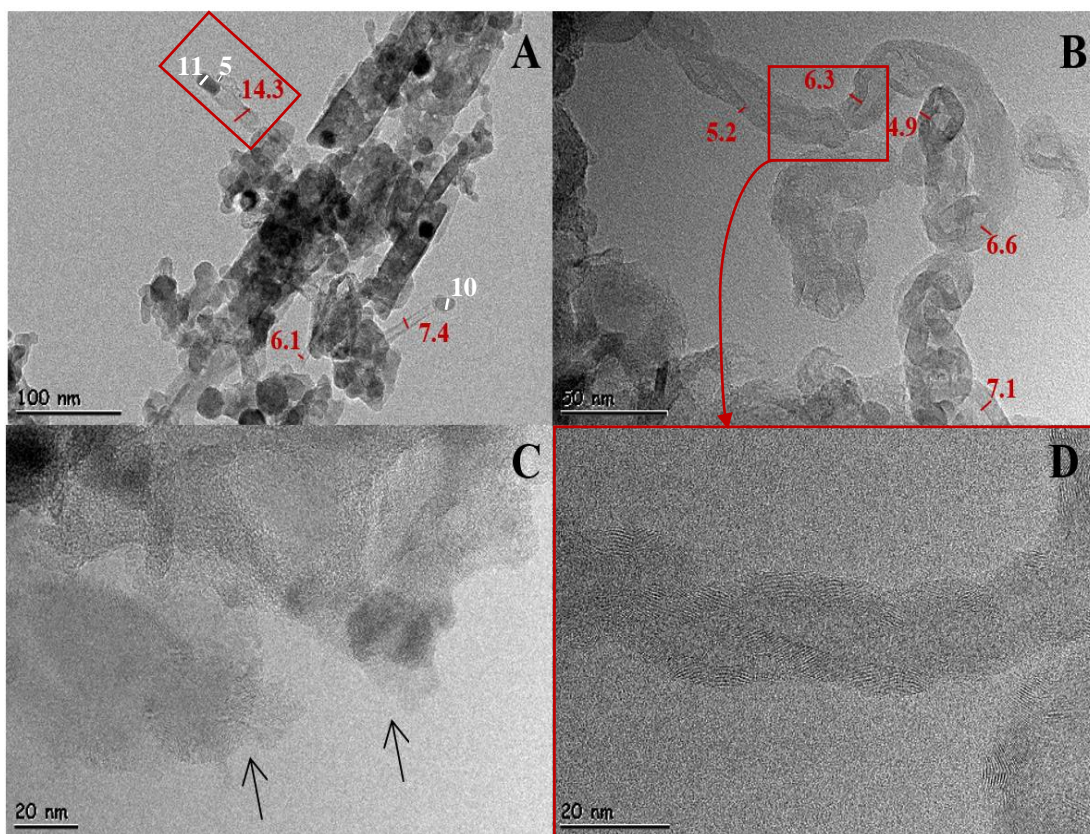


Figure 7.22. TEM images of long term used Ni@10CeO<sub>2</sub>-Al<sub>2</sub>O<sub>3</sub>-EISA catalyst in DSR activity test (Size units are in nm).

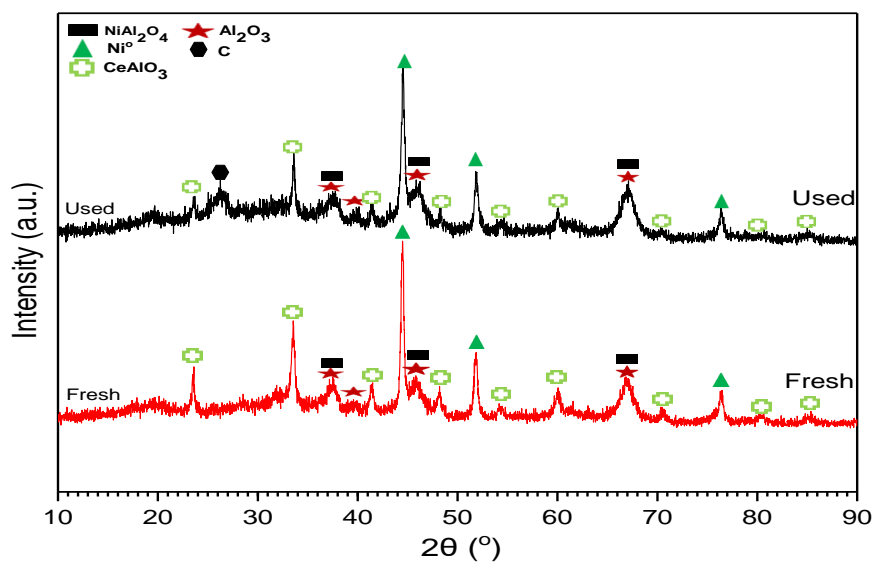


Figure 7.23. XRD patterns of Ni@10CeO<sub>2</sub>-Al<sub>2</sub>O<sub>3</sub>-EISA catalyst; fresh and used in long term DSR activity test.



## CHAPTER 8

### PROMOTION EFFECT OF TUNGSTEN, CERIA AND MAGNESIUM ON NICKEL ALUMINA CATALYSTS TOWARDS DIESEL STEAM AND AUTOTHERMAL REFORMING REACTIONS

#### 8.1. Characterization Results

Characterization studies were performed for the synthesized Al<sub>2</sub>O<sub>3</sub>-EISA support, metal incorporated support materials, and nickel impregnated catalysts (10 wt.% nickel). Nickel impregnated catalysts were reduced before the analysis (except for TPR analysis). Characterization results were discussed throughout this section in terms of the effect of the type of metal/metal oxide (10 wt.% Mg or 10 wt.% W), or the combination of different metal/metal oxide (10 wt.% Mg and 10 wt.% W or 10 wt.% CeO<sub>2</sub> and 10 wt.% W) that was incorporated and the effect of metal incorporation amount (for W; 10 wt.% or 20 wt.%).

The physical properties of the Ni@10Mg-Al<sub>2</sub>O<sub>3</sub>-EISA, Ni@10W-10Mg-Al<sub>2</sub>O<sub>3</sub>-EISA, Ni@10W-10CeO<sub>2</sub>-Al<sub>2</sub>O<sub>3</sub>-EISA, Ni@10W-Al<sub>2</sub>O<sub>3</sub>-EISA and Ni@20W-Al<sub>2</sub>O<sub>3</sub>-EISA catalysts and their support materials are presented in Table 8.1. The physical properties of support materials shows differences from each other in terms of surface area, pore volume, pore diameter and microporosity percent according to their metal content/type. Mg incorporated catalyst (10Mg-Al<sub>2</sub>O<sub>3</sub>-EISA) presented the highest surface area with the largest pore volume and 7.9% microporosity. The smallest surface area value was observed with the 10W-10CeO<sub>2</sub>-Al<sub>2</sub>O<sub>3</sub>-EISA material with a microporosity percent of 15.3. Results indicate that incorporated metal type and amount significantly affect the pore structure of the resultant material. As can be seen from the results of nickel impregnated catalysts given in Table 8.1, nickel impregnation decreased surface area and pore volume values of these materials. The

decrease of pore diameter was observed for the Ni@10W-10Mg-Al<sub>2</sub>O<sub>3</sub>-EISA catalyst after nickel impregnation, indicating deposition of Ni in the pores of 10W-10Mg-Al<sub>2</sub>O<sub>3</sub>-EISA which are higher in diameter (47 nm) compared to the range of diameter values of other support materials (10.1-27.6 nm). However, an increase in average pore diameter, along with slight decrease in surface area and pore volume values were observed for Ni@10Mg-Al<sub>2</sub>O<sub>3</sub>-EISA and Ni@10W-Al<sub>2</sub>O<sub>3</sub>-EISA materials after nickel impregnation. These results indicate that nickel blocked some pores of these materials, which caused an increase in the average pore diameter along with the microporosity percent. Nickel impregnation to 10W-10CeO<sub>2</sub>-Al<sub>2</sub>O<sub>3</sub>-EISA and 20W-Al<sub>2</sub>O<sub>3</sub>-EISA lead to a decrease in the microporosity percent of the materials. As can be seen from these results, change of the incorporated metal type alters the formation structure of mesopores that lead to materials with quite different pore diameter and surface area values.

Table 8.1 Physical properties of catalysts

Material	Multi Point BET Surface Area (m <sup>2</sup> /g)	BJH Desorption Pore Volume (cm <sup>3</sup> /g)	BJH Desorption Average Pore Diameter (nm)	Microporosity %
10Mg-Al <sub>2</sub> O <sub>3</sub> -EISA	148.28	0.55	10.1	7.9
<b>Ni@10Mg-Al<sub>2</sub>O<sub>3</sub>-EISA</b>	<b>78.78</b>	<b>0.29</b>	<b>11.0</b>	<b>8.1</b>
10W-10Mg-Al <sub>2</sub> O <sub>3</sub> -EISA	74.33	0.58	47.3	9.1
<b>Ni@10W-10Mg-Al<sub>2</sub>O<sub>3</sub>-EISA</b>	<b>45.13</b>	<b>0.34</b>	<b>29.6</b>	<b>11.2</b>
10W-10CeO <sub>2</sub> -Al <sub>2</sub> O <sub>3</sub> -EISA	44.77	0.42	27.6	15.3
<b>Ni@10W-10CeO<sub>2</sub>-Al<sub>2</sub>O<sub>3</sub>-EISA</b>	<b>39.55</b>	<b>0.34</b>	<b>33.6</b>	<b>13.4</b>
10W-Al <sub>2</sub> O <sub>3</sub> -EISA	96.00	0.56	18.9	5.2
<b>Ni@10W-Al<sub>2</sub>O<sub>3</sub>-EISA</b>	<b>63.17</b>	<b>0.39</b>	<b>19.2</b>	<b>5.9</b>
20W-Al <sub>2</sub> O <sub>3</sub> -EISA	67.35	0.54	25.5	10.8
<b>Ni@20W-Al<sub>2</sub>O<sub>3</sub>-EISA</b>	<b>47.04</b>	<b>0.33</b>	<b>21.9</b>	<b>7.5</b>

Nitrogen adsorption/desorption isotherms of all supports are given in Figure 8.1-A, these materials can be classified as Type IV with H1 type hysteresis loop. Type IV isotherm is a characteristic feature of mesoporous materials and H1 type hysteresis loop indicates presence of narrow uniform pore size distribution. Sharp inflections on the adsorption and desorption branches were caused by the capillary condensation of nitrogen in the mesopores. However, pore size distributions of support materials given in Figure 8.1-B showed the narrow pore size distribution for 10Mg-Al<sub>2</sub>O<sub>3</sub>-EISA and 10W-Al<sub>2</sub>O<sub>3</sub>-EISA materials. Wide and non-uniform pore size distribution and shift in the hysteresis loops to higher P/P<sub>0</sub> values were observed for 10W-10CeO<sub>2</sub>-Al<sub>2</sub>O<sub>3</sub>-EISA, 10W-10Mg-Al<sub>2</sub>O<sub>3</sub>-EISA and 20W-Al<sub>2</sub>O<sub>3</sub>-EISA materials (Figure 8.1-A&B). These results suggest the presence of a different pore size structure formation compared to the 10Mg-Al<sub>2</sub>O<sub>3</sub>-EISA and 10W-Al<sub>2</sub>O<sub>3</sub>-EISA materials. Figure 8.2 also shows Type IV with H1 type hysteresis loops for nickel impregnated catalysts with diminished adsorbed quantity values compared to the hysteresis loops of support materials. Hysteresis loop of the Ni@10Mg-Al<sub>2</sub>O<sub>3</sub>-EISA material still positioned at the lowest P/P<sub>0</sub> value. Figure 8.2-B shows lower pore diameter values for the Ni@10W-10Mg-Al<sub>2</sub>O<sub>3</sub>-EISA and Ni@20W-Al<sub>2</sub>O<sub>3</sub>-EISA materials compared to their supports, indicating deposition of nickel into pores.

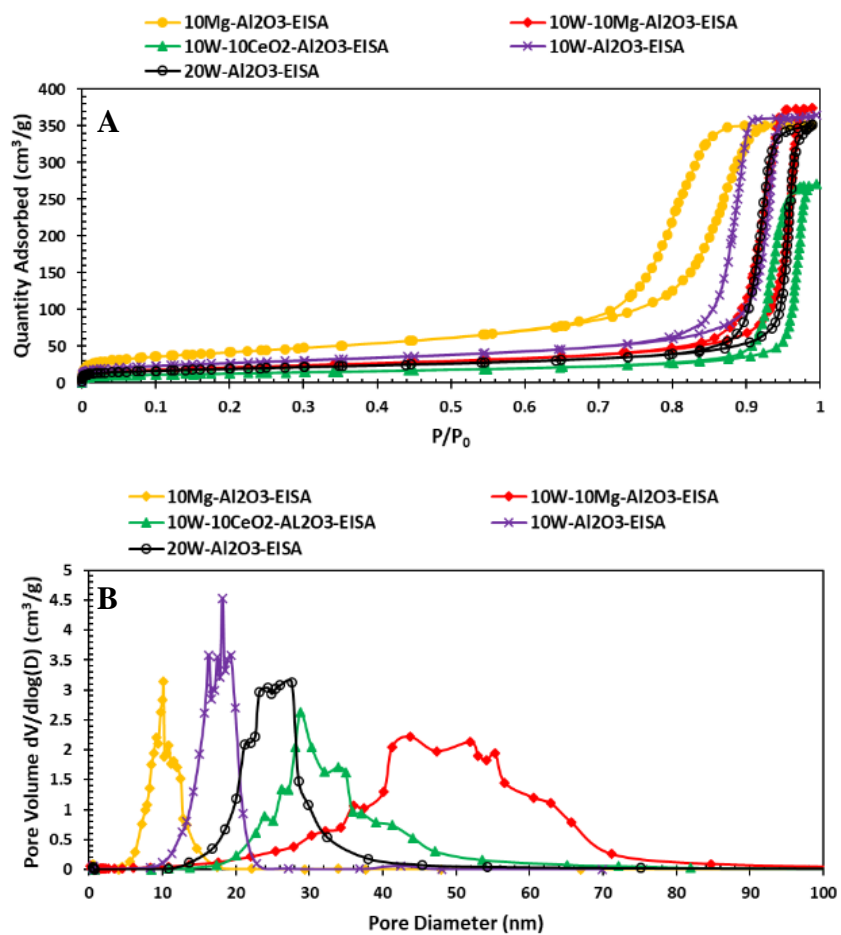


Figure 8.1. N<sub>2</sub> adsorption/desorption isotherms (A) and pore size distributions (B) of the synthesized support materials.

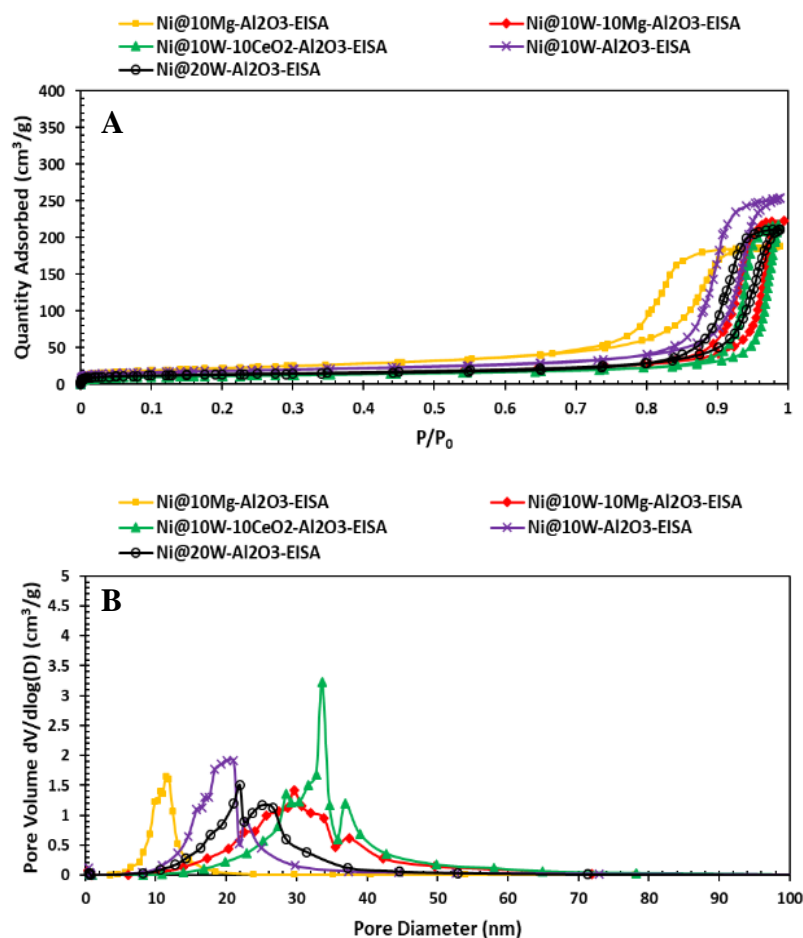


Figure 8.2. N<sub>2</sub> adsorption/desorption isotherms (A) and pore size distributions (B) of the synthesized nickel impregnated materials.

X-ray diffraction patterns of the synthesized catalysts are presented in Figure 8.3. XRD patterns of tungsten incorporated materials showed the characteristic peaks of Ni<sub>4</sub>W (PDF card No. 01-072-2650) and W (PDF card No. 01-089-3728). When the XRD patterns of Ni@10W-Al<sub>2</sub>O<sub>3</sub>-EISA and Ni@20W-Al<sub>2</sub>O<sub>3</sub>-EISA materials were compared, it can be clearly observed that the intensity of W peaks increases with an increase in W loadings. Even though sharper W peaks were observed with the Ni@20W-Al<sub>2</sub>O<sub>3</sub>-EISA material, W (52 nm) and Ni<sub>4</sub>W (38 nm) crystal sizes obtained using Scherrer equation were almost the same for the Ni@10W-Al<sub>2</sub>O<sub>3</sub>-EISA and Ni@20W-Al<sub>2</sub>O<sub>3</sub>-EISA catalysts. A small peak is observed in the patterns of the

Ni@10W-Al<sub>2</sub>O<sub>3</sub>-EISA and Ni@20W-Al<sub>2</sub>O<sub>3</sub>-EISA catalyst at a 2θ value of 44.2°, indicating presence of Ni<sup>0</sup> (PDF card No. 01-071-4653).

With CeO<sub>2</sub> incorporation (Ni@10W-10CeO<sub>2</sub>-Al<sub>2</sub>O<sub>3</sub>-EISA), the intensity values of characteristic peaks of W and Ni<sub>4</sub>W were decreased, compared to the Ni@10W-Al<sub>2</sub>O<sub>3</sub>-EISA and Ni@20W-Al<sub>2</sub>O<sub>3</sub>-EISA catalysts. Lower peak intensities observed for W and Ni<sub>4</sub>W crystals suggest a different metal-surface interaction probably due to the presence of CeAlO<sub>3</sub> crystals (PDF card No. 01-081-1185). While XRD patterns indicated the presence of γ-Al<sub>2</sub>O<sub>3</sub> phase for just W loaded materials, the presence of NiAl<sub>2</sub>O<sub>4</sub> (PDF card No. 00-010-0339) was also observed for the Ni@10W-10CeO<sub>2</sub>-Al<sub>2</sub>O<sub>3</sub>-EISA catalyst.

Mg incorporation lead to the formation of a Mg-Al spinel in the form of (Mg<sub>0.782</sub>Al<sub>0.218</sub>)(Al<sub>1.782</sub>Mg<sub>0.218</sub>)O<sub>4</sub> (PDF card No. 01-070-6013) for both the Ni@10Mg-Al<sub>2</sub>O<sub>3</sub>-EISA and Ni@10W-10Mg-Al<sub>2</sub>O<sub>3</sub>-EISA catalysts. Characteristic peaks of Ni<sup>0</sup> (PDF card No. 01-071-4653) and NiO (PDF card No. 4-835) were observed and the presence of γ-Al<sub>2</sub>O<sub>3</sub> or NiAl<sub>2</sub>O<sub>4</sub> was not observed in the XRD patterns of these materials. W and Ni<sub>4</sub>W were still present in the pattern of Ni@10W-10Mg-Al<sub>2</sub>O<sub>3</sub>-EISA.

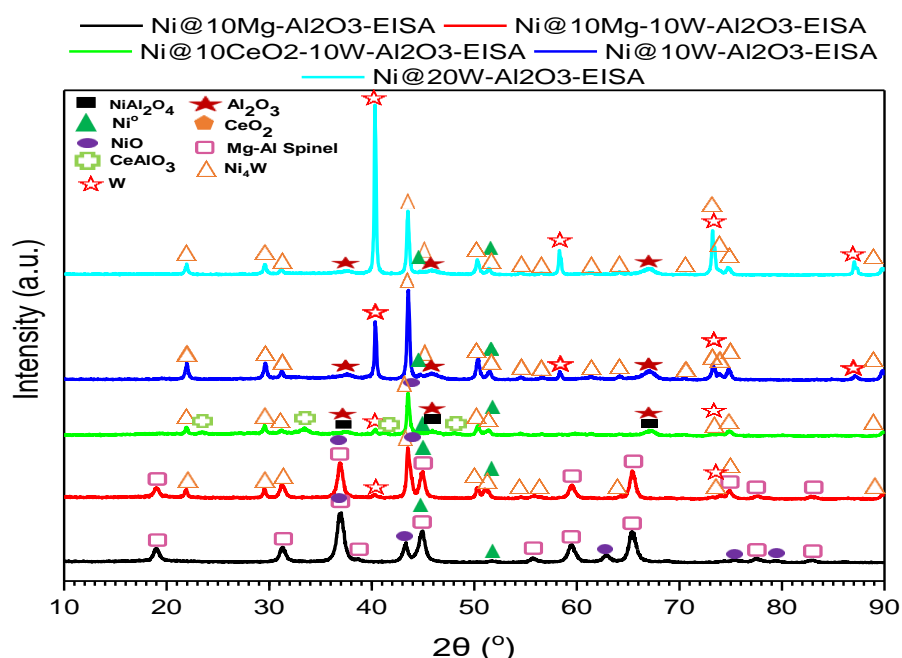


Figure 8.3 X-Ray diffraction patterns of synthesized materials

The results of temperature programmed reduction analysis (TPR) of the support materials and nickel impregnated catalysts are given in Figure 8.4. The absence of any TPR peaks in the Mg-Al<sub>2</sub>O<sub>3</sub>-EISA material suggested that the Mg-Al spinel structure observed in the XRD patterns (Figure 8.3) formed during the synthesis of the support material. After nickel impregnation into 10Mg-Al<sub>2</sub>O<sub>3</sub>-EISA, seven different reduction peaks were observed at 345 °C, 385 °C, 500 °C, 532 °C, 674 °C, 814 °C, and 842 °C. Since the XRD pattern of reduced material showed only the characteristic peaks of NiO and Ni<sup>0</sup>, observed peaks indicate the reduction of NiO species that has different interactions with the support surface. Reducibility depends on distribution of NiO in the support material and well distributed metal oxides have a stronger interaction with the support that would lead to a higher reduction temperature<sup>111</sup>. Reduction at 300-500 °C suggests that some NiO particles did not completely integrate to the spinel structure. Small peak located at 674 °C could be due to the reduction of NiO interacting with the Al<sub>2</sub>O<sub>3</sub> surface and the high temperature peaks (>800 °C) are due to the reduction of NiO that has strongly interacted with Mg-Al spinel<sup>112</sup>.

The TPR result of the 10W-Al<sub>2</sub>O<sub>3</sub>-EISA material presented a reduction peak (0.75 mmol/g<sub>cat</sub>) at 817 °C indicating reduction of WO<sub>x</sub> species. The reduction of WO<sub>x</sub> species in the 20W-Al<sub>2</sub>O<sub>3</sub>-EISA material occurred at five different temperatures, namely at 657 °C, 719 °C, 766 °C, 804 °C, and 848 °C. These results indicate that higher W loading affects the interaction of W and Al<sub>2</sub>O<sub>3</sub>, resulting in easier reduction of loosely bounded W species. Similar total H<sub>2</sub> consumption values were observed between 10W-Al<sub>2</sub>O<sub>3</sub>-EISA (0.75 mmol/g<sub>cat</sub>) and 20W-Al<sub>2</sub>O<sub>3</sub>-EISA (0.66 mmol/g<sub>cat</sub>) at a temperature range of 800-820 °C. This suggests that 10 wt.% W loading created similar degree of interaction, but further W loading causes lower interaction between W and support.

The TPR result of the 10W-10CeO<sub>2</sub>-Al<sub>2</sub>O<sub>3</sub>-EISA material presented a reduction peak that has higher temperature (865 °C) and lower H<sub>2</sub> uptake (0.28 mmol/g<sub>cat</sub>) compared to 10W-Al<sub>2</sub>O<sub>3</sub>-EISA, suggesting a strong interaction between WO<sub>x</sub> species and CeO<sub>2</sub>-Al<sub>2</sub>O<sub>3</sub> surface. The TPR result of the 10W-10Mg-Al<sub>2</sub>O<sub>3</sub>-EISA material did

not show a reduction peak except a small peak located at 705 °C (0.05 mmol/g<sub>cat</sub>), suggesting even a stronger interaction of WO<sub>x</sub> species with Mg-Al spinel structure preventing reduction to W. Nickel impregnated tungsten incorporated materials presented larger amounts of peaks compared to its supports. For the Ni@10W-Al<sub>2</sub>O<sub>3</sub>-EISA, Ni@20W-Al<sub>2</sub>O<sub>3</sub>-EISA, Ni@10W-10CeO<sub>2</sub>-Al<sub>2</sub>O<sub>3</sub>-EISA, and Ni@10W-10Mg-Al<sub>2</sub>O<sub>3</sub>-EISA materials, common peaks between 766 °C and 792 °C were observed that have an H<sub>2</sub> uptake value of 1.53, 2.85, 2.40, and 2.10 mmol/g<sub>cat</sub>, respectively, indicating the formation of Ni<sub>4</sub>W crystals. Higher W loading of Ni@20W-Al<sub>2</sub>O<sub>3</sub>-EISA material apparently increased the amount of transformed Ni<sub>4</sub>W crystals. The difference in the H<sub>2</sub> uptake results of WO<sub>x</sub> species for nickel loaded catalysts and support materials can be observed from Figure 8.4. The difference in H<sub>2</sub> uptake difference suggests that presence of nickel increases the reduction of WO<sub>x</sub> species. Observation of different reduction temperatures for WO<sub>x</sub> species between the supports and catalysts is probably due to differences in the material surface interactions after nickel impregnation.

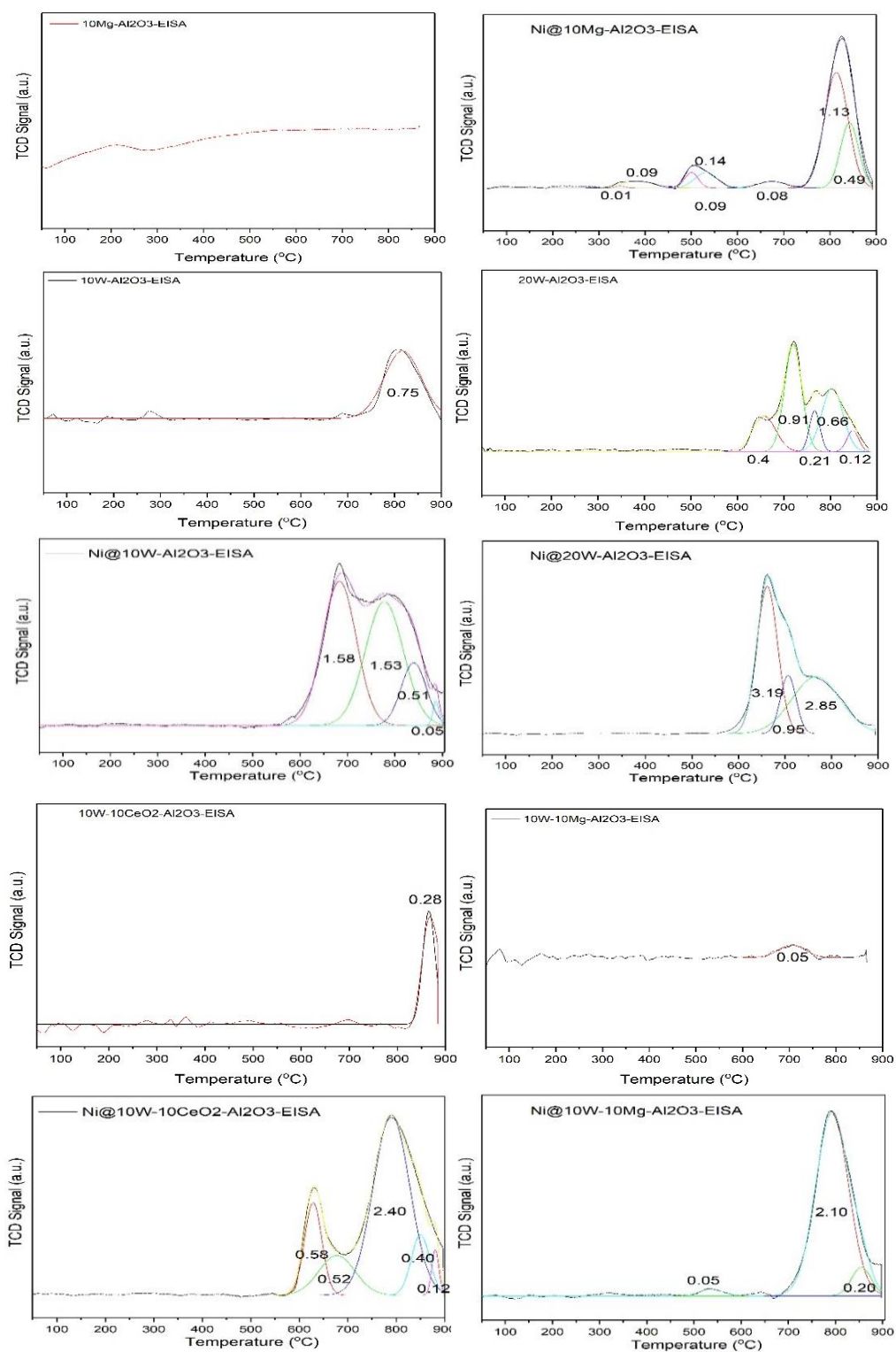


Figure 8.4 The TPR results of the synthesized support materials and nickel impregnated catalysts with baseline correction and deconvolution of TPR spectra.

NH<sub>3</sub>-TPD experiments were performed after saturating the samples with ammonia and the desorption curve of NH<sub>3</sub> with respect to temperature was presented in Figure 8.5. Peaks in each profile corresponded to NH<sub>3</sub> desorption from the acid sites of the catalysts. The temperature of desorption gives an idea about the acid strength in materials; the higher desorption temperature indicates the presence of stronger acid sites. Table 8.2 shows the total acid capacity for each catalyst. According to these results, the synthesis of Al<sub>2</sub>O<sub>3</sub> with W incorporation instead of Mg incorporation resulted in a material with higher acid capacity with a sharp desorption peak located at around 450°C. The increase of W incorporation also led to a slight increase in the acid capacity. Desorption peak at a temperature range of moderate acidity was sharper for the Ni@10W-10CeO<sub>2</sub>-Al<sub>2</sub>O<sub>3</sub>-EISA material. This indicates that incorporation of W together with CeO<sub>2</sub> diminished the acid capacity by diminishing strong acidity of the material according to Figure 8.5. With the Ni@10W-10Mg-Al<sub>2</sub>O<sub>3</sub>-EISA catalyst, desorption peak was widened and occurred at a temperature between moderate and strong acidity. However, for the Ni@10Mg-Al<sub>2</sub>O<sub>3</sub>-EISA material, the total acid capacity was quite low compared to W incorporated materials with a small desorption peak located at lower temperatures indicating moderate acidity. This is an expected result considering the basic nature of magnesium.

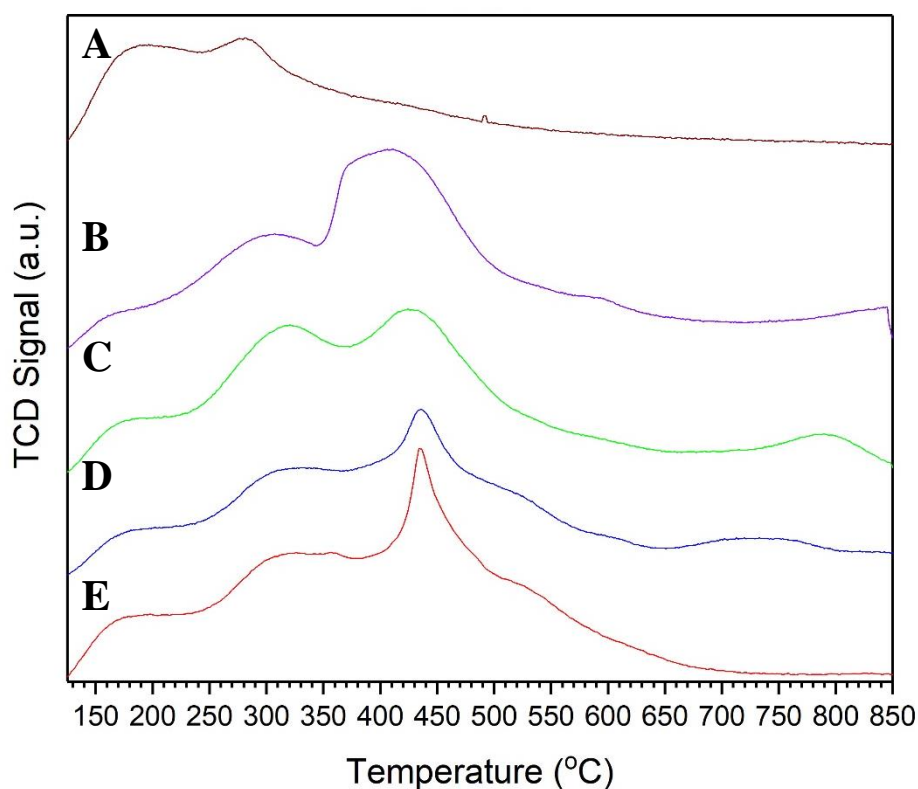


Figure 8.5 NH<sub>3</sub>-TPD results of synthesized materials: A) Ni@10Mg-Al<sub>2</sub>O<sub>3</sub>-EISA, B) Ni@10W-10Mg-Al<sub>2</sub>O<sub>3</sub>-EISA, C) Ni@10W-10CeO<sub>2</sub>-Al<sub>2</sub>O<sub>3</sub>-EISA, D) Ni@20W-Al<sub>2</sub>O<sub>3</sub>-EISA, and E) Ni@10W-Al<sub>2</sub>O<sub>3</sub>-EISA.

Table 8.2. Total acid capacity of the catalysts synthesized with EISA method.

Catalyst Name	Acid Capacity (mmol/g <sub>cat</sub> )
Ni@10Mg-Al <sub>2</sub> O <sub>3</sub> -EISA	0.14
Ni@10W-10CeO <sub>2</sub> -Al <sub>2</sub> O <sub>3</sub> -EISA	0.28
Ni@10W-10Mg-Al <sub>2</sub> O <sub>3</sub> -EISA	0.30
Ni@10W-Al <sub>2</sub> O <sub>3</sub> -EISA	0.33
Ni@20W-Al <sub>2</sub> O <sub>3</sub> -EISA	0.38

The nature of the acid sites of the catalysts was also analyzed with the Diffuse Reflectant FTIR analysis (DRIFTS) technique using pyridine adsorbed samples. Figure 8.6 illustrates the DRIFTS spectra of the difference between pyridine adsorbed and fresh samples for synthesized support materials. For the 20W-Al<sub>2</sub>O<sub>3</sub>-EISA and

10W-10CeO<sub>2</sub>-Al<sub>2</sub>O<sub>3</sub>-EISA materials, the presence of strong Brønsted type acidity was observed with the transmission bands located at 1638 cm<sup>-1</sup> vibrations. Lewis and Brønsted acidities can be compared for these materials by taking the ratio of peak intensities of 1445 cm<sup>-1</sup> and 1638 cm<sup>-1</sup> transmission bands. Lewis to Brønsted acidity ratios for 20W-Al<sub>2</sub>O<sub>3</sub>-EISA, 10W-10CeO<sub>2</sub>-Al<sub>2</sub>O<sub>3</sub>-EISA and 10W-10Mg-Al<sub>2</sub>O<sub>3</sub>-EISA materials are found to be 4.8, 11.0, 19.5, respectively. This indicates that Brønsted type acidity of W is suppressed by the incorporation of Mg and CeO<sub>2</sub>. Figure 8.7 illustrates the DRIFTS spectra of the difference between pyridine adsorbed and fresh samples for nickel impregnated catalysts. Brønsted type strong acidity was not observed for nickel impregnated catalysts suggesting an interaction between nickel and Brønsted acid sites of alumina support. For all materials, transmission bands were located at 1445 cm<sup>-1</sup>, 1575 cm<sup>-1</sup>, and 1614 cm<sup>-1</sup> for the Ni impregnated materials, which indicate presence of Lewis acid sites. The transmission band located at 1485 cm<sup>-1</sup> is attributed to both weak Lewis and weak Brønsted acid sites and the transmission band located at 1590 cm<sup>-1</sup> is due to presence of H-bond that could be due to weak Brønsted acidity.

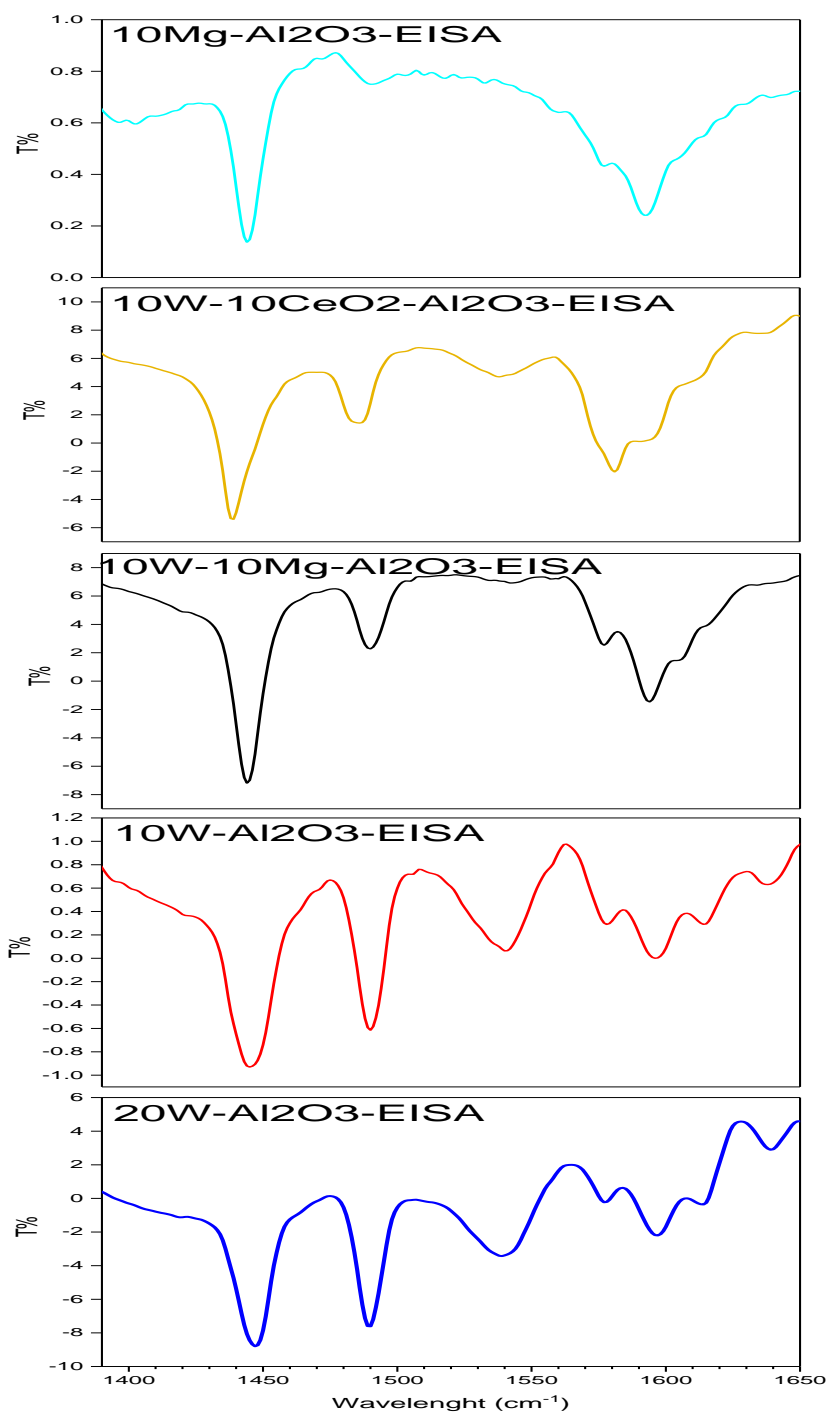


Figure 8.6 DRIFTS spectra of the difference between pyridine adsorbed and fresh samples of the 10Mg-Al<sub>2</sub>O<sub>3</sub>-EISA, 10W-10CeO<sub>2</sub>-Al<sub>2</sub>O<sub>3</sub>-EISA, 10W-10Mg-Al<sub>2</sub>O<sub>3</sub>-EISA, 20W-Al<sub>2</sub>O<sub>3</sub>-EISA, and 10W-Al<sub>2</sub>O<sub>3</sub>-EISA supports.

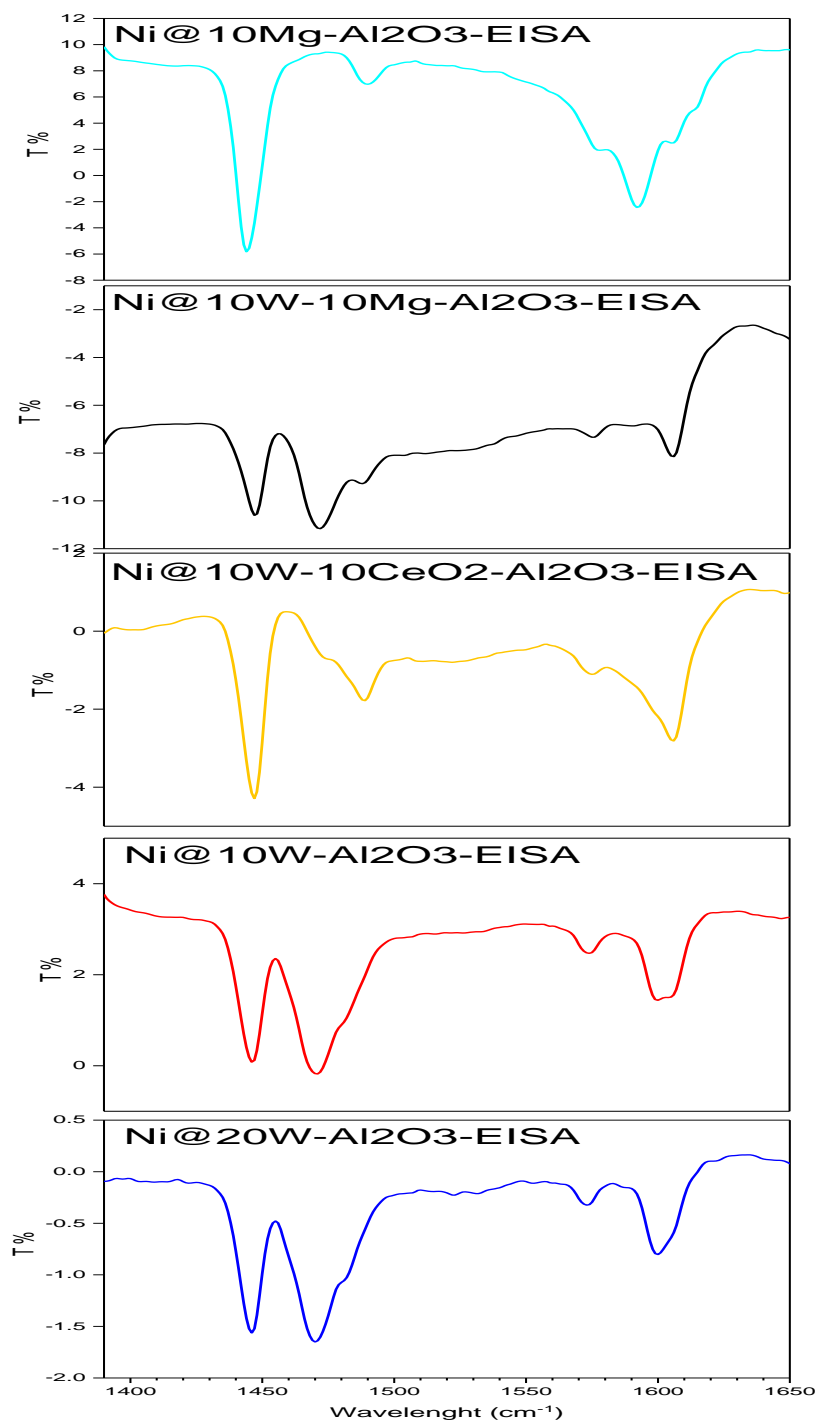


Figure 8.7 DRIFTS spectra of the difference between pyridine adsorbed and fresh samples of synthesized Ni@10Mg-Al<sub>2</sub>O<sub>3</sub>-EISA, Ni@10W-10CeO<sub>2</sub>-Al<sub>2</sub>O<sub>3</sub>-EISA, Ni@10W-10Mg-Al<sub>2</sub>O<sub>3</sub>-EISA, Ni@20W-Al<sub>2</sub>O<sub>3</sub>-EISA, and Ni@10W-Al<sub>2</sub>O<sub>3</sub>-EISA catalysts.

SEM electron detector and backscattering electron detector images of Ni@10Mg-Al<sub>2</sub>O<sub>3</sub>-EISA, Ni@10W-10CeO<sub>2</sub>-Al<sub>2</sub>O<sub>3</sub>-EISA, and Ni@10W-10Mg-Al<sub>2</sub>O<sub>3</sub>-EISA materials are presented in Figure 8.8. SEM image of Ni@10Mg-Al<sub>2</sub>O<sub>3</sub>-EISA material (Figure 8.8-A&D) shows the presence of particle clusters that have cluster sizes ranging from 50 to 130 nm. Tungsten and magnesium incorporated catalyst (Ni@10W-10Mg-Al<sub>2</sub>O<sub>3</sub>-EISA, Figure 8.8-B&E) shows more dispersed particles with diameters of 40 nm, 50 nm, 60 nm, and 100 nm. Ni@10W-10CeO<sub>2</sub>-Al<sub>2</sub>O<sub>3</sub>-EISA (Figure 8.8-C&F) presented a different surface structure compared to the other materials which include a cloudy material that might be due to cerium aluminate crystals which are observed on the XRD pattern of the material (Figure 8.3). SEM electron detector and backscattering electron detector images of Ni@10W-Al<sub>2</sub>O<sub>3</sub>-EISA and Ni@20W-Al<sub>2</sub>O<sub>3</sub>-EISA materials are presented in Figure 8.9. SEM images of Ni@10W-Al<sub>2</sub>O<sub>3</sub>-EISA (Figure 8.9-A&C) and Ni@20W-Al<sub>2</sub>O<sub>3</sub>-EISA (Figure 8.9-B&D) materials presented agglomerated particles. Agglomerated particles might be originating from both Ni<sub>4</sub>W or W crystals, since their crystal sizes were calculated by using XRD patterns and Scherrer equation as 38 nm and 52 nm, respectively.

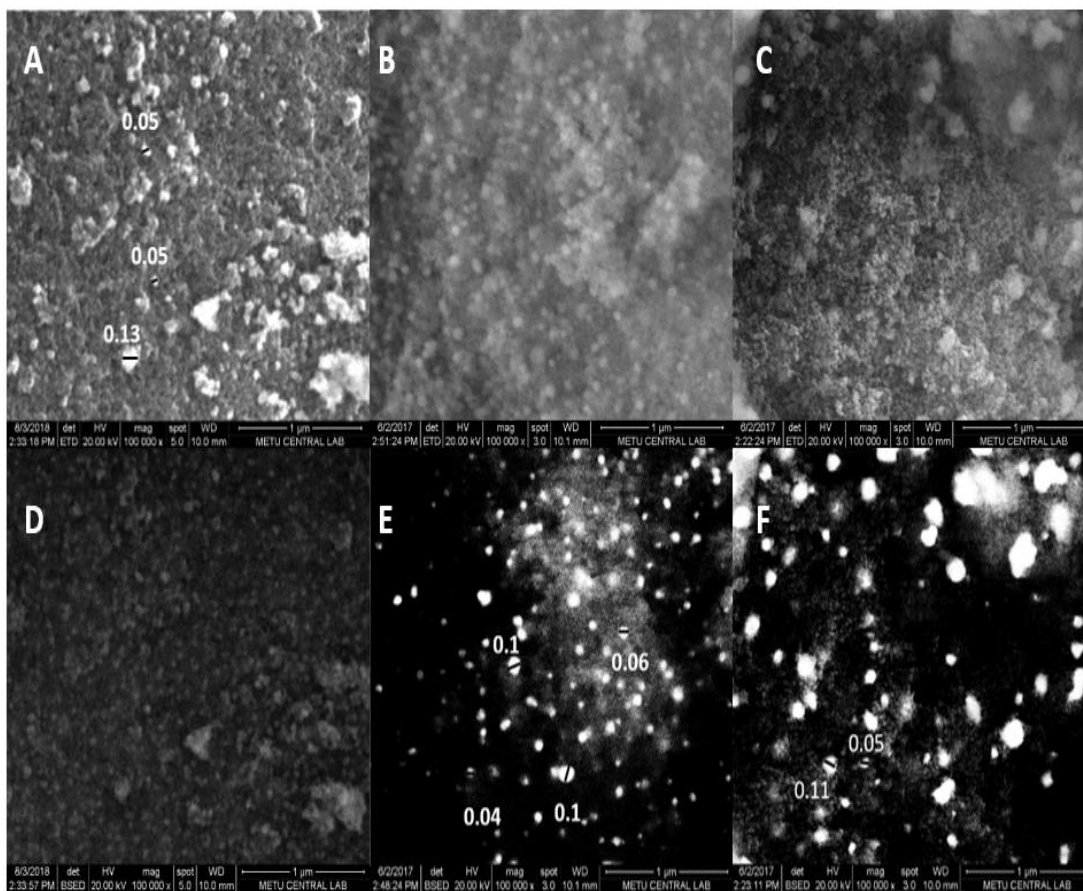


Figure 8.8 Scanning electron detector image of A) Ni@10Mg-Al<sub>2</sub>O<sub>3</sub>-EISA, B) Ni@10W-10Mg-Al<sub>2</sub>O<sub>3</sub>-EISA, C) Ni@10W-10CeO<sub>2</sub>-Al<sub>2</sub>O<sub>3</sub>-EISA, and backscattering electron detector image of D) Ni@10Mg-Al<sub>2</sub>O<sub>3</sub>-EISA, E) Ni@10W-10Mg-Al<sub>2</sub>O<sub>3</sub>-EISA and F) Ni@10W-10CeO<sub>2</sub>-Al<sub>2</sub>O<sub>3</sub>-EISA (Size units are in μm, magnification: 100000 and the scale: 1 μm in all images).

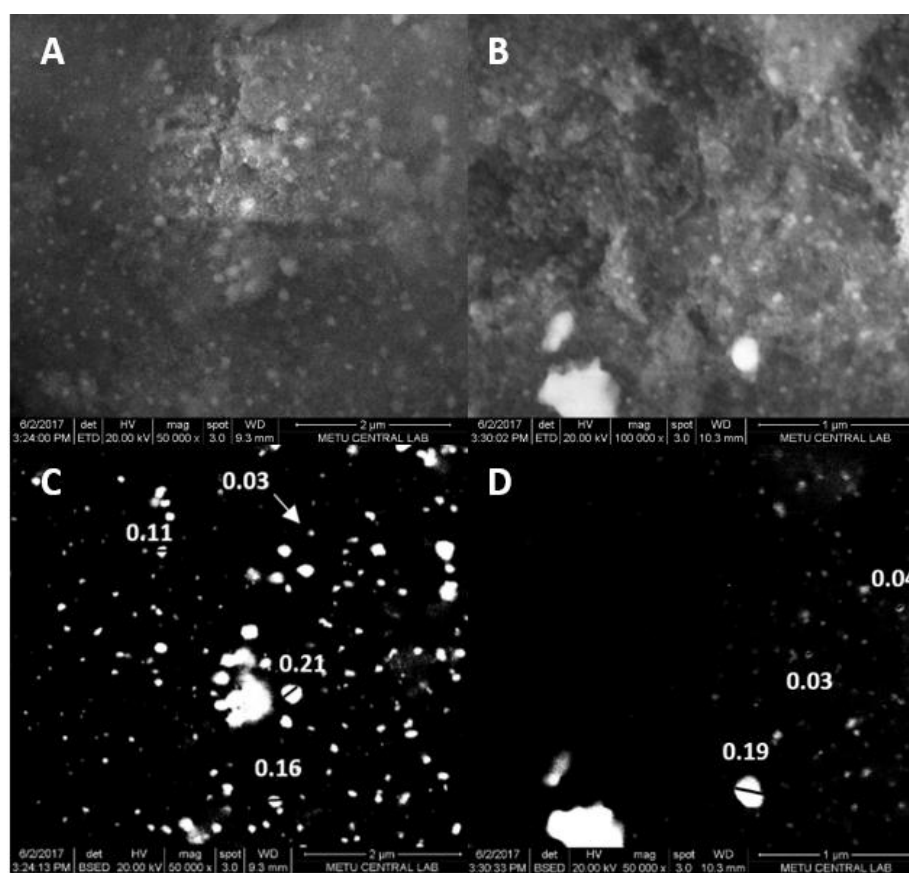


Figure 8.9 Scanning electron detector image of A) Ni@10W-Al<sub>2</sub>O<sub>3</sub>-EISA (Magnification: 50000 and the scale: 2 μm), B) Ni@20W-Al<sub>2</sub>O<sub>3</sub>-EISA (Magnification: 100000 and the scale: 1 μm), and backscattering electron detector image of D) Ni@10W-Al<sub>2</sub>O<sub>3</sub>-EISA, E) Ni@20W-Al<sub>2</sub>O<sub>3</sub>-EISA.

EDX analysis results suggested that the targeted metal loading was mostly achieved (Table 8.3). Some differences of the results from targeted loading amounts could be due to non-homogeneous dispersion of metals.

Table 8.3 Metal content of synthesized catalysts according to EDX analysis results.

Material	Metal Content (wt. %)							
	Ce		W		Mg		Ni	
	Target	EDX	Target	Target	Target	EDX	Target	EDX
Ni@10Mg-Al <sub>2</sub> O <sub>3</sub> -EISA	-	-	-	-	10.0	12.8	10.0	5.5
Ni@10W-10Mg-Al <sub>2</sub> O <sub>3</sub> -EISA	-	-	10.0	12.6	10.0	10.9	10.0	14.9
Ni@10W-10CeO <sub>2</sub> -Al <sub>2</sub> O <sub>3</sub> -EISA	10.0	10.2	10.0	13.8	-	-	10.0	7.5
Ni@10W-Al <sub>2</sub> O <sub>3</sub> -EISA	-	-	10.0	14.1	-	-	10.0	14.1
Ni@20W-Al <sub>2</sub> O <sub>3</sub> -EISA	-	-	20.0	22.1	-	-	10.0	8.4

## 8.2. Catalytic Activity Test Results

### 8.2.1. The Effect of Catalyst Composition on Hydrogen Production in Diesel Steam Reforming Reaction

The catalytic activity results of the synthesized catalysts towards diesel steam reforming reaction were presented in Figure 8.10 in terms of gas product composition and in Table 8.4 in terms of hydrogen yield, the molar ratio of produced CO to CO<sub>2</sub> and coke deposition after six hours of reaction. The analysis of liquid samples showed negligible amount of hydrocarbon. For all samples, the total amount of hydrocarbons in the liquid was less than 0.3 mol% of the diesel feed. Considering these results, complete diesel conversion assumption can be made for all experiments. The highest hydrogen production with minimum side product formation was obtained with the Ni@10Mg-Al<sub>2</sub>O<sub>3</sub>-EISA catalyst in the DSR reaction due to the presence of metallic nickel, (Table 8.2) and high surface area (Table 8.1) compared to tungsten incorporated catalysts. Acid sites in a reforming catalyst increases the occurrence of cracking reactions leading to the formation of CH<sub>4</sub>, C<sub>2</sub>H<sub>4</sub> and C<sub>2</sub>H<sub>6</sub>. Higher surface area on the other hand increases the reaction rate in a reforming catalysts. These results proved that Mg incorporation into the alumina support decreased surface acidity and helped to decrease formation of methane. Mg incorporation also facilitated the occurrence of water gas shift reaction, causing an increase in the CO<sub>2</sub>/CO ratio and hence in hydrogen yield.

Tungsten incorporated catalysts showed significantly lower H<sub>2</sub> and CO<sub>2</sub> and higher CO, CH<sub>4</sub>, C<sub>2</sub>H<sub>4</sub>, and C<sub>2</sub>H<sub>6</sub> in the product stream. The amounts of H<sub>2</sub>, CO<sub>2</sub> and CO gases in the product distribution suggest lower WGSR rate for tungsten catalysts compared to the other catalysts. Other than WGSR, higher amounts of side products suggest low reforming rate for these catalysts compared to magnesium-alumina supported catalyst. The main reason of this situation is the formation of Ni<sub>4</sub>W crystals in tungsten incorporated catalysts as can be seen from Figure 8.3, whereas nickel takes the form of Ni<sup>0</sup> and NiO crystals for Ni@10Mg-Al<sub>2</sub>O<sub>3</sub>-EISA. When H<sub>2</sub>, CO, and CO<sub>2</sub>

compositions in the gas product were analyzed, the formation of low amounts of CO<sub>2</sub> and high amounts of CO can be observed with tungsten incorporated catalysts compared to Ni@10Mg-Al<sub>2</sub>O<sub>3</sub>-EISA. From these results, it can be deduced that the activity loss brought by Ni<sub>4</sub>W crystal is mainly due to its low activity in the water gas shift reaction followed by its low activity in reforming reaction. When the average H<sub>2</sub>, CO, and CO<sub>2</sub> compositions obtained using tungsten incorporated catalysts were compared with the compositions obtained with magnesium incorporated catalysts, the major difference is in CO<sub>2</sub> production. CO<sub>2</sub> molar composition in the product gas is 10.8% for Ni@10Mg-Al<sub>2</sub>O<sub>3</sub>-EISA, whereas it is 7.4% for Ni@10W-10Mg-Al<sub>2</sub>O<sub>3</sub>-EISA, 6.6% for Ni@10W-10CeO<sub>2</sub>-Al<sub>2</sub>O<sub>3</sub>-EISA, 5.7% for Ni@10W-Al<sub>2</sub>O<sub>3</sub>-EISA and 4.7% for Ni@20W-Al<sub>2</sub>O<sub>3</sub>-EISA. The difference in the compositions obtained in steam reforming reaction proves the importance of water gas shift reaction in hydrogen production. The Ni<sub>4</sub>W crystal of tungsten incorporated catalysts lead to lower activity in reforming reaction with higher side product formation (CH<sub>4</sub>, C<sub>2</sub>H<sub>4</sub>, C<sub>2</sub>H<sub>6</sub>) compared to Ni@10Mg-Al<sub>2</sub>O<sub>3</sub>-EISA catalyst.

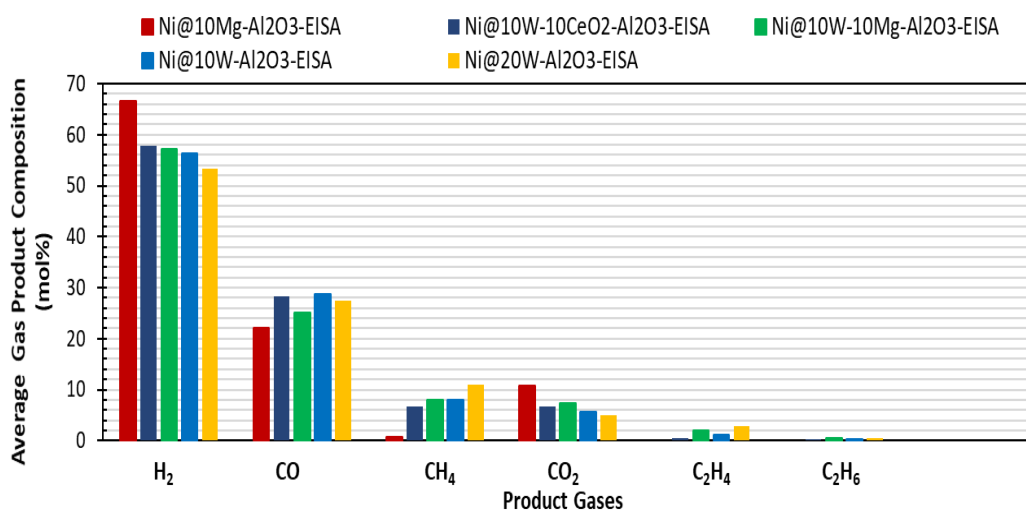


Figure 8.10. Effect of catalyst content on the average product gas composition during DSR experiments (GHSV=7500 h<sup>-1</sup>, H<sub>2</sub>O/C=2.5, 800°C).

The activities of tungsten incorporated four catalysts also differ according to their different properties. According to Figure 8.10 and Table 8.4, higher tungsten loaded

Ni@20W-Al<sub>2</sub>O<sub>3</sub>-EISA presented lower activity in reforming reaction with higher CH<sub>4</sub>, C<sub>2</sub>H<sub>4</sub>, and C<sub>2</sub>H<sub>6</sub> formation. According to their characterization results, Ni@10W-Al<sub>2</sub>O<sub>3</sub>-EISA possesses higher surface area, pore volume and lower pore diameter compared to Ni@20W-Al<sub>2</sub>O<sub>3</sub>-EISA material. TPR results also suggested the increase in the amount of nickel transformation to Ni<sub>4</sub>W with higher tungsten loading, which might have led to a decrease in reforming rate. Higher acid capacity (Table 8.2) of Ni@20W-Al<sub>2</sub>O<sub>3</sub>-EISA compared to other tungsten loaded catalysts might be another factor in its low activity due to the occurrence of cracking reactions on the acid sites. Incorporation of magnesium and ceria had a positive promoting effect on tungsten incorporated catalysts in terms of hydrogen production. Compared to the Ni@10W-Al<sub>2</sub>O<sub>3</sub>-EISA catalyst which showed a hydrogen yield value of 21.2 (maximum theoretical hydrogen yield value is 35), hydrogen yields were 21.4 and 23.0 for Ni@10W-10Mg-Al<sub>2</sub>O<sub>3</sub>-EISA and Ni@10W-10CeO<sub>2</sub>-Al<sub>2</sub>O<sub>3</sub>-EISA catalysts, respectively.

Rate of hydrogen formation per surface area of catalyst was calculated using the hydrogen production molar flow rate, catalyst amount used in the reaction and lastly surface area (Table 8.1) obtained from N<sub>2</sub> adsorption/desorption analysis, through Eq. 1 given in section 7.2.1. When the average steady state hydrogen production rate values (Table 8.4) obtained using different catalysts were compared; higher hydrogen formation rate was observed with Ni@10W-10CeO<sub>2</sub>-Al<sub>2</sub>O<sub>3</sub>-EISA compared to the Ni@10W-Al<sub>2</sub>O<sub>3</sub>-EISA and Ni@10W-10Mg-Al<sub>2</sub>O<sub>3</sub>-EISA catalysts. The presence of CeO<sub>2</sub> mainly reduced the formation of CH<sub>4</sub> and C<sub>2</sub>H<sub>4</sub> due to lower cracking activity of the catalyst caused by lower acid capacity of the material according to the NH<sub>3</sub>-TPD analysis results given in Table 8.2. It is proposed in section 4.1 that hydrocarbons with higher molecular weights in diesel are firstly cracked into C<sub>2</sub>-C<sub>3</sub> compounds which are then reformed into desired products. Cracking reactions do not take place at a higher rate compared to reforming reactions with a catalyst having low acid capacity. Thus, the formation of side products are suppressed as in the case of Ni@10W-10CeO<sub>2</sub>-Al<sub>2</sub>O<sub>3</sub>-EISA. The reducing effect of CeO<sub>2</sub> on the acid capacity of the material

was probably due to the stronger interaction of  $\text{WO}_x$  species with  $\text{CeO}_2\text{-Al}_2\text{O}_3$  surface (Figure 8.4). For  $\text{Ni@10W-10Mg-Al}_2\text{O}_3\text{-EISA}$ , enhanced  $\text{H}_2$  and  $\text{CO}_2$  and diminished  $\text{CO}$  formation suggest increased water gas shift reaction rate which can be clearly observed from the molar ratio of  $\text{CO}$  to  $\text{CO}_2$  produced given in Table 8.4. However, the reforming rate of  $\text{Ni@10W-10Mg-Al}_2\text{O}_3\text{-EISA}$  catalyst was slower compared to the  $\text{Ni@10W-Al}_2\text{O}_3\text{-EISA}$  catalyst. Slow reforming rate leads to high ethylene formation, probably due to the low surface area of the catalyst (Table 8.1).

Higher coke deposition (Table 8.4) observed in the  $\text{Ni@10Mg-Al}_2\text{O}_3\text{-EISA}$  material was probably due to the higher activity of  $\text{Ni}^0$  towards both coking and reforming reactions. Coke minimization was achieved on tungsten incorporated catalysts despite their higher acid capacity which is known for increasing coke deposition through catalyzing cracking reactions. The minimizing effect of tungsten incorporation to nickel catalysts was proven and the main carbon minimizing effect of the developed tungsten-nickel catalysts was due to the redox ability of  $\text{WO}_x$  according to Arbag et al.<sup>64</sup>. Redox reactions that occurred on the  $\text{WO}_x$  sites were responsible for coke elimination and the XRD patterns of spent catalyst presented tungsten carbide crystals formed due to  $\text{WO}_x$  reacting with the deposited coke on the catalyst surface<sup>64</sup>. Reduced coke deposition might be also due to low solubility of carbon in  $\text{Ni}_4\text{W}$  crystals<sup>98</sup>. Low solubility of carbon means that even a small presence of carbon leads to an equilibrium between the carbon and  $\text{Ni}_4\text{W}$  crystals and its carbide forms, preventing further carbon deposition. The comparison of the XRD patterns of fresh and used  $\text{Ni@10W-Al}_2\text{O}_3\text{-EISA}$  catalyst given in Figure 8.11 shows a significant change in the material crystal structure after reforming reaction. The characteristic peaks of  $\text{W}$  crystal is not observed in the XRD pattern of the used catalyst. However, the presence of the characteristic peaks of  $\text{WC}$  (PDF card No. 25-1047) are observed. The major characteristic peak of  $\text{Ni}_4\text{W}$  is still present with lower peak intensity, but  $\text{Ni}_4\text{WC}$  crystal formation was not observed for this material. The absence of  $\text{Ni}_4\text{WC}$  crystal suggests that carbon phase in the reaction zone reacted with tungsten crystals leading to the formation of tungsten carbide.

The increase of tungsten loading from 10 wt.% to 20 wt.% enhanced total acid capacity which may have caused higher ethylene formation. The increase of tungsten loading also minimized coke deposition probably due to the formation of WC crystals. The addition of CeO<sub>2</sub> together with W did not have a significant effect on the coke resistivity of the catalyst despite increasing hydrogen productivity, but the incorporation of W together with Mg slightly diminished coke deposition (Table 8.4).

Table 8.4 Activity test results of catalysts in DSR in terms of H<sub>2</sub> yield, the ratio of CO to CO<sub>2</sub> formation, produced average side product amount (in ppm), hydrogen formation rate per catalyst surface area and coke deposition (GHSV= 7500 h<sup>-1</sup>, 800 °C, H<sub>2</sub>O/C=2.5).

Catalyst	Average H <sub>2</sub> Yield ( $\frac{\text{max}^{\text{theoretical}}}{=35}$ )	$\frac{\dot{N}_{\text{CO}}}{\dot{N}_{\text{CO}_2}}$	Average Side Product Composition (ppm, molar)			Rate <sub>H<sub>2</sub></sub> (mmolH <sub>2</sub> /h.m <sub>cat</sub> <sup>2</sup> )	Coke% ( $\frac{\text{g}_{\text{coke}}}{\text{g}_{\text{used catalyst}}}$ )
			CH <sub>4</sub>	C <sub>2</sub> H <sub>4</sub>	C <sub>2</sub> H <sub>6</sub>		
Ni@10Mg-Al <sub>2</sub> O <sub>3</sub> -EISA	33.8	2.0	6000	0	0	0.65	8.7
Ni@10W-10CeO <sub>2</sub> -Al <sub>2</sub> O <sub>3</sub> -EISA	23.0	4.3	66000	5000	1800	0.94	1.2
Ni@10W-10Mg-Al <sub>2</sub> O <sub>3</sub> -EISA	21.4	3.4	80000	21000	4000	0.74	0.9
Ni@10W-Al <sub>2</sub> O <sub>3</sub> -EISA	21.2	5.0	80000	11000	2600	0.54	1.3
Ni@20W-Al <sub>2</sub> O <sub>3</sub> -EISA	18.1	5.6	109000	29000	5400	0.60	0

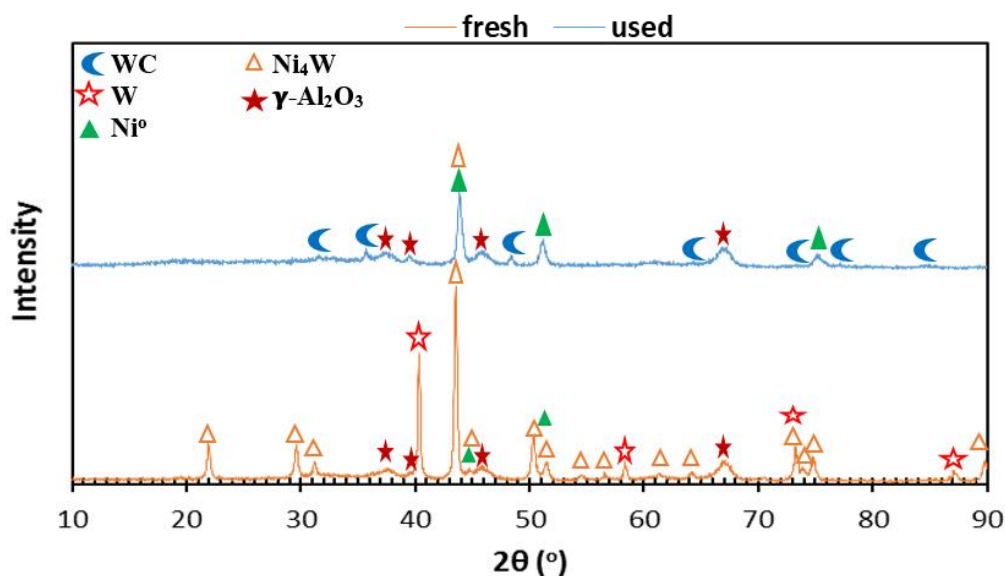


Figure 8.11. X-Ray diffraction patterns of fresh and used Ni@10W-Al<sub>2</sub>O<sub>3</sub>-EISA catalyst (6 h DSR reaction, GHSV= 7500 h<sup>-1</sup>, 800 °C, H<sub>2</sub>O/C=2.5).

### 8.2.2. The effect of Catalyst Composition on Hydrogen Production in the Diesel Autothermal Reforming Reaction

Among W, Mg, W-Mg and W-CeO<sub>2</sub> incorporated catalysts the most successful results were obtained with the Ni@10Mg-Al<sub>2</sub>O<sub>3</sub>-EISA catalyst towards the diesel steam reforming reaction (DSR). The Ni@10Mg-Al<sub>2</sub>O<sub>3</sub>-EISA and Ni@10W-10CeO<sub>2</sub>-Al<sub>2</sub>O<sub>3</sub>-EISA catalysts which showed the second highest hydrogen yield, were also tested towards the diesel autothermal reforming reaction (ATR), for comparison. The results presented in Figure 8.12 show catalytic activity test results towards both the ATR and DSR reactions for the two catalysts. Similar to the DSR results, Ni@10Mg-Al<sub>2</sub>O<sub>3</sub>-EISA showed superior performance compared to the Ni@10W-10CeO<sub>2</sub>-Al<sub>2</sub>O<sub>3</sub>-EISA catalyst in terms of hydrogen production. Lower hydrogen production was observed in the ATR test for both catalysts. Lower hydrogen composition in the gas products was expected considering the stoichiometry of the two reactions. 35 moles of hydrogen and 26.5 moles of hydrogen can be obtained from one mole of diesel (C<sub>17</sub>H<sub>36</sub>) in DSR and ATR reactions, respectively. Higher CO<sub>2</sub> production observed

(Figure 8.12) in the ATR was probably caused by oxidation of carbon containing compounds at high operating temperatures.

The thermogravimetric analysis (TGA) of used catalysts in the ATR reaction showed that coke deposition was 2.3 wt.% for Ni@10W-10CeO<sub>2</sub>-Al<sub>2</sub>O<sub>3</sub>-EISA and 13.2 wt.% for Ni@10Mg-Al<sub>2</sub>O<sub>3</sub>-EISA. Figure 8.13 shows the comparison of coke depositions obtained after DSR and ATR for the Ni@10Mg-Al<sub>2</sub>O<sub>3</sub>-EISA catalyst. Higher coke formation observed after the autothermal reforming reaction (12.3 wt.%) compared to the diesel steam reforming reaction (8.7 wt.%, Table 8.4) was due to the presence of higher amounts of side products (methane and ethylene) which induce coke deposition. Moreover, the type of coke deposited differs in two reactions according to the TGA and DTA results given in Figure 8.13. Amorphous and filamentous carbon is expected to be oxidized at temperatures below 550°C, whereas more stable graphitized carbon is expected to be oxidized at higher temperatures during TGA analysis. DTA results of used catalysts show major oxidation peaks located at the graphitic carbon region for both materials. The DTA result of the catalyst that was used in the DSR test also shows a minor peak located at 540 °C that could be due to filamentous carbon oxidation. Higher oxidation temperature observed after the diesel steam reforming (688 °C) compared to the oxidation temperature obtained after the autothermal reforming reaction (651 °C) indicates higher degree of graphitization of the deposited coke<sup>113</sup>.

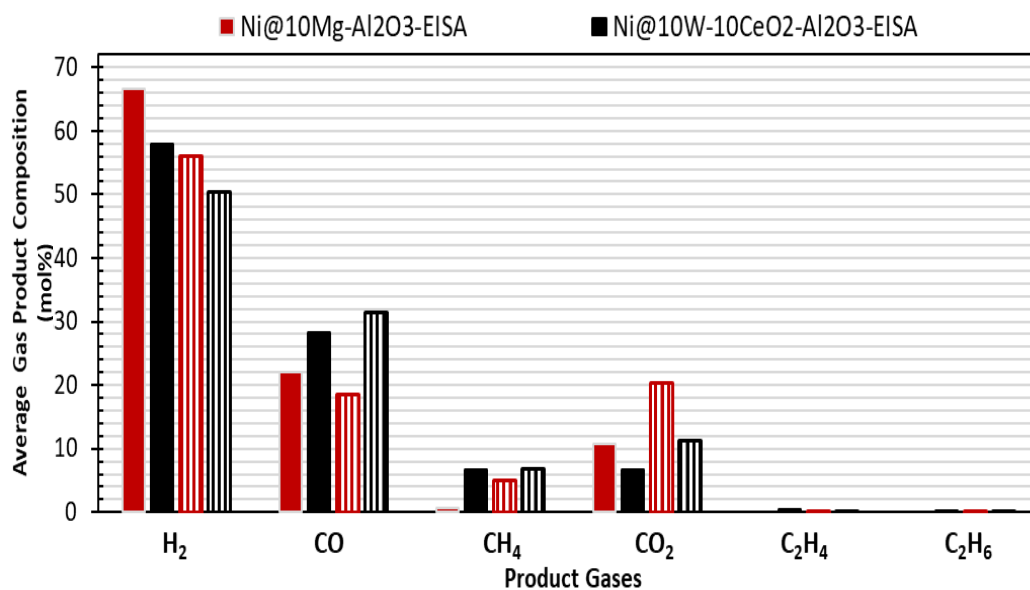


Figure 8.12. Comparison of average gas product composition obtained from the DSR reaction and the ATR reaction in the presence of Ni@10Mg-Al<sub>2</sub>O<sub>3</sub>-EISA and Ni@10W-10CeO<sub>2</sub>@Al<sub>2</sub>O<sub>3</sub>-EISA catalysts (GHSV=7500 h<sup>-1</sup>, H<sub>2</sub>O/C=2.5, O<sub>2</sub>/C=0.5 (ATR), 800°C) (Filled bar: DSR, Striped bar: ATR).

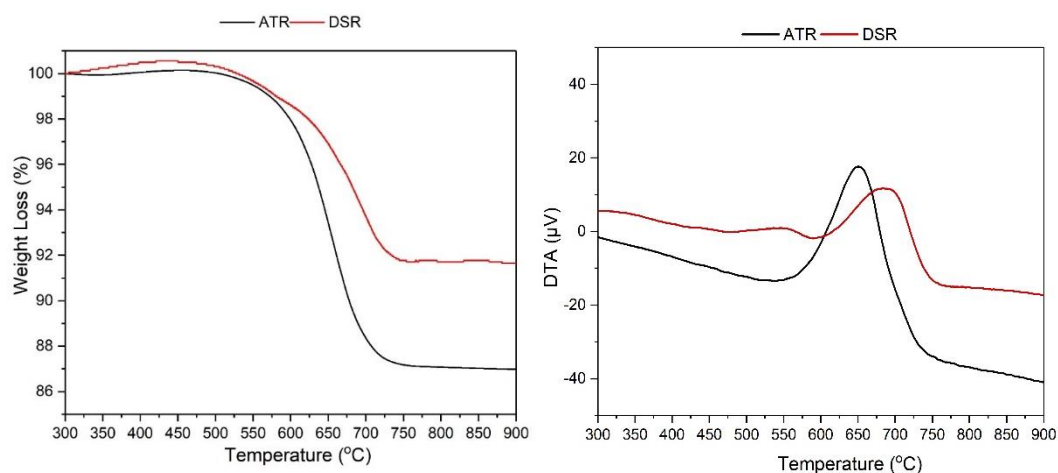


Figure 8.13. Coke deposition comparison of Ni@10Mg-Al<sub>2</sub>O<sub>3</sub>-EISA catalyst after the DSR and ATR reactions.

### 8.2.3. Long Term Diesel Steam Reforming Test Results with the Ni@10Mg-Al<sub>2</sub>O<sub>3</sub>-EISA Catalyst

In order to observe the effect of coke deposition on the catalytic activity of Ni@10Mg-Al<sub>2</sub>O<sub>3</sub>-EISA catalyst in the steam reforming reaction, a long term DSR reaction was conducted at a reaction time of 54 h. During the activity test, activity loss or the C<sub>2</sub> products formation were not observed (Figure 8.14). The average hydrogen yield was around 33.9 (theoretical maximum hydrogen yield value is 35.0). There was no indication of any hydrocarbon in the liquid sample collected after the long term experiment. Considering these results, in addition to significant hydrogen production success obtained with the Ni@10Mg-Al<sub>2</sub>O<sub>3</sub>-EISA catalyst, complete diesel conversion was also achieved during the 54 h of experiment.

Figure 8.15 also shows hydrogen yield and the molar ratio of side products to diesel feed with respect to time. Other than some fluctuation observed due to experimental errors, catalyst showed stable activity throughout the reaction. Thermogravimetric analysis conducted on samples taken from two different parts of the used catalyst after the 54 h reaction period showed coke depositions as 6 wt.% and 7.5 wt.%. Weight loss during the thermogravimetric analysis occurred at a temperature range of 450-700 °C, indicating the presence of both filamentous carbon which is generally oxidized below 550 °C and graphitic carbon that can be oxidized at higher temperatures according to the degree of graphitization of coke deposits<sup>51,113</sup>. As given in Table 8.4, the previous analysis conducted on the sample of six hours DSR reaction experiment resulted in 33.8, close to the maximum theoretical hydrogen yield value, and 8.7 wt.% coke deposition. Approximately the same value indicates that coke deposition might be occurring during the initial stages of the reaction. For both six and fifty four hours of reaction times, coke deposition amounts were close to each other and there was no significant change in the remaining reaction time.

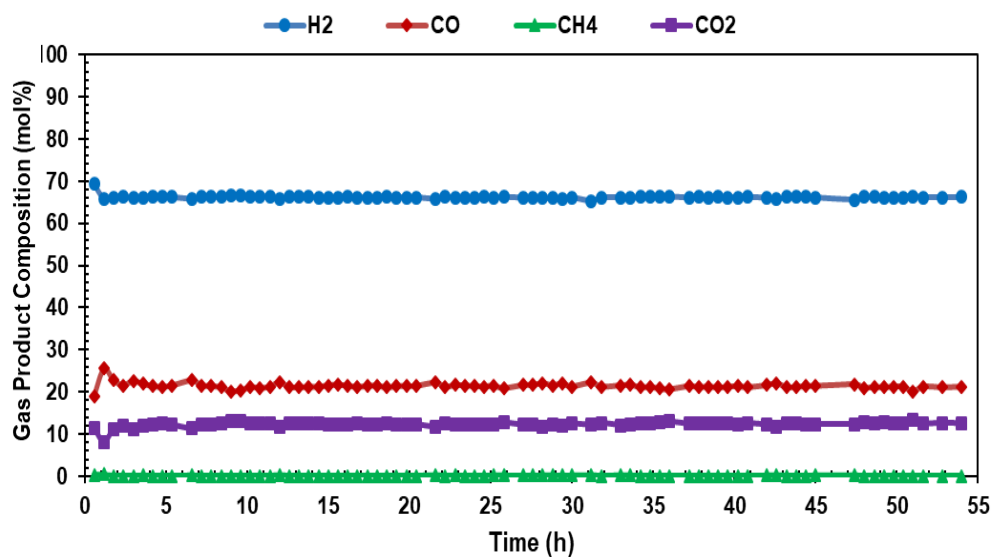


Figure 8.14. Long term Ni@10Mg-Al<sub>2</sub>O<sub>3</sub>-EISA activity test result in the DSR reaction (GHSV=7500 h<sup>-1</sup>, H<sub>2</sub>O/C=2.5, 800°C).

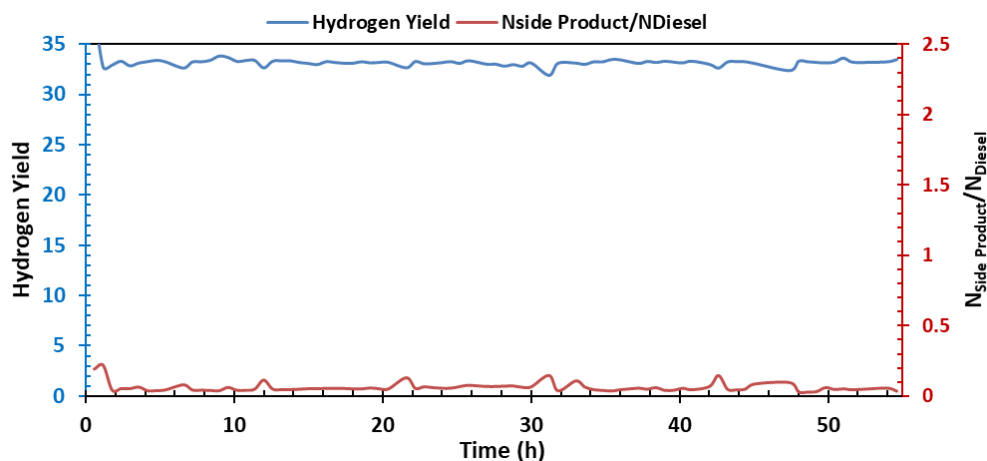


Figure 8.15. Long-term Ni@10Mg-Al<sub>2</sub>O<sub>3</sub>-EISA activity test result in the DSR reaction in terms of hydrogen yield and molar side product formation to diesel (GHSV= 7500 h<sup>-1</sup>, 800 °C, H<sub>2</sub>O/C=2.5).

Scanning and backscattering electron detector images of the used Ni@10Mg-Al<sub>2</sub>O<sub>3</sub>-EISA, long term used Ni@10Mg-Al<sub>2</sub>O<sub>3</sub>-EISA catalysts were presented in Figure 8.16. The used Ni@10Mg-Al<sub>2</sub>O<sub>3</sub>-EISA material presented a more homogeneous surface (Figure 8.16-A&B) compared to the fresh material (Figure 8.8).

XRD pattern of Ni@10Mg-Al<sub>2</sub>O<sub>3</sub>-EISA material showed the presence of NiO, Ni<sup>0</sup>, and Mg-Al spinel crystals in Figure 8.3. Crystal size calculated for Ni<sup>0</sup> crystal was about 12 nm. The size range of particles, that might be nickel, visible on the surface are 60 and 80 nm. The image given in Figure 8.16-C for the used Ni@10Mg-Al<sub>2</sub>O<sub>3</sub>-EISA material shows carbon whisker/nanotube type material formation with the thicknesses in the range of 40-70 nm. Tip growth mechanism for carbon nanotubes was observed and Ni particle with a size of 110 nm can be seen at the top of the carbon whiskers. Ni particles may act as a catalyst for the growth of nanotubes.

Images D and E in Figure 8.16 show scanning electron detector images, and image F shows backscattering detector image of the Ni@10Mg-Al<sub>2</sub>O<sub>3</sub>-EISA material after long term activity test. Agglomerated nickel clusters that have sizes in the range of 10-90 nm are visible in these images. A carbon whisker (orange circle) with a diameter of 20 nm is also captured and can be seen in Figure 8.16-E&F. Figure 8.17 show scanning electron detector and backscattering detector images of Ni@10W-Al<sub>2</sub>O<sub>3</sub>-EISA material after activity test. Carbon fiber with about 50 nm diameter was also observed for the used Ni@10W-Al<sub>2</sub>O<sub>3</sub>-EISA catalyst. The most bright dots on the backscattering electron detector (Figure 8.17-B) image indicate the presence of particles with higher molecular weights. The bright particles which can be clearly observed in Figure 8.17-B suggest the presence of W or Ni<sub>4</sub>W particles/clusters (90 nm). Observed agglomerated large W or Ni<sub>4</sub>W particles/clusters are similar to those observed on the SEM image of the fresh material.

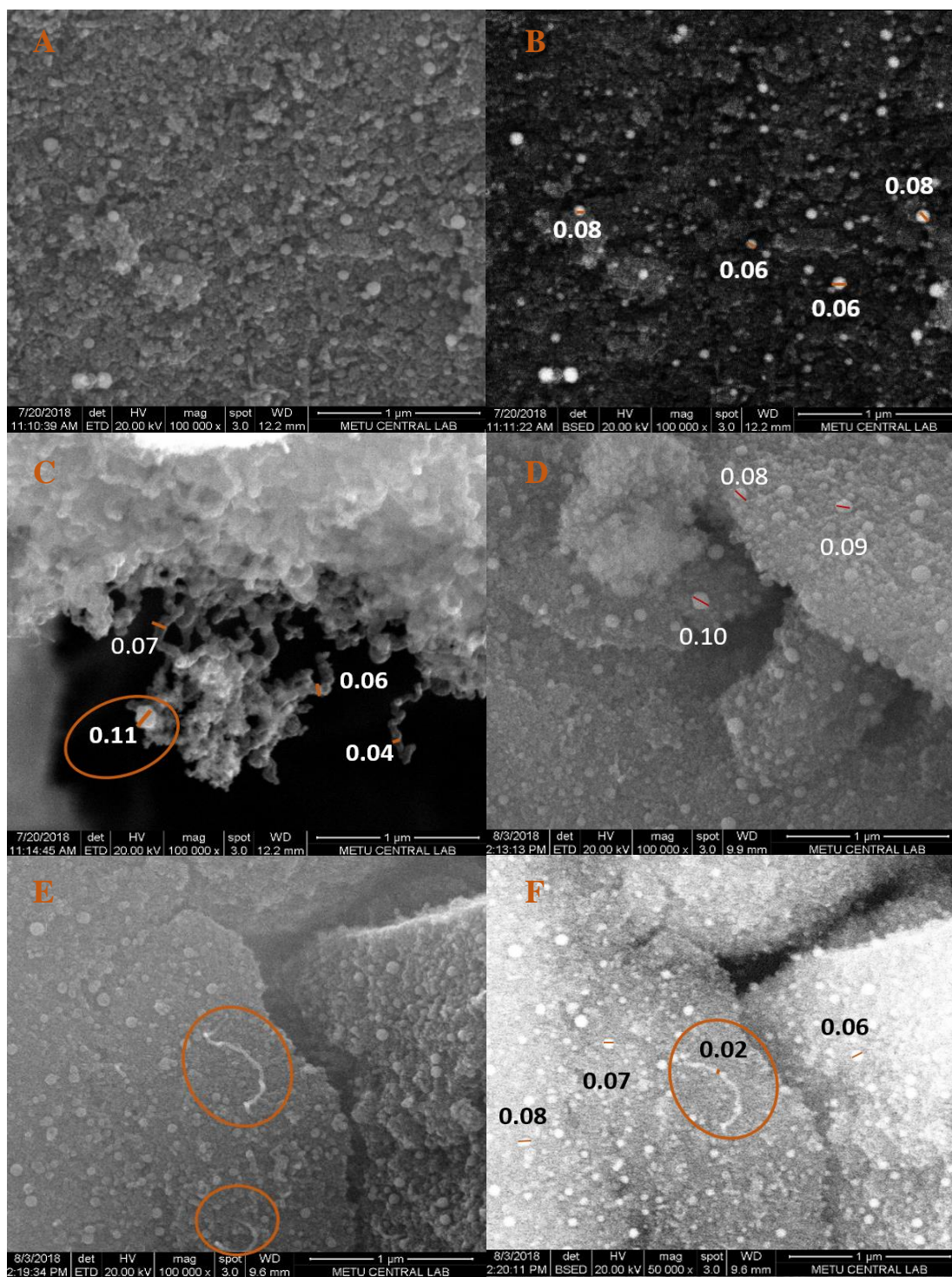


Figure 8.16. Scanning electron detector images of used catalysts A, C) Ni@10Mg-Al<sub>2</sub>O<sub>3</sub>-EISA, D, E) Long Term Ni@10Mg-Al<sub>2</sub>O<sub>3</sub>-EISA, and backscattering electron detector image of B) Ni@10Mg-Al<sub>2</sub>O<sub>3</sub>-EISA, and F) Long Term Ni@10Mg-Al<sub>2</sub>O<sub>3</sub>-EISA (Magnification: 100000, and the scale: 1 μm).

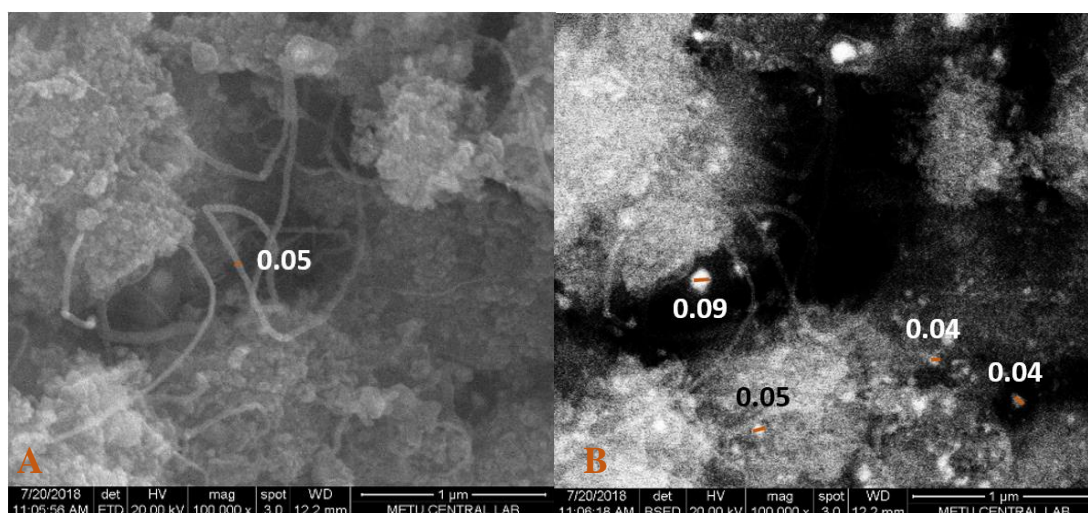


Figure 8.17. SEM images of used Ni@10W-Al<sub>2</sub>O<sub>3</sub>-EISA catalyst: A) scanning electron detector, B) backscattering electron detector (Magnification: 100000, and the scale: 1 μm).

As mentioned in the SEM results of the used catalyst, there is no significant change in the surface of the Ni@10Mg-Al<sub>2</sub>O<sub>3</sub>-EISA material after the DSR reaction, except for whisker type carbon formation. This observation was also confirmed by N<sub>2</sub> adsorption/desorption analysis results (Figure 8.18). Other than slight decrease in pore volume, and tightening of the pore size distribution caused by blockage of pores by coke deposition, the type of the isotherm and hysteresis loop can still be identified as Type 4 and H1, respectively. Microporosity percent in the long term used Ni@10Mg-Al<sub>2</sub>O<sub>3</sub>-EISA catalyst is 9.9, which was 8.1 for fresh catalyst. This indicates that coke deposition blocked some mesopores and lead to transformation of mesopores to micropores. This also suggests that the reactions leading to coke deposition including cracking and diesel steam reforming reactions might have took place in the mesopores of the Ni@10Mg-Al<sub>2</sub>O<sub>3</sub>-EISA catalyst. XRD pattern of the used catalyst (Figure 8.19) presented the formation of carbon deposition. The presence of characteristic NiO peaks were not observed after the long term experiment which were reduced during the reforming experiment.

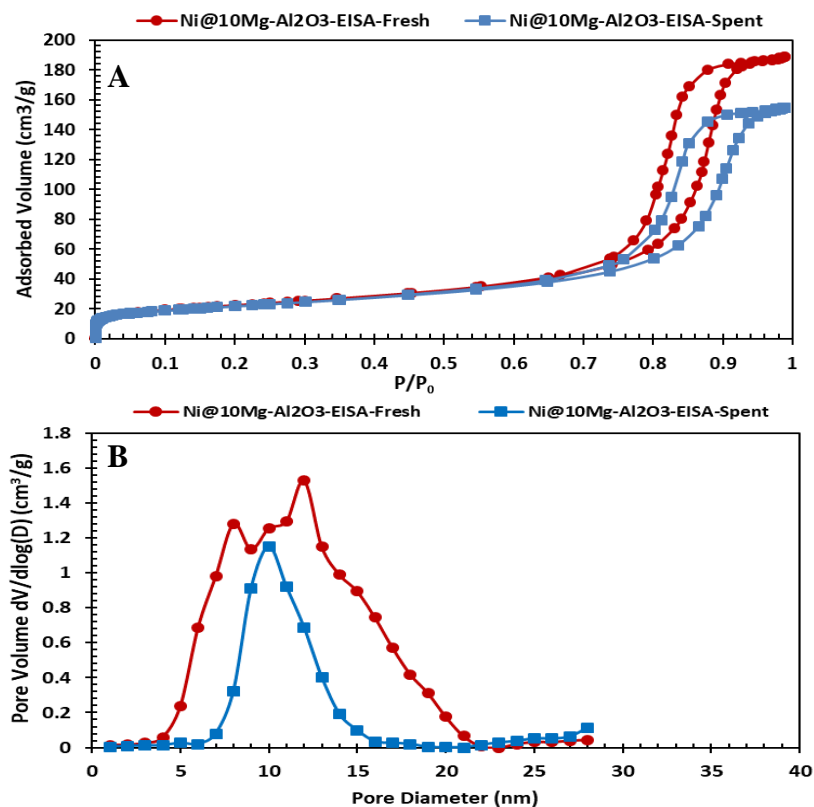


Figure 8.18. N<sub>2</sub> adsorption/desorption isotherms (A) and pore size distributions (B) of fresh and used in long term DSR activity test (Ni@10Mg-Al<sub>2</sub>O<sub>3</sub>-EISA).

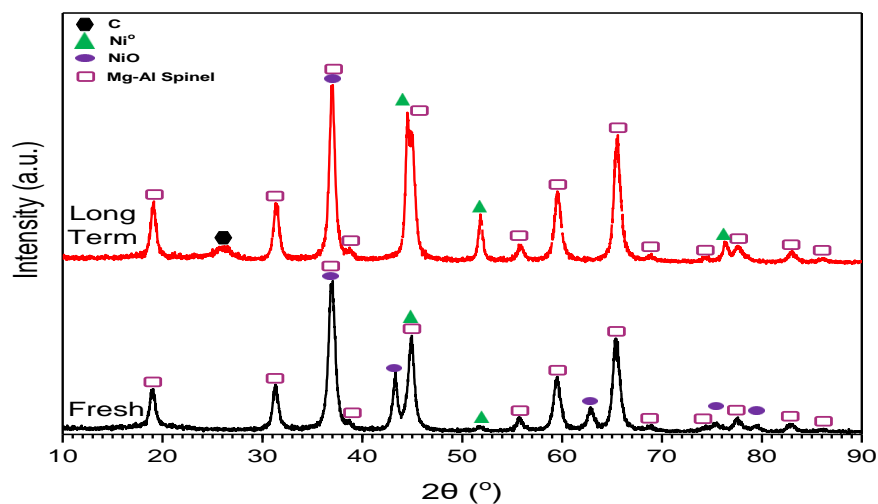


Figure 8.19 XRD patterns of fresh and used Ni@10Mg-Al<sub>2</sub>O<sub>3</sub>-EISA catalyst in long term DSR activity test.

TEM images of Ni@10Mg-Al<sub>2</sub>O<sub>3</sub>-EISA catalyst that was used in the long term DSR reaction are presented in Figure 8.20. Figure 8.20-A shows crystalline and non-crystalline material structures. The circled dark sphere type materials do not present a crystalline structure which might be due to the thickness of corresponding zone or the nature of those materials. Besides dark regions which might be due to an impurity or the presence of nickel on support surface, the surface is crystalline with clear diffraction lines. Crystalline surfaces also present some differences which can be more clearly seen in Figure 8.20-B. The diffraction lines of number 1 surface are clearly distinct and different from the other marked surfaces (2, 3 and 4) and resembles to nanotube or graphene sheet formation. However, the distance between the lines is about 0.15 nm in average, and the wall thickness of the lines is about 0.16 nm in average. Thus the surface marked with number 1 might not be graphene since the single-crystal graphite thickness is 0.335 nm and interlayer spacing in graphite is 0.34<sup>110</sup>. Considering the diameter of nickel, aluminum and magnesium atoms which are 0.16, 0.14 and 0.17, the diffraction lines might belong to nickel, aluminum or magnesium. Surfaces marked with number 2 and 3 given in Figure 8.20-B and surfaces marked with number 1 given in Figure 8.20-C could be also due to Ni<sup>0</sup>, NiAl<sub>2</sub>O<sub>4</sub>, Mg-Al spinel or carbon structures which was observed in the XRD patterns of used catalysts (Figure 8.19). The distance between the lines given on the surface marked with number 2 in Figure 8.20-C is about 0.2 nm in average, and the wall thickness of the lines is about 0.2 nm in average. The values also suggest that the diffraction lines might belong to nickel, aluminum or magnesium. Detached nickel (1) with a particle size of 12 nm from the catalyst can be seen in Figure 8.20-D probably as a result of tip growth mechanism of carbon nanotubes (2). Detachment of nickel particle is also observed on the SEM image of used material (Figure 8.16) and nickel crystal size according to the XRD pattern (Figure 8.3) and Scherrer equation is also about 12 nm.

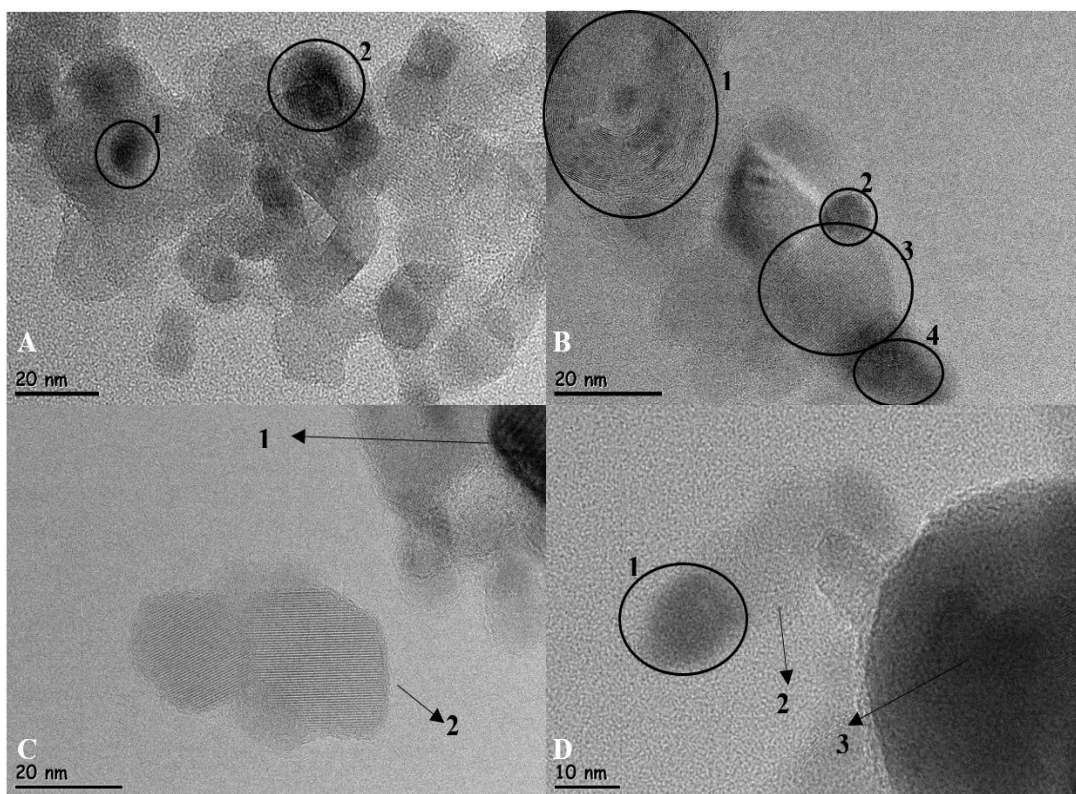


Figure 8.20. TEM images of long term used Ni@10Mg-Al<sub>2</sub>O<sub>3</sub>-EISA catalyst in DSR reaction.



## CHAPTER 9

### DETERMINATION OF THE BEST CATALYST AMONG THE SYNTHESIZED CATALYSTS FOR THE ATR AND DSR

The aim of this thesis was to determine the most effective catalyst promoter for Ni/Al<sub>2</sub>O<sub>3</sub> catalysts towards diesel reforming reaction. For this reason, several promoters were selected and tested in a laboratory scale diesel reforming experimental test set-up. Two type of catalysts were studied in scope of this thesis; commercial Al<sub>2</sub>O<sub>3</sub> supported metal/metal oxide impregnated catalysts and mesoporous metal/metal oxide-Al<sub>2</sub>O<sub>3</sub> catalysts that were synthesized through “evaporation induced self-assembly method” as a one-pot approach. The resulting support materials were impregnated with 10 wt.% nickel.

The performances of synthesized catalysts (both commercial Al<sub>2</sub>O<sub>3</sub> supported and synthesized through EISA method) are presented in Figure 9.1 in terms of average hydrogen yield values and coke deposition measured after six hour DSR tests. According to Figure 9.1, the highest coke deposition with the lowest hydrogen yield was obtained with the 1.5Ru@20CeO<sub>2</sub>@Al<sub>2</sub>O<sub>3</sub> catalyst. Nickel impregnated and W incorporated commercial Al<sub>2</sub>O<sub>3</sub> supported and EISA catalysts presented lower hydrogen yield and lower coke deposition compared to other nickel impregnated catalysts. Comparison of Ni@Al<sub>2</sub>O<sub>3</sub> and Ni@Al<sub>2</sub>O<sub>3</sub>-EISA catalyst presents that EISA catalyst had lower coke deposition which indicates higher success in the DSR reaction. Ruthenium incorporation to commercial Al<sub>2</sub>O<sub>3</sub> above 1 wt.% resulted in a similar hydrogen yield and coke deposition as the Ni@Al<sub>2</sub>O<sub>3</sub> catalyst. However, 0.5 wt.% Ru impregnated Ni@0.5Ru@Al<sub>2</sub>O<sub>3</sub> catalyst showed higher hydrogen yield and lower coke deposition compared to the Ni@Al<sub>2</sub>O<sub>3</sub> catalyst. 20 wt.% CeO<sub>2</sub> impregnated EISA catalyst showed lower hydrogen yield and higher coke deposition compared to the Ni@Al<sub>2</sub>O<sub>3</sub>, catalyst synthesized with 20 wt.% CeO<sub>2</sub> by one-pot method, and 20 wt.% CeO<sub>2</sub> impregnated commercial Al<sub>2</sub>O<sub>3</sub> supported catalyst. Incorporation of 10 wt.%

CeO<sub>2</sub> to both commercial Al<sub>2</sub>O<sub>3</sub> (impregnation) and EISA Al<sub>2</sub>O<sub>3</sub> (one-pot) showed higher hydrogen yield compared to other CeO<sub>2</sub> incorporated catalysts. Ni@10CeO<sub>2</sub>-Al<sub>2</sub>O<sub>3</sub>-EISA catalyst also showed lower coke deposition along with its higher hydrogen yield.

When the DSR test results of four sections were analyzed, it can be seen that the most successful catalysts in those sections are: Ni@10CeO<sub>2</sub>@Al<sub>2</sub>O<sub>3</sub>, Ni@0.5Ru@Al<sub>2</sub>O<sub>3</sub>, Ni@10CeO<sub>2</sub>-Al<sub>2</sub>O<sub>3</sub>-EISA, Ni@8CeO<sub>2</sub>-2ZrO<sub>2</sub>-Al<sub>2</sub>O<sub>3</sub>-EISA, and Ni@10Mg-Al<sub>2</sub>O<sub>3</sub>-EISA. Figure 9.1 clearly indicates the success of Ni@0.5Ru@Al<sub>2</sub>O<sub>3</sub>, Ni@8CeO<sub>2</sub>-2ZrO<sub>2</sub>-Al<sub>2</sub>O<sub>3</sub>-EISA, Ni@10CeO<sub>2</sub>-Al<sub>2</sub>O<sub>3</sub>-EISA, and Ni@10Mg-Al<sub>2</sub>O<sub>3</sub>-EISA catalysts in terms of hydrogen yield over all synthesized catalysts. In terms of coke deposition, the most successful catalysts with the lowest coke deposition values are; Ni@8CeO<sub>2</sub>-2ZrO<sub>2</sub>-Al<sub>2</sub>O<sub>3</sub>-EISA, Ni@10W-10CeO<sub>2</sub>@Al<sub>2</sub>O<sub>3</sub>, and Ni@20W@Al<sub>2</sub>O<sub>3</sub>. Considering both the success in hydrogen yield and coke deposition values, the most successful catalyst within this study appears to be Ni@8CeO<sub>2</sub>-2ZrO<sub>2</sub>-Al<sub>2</sub>O<sub>3</sub>-EISA. However, section 7 showed that even though the hydrogen production and coke deposition over Ni@8CeO<sub>2</sub>-2ZrO<sub>2</sub>-Al<sub>2</sub>O<sub>3</sub>-EISA is promising, the gas product results during six hour DSR test was unstable. The next best result in terms of hydrogen yield and coke deposition after Ni@8CeO<sub>2</sub>-2ZrO<sub>2</sub>-Al<sub>2</sub>O<sub>3</sub>-EISA catalyst was obtained with the Ni@10CeO<sub>2</sub>-Al<sub>2</sub>O<sub>3</sub>-EISA catalyst. Considering both hydrogen yield and coke deposition values of six hour and long term DSR tests, Ni@10CeO<sub>2</sub>-Al<sub>2</sub>O<sub>3</sub>-EISA catalyst is selected as the best performing catalyst also considering its stability.

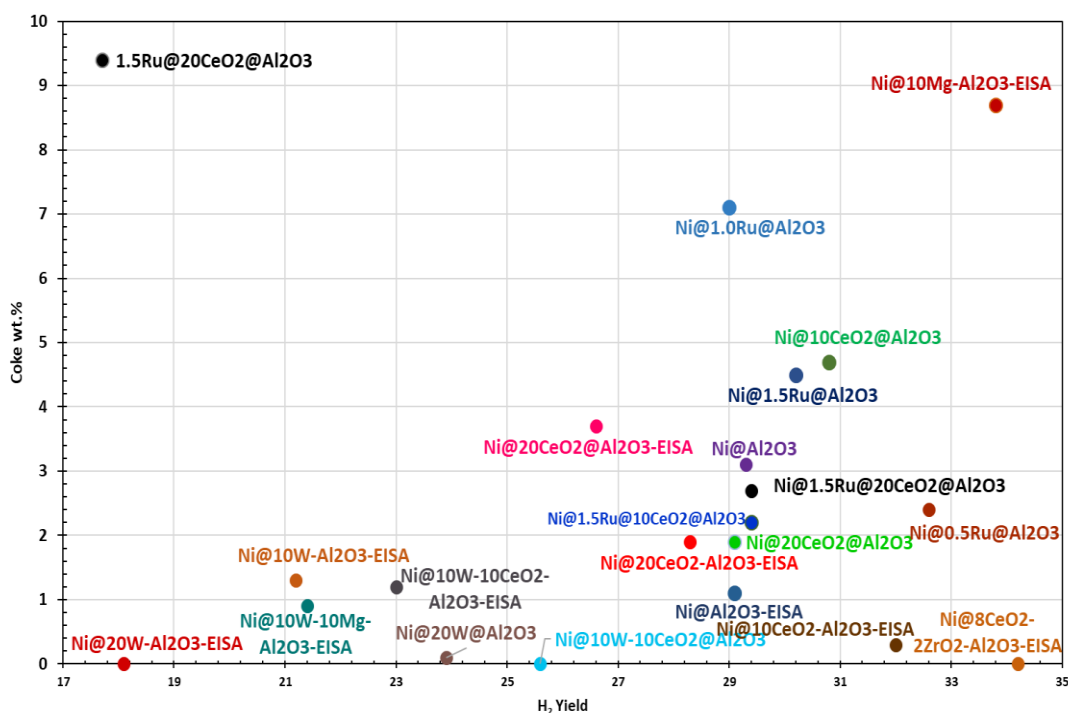


Figure 9.1. Performance of synthesized catalysts in the DSR reaction (GHSV= 7500 h<sup>-1</sup>, 800 °C, H<sub>2</sub>O/C=2.5).

Performances of selected catalysts are presented in Figure 9.2 in terms of average hydrogen yield values and coke deposition measured after six hour ATR tests. According to Figure 9.2, the highest hydrogen yield was obtained with the Ni@10CeO<sub>2</sub>-Al<sub>2</sub>O<sub>3</sub>-EISA catalyst. Ni@8CeO<sub>2</sub>-2ZrO<sub>2</sub>-Al<sub>2</sub>O<sub>3</sub>-EISA and Ni@0.5Ru@Al<sub>2</sub>O<sub>3</sub> catalysts presented similar hydrogen yield, but higher coke deposition in the ATR reaction compared to Ni@10CeO<sub>2</sub>-Al<sub>2</sub>O<sub>3</sub>-EISA catalyst. Ni@10W-10CeO<sub>2</sub>@Al<sub>2</sub>O<sub>3</sub> showed even lower success compared to the other synthesized catalysts in ATR compared to DSR reaction.

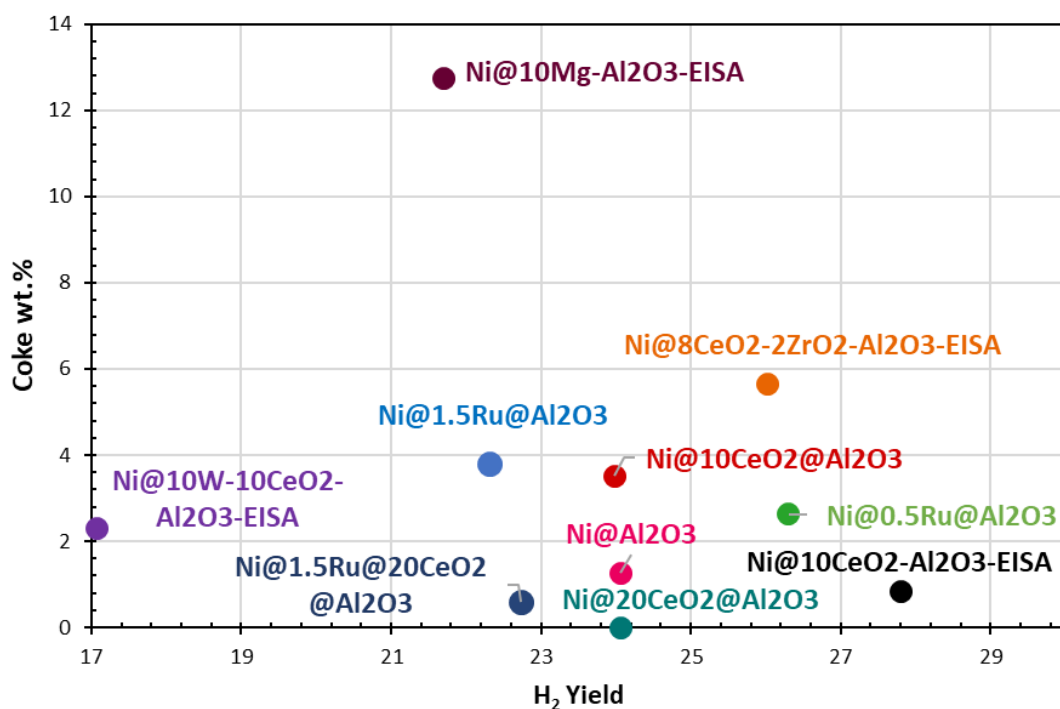


Figure 9.2. Performance of synthesized catalysts in the ATR reaction (GHSV= 7500 h<sup>-1</sup>, 800 °C, H<sub>2</sub>O/C=2.5, O<sub>2</sub>/C=0.5).

The differences in the activities of the catalysts are directly related to different physical and chemical properties of the catalysts. Characterization results were presented in detail in the result section for each catalyst group. The major properties that influence the catalytic activities significantly other than the amount and the type of promoter are: surface area, total acid capacity, crystalline type & size and reducibility. In order to eliminate the effect of some of these properties and to understand the effect of promoter better, the reaction rates in DSR were normalized with respect to surface area and acid capacities of materials. However, since material properties affect the activity of the catalysts, comparison of all catalysts in terms of normalized rate will not be correct. For this reason, the normalized rates that show the comparison in minimum error were given and other properties were discussed by using the characterization results given in the result section of each chapter.

Figure 9.3 shows the coke deposition with respect to reaction rate in terms of hydrogen production rate per mass of catalyst (mmol/h.g<sub>catalyst</sub>, Figure 9.3-A),

hydrogen production rate per surface area of catalyst ( $\text{mmol/h.m}^2_{\text{catalyst}}$ , Figure 9.3-B) and hydrogen production rate per acid capacity of catalyst ( $\text{mmol/h.mmol}_{\text{acid sites}}$ , Figure 9.3-C) for ceria and tungsten incorporated commercial alumina supported catalysts. Similar to coke deposition and hydrogen yield results of ceria and tungsten incorporated commercial alumina supported catalysts given in Figure 9.1, the highest hydrogen production rate per mass of catalyst was observed with 10 wt.%  $\text{CeO}_2$  incorporated material ( $\text{Ni@10CeO}_2@\text{Al}_2\text{O}_3$ ), followed by  $\text{Ni@Al}_2\text{O}_3$  and 20 wt.%  $\text{CeO}_2$  incorporated material (Figure 9.3-A). Lowest coke deposition was observed with  $\text{Ni@20W@Al}_2\text{O}_3$  and  $\text{Ni@10W-10CeO}_2@\text{Al}_2\text{O}_3$ . Since rate presented in Figure 9.3-A does not involve the effect of material properties, it presents that the  $\text{Ni@Al}_2\text{O}_3$  is better in terms of hydrogen production compared to all tungsten/ceria incorporated materials. The importance of surface area can be observed when the results given in Figure 9.3-A are compared to the results given in Figure 9.3-B which are in terms of hydrogen production rate per surface area of catalyst. According to Figure 9.3-B, the highest hydrogen rate with the lowest coke deposition belongs to the  $\text{Ni@10W-10CeO}_2@\text{Al}_2\text{O}_3$  catalyst. The  $\text{Ni@Al}_2\text{O}_3$  catalyst is not successful compared to promoter incorporated materials when the effect of surface area is eliminated. Similarly,  $\text{Ni@10CeO}_2@\text{Al}_2\text{O}_3$  is not superior to  $\text{Ni@20CeO}_2@\text{Al}_2\text{O}_3$  and the two catalysts showed almost the same rate when the effect of surface area of  $\text{Ni@10CeO}_2@\text{Al}_2\text{O}_3$  is eliminated. With similar activity, it can be concluded that higher  $\text{CeO}_2$  loading is beneficial for  $\text{Ni/Al}_2\text{O}_3$  catalysts since it decreases coke deposition. Among these five catalysts, when synthesized with a method leading to much higher surface area,  $\text{Ni@10W-10CeO}_2@\text{Al}_2\text{O}_3$  would have a significant activity in the diesel steam reforming reaction. The effect of material acidity was also analyzed by normalizing the rate result with respect to total acid capacity obtained from  $\text{NH}_3$ -TPD analysis. It can be seen from Figure 9.3-C that the order of catalyst performance among these five catalyst does not change when compared to hydrogen production rate per mass of catalyst (Figure 9.3-A), except for  $\text{Ni@Al}_2\text{O}_3$ . It can be inferred that the catalytic activity of  $\text{Ni@Al}_2\text{O}_3$  is partly coming from its high acidity that probably enhanced cracking reactions.

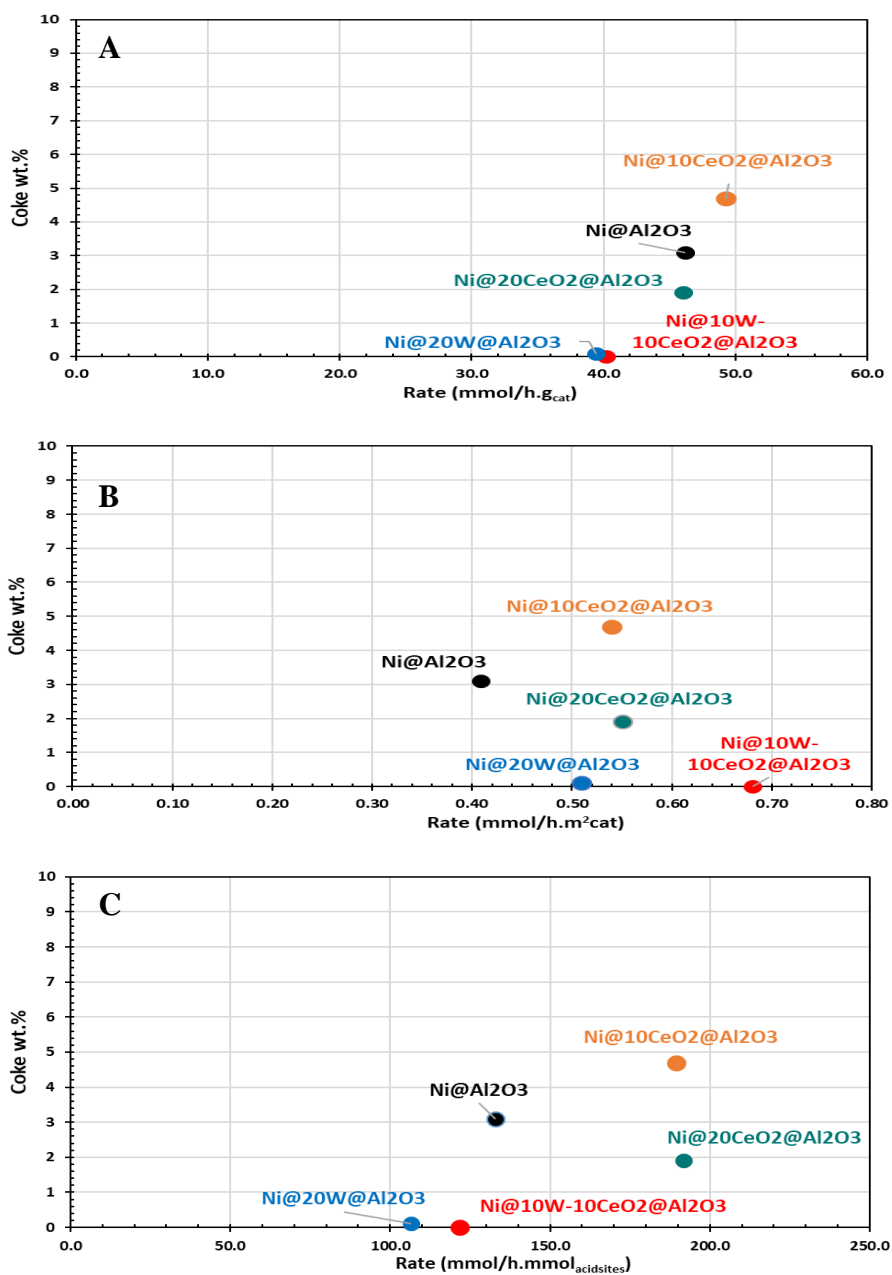


Figure 9.3. Hydrogen formation rate and coke deposition results of synthesized commercial  $\text{Al}_2\text{O}_3$  supported W and/or  $\text{CeO}_2$  incorporated catalysts in the DSR reaction: A) Hydrogen production rate per mass of catalyst ( $\text{mmol/h.g}_{\text{catalyst}}$ ), B) Hydrogen production rate per surface area of catalyst ( $\text{mmol/h.m}^2_{\text{catalyst}}$ ), and C) Hydrogen production rate per acid capacity of catalyst ( $\text{mmol/h.mmol}_{\text{acid sites}}$ ), ( $\text{GHSV} = 7500 \text{ h}^{-1}$ ,  $800 \text{ }^\circ\text{C}$ ,  $\text{H}_2\text{O}/\text{C} = 2.5$ ).

Figure 9.4 shows the coke with respect to hydrogen production rate per mass of catalyst ( $\text{mmol/h.g}_{\text{catalyst}}$ , A), hydrogen production rate per surface area of catalyst ( $\text{mmol/h.m}^2_{\text{catalyst}}$ , B) for ruthenium and ceria incorporated catalysts. The catalyst that does not contain any nickel has the lowest rate result in both graphs. While the Ni@0.5Ru@Al<sub>2</sub>O<sub>3</sub> catalyst has the highest rate in Figure 9.4-A, the normalized rate obtained using the material is lower compared to 1.5 wt.% Ru loaded one indicating 0.5 wt.% loading lead to higher surface area which is the main property that affects the catalytic activity for Ru loaded materials. 0.5 wt.% Ru loaded material has lower normalized reaction rate compared to 10 wt.% and 20 wt.% CeO<sub>2</sub> loaded materials. The highest hydrogen production rate per surface area was observed with Ni@1.5Ru@20CeO<sub>2</sub>@Al<sub>2</sub>O<sub>3</sub> that has the highest total metal loading amount.



(Ni@20CeO<sub>2</sub>-Al<sub>2</sub>O<sub>3</sub>-EISA and Ni@20CeO<sub>2</sub>@Al<sub>2</sub>O<sub>3</sub>-EISA) and tungsten incorporated materials lead to lower rate results. In order to eliminate the effect of surface area and total acid capacity from the performance of the catalysts, Figure 9.5-B and Figure 9.5-C can be observed, respectively. Figure 9.5-B presents that the high activity of magnesium incorporated material was due to its high surface area. Hydrogen production rate per surface area of Ni@8CeO<sub>2</sub>-2ZrO<sub>2</sub>-Al<sub>2</sub>O<sub>3</sub>-EISA is the highest among all materials. The Ni@Al<sub>2</sub>O<sub>3</sub>-EISA catalyst has the lowest hydrogen production rate per surface area value. Results also show that the increase of tungsten loading enhances rate and also diminishes coke formation. Incorporation of tungsten together with ceria or magnesium also enhanced both the rate and coke resistivity. When only ceria incorporated materials are analyzed in terms of their rates, it can be seen that increase of ceria loading enhances rate, but the addition of ceria by impregnation method instead of one-pot synthesis decreases the hydrogen production rate per surface area. Figure 9.5-C shows that Ni@10Mg-Al<sub>2</sub>O<sub>3</sub>-EISA and Ni@20CeO<sub>2</sub>@Al<sub>2</sub>O<sub>3</sub>-EISA catalysts which have the lowest acid capacity values among EISA catalysts have higher hydrogen production rate per acid capacity compared to other catalysts.

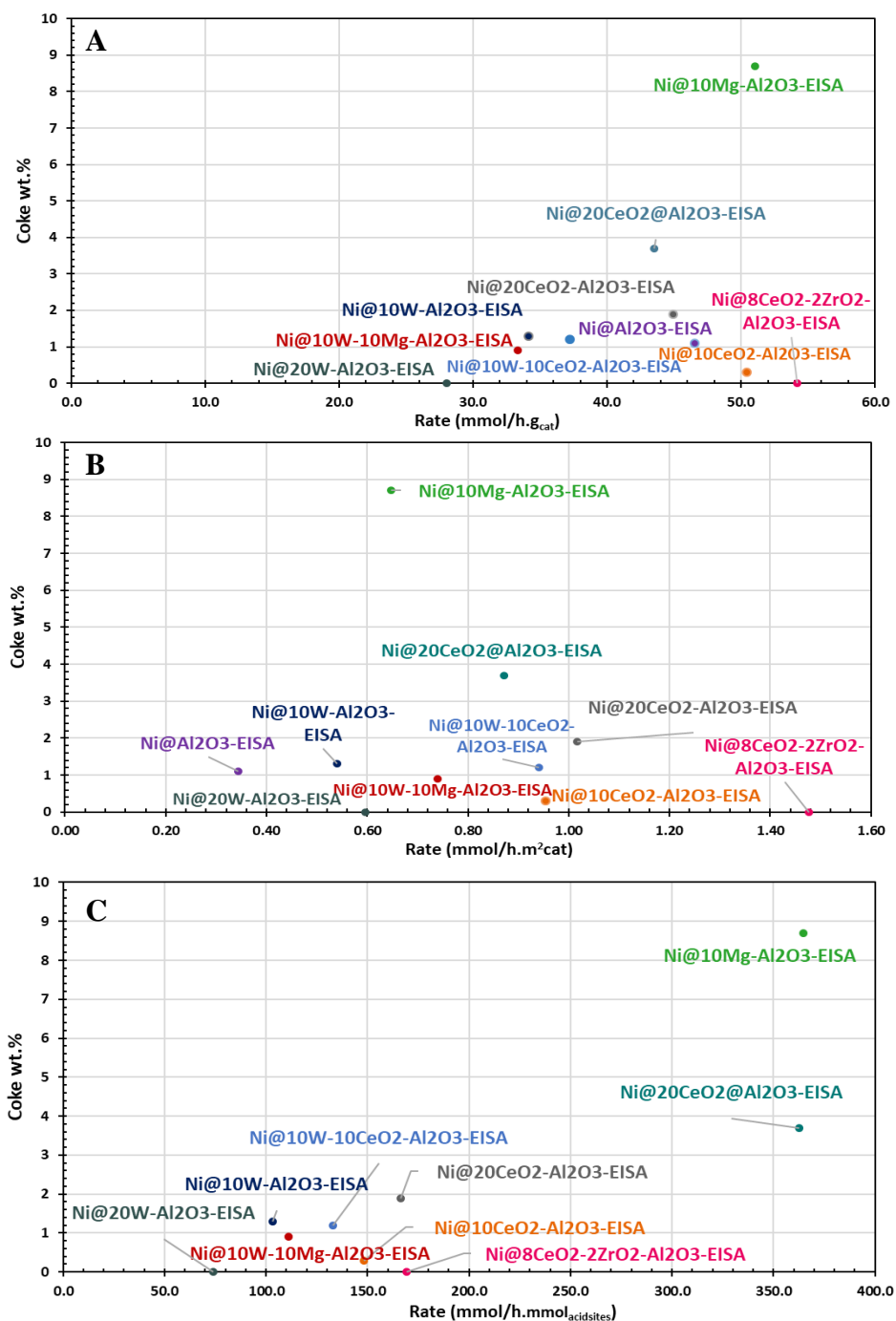


Figure 9.5. Hydrogen formation rate and coke deposition results of synthesized tungsten, ceria, magnesium, zirconia incorporated EISA catalysts in the DSR reaction A) Hydrogen production rate per mass of catalyst (mmol/h.g<sub>catalyst</sub>), B) Hydrogen production rate per surface area of catalyst (mmol/h.m<sup>2</sup><sub>catalyst</sub>), and C) Hydrogen production rate per acid capacity of catalyst (mmol/h.mmol<sub>acid sites</sub>), (GHSV= 7500 h<sup>-1</sup>, 800 °C, H<sub>2</sub>O/C=2.5).

Major findings of this study are summarized below:

- This study includes the use of two different application of two different Al<sub>2</sub>O<sub>3</sub> supports: commercial and synthesized through EISA method and also two different synthesis techniques for promoter incorporation: impregnation to commercial Al<sub>2</sub>O<sub>3</sub> support and one-pot synthesis using EISA method. Ni@Al<sub>2</sub>O<sub>3</sub> and Ni@Al<sub>2</sub>O<sub>3</sub>-EISA catalysts showed similar hydrogen yield, but coke deposition in Ni@Al<sub>2</sub>O<sub>3</sub> catalyst was higher which could be due to its higher total acid capacity (0.49 mmol/g<sub>cat</sub>, Table 5.2) compared to Ni@Al<sub>2</sub>O<sub>3</sub>-EISA (0.35 mmol/g<sub>cat</sub>, Table 7.2). When the incorporation method for the promoters are compared for 20 wt.% W, 10 wt.% and 20 wt.% CeO<sub>2</sub>, and 10 wt.% W & 10 wt.% CeO<sub>2</sub> incorporated catalysts in terms of their hydrogen yield and coke deposition given in Figure 9.1 that one method is not superior to the other. One-pot incorporation through EISA method resulted to be more successful compared to impregnation onto commercial Al<sub>2</sub>O<sub>3</sub> for just 10 wt.% CeO<sub>2</sub> incorporation. Catalysts impregnated onto commercial Al<sub>2</sub>O<sub>3</sub> with 20 wt.% W and 10 wt.% W & 10 wt.% CeO<sub>2</sub> lead to higher hydrogen yields compared to the EISA catalysts.
- Tungsten incorporation into Ni/Al<sub>2</sub>O<sub>3</sub> catalysts significantly enhances coke minimization through the formation of Ni<sub>4</sub>W crystals. However, tungsten incorporated Ni/Al<sub>2</sub>O<sub>3</sub> catalysts are not active towards water gas shift reaction which diminishes overall hydrogen formation.
- Incorporation of CeO<sub>2</sub> or CeO<sub>2</sub>-ZrO<sub>2</sub> at a total amount of 10 wt.% via one-pot synthesis route (EISA) significantly improves catalytic activity and coke resistivity of the catalysts. CeO<sub>2</sub>-ZrO<sub>2</sub> incorporated catalyst showed poor stability during DSR reaction test. Ni@10CeO<sub>2</sub>-Al<sub>2</sub>O<sub>3</sub>-EISA catalyst proved its stability during long term DSR test. Moreover, higher hydrogen production and lower coke deposition was observed in ATR reaction with Ni@10CeO<sub>2</sub>-Al<sub>2</sub>O<sub>3</sub>-EISA catalyst compared to Ni@8CeO<sub>2</sub>-2ZrO<sub>2</sub>-Al<sub>2</sub>O<sub>3</sub>-EISA catalyst.

- Ni@10Mg-Al<sub>2</sub>O<sub>3</sub>-EISA catalyst has high hydrogen productivity in DSR and ATR reactions. Even though high coke deposition was observed with Ni@10Mg-Al<sub>2</sub>O<sub>3</sub>-EISA catalyst through the six hour standard DSR reaction, a similar coke deposition result was obtained after the long term DSR reaction (54 h) with highly stable activity. Similar coke deposition results suggest that the coke deposition occurs at the initial stages of the experiment. Ni@10Mg-Al<sub>2</sub>O<sub>3</sub>-EISA catalyst is a promising material to be used in commercial application of diesel steam reforming reaction.
- Long term DSR reaction with the Ni@10CeO<sub>2</sub>-Al<sub>2</sub>O<sub>3</sub>-EISA and Ni@0.5Ru@Al<sub>2</sub>O<sub>3</sub> catalysts lead to formation of slightly higher coke deposition compared to six hours of DSR reaction. However, six hours and fifty-four hours of DSR reactions with the Ni@10Mg-Al<sub>2</sub>O<sub>3</sub>-EISA catalyst showed similar coke deposition indicating that coke deposition occurs at the initial stages of the experiment over the Ni@10Mg-Al<sub>2</sub>O<sub>3</sub>-EISA catalyst. The reason of the differences in coke deposition periods between catalysts could be due to incomplete reduction of NiO in the Ni@10Mg-Al<sub>2</sub>O<sub>3</sub>-EISA catalyst. NiO present in the catalysts was reduced during the DSR reaction under hydrogen atmosphere according to the XRD results of long term used catalysts. Whereas, the characteristic peaks of NiO were not observed in the XRD patterns of Ni@10CeO<sub>2</sub>-Al<sub>2</sub>O<sub>3</sub>-EISA and Ni@0.5Ru@Al<sub>2</sub>O<sub>3</sub> catalysts. It can be inferred that NiO may have a tendency towards cracking reactions leading to coke deposition.
- Considering hydrogen production capabilities, coke deposition values and also stabilities through six hour and long term DSR reaction periods showed that the most successful catalysts analyzed in this study are Ni@10Mg-Al<sub>2</sub>O<sub>3</sub>-EISA, Ni@10CeO<sub>2</sub>-Al<sub>2</sub>O<sub>3</sub>-EISA, and Ni@0.5Ru@Al<sub>2</sub>O<sub>3</sub>. High coke deposition observed for Mg incorporated one is shown to have no affect on the long term DSR activity of the catalyst. All three catalysts proved their long term activity and stability. Selection of the most active catalysts should also be based on the feasibility of their production. When the costs are compared just

considering the differences in the prices of metal precursors, the highest price was observed for Ru precursor (26.5 €/g), followed by Ce precursor (11.1 €/g) and lastly Mg precursor (0.15 €/g). However, loading amounts of promoters are not equal. For 1 g catalysts synthesis, 10 wt.% Mg cost is 0.15 €, 10 wt.% Ce cost is 3.4 € and 0.5 wt.% Ru cost is 0.28 €. The differences between the costs associated with each promoter indicates the Ni@10Mg-Al<sub>2</sub>O<sub>3</sub>-EISA catalyst would be the clear choice among the three best catalysts for diesel reforming reaction. In addition to the financial aspect of the catalysts, Ru is considered as a precious metal and Ce is accepted as a rare earth element. Considering the economics, availability and long term sustainability of the developed catalyst, Ni@10Mg-Al<sub>2</sub>O<sub>3</sub>-EISA catalyst is the best choice.

- Ni@10CeO<sub>2</sub>-Al<sub>2</sub>O<sub>3</sub>-EISA catalyst which presented the highest hydrogen yield with low coke deposition in ATR reaction, was not tested in long term ATR reaction. Long term DSR study was performed to observe the effect of coke deposition on the catalytic stability showed its applicability. The use of Ni@10CeO<sub>2</sub>-Al<sub>2</sub>O<sub>3</sub>-EISA catalyst in ATR reaction is the best choice in terms of hydrogen production.
- To sum up, the Ni@10Mg-Al<sub>2</sub>O<sub>3</sub>-EISA catalyst in DSR reaction and Ni@10CeO<sub>2</sub>-Al<sub>2</sub>O<sub>3</sub>-EISA catalyst in ATR reaction were found to be the best catalysts in terms of maximizing hydrogen yield and long term catalyst stability in this study. With these catalysts, the hydrogen yield values were higher than the hydrogen yield values reported in literature. In literature, higher hydrogen yield values were obtained by only using n-hexadecane as the feed instead of diesel<sup>32</sup> and by operating at higher reaction temperature (900 °C)<sup>44</sup>.



## CHAPTER 10

### CONCLUSIONS AND RECOMMENDATIONS

Results of this work proved the importance of operating conditions such as GHSV, H<sub>2</sub>O/C ratio, O<sub>2</sub>/C ratio and the effect of promoters in Ni/Al<sub>2</sub>O<sub>3</sub> catalyst in hydrogen production and coke deposition in DSR and ATR reactions.

It was concluded that:

- As GHSV decreases from 25000 h<sup>-1</sup> to 7500 h<sup>-1</sup>, formation of side products such as CH<sub>4</sub>, C<sub>2</sub>H<sub>4</sub>, C<sub>2</sub>H<sub>6</sub> and C<sub>3</sub>H<sub>6</sub> decreases in the DSR reaction. Enhancement in H<sub>2</sub> production at high contact time suggests that hydrocarbons with higher molecular weight are firstly cracked into C<sub>2</sub>-C<sub>3</sub> compounds which are then reformed into the desired products. An increase in steam content of the feed enhanced WGS rate and diminished coke deposition.
- Promotion of commercial Al<sub>2</sub>O<sub>3</sub> supported nickel catalyst with CeO<sub>2</sub> enhanced WGS and reforming activity of the catalyst. According to catalyst performance tests, lower CeO<sub>2</sub> loading is more beneficial in terms of hydrogen yield probably due to its higher surface area and slightly higher acidity, when compared to 20 wt.% CeO<sub>2</sub> loaded material.
- Despite lower hydrogen yield due to lower WGS rate in the presence of the commercial Al<sub>2</sub>O<sub>3</sub> supported nickel-tungsten catalyst, W loaded catalysts are successful in the DSR reaction in terms of coke deposition. Success of W catalysts in DSR was mostly due to the formation of Ni<sub>4</sub>W crystals, whereas nickel takes the form of Ni<sup>0</sup> and NiAl<sub>2</sub>O<sub>4</sub> crystals for others according to the X-ray diffraction patterns of the materials. W incorporation leads to a decrease and even eliminates coke deposition, at high W loadings.

- Parameter optimization tests towards ATR reaction showed that increase of GHSV and molar ratio of oxygen to carbon in the feed diminishes hydrogen production by enhancing methane formation. Increase of steam to carbon ratio of the feed significantly enhances hydrogen production by both diminishing side product formation and also enhancing water gas shift reaction, similar to the results observed in diesel steam reforming reaction.
- The effect of Ru and CeO<sub>2</sub> incorporation as promoter into commercial Al<sub>2</sub>O<sub>3</sub> supported nickel catalyst was investigated in both DSR and ATR reactions. Comparison of Ru/CeO<sub>2</sub>/Al<sub>2</sub>O<sub>3</sub> and Ni/Ru/CeO<sub>2</sub>/Al<sub>2</sub>O<sub>3</sub> showed the importance of nickel in the bond breaking capability of the catalyst in the DSR. Without nickel in the catalyst, significant amount of side products was observed which lead to coke deposition. Catalyst investigations showed that among Ru and Ru-CeO<sub>2</sub> incorporated catalysts, 0.5 wt.% ruthenium loading lead to the highest hydrogen production in both DSR and ATR reactions. Higher activity of this material was mostly due to its higher surface area and easier reducibility of nickel on Ni@0.5Ru@Al<sub>2</sub>O<sub>3</sub>.
- The long term DSR reaction of Ni@0.5Ru@Al<sub>2</sub>O<sub>3</sub> showed that the catalyst is both active and stable. Characterization analysis suggested that the only difference between fresh and used catalyst is the deposited coke that had no significant impact in the performance of the catalyst.
- Results of the promoter investigation for CeO<sub>2</sub> or CeO<sub>2</sub>/ZrO<sub>2</sub> incorporated (one-pot) mesoporous Al<sub>2</sub>O<sub>3</sub> supported nickel impregnated EISA catalysts showed that in the DSR reaction the most successful catalyst is Ni@8CeO<sub>2</sub>-2ZrO<sub>2</sub>@Al<sub>2</sub>O<sub>3</sub>-EISA followed by Ni@10CeO<sub>2</sub>-Al<sub>2</sub>O<sub>3</sub>-EISA in terms of both hydrogen yield and also coke resistivity. Incorporation of 10 wt.% CeO<sub>2</sub> to Ni@Al<sub>2</sub>O<sub>3</sub>-EISA enhanced hydrogen yield from 29.1 (Ni@Al<sub>2</sub>O<sub>3</sub>-EISA) to 32.0 and decreased carbon deposition over six hour of the DSR reaction from 1.1 wt.% (Ni@Al<sub>2</sub>O<sub>3</sub>-EISA) to 0.3 wt.%. Incorporation of

CeO<sub>2</sub> & ZrO<sub>2</sub> further enhanced hydrogen yield to 34.2 and coke deposition to almost zero.

- Higher hydrogen production over Ni@8CeO<sub>2</sub>-2ZrO<sub>2</sub>@Al<sub>2</sub>O<sub>3</sub>-EISA in the DSR reaction was observed due to higher WGS rate according to the molar ratio of CO to CO<sub>2</sub> (1.4). It may be due to the presence of cubic CeO<sub>2</sub> crystals along with CeAlO<sub>3</sub> crystals according to XRD results. Moreover, presence of CeO<sub>2</sub> in Ni@8CeO<sub>2</sub>-2ZrO<sub>2</sub>@Al<sub>2</sub>O<sub>3</sub>-EISA catalyst also provided coke minimization probably due to active role played by CeO<sub>2</sub> in increasing water adsorption and dissociation over the catalyst. However, instabilities observed in DSR and also lower activity of Ni@8CeO<sub>2</sub>-2ZrO<sub>2</sub>@Al<sub>2</sub>O<sub>3</sub>-EISA in ATR suggested that in the long term use of Ni@10CeO<sub>2</sub>-Al<sub>2</sub>O<sub>3</sub>-EISA is more preferable. Long term DSR test (26 h) with the Ni@10CeO<sub>2</sub>-Al<sub>2</sub>O<sub>3</sub>-EISA catalyst showed superior activity along with stability and lead to no structural change except for coke formation. Deposited coke did not cause a change in the activity of Ni@10CeO<sub>2</sub>-Al<sub>2</sub>O<sub>3</sub>-EISA catalyst in the long term experiment.
- Investigation of the effect of amount and synthesis route used for CeO<sub>2</sub> incorporation into Ni/Al<sub>2</sub>O<sub>3</sub>-EISA catalysts showed that increase of CeO<sub>2</sub> loading decreases both surface area and total acid capacity. Increase of loading also leads to a change in the reducibility of nickel. Lower hydrogen production with increased coke production was observed when 20 wt.% and 10 wt.% CeO<sub>2</sub> loaded materials (via one-pot method) were compared. Incorporation of CeO<sub>2</sub> into Ni/Al<sub>2</sub>O<sub>3</sub> via impregnation lead to even lower acid capacity and decreased the interaction of nickel with the support surface. Hydrogen production was lower and coke deposition was higher with the material synthesized through impregnation method. Results show that Ni@10CeO<sub>2</sub>-Al<sub>2</sub>O<sub>3</sub>-EISA is a promising catalyst with its high activity and coking resistance, to be used in long term hydrogen production for fuel cell applications.

- The effect of W, W&CeO<sub>2</sub> or W&Mg incorporation (one-pot) into mesoporous Al<sub>2</sub>O<sub>3</sub>-EISA supported nickel impregnated catalysts was investigated in the DSR and ATR reactions. DSR reaction showed the most successful catalyst as Ni@10Mg-Al<sub>2</sub>O<sub>3</sub>-EISA with an average hydrogen yield value of 33.8 and 8.7 wt.% coke deposition. Ni@10Mg-Al<sub>2</sub>O<sub>3</sub>-EISA catalyst presented formation of Ni<sup>0</sup> crystals with XRD patterns and has a surface area of 79 m<sup>2</sup>/g and a number of acid sites of 0.14 mmol/g<sub>cat</sub>. Incorporation of tungsten lead to lower surface area and higher acidity in synthesized catalysts and caused the transformation of nickel into Ni<sub>4</sub>W crystals. DSR and ATR activities of W incorporated catalysts suffered from mainly low water gas shift reaction rate and low reforming rate leading to formation of CH<sub>4</sub>, C<sub>2</sub>H<sub>4</sub> and C<sub>2</sub>H<sub>6</sub> as side products. However, significant coke minimization was achieved with W catalysts due to low solubility of carbon in Ni<sub>4</sub>W crystals.
- Long term activity test of the Ni@10Mg-Al<sub>2</sub>O<sub>3</sub>-EISA catalyst showed the same high activity with stable product gas composition during fifty four hours of the reaction time. Moreover, similar coke deposition was observed after the long term test (6.7 wt.% in average) compared to the six hours of activity test (8.7 wt.%) showing that the carbon deposition occurs during the initial stages of the DSR reaction and does not affect the catalytic activity. XRD analysis showed the presence of carbon with crystalline structure that did not affected the catalytic activity during the long term activity tests.
- Catalyst characterization and DSR & ATR reaction results showed the importance of the crystal states in the catalysts. CeO<sub>2</sub> crystal compared to CeAlO<sub>3</sub> is suggested to be more effective in enhancing the hydrogen production capability and coke resistivity of the Ni/Al<sub>2</sub>O<sub>3</sub> catalyst in DSR reaction. Moreover, Ni<sup>0</sup> crystal was proven to be more active in DSR and ATR compared to NiAl<sub>2</sub>O<sub>4</sub> and Ni<sub>4</sub>W crystals.

- This study showed that the Ni@10Mg-Al<sub>2</sub>O<sub>3</sub>-EISA catalyst is an optimum catalyst for DSR to achieve high hydrogen concentration in the product gas with long term stability. Considering feasibility and sustainability in the commercial applications of DSR, Ni@10Mg-Al<sub>2</sub>O<sub>3</sub>-EISA catalyst can be considered as the best performing catalyst.
- The highest hydrogen production with low coke deposition in ATR reaction was obtained with Ni@10CeO<sub>2</sub>-Al<sub>2</sub>O<sub>3</sub>-EISA catalyst, which can be used in an APUs equipped with a reformer unit to produce hydrogen for solid oxide fuel cells.

This study investigated the effects of different promoters (Ru, W, CeO<sub>2</sub>, Mg, ZrO<sub>2</sub>) and their combinations (Ru & CeO<sub>2</sub>, Mg, CeO<sub>2</sub> & ZrO<sub>2</sub>, W & CeO<sub>2</sub>, W & Mg) for Ni/Al<sub>2</sub>O<sub>3</sub> catalysts in DSR and ATR reactions. Performances of CeO<sub>2</sub>, CeO<sub>2</sub> & ZrO<sub>2</sub>, Mg and Ru promoters were successful in terms of hydrogen production. Performances of CeO<sub>2</sub>, CeO<sub>2</sub> & ZrO<sub>2</sub> and all W incorporated catalysts were promising in terms of coke deposition. The following improvements are suggested to improve hydrogen production capabilities of the synthesized catalysts:

- Ni@8CeO<sub>2</sub>-2ZrO<sub>2</sub>-Al<sub>2</sub>O<sub>3</sub>-EISA catalyst was very successful in DSR in terms of hydrogen production and coke deposition, but presented poor stability. Instability of CeO<sub>2</sub>-ZrO<sub>2</sub> incorporated catalyst in DSR can be improved by the optimization of the catalyst properties. Moreover, if the synthesis of CeO<sub>2</sub> incorporated Ni/Al<sub>2</sub>O<sub>3</sub> catalyst with cubic CeO<sub>2</sub> crystals can be achieved after calcination and reduction at 900°C, it can lead to a similar success in diesel reforming.
- Low activity of W incorporated Ni/Al<sub>2</sub>O<sub>3</sub> catalysts towards WGS which diminishes overall hydrogen formation can be improved with additional steam feed. Optimization of DSR and ATR parameters over Ni/W/Al<sub>2</sub>O<sub>3</sub> catalyst for hydrogen production maximization is suggested due to superior coke resistivity of Ni/W/Al<sub>2</sub>O<sub>3</sub>. Moreover, the application of a secondary

reactor for WGSR or addition of a secondary catalyst layer for WGSR can be considered for further improvement. Combined with a higher WGSR performance, W incorporated catalysts are promising with their coke resistive properties for long term operation of DSR reaction for hydrogen production to be used in fuel cell component of APUs.

- Tungsten catalysts can be studied in diesel reforming reactions by using ruthenium and other precious metals that could not transform into metal-tungsten crystals as in the case observed in this study for nickel ( $\text{Ni}_4\text{W}$ ). Tungsten catalysts can be also used in reforming reactions that can be performed at lower temperatures at which Ni will not react with W crystals.
- This study investigated the effects of magnesium and ceria incorporation to nickel-tungsten-alumina catalysts. However, the impregnation order of metals was not in the scope. A detailed study can be performed aiming to observe the effect of incorporation order whether with one-pot method or with impregnation to commercial alumina supports. Proposed study will further help understanding the interactions between tungsten and support materials.
- $\text{Ni}@10\text{Mg}-\text{Al}_2\text{O}_3\text{-EISA}$  catalyst was very successful in DSR in terms of hydrogen production with long term stability. The effect of Mg incorporation can be further analyzed by the application of different loading amounts. Moreover, different synthesis methods can be applied for the synthesis of  $\text{Mg}-\text{Al}_2\text{O}_3$  support.
- This study did not analyze the effect of Ru & Mg incorporation into  $\text{Ni}/\text{Al}_2\text{O}_3$  catalyst in DSR and ATR reactions. Both Ru and Mg incorporation was proven to be beneficial to enhance hydrogen production in DSR and ATR reactions, when incorporated separately. The combined effect of these promoters should be studied in terms of their effect of hydrogen yield enhancement and coke minimization.

## REFERENCES

1. Schumacher, E. F. *Schumacher on energy: speeches and writings of E.F. Schumacher*. (Jonathan Cape Ltd, 1982).
2. Giacomelli, G. The energy problem. *Radiati Meas* 44, 707–716 (2009).
3. Midilli, A. & Dincer, I. Key strategies of hydrogen energy systems for sustainability. *Int. J. Hydrogen Energy* 32, 511–524 (2007).
4. Cipriani, G. et al. Perspective on hydrogen energy carrier and its automotive applications. *Int J Hydrog. Energ* 39, 8482–8494 (2014).
5. Alberton, A. L., Souza, M. M. V. M. & Schmal, M. Carbon formation and its influence on ethanol steam reforming over Ni/Al<sub>2</sub>O<sub>3</sub> catalysts. *Catal Today* 123, 257–264 (2007).
6. Arslan, A. *Ethanol Steam Reforming With Zirconia Based Catalysts*. (Middle East Technical University, 2014).
7. Ibrahim, H. H., Kumar, P. & Idem, R. O. Reforming of Isooctane over Ni - Al<sub>2</sub>O<sub>3</sub> Catalysts for Hydrogen Production : Effects of Catalyst Preparation Method and Nickel Loading. *Energ Fuel* 21, 570–580 (2007).
8. Balcombe, P. et al. The role of hydrogen and fuel cells in the global energy system. *Energy Environ. Sci.* 463–491 (2018). doi:10.1039/c8ee01157e
9. Guggilla, V. S. et al. H<sub>2</sub> Production by Autothermal Reforming of n -Dodecane over Highly Active Ru–Ni–Ce–Al<sub>2</sub>O<sub>3</sub> Catalyst. *Ind. Eng. Chem. Res.* 52, 121227134624003 (2012).
10. Martin, S. et al. Direct steam reforming of diesel and diesel–biodiesel blends for distributed hydrogen generation. *Int. J. Hydrogen Energy* 40, 75–84 (2015).
11. Staffell, I. Zero carbon infinite COP heat from fuel cell CHP. *Appl. Energy* 147, 373–385 (2015).
12. Stations, H. R. & Vehicles, F. C. Utilization of Hydrogen Energy. in *Science and Engineering of Hydrogen-Based Energy Technologies* 237–258 (2019). doi:10.1016/b978-0-12-814251-6.00012-5
13. Hart, D., Lehner, F., Jones, S., Lewis, J. & Klippenstein, M. *The Fuel Cell Industry Review 2017*. E4tech (2018).
14. Zhang, G., Du, Y., Zhang, Y. & Xu, Y. Desulfurization reaction model and experimental analysis of high sulfur coal under hydrogen atmosphere. *J. Ind. Eng. Chem.* 20, 487–493 (2014).
15. Xu, X., Li, P. & Shen, Y. Small-scale reforming of diesel and jet fuels to make hydrogen and syngas for fuel cells: A review. *Appl. Energy* 108, 202–217 (2013).

16. Midilli, A., Ay, M., Dincer, I. & Rosen, M. A. On hydrogen and hydrogen energy strategies II: future projections affecting global stability and unrest. *Renew. Sustain. Energy Rev.* 9, 273–287 (2005).
17. Schjøberg, I., Hulteberg, C., Yasuda, I. & Nelsson, C. Small scale reformers for on-site hydrogen supply. *Energy Procedia* 29, 559–566 (2012).
18. Guggilla, V. S., Akyurtlu, J., Akyurtlu, A. & Blankson, I. Steam Reforming of n -Dodecane over Ru - Ni-Based Catalysts. *Ind. Eng. Chem. Res.* 49, 8164–8173 (2010).
19. González, A. V. & Pettersson, L. J. Full-scale autothermal reforming for transport applications: The effect of diesel fuel quality. *Catal. Today* 210, 19–25 (2013).
20. Cheekatamarla, P. K. & Lane, A. M. Catalytic autothermal reforming of diesel fuel for hydrogen generation in fuel cells: II. Catalyst poisoning and characterization studies. *J. Power Sources* 154, 223–231 (2006).
21. Pasel, J., Samsun, R. C., Tschauder, A., Peters, R. & Stolten, D. A novel reactor type for autothermal reforming of diesel fuel and kerosene. *Appl. Energy* 150, 176–184 (2015).
22. Qi, D. H., Yang, K., Zhang, D. & Chen, B. Combustion and emission characteristics of diesel-tung oil-ethanol blended fuels used in a CRDI diesel engine with different injection strategies. *Appl. Therm. Eng.* 111, 927–935 (2017).
23. Fuel Cell Market Analysis and Segment Forecast to 2025. (2018).
24. Berger, R. Fuel Cells and Hydrogen for Green Energy in European Cities and Regions: A Study for the Fuel Cells and Hydrogen Joint Undertaking. (2018).
25. Ruf, Y. et al. Fuel Cells and Hydrogen Applications for Regions and Cities Vol 2: Cost and high-level business case analysis. 2, (2017).
26. Megaritis, A., Tsolakis, A., Wyszynski, M. L. & Golunski, S. E. Fuel reforming for diesel engines. in *Advanced Direct Injection Combustion Engine Technologies and Development: Diesel Engines* 543–561 (Woodhead Publishing Limited, 2009). doi:10.1533/9781845697457
27. Villoria, J. A. et al. Oxidative reforming of diesel fuel over LaCoO<sub>3</sub> perovskite derived catalysts: Influence of perovskite synthesis method on catalyst properties and performance. *Appl. Catal. B Environ.* 105, 276–288 (2011).
28. Fauteux-Lefebvre, C., Abatzoglou, N., Braidy, N. & Achouri, I. E. Diesel steam reforming with a nickel-alumina spinel catalyst for solid oxide fuel cell application. *J. Power Sources* 196, 7673–7680 (2011).
29. Şahin, Z. Experimental and Theoretical Investigation of the Effects of Gasoline Blends on Single-Cylinder Diesel Engine Performance and Exhaust Emissions. *Energy & Fuels* 22, 3201–3212 (2008).

30. F. Brown, L. A comparative study of fuels for on-board hydrogen production for fuel-cell-powered automobiles. *Int. J. Hydrogen Energy* 26, 381–397 (2001).
31. Lindermeir, A., Kah, S., Kavurucu, S. & Mühlner, M. On-board diesel fuel processing for an SOFC-APU-Technical challenges for catalysis and reactor design. *Appl. Catal. B Environ.* 70, 488–497 (2007).
32. Fauteux-Lefebvre, C., Abatzoglou, N., Blanchard, J. & Gitzhofer, F. Steam reforming of liquid hydrocarbons over a nickel-alumina spinel catalyst. *J. Power Sources* 195, 3275–3283 (2010).
33. Shigarov, A. B., Kireenkov, V. V., Kuzmin, V. a., Kuzin, N. a. & Kirillov, V. a. Autothermal reforming of diesel fuel in a structured porous metal catalyst: Both kinetically and transport controlled reaction. *Catal. Today* 144, 341–349 (2009).
34. Berry, D., Shekhawat, D. & Gardner, T. H. Hydrogen, Fuel Cells and Infrastructure Technologies Program. FY 2003 Progress Report (2003).
35. Kaila, R. K. & Krause, a. O. I. Autothermal reforming of simulated gasoline and diesel fuels. *Int. J. Hydrogen Energy* 31, 1934–1941 (2006).
36. Parmar, R. D., Kundu, A. & Karan, K. Thermodynamic analysis of diesel reforming process: Mapping of carbon formation boundary and representative independent reactions. *J. Power Sources* 194, 1007–1020 (2009).
37. Kopasz, J. P. et al. Reforming of Diesel Fuel for Transportation Applications in ANL FY Progress Report “Hydrogen, Fuel Cells, and Infrastructure Technologies”. (2003).
38. Ibarreta, A. F. & Sung, C. J. Optimization of Jet-A fuel reforming for aerospace applications. *Int. J. Hydrogen Energy* 31, 1066–1078 (2006).
39. Cheekatamarla, P. K. & Lane, A. M. Catalytic autothermal reforming of diesel fuel for hydrogen generation in fuel cells: I. Activity tests and sulfur poisoning. *J. Power Sources* 152, 256–263 (2005).
40. Creaser, D., Karatzas, X., Lundberg, B., Pettersson, L. J. & Dawody, J. Modeling study of 5kWe-scale autothermal diesel fuel reformer. *Appl. Catal. A Gen.* 404, 129–140 (2011).
41. Pasel, J., Samsun, R. C., Peters, R. & Stolten, D. Fuel Processing of Diesel and Kerosene for Auxiliary Power Unit Applications. *Energ Fuel* 27, 4386–4394 (2013).
42. Achouri, I. E., Abatzoglou, N., Fauteux-Lefebvre, C. & Braidly, N. Diesel steam reforming: Comparison of two nickel aluminate catalysts prepared by wet-impregnation and co-precipitation. *Catal. Today* 207, 13–20 (2013).
43. Sotelo-boya, R. & Froment, G. F. Fundamental Kinetic Modeling of Catalytic Reforming. 1107–1119 (2009).
44. Kim, D. H. et al. Steam reforming of n-hexadecane over noble metal-modified Ni-based catalysts. *Catal. Today* 136, 228–234 (2008).

45. Karatzas, X., Jansson, K., González, A., Dawody, J. & Pettersson, L. J. Autothermal reforming of low-sulfur diesel over bimetallic RhPt supported on Al<sub>2</sub>O<sub>3</sub>, CeO<sub>2</sub>-ZrO<sub>2</sub>, SiO<sub>2</sub> and TiO<sub>2</sub>. *Appl. Catal. B Environ.* 106, 476–487 (2011).
46. Haynes, D. J. & Shekhawat, D. *Oxidative Steam Reforming. Fuel Cells: Technologies for Fuel Processing* (Elsevier, 2011). doi:10.1016/B978-0-444-53563-4.10006-9
47. Ni, J., Zhao, J., Chen, L., Lin, J. & Kawi, S. Lewis Acid Sites Stabilized Nickel Catalysts for Dry (CO<sub>2</sub>) Reforming of Methane. 3732–3739 (2016). doi:10.1002/cctc.201601002
48. Richardson, J. T., Turk, B. & Twigg, M. V. Reduction of model steam reforming catalysts: Effect of oxide additives. *Appl. Catal. A Gen.* 148, 97–112 (1996).
49. Horiuchi, T. et al. Suppression of carbon deposition in the CO<sub>2</sub>-reforming of CH<sub>4</sub> by adding basic metal oxides to a Ni/Al<sub>2</sub>O<sub>3</sub> catalyst. *Appl. Catal. A Gen.* 144, 111–120 (1996).
50. Borowiecki, T., Giecko, G. & Panczyk, M. Effects of small MoO<sub>3</sub> additions on the properties of nickel catalysts for the steam reforming of hydrocarbons: II. Ni-Mo/Al<sub>2</sub>O<sub>3</sub> catalysts in reforming, hydrogenolysis and cracking of n-butane. *Appl. Catal. A Gen.* 230, 85–97 (2002).
51. Arslan, A., Gunduz, S. & Dogu, T. Steam reforming of ethanol with zirconia incorporated mesoporous silicate supported catalysts. *Int J Hydrog. Energ* 39, 18264–18272 (2014).
52. Thormann, J. et al. Steam reforming of hexadecane over a Rh/CeO<sub>2</sub> catalyst in microchannels: Experimental and numerical investigation. *Int. J. Hydrogen Energy* 34, 5108–5120 (2009).
53. Damyanova, S., Perez, C. A., Schmal, M. & Bueno, J. M. C. Characterization of ceria-coated alumina carrier. *Appl Catal A-Gen* 234, 271–282 (2002).
54. Luisetto, I., Tuti, S., Battocchio, C., Lo, S. & Sodo, A. *Applied Catalysis A : General Ni/CeO<sub>2</sub>-Al<sub>2</sub>O<sub>3</sub> catalysts for the dry reforming of methane : The effect of CeAlO<sub>3</sub> content and nickel crystallite size on catalytic activity and coke resistance.* "Applied Catal. A, Gen. 500, 12–22 (2015).
55. Kim, T. Y., Kim, S. M., Lee, W. S. & Woo, S. I. Effect and behavior of cerium oxide in Ni/g-Al<sub>2</sub>O<sub>3</sub> catalysts on autothermal reforming of methane : CeAlO<sub>3</sub> formation and its role on activity. *Int. J. Hydrogen Energy* 38, 6027–6032 (2013).
56. Wang, S. & Lu, G. Q. M. Role of CeO<sub>2</sub> in Ni/CeO<sub>2</sub>±Al<sub>2</sub>O<sub>3</sub> catalysts for carbon dioxide reforming of methane. 19, (1998).
57. Kline, C. H. & Kollonitsch, V. Catalytic activity of Tungsten. *Ind. Eng. Chem.* 57, 53–60 (1965).

58. Lassner, E. & Schubert, W. Properties, Chemistry, Technology of the Element, Alloys, and Chemical Compounds Erik Lassner and Wolf-Dieter Schubert. (1999).
59. Sheng, J., Yi, X., Li, F. & Fang, W. Effects of tungsten on the catalytic activity of Ni – W catalysts for the hydrogenation of aromatic hydrocarbons. *Reac Kinet Mech Cat* 99, 371–379 (2010).
60. Arbag, H. et al. Coke minimization during conversion of biogas to syngas by bimetallic tungsten-nickel incorporated mesoporous alumina synthesized by the one-pot route. *Ind. Eng. Chem. Res.* 54, 2290–2301 (2015).
61. Slagtern, A. & Olsbye, U. Partial oxidation of methane to synthesis gas using La-M-O catalysts. *Appl. Catal. A Gen.* 110, 99–108 (1994).
62. Murata, K. et al. Hydrogen production from steam reforming of hydrocarbons over alkaline-earth metal-modified Fe- or Ni-based catalysts. *Energy and Fuels* 18, 122–126 (2004).
63. Wang, L., Murata, K., Matsumura, Y. & Inaba, M. Lower-temperature catalytic performance of bimetallic Ni - Re/Al<sub>2</sub>O<sub>3</sub> catalyst for gasoline reforming to produce hydrogen with the inhibition of methane formation. *Energy and Fuels* 20, 1377–1381 (2006).
64. Arbag, H., Yasyerli, S., Yasyerli, N., Dogu, T. & Dogu, G. Coke Minimization in Dry Reforming of Methane by Ni Based Mesoporous Alumina Catalysts Synthesized Following Different Routes: Effects of W and Mg. *Top Catal* 56, 1695–1707 (2013).
65. Kaila, R. K. et al. Zirconia-supported bimetallic RhPt catalysts: Characterization and testing in autothermal reforming of simulated gasoline. *Appl. Catal. B Environ.* 84, 223–232 (2008).
66. Kaila, R. K., Gutiérrez, A. & Krause, a. O. I. Autothermal reforming of simulated and commercial diesel: The performance of zirconia-supported RhPt catalyst in the presence of sulfur. *Appl. Catal. B Environ.* 84, 324–331 (2008).
67. Betancourt, P., Rives, A., Hubaut, R., Scott, C. . & Goldwasser, J. A study of the ruthenium–alumina system. *Appl. Catal. A Gen.* 170, 307–314 (1998).
68. Suzuki, T., Iwanami, H. I. & Yoshinari, T. Steam reforming of kerosene on Ru/Al<sub>2</sub>O<sub>3</sub> catalyst to yield hydrogen. *Int. J. Hydrogen Energy* 25, 119–126 (2000).
69. Mota, N. et al. Insights on the role of Ru substitution in the properties of LaCoO<sub>3</sub>-based oxides as catalysts precursors for the oxidative reforming of diesel fuel. *Appl. Catal. B Environ.* 113–114, 271–280 (2012).
70. Baker, R. T. K., Kim, M. S., Chambers, A., Park, C. & Rodrigues, N. M. The Relationship Between Metal Particle Morphology and the Structural Characteristics of Carbon Deposits. in *Studies in Surface Science and Catalysis Catalyst Deactivation 1997* (eds Bartholomew, C. H. & Fuentes, G. A.) 99–110 (1997).
71. J. R. Rostrup-Nielsen. *Catalytic Steam Reforming*. Springer (1984).

72. Ming, Q., Healey, T., Allen, L. & Irving, P. Steam reforming of hydrocarbon fuels. *Catal. Today* 77, 51–64 (2002).
73. Lin, J., Trabold, T. A., Walluk, M. R. & Smith, D. F. Bio-fuel reforming for solid oxide fuel cell applications. Part 2: Biodiesel. *Int. J. Hydrogen Energy* 39, 183–195 (2014).
74. Martin, S., Kraaij, G., Ascher, T., Wails, D. & Wörner, A. An experimental investigation of biodiesel steam reforming. *Int. J. Hydrogen Energy* 40, 95–105 (2015).
75. Joensen, F., Joensen, F. & Rostrup-nielsen, J. R. Conversion of Hydrocarbons and Alcohols for Fuel Cell Conversion of hydrocarbons and alcohols for fuel cells. *J. power* 7753, 1–8 (2014).
76. Yoon, S., Kang, I. & Bae, J. Effects of ethylene on carbon formation in diesel autothermal reforming. *Int. J. Hydrogen Energy* 33, 4780–4788 (2008).
77. Kang, I., Bae, J. & Bae, G. Performance comparison of autothermal reforming for liquid hydrocarbons, gasoline and diesel for fuel cell applications. *J. Power Sources* 163, 538–546 (2006).
78. Shoynkhorova, T. B. et al. Highly dispersed Rh-, Pt-, Ru/Ce<sub>0.75</sub>Zr<sub>0.25</sub>O<sub>2-δ</sub> catalysts prepared by sorption-hydrolytic deposition for diesel fuel reforming to syngas. *Appl. Catal. B Environ.* 237, 237–244 (2018).
79. Younis, M. N., Malaibari, Z. O., Ahmad, W. & Ahmed, S. Hydrogen Production through Steam Reforming of Diesel over Highly Efficient Promoted Ni/ $\gamma$ -Al<sub>2</sub>O<sub>3</sub> Catalysts Containing Lanthanide Series (La, Ce, Eu, Pr, and Gd) Promoters. *Energy & Fuels* 32, 7054–7065 (2018).
80. Nikulshina, M. S. et al. Molecular approach to prepare mixed MoW alumina supported hydrotreatment catalysts using H<sub>4</sub>SiMo<sub>12</sub>N<sub>40</sub> heteropolyacids. *Catal. Sci. Technol.* 8, 5557–5572 (2018).
81. Vroulias, D., Gkoulemani, N., Papadopoulou, C. & Matralis, H. W-modified Ni/Al<sub>2</sub>O<sub>3</sub> catalysts for the dry reforming of methane: Effect of W loading. *Catal. Today* (2019). doi:10.1016/j.cattod.2019.05.066
82. Claridge, J. B. et al. New Catalysts for the Conversion of Methane to Synthesis Gas: Molybdenum and Tungsten Carbide. *J. Catal.* 180, 85–100 (1998).
83. York, A. P. E., Suhartanto, T. & Green, M. L. H. Influence of molybdenum and tungsten dopants on nickel catalysts for the dry reforming of methane with carbon dioxide to synthesis gas. *Studies in Surface Science and Catalysis* 119, (Elsevier Masson SAS, 1998).
84. Gündüz, S. & Dogu, T. Hydrogen by steam reforming of ethanol over Co–Mg incorporated novel mesoporous alumina catalysts in tubular and microwave reactors. *Appl. Catal. B Environ.* 168–169, 497–508 (2015).

85. Liu, H., Lin, Y. & Ma, Z. Rh<sub>2</sub>O<sub>3</sub>/mesoporous MO<sub>x</sub>-Al<sub>2</sub>O<sub>3</sub> (M = Mn, Fe, Co, Ni, Cu, Ba) catalysts: Synthesis, characterization, and catalytic applications. *Chinese J. Catal.* 37, 73–82 (2016).
86. Arslan, A. & Doğu, T. Effect of calcination/reduction temperature of Ni impregnated CeO<sub>2</sub>-ZrO<sub>2</sub> catalysts on hydrogen yield and coke minimization in low temperature reforming of ethanol. *Int. J. Hydrogen Energy* 41, 16752–16761 (2016).
87. Kang, I. & Bae, J. Autothermal reforming study of diesel for fuel cell application. *J. Power Sources* 159, 1283–1290 (2006).
88. US-EPA, B, R. & US-EPA, E. P. A. Method 1664, Revision B: n-Hexane Extractable Material (HEM; Oil and Grease) and Silica Gel Treated n-Hexane Extractable Material (SGT-HEM; Non-polar Material) by Extraction and Gravimetry. EPA-821-R-10-001, US Environmental Protection Agency, Office of Water (2010).
89. Sing, K. S. W. et al. Reporting physisorption data for gas/solid systems with special reference to the determination of surface area and porosity. *Pure Appl Chem* 54, 2201–2218 (1985).
90. Lowell, S., Shields, J. E., Thomas, M. A. & Thommes, M. *Characterization of Porous Solids and Powders : Surface Area , Pore Size and Density.* (Kluwer Academic Publishers, 2004). doi:10.1007/978-1-4020-2303-3
91. Wefers, K. & Misra, C. *Oxides and Hydroxides of Aluminum.* Alcoa Technical Paper 19, (1987).
92. Paglia, G. et al. Boehmite Derived  $\gamma$ -Alumina System. 1. Structural Evolution with Temperature, with the Identification and Structural Determination of a New Transition Phase,  $\gamma'$ -Alumina. *Chem. Mater.* 16, 220–236 (2004).
93. Che, M. & Védrine, J. *Characterization of solid materials and heterogeneous catalysts. From structure to surface reactivity.* Wiley-VCH (2012).
94. Cui, W. et al. Hydroprocessing of Low-Temperature Coal Tar for the Production of Clean Fuel over Fluorinated NiW/Al<sub>2</sub>O<sub>3</sub>-SiO<sub>2</sub> Catalyst. *Energy and Fuels* 31, 3768–3783 (2017).
95. Cai, X., Cai, Y. & Lin, W. Autothermal reforming of methane over Ni catalysts supported over ZrO<sub>2</sub>-CeO<sub>2</sub>-Al<sub>2</sub>O<sub>3</sub>. *J. Nat. Gas Chem.* 17, 201–207 (2008).
96. Wang, H., Dai, F., Li, Z. & Li, C. Upgrading Shale Oil Distillation to Clean Fuel by Coupled Hydrogenation and Ring Opening Reaction of Aromatics on W-Ni/ $\gamma$ -Al<sub>2</sub>O<sub>3</sub> Catalysts. *Energy and Fuels* 29, 4902–4910 (2015).
97. Shoji, M. L. et al. Hydrogenolysis of Glycerol to Monoalcohols over Supported Mo and W Catalysts. *ACS Sustain. Chem. Eng.* 4, 5752–5760 (2016).
98. Cury, R., Joubert, J. M., Tusseau-Nenez, S., Leroy, E. & Allavena-Valette, A. On the existence and the crystal structure of Ni<sub>4</sub>W, NiW and NiW<sub>2</sub> compounds. *Intermetallics* 17, 174–178 (2009).

99. Wang, S. & Lu, G. . (Max). Role of CeO<sub>2</sub> in Ni/CeO<sub>2</sub>-Al<sub>2</sub>O<sub>3</sub> catalysts for carbon dioxide reforming of methane. *Appl Catal B Env.* 19, 267–277 (1998).
100. Rouquerol, F., Rouquerol, J., Sing, K. S. W., Llewellyn, P. & Maurin, G. *Adsorption by Powders and Porous Solids Principles, Methodology and Applications.* (Elsevier, 2014).
101. Chen, X., Zou, H., Chen, S., Dong, X. & Lin, W. Selective Oxidation of CO in Excess H<sub>2</sub> over Ru/Al<sub>2</sub>O<sub>3</sub> Catalysts Modified with Metal Oxide. *J. Nat. Gas Chem.* 16, 409–414 (2007).
102. Jeong, J. H. et al. Ru-doped Ni catalysts effective for the steam reforming of methane without the pre-reduction treatment with H<sub>2</sub>. *Appl. Catal. A Gen.* 302, 151–156 (2006).
103. Zhou, L., Guo, Y., Basset, J. M. & Kameyama, H. Structured Ni catalysts on porous anodic alumina membranes for methane dry reforming: NiAl<sub>2</sub>O<sub>4</sub> formation and characterization. *Chem. Commun.* 51, 12044–12047 (2015).
104. Ding, C. et al. One step synthesis of mesoporous NiO-Al<sub>2</sub>O<sub>3</sub> catalyst for partial oxidation of methane to syngas: The role of calcination temperature. *Fuel* 162, 148–154 (2015).
105. Damyanova, S. et al. Structure and surface properties of ceria-modified Ni-based catalysts for hydrogen production. *Appl. Catal. B Environ.* 225, 340–353 (2018).
106. Piras, A. et al. Structural and morphological investigation of ceria-promoted Al<sub>2</sub>O<sub>3</sub> under severe reducing/oxidizing conditions. *J. Phys. Chem. B* 109, 11110–11118 (2005).
107. Giordano, F., Trovarelli, A., De Leitenburg, C. & Giona, M. A Model for the Temperature-Programmed Reduction of Low and High Surface Area Ceria. *J. Catal.* 193, 273–282 (2000).
108. Alvarez-Galvan, M. C. et al. Performance of La,Ce-modified alumina-supported Pt and Ni catalysts for the oxidative reforming of diesel hydrocarbons. *Int. J. Hydrogen Energy* 33, 652–663 (2008).
109. Baker, R. T. K. *Catalytic Growth.* Carbon N. Y. 27, 315–323 (1989).
110. Ajayan, P. M. Nanotubes from Carbon. *Chem. Rev.* 99, 1787–1799 (1999).
111. Guo, J., Lou, H., Zhao, H., Chai, D. & Zheng, X. Dry reforming of methane over nickel catalysts supported on magnesium aluminate spinels. *Appl. Catal. A Gen.* 273, 75–82 (2004).
112. Nuernberg, G. D. B. et al. Direct decomposition of methane over Ni catalyst supported in magnesium aluminate. *J. Power Sources* 208, 409–414 (2012).
113. Cerritos, C. et al. Steam Reforming of Ethanol over Ni/Al<sub>2</sub>O<sub>3</sub> - La<sub>2</sub>O<sub>3</sub> Catalysts Synthesized by Sol - Gel. *Ind Eng Chem* 50, 2576–2584 (2011).

## APPENDICES

### A. Applied Reactant Composition in Equilibrium Calculations

The analysis of the diesel fuel that was used in the diesel steam and autothermal reforming reactions was performed with a gas chromatography by METU Petroleum Analysis Laboratory (PAL). The results of the diesel composition were applied during the calculation of equilibrium with Aspen HYSYS. Table A.1 shows an example of applied reactant composition and effluent stream composition for diesel steam reforming reaction.

Table A.1 An example of applied reactant composition (PAL results) and effluent stream composition for diesel steam reforming reaction (800 °C, H<sub>2</sub>O/C=2.5)

Component	Reactant Molar Composition	Effluent Molar Composition
H <sub>2</sub> O	0.977	0.26862
Hydrogen	-	0.51715
CO	-	0.13679
CO <sub>2</sub>	-	0.07696
Methane	-	0.00048
Ethylene	-	0.00000
Ethane	-	0.00000
Propane	-	0.00000
n-Butane	-	0.00000
n-Pentane	-	0.00000
n-Hexane	-	0.00000
n-Heptane	-	0.00000
n-Octane	-	0.00000
n-Nonane	-	0.00000
n-Decane	0.00113	0.00000
n-C11	0.00123	0.00000
n-C12	0.00180	0.00000
n-C13	0.00163	0.00000
n-C14	0.00156	0.00000
n-C15	0.00237	0.00000
n-C16	0.00262	0.00000

Table A.1 (cont'd) An example of applied reactant composition (PAL results) and effluent stream composition for diesel steam reforming reaction (800 °C, H<sub>2</sub>O/C=2.5)

Component	Reactant Molar Composition	Effluent Molar Composition
n-C17	0.00243	0.00000
n-C18	0.00211	0.00000
n-C19	0.00171	0.00000
n-C20	0.00144	0.00000
n-C21	0.00100	0.00000
n-C22	0.00078	0.00000
n-C23	0.00056	0.00000
n-C24	0.00037	0.00000
n-C25	0.00017	0.00000
n-C26	0.00007	0.00000
n-C27	0.00003	0.00000
n-C28	0.00001	0.00000

## B. Diesel Steam and Autothermal Reforming Experimental Methods

### B.1 Conditions Applied for GC Analysis

The effluent gas of diesel steam reforming and diesel autothermal reforming experiments were analyzed with an online gas chromatography (SRI 8610-C Multigas #1 gas chromatograph with a thermal conductivity detector and a carbosphere packed column) to determine its composition in terms of moles. Appendix section B.2 presents the conversion procedure from TCD signal to number of moles of the compounds. Table B.1 shows the applied oven heating program including temperature ramp and the hold times. TCD temperature was kept at 200 °C and carrier argon gas pressure was 40 psi at all experiments.

Table B.1 GC oven program applied for DSR and ATR experiments.

<b>Initial Temperature (°C)</b>	<b>Final Temperature (°C)</b>	<b>Hold (min)</b>	<b>Ramp (°C/min)</b>
130	130	7	-
130	250	-	40
250	250	21	-

### B.2 Gas chromatography calibration factor calculation of product gases

Gas chromatography used for the online measurements of the gas effluent stream of both diesel steam and autothermal reforming reactions experimental tests was calibrated by using two standard gas mixtures. First gas mixture was composed of 1% H<sub>2</sub>, 1% CO<sub>2</sub>, 1% CO, 1% CH<sub>4</sub>, 1% C<sub>2</sub>H<sub>4</sub> and 95% Ar (volume content). The content of the second gas mixture was 1% CH<sub>4</sub>, 1% C<sub>2</sub>H<sub>6</sub>, 1% C<sub>3</sub>H<sub>6</sub>, 1% C<sub>4</sub>H<sub>10</sub> and 96% N<sub>2</sub> (in volume).

Calibration factor for each component was calculated by using the formula given in Eqn B.1, where the calibration factor,  $\beta$ , for CH<sub>4</sub> was taken as 1, since CH<sub>4</sub> is the only gas that was in both standard gas mixtures. Calibration factors for these gases were given in Table B.2.

$$\frac{n_i}{n_{CH_4}} = \frac{A_i \beta_i}{A_{CH_4} \beta_{CH_4}} \quad (\text{Eqn.B1})$$

*n*: moles of the gas

*A*: Area of the gas

$\beta$ : Calibration factor

Table B.2 Calibration factors for the components that can be found in the reactor gas effluent stream.

Component	Calibration Factor
H <sub>2</sub>	0.32
N <sub>2</sub>	0.05
CO	3.96
CH <sub>4</sub>	1.00
CO <sub>2</sub>	3.25
C <sub>2</sub> H <sub>4</sub>	0.99
C <sub>2</sub> H <sub>6</sub>	0.88
C <sub>3</sub> H <sub>6</sub>	1.76
C <sub>4</sub> H <sub>10</sub>	1.18

### **B.3 Sample calculation for conversion of TCD signal into mole fraction and hydrogen yield**

GC analysis produces results in terms of signals which are required to be converted into mole fractions. A sample result of GC signal and its conversion to number of moles and then mole fraction of the components are presented in Table B.3. During this calculation, the area obtained for each gas was multiplied with its corresponding beta factor calculated in section B.2 which provides the number of moles of each gas component. Mole fractions of each component was then calculated by dividing the moles of that component to the summation of the total number of moles.

Table B.3 A sample conversion of TCD signal to mole fraction of gas effluent stream.

Component	TCD Signal (Area)	$\beta_i$	$N_i$ (Moles)	$Y_i$ (Mole Fraction)
H <sub>2</sub>	5143.29	0.32	1649.18	64.92
CO	154.41	3.96	611.26	0.48
CH <sub>4</sub>	12.21	1.00	12.21	10.48
CO <sub>2</sub>	81.84	3.25	266.29	0.03
C <sub>2</sub> H <sub>4</sub>	0.81	0.99	0.80	0.02
C <sub>2</sub> H <sub>6</sub>	0	0.88	0	0
C <sub>3</sub> H <sub>6</sub>	0	1.18	0	0

Hydrogen yield calculation was performed by assuming the molecular formula of diesel as C<sub>17</sub>H<sub>36</sub>. This assumption was based on the analysis result of diesel which showed an average carbon number value of 17 (Figure B.1). Theoretical maximum H<sub>2</sub> mole that can be produced from one mole of diesel is 35 for steam reforming and 26.5 for autothermal reforming reactions, according to B.R.1 and B.R.2, respectively.

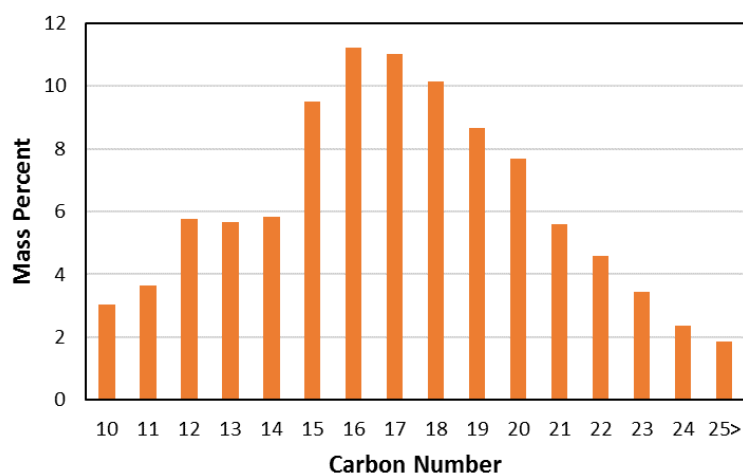


Figure B.1 Carbon number distribution of diesel (analyzed at PAL, METU)

Application of following equations (Eq. B.1 for the determination of total number of moles of diesel feed assuming there is no hydrocarbon presence of the liquid effluent, Eq. B.2 for the determination of hydrogen yield) to determine hydrogen yield value of the sample result given in Table B.3 results in a H<sub>2</sub> yield value of 31.5.

$$\dot{N}_{\text{diesel}} = \frac{(N_{\text{product,CO}} + N_{\text{product,CH}_4} + N_{\text{product,CO}_2} + N_{\text{product,C}_2\text{H}_4} \times 2 + N_{\text{product,C}_2\text{H}_6} \times 2)}{17} \quad (\text{Eq. B.1})$$

$$\text{H}_2 \text{ yield} = \frac{N_{\text{product,H}_2}}{N_{\text{diesel}}} \quad (\text{Eq. B.2})$$

#### **B.4 Liquid Sample Analysis Methods**

The analysis of the hexane rich samples which were collected after DSR and ATR experiments and separated from their water content were performed by the application of two analysis methods. Firstly, all samples were analyzed with simulated-distillation analysis (SIM-DIS, ASTM D7169.23648) using a high temperature gas chromatography to determine the range of hydrocarbons present in the sample. This analysis showed the presence of hydrocarbons qualitatively. According to the results of SIM-DIS analysis, some of the samples were further analyzed quantitatively with high-resolution gas chromatography (DHA, ASTM D6730-01), in detail. Both analyses were performed by the standard test methods given below.

*Astm D7169.23648: Standard Test Method For Boiling Point Distribution Of Samples With Residues Such As Crude Oils And Atmospheric And Vacuum Residues By High Temperature Gas Chromatography – Sim-Dis:*

This test method covers the determination of the boiling point distribution of crude oils and residues by using high temperature gas chromatography. Capillary column and flame ionization detector were used. Table B.4 shows the gas chromatography conditions suggested in the ASTM D7169.23648 document.

Table B.4 Typical gas chromatographic conditions (ASTM D7169.23648)

INITIAL OVEN TEMPERATURE	-20 °C
OVEN TEMPERATURE PROGRAM	15 °C/min
FINAL OVEN TEMPERATURE	425 °C to 435 °C
FINAL HOLD TIME	10 min
INLET INITIAL TEMPERATURE	50 °C
INLET TEMPERATURE PROGRAM	15 °C/min
INLET FINAL TEMPERATURE	425 °C
COLUMN	5 m × 0.53 mm × 0.09B -0.15 µm PDMS (polydimethylsiloxane)
COLUMN FLOW	20 mL/min
CARRIER CONTROL	Constant Flow
DETECTOR	FID
DETECTOR TEMPERATURE	435 °C
DETECTOR GASES:	
HYDROGEN	40 mL/min
AIR	450 mL/min
MAKE-UP (N <sub>2</sub> , HE)	15 mL/min
VOLUME INJECTED	0.2 µL-0.5 µL-1.0 µL
SAMPLE CONCENTRATION	2% (m/m)

*ASTM D6730-01: Standard Test Method for Determination of Individual Components in Spark Ignition Engine Fuels by 100–Metre Capillary (with Precolumn) High-Resolution Gas Chromatography – DHA:*

This test method covers the determination of light liquid hydrocarbon mixtures typically encountered in petroleum refining operations, such as blending stocks (naphthas, reformates, alkylates, and so forth). The minimum detectable component composition is 0.01 % by weight.

Sample of the petroleum liquid was analyzed with a gas chromatograph equipped with an open tubular (capillary) column coated with a methyl silicone liquid phase, modified with a capillary precolumn. Helium was used as the carrier gas which transports the vaporized sample through the column, in which it is partitioned into individual components which are sensed with a flame ionization detector as they elute from the end of the column. The column used for this operation should have the properties given in Table B.5 and GC operating conditions were presented in Table B.6, according to the standard ASTM D6730-01.

Table B.5 Column properties (ASTM D6730-01)

<b>MATERIAL</b>	fused silica
<b>LENGTH</b>	100 m
<b>INTERNAL DIAMETER</b>	0.25 mm
<b>LIQUID PHASE</b>	methyl silicone
<b>FILM THICKNESS</b>	0.50 $\mu\text{m}$
<b>THEORETICAL PLATES, N, PENTANE AT 35 °C</b>	~400 000 to 500 000
<b>RETENTION FACTOR, K, PENTANE AT 35 °C</b>	0.45 to 0.50
<b>RESOLUTION, R, T-BUTANOL AND 2-METHYLBUTENE-2 AT 35 °C</b>	3.25 to 5.25
<b>PEAK SYMMETRY, T-BUTANOL AT 35 °C</b>	> 1.0 to < 5.0
<b>PRE-COLUMN PROPERTIES</b>	variable length (1 m to 4 m) of 5 % phenyl/95 % dimethylpolysiloxane fused silica open tubular column (0.25 mm inside diameter)

Table B.6 GC Operating Conditions (ASTM D6730-01)

<b>COLUMN TEMPERATURE PROGRAM</b>	
<b>INITIAL TEMPERATURE</b>	5 °C
<b>INITIAL TIME</b>	10 Min
<b>FIRST PROGRAM RATE</b>	5.0 °C/Min
<b>FIRST HOLD TEMPERATURE</b>	50 °C
<b>FIRST HOLD TIME</b>	~50 Min
<b>SECOND PROGRAM RATE</b>	1.5 °C/Min
<b>FINAL TEMPERATURE</b>	200 °C
<b>FIRST HOLD TEMPERATURE</b>	5 Min
<b>INJECTOR</b>	
<b>TEMPERATURE</b>	250 °C
<b>SPLIT RATIO</b>	150:1
<b>SAMPLE SIZE</b>	0.1 Ml -0.2 Ml
<b>DETECTOR</b>	
<b>TYPE</b>	Flame Ionization
<b>TEMPERATURE</b>	250 °C
<b>DETECTOR GASES:</b>	
<b>HYDROGEN</b>	30 Ml/Min
<b>AIR</b>	300 Ml/Min
<b>MAKE-UP (N<sub>2</sub>)</b>	20 Ml/Min
<b>CARRIER GAS</b>	
<b>TYPE</b>	Helium
<b>PRESSURE</b>	~277 Kpa (40 Psig)
<b>AVERAGE LINEAR VELOCITY</b>	24 Cm/S At 35 °C

## B.5 Reactant Flow Rate Calculation Method

Reactant flow rates (diesel and water) and carrier gas flow rate were calculated by specifying the operating conditions which are GHSV and steam to carbon ratio. As mentioned in the method, argon, which was used as the carrier for liquid reactants constitutes of a 60% of the inlet gas stream volumetric flow rate at the entrance of the catalyst bed (800 °C). 40% of the specified total flow rate was diesel and water streams which were calculated according to the specified steam to carbon ratio value. Since, 1 g of catalyst was used in all performed experiments, the diameter of the bed (D=2.5 cm) and the length of the catalyst bed (L=0.4 cm) was kept constant. A sample calculation for diesel steam reforming reaction with a GHSV value of 7500 h<sup>-1</sup> and a steam to carbon ratio of 2.5 is given below. A steam to carbon ratio value of 2.5 indicates that for each mol of diesel (C<sub>17</sub>H<sub>36</sub>), 42.5 mol of water is required.

The below part of the calculation shows the flow rates at the reaction temperature (800 °C).

$$\text{GHSV}=7500$$

$$\text{H}_2\text{O}/\text{C}=2.5$$

$$D=2.5 \text{ cm}$$

$$L=0.4 \text{ cm}$$

$$V_{\text{cat}}=3.14 \times D^2/4L=1.963 \text{ cm}^3$$

$$Q_{\text{gas}}=\text{GHSV} \times V_{\text{cat}}=14720 \text{ cm}^3/\text{h}$$

$$Q_{\text{water\&diesel}}=Q_{\text{gas}} \times 2/5=5888 \text{ cm}^3/\text{h}$$

$$Q_{\text{diesel}}=Q_{\text{water\&diesel}}/43.5=135.345 \text{ cm}^3/\text{h}$$

$$Q_{\text{water}}=Q_{\text{water\&diesel}} \times 42.5/43.5=5752 \text{ cm}^3/\text{h}$$

In order to calculate the water and diesel flow rates at room temperature, ideal gas law was used to convert gas flow rates at 800°C to molar flow rates. Molecular weight of diesel was assumed to be the same as the molecular weight of C<sub>17</sub>H<sub>36</sub> and density of diesel was obtained from diesel analysis results.

$$P=1.05 \times 10^5 \text{ atm}$$

$$R=8.314$$

$$T=1073 \text{ K}$$

$$N_{\text{diesel}}=P \times Q_{\text{diesel}} \times 10^{-6} / (R \times T) = 1.593 \times 10^{-3}$$

$$Q_{\text{diesel}}^{25\text{C}} = N_{\text{diesel}} \times MW_{\text{diesel}} / \rho_{\text{diesel}} = \mathbf{0.455 \text{ ml/h}}$$

$$N_{\text{water}}=P \times Q_{\text{water}} \times 10^{-6} / (R \times T) = 0.068$$

$$Q_{\text{water}}^{25\text{C}} = N_{\text{water}} \times MW_{\text{water}} / \rho_{\text{water}} = \mathbf{1.219 \text{ ml/h}}$$

$$Q_{\text{argon}}^{800\text{C}} = Q_{\text{gas}} \times 3 / (5 \times 60) = 147.2 \text{ ml/min}$$

$$Q_{\text{argon}}^{25\text{C}} = Q_{\text{argon}}^{800\text{C}} \times 298 / 1073 = \mathbf{40.878 \text{ ml/min}}$$

For diesel autothermal reforming reaction, the flow rate calculation of diesel and water was exactly the same, the only difference was instead of using 40.8 ml/min argon, the necessary amount of air feed was calculated according to oxygen to carbon ratio and the resulting flow rate of air and the flow rate of argon corresponded to 40.8 ml/min total gas flow rate.

### C. Hexadecane Reforming Test Results

In order to confirm the calculations made for diesel reforming reactions, n-hexadecane ( $C_{16}H_{34}$ ) which has been used as a substitute for diesel, was also tested for both steam reforming (HSR, C.R.1) and autothermal reforming (HAR, C.R.2) reactions and results were compared with the results of diesel at the same experimental conditions.



For n-hexadecane steam reforming reaction, two catalysts were tested at the selected conditions and compared with the results of the diesel steam reforming reaction with the same catalyst. Hydrogen yield calculation was made by making the same assumptions that were made for diesel and presented in equation Eq. C1-C3. In this case, carbon number is 16 and theoretical maximum  $H_2$  mole produced from diesel is 33 according to C.R.1.

$$\dot{N}_{n\text{-hexadecane}} = \frac{(N_{\text{product,CO}} + N_{\text{product,CH}_4} + N_{\text{product,CO}_2} + N_{\text{product,C}_2\text{H}_4} \times 2 + N_{\text{product,C}_2\text{H}_6} \times 2)}{\text{Carbon number of n-hexadecane}} \quad (\text{Eq. C.1})$$

$$H_2 \text{ yield} = \frac{N_{\text{product,H}_2}}{\dot{N}_{n\text{-hexadecane,from product gases}}} \quad (\text{Eq. C.2})$$

$$y_{H_2} \% = \frac{H_2 \text{ yield}}{\text{Theoretical maximum } H_2 \text{ mole produced from 1 mole of n-hexadecane}} \times 100 \quad (\text{Eq. C.3})$$

Product gas distribution obtained in HSR with Ni@Al<sub>2</sub>O<sub>3</sub> catalyst is presented in Figure C.1. Gas composition was stable throughout the experiment.

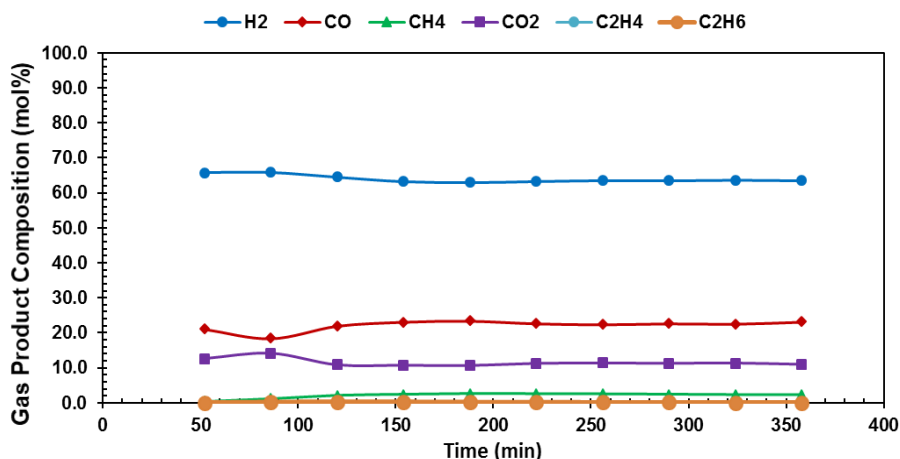


Figure C.1. Change of product molar gas composition with respect to time for n-hexadecane steam reforming reaction with the Ni@Al<sub>2</sub>O<sub>3</sub> catalyst (GHSV=7500, H<sub>2</sub>O/C=2.5, 800 °C).

HSR experiment was also performed with the Ni@20CeO<sub>2</sub>@Al<sub>2</sub>O<sub>3</sub> catalyst and product gas composition is presented in Figure C.2.

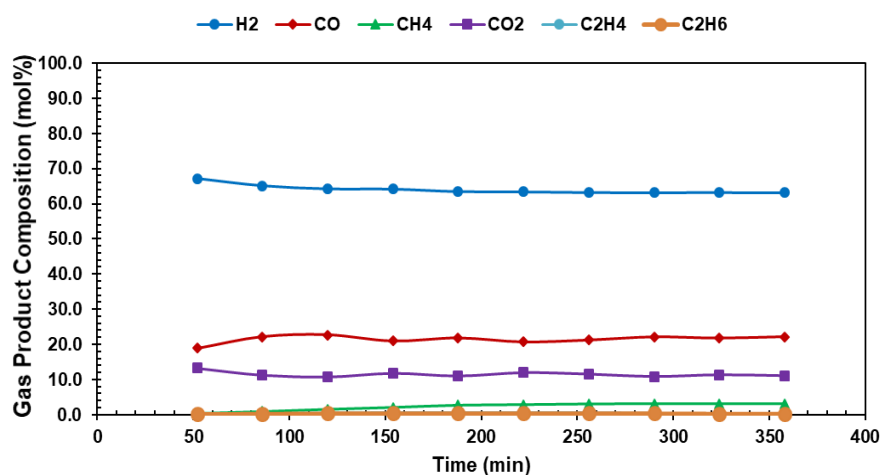


Figure C.2. Change of product molar gas composition (molar %) with respect to time for n-hexadecane steam reforming reaction with the Ni@20CeO<sub>2</sub>@Al<sub>2</sub>O<sub>3</sub> catalyst (GHSV=7500, H<sub>2</sub>O/C=2.5, 800 °C).

Product gas compositions that were obtained with Ni@20CeO<sub>2</sub>@Al<sub>2</sub>O<sub>3</sub> catalysts for n-hexadecane autothermal reforming reaction were presented in Figure C.3

together with maximum hydrogen production limits of HAR. Results were stable in terms of hydrogen and side products production.

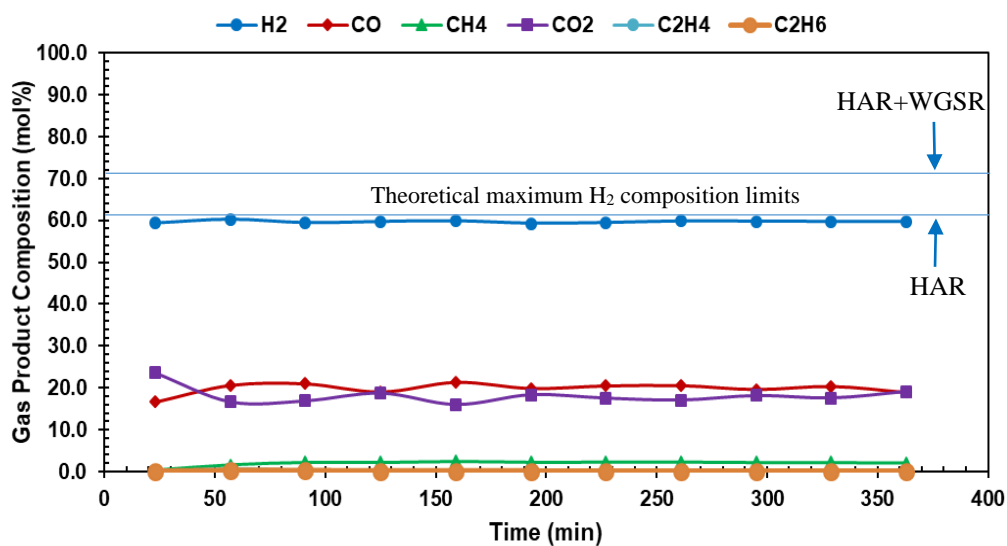


Figure C.3. Change of product molar gas composition with respect to time for n-hexadecane autothermal reforming reaction with the Ni@20CeO<sub>2</sub>@Al<sub>2</sub>O<sub>3</sub> catalyst (GHSV=7500, H<sub>2</sub>O/C=2.5, O<sub>2</sub>/C=0.5, 800 °C).



## D. Liquid product analysis results

The analysis results of liquid samples collected after diesel steam and autothermal reforming experiments are presented in this section. Procedure of liquid sample analysis was described in detail in Chapter 3.4.

Figures D.1-D.5 show the simulated distillation (SIM-DIS) analysis results of liquid hexane rich samples of the experiments performed at GHSV range of 5000 h<sup>-1</sup>, and 17000 h<sup>-1</sup>. All results show the presence of trace amounts of hydrocarbons, which could be due to the impurities present in the used hexane solvent. It can be safely assumed that there is no measurable amount of hydrocarbon in liquid samples collected after steam reforming experiments. In order further prove this assumption, the sample of the experiment performed with a GHSV value of 10000 h<sup>-1</sup> was analyzed by detailed hydrocarbon analysis method (DHA) that was explained in Section 3.4 (ASTM D6730-01). The results of detailed hydrocarbon analysis showed the presence of hydrocarbons corresponding to only 0.1% (molar) of the total diesel feed.

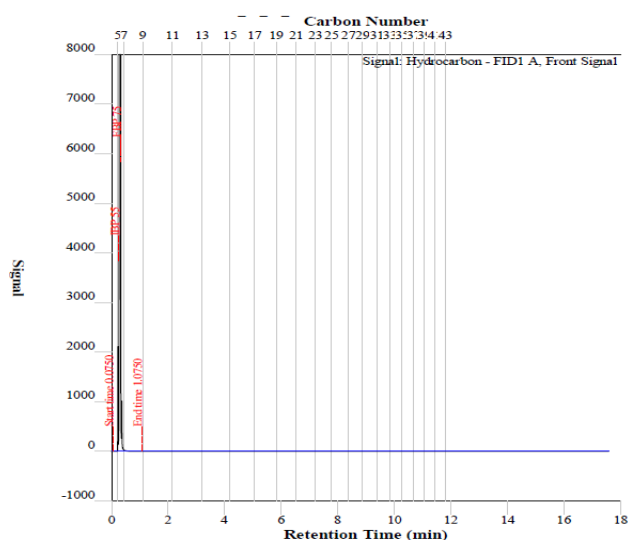


Figure D.1 SIM-DIS result of the experiment: DSR, GHSV=5000 h<sup>-1</sup>, H<sub>2</sub>O/C=2.5,  
Ni@20CeO<sub>2</sub>@Al<sub>2</sub>O<sub>3</sub>

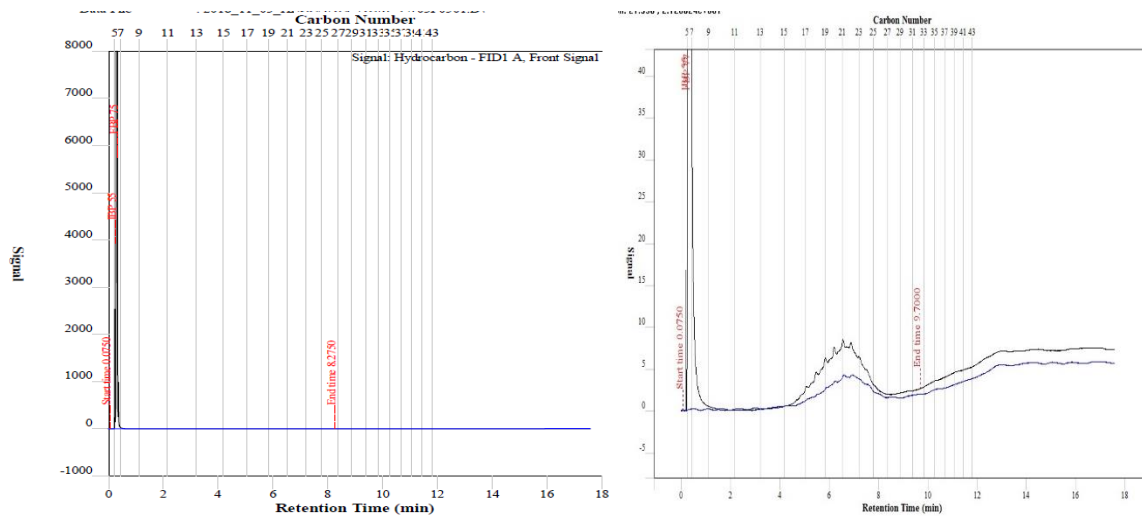


Figure D.2 SIM-DIS result of the experiment (left: SIM-DIS result, right: zoomed result) DSR, GHSV=7500 h<sup>-1</sup>, H<sub>2</sub>O/C=2.5, Ni@20CeO<sub>2</sub>@Al<sub>2</sub>O<sub>3</sub>

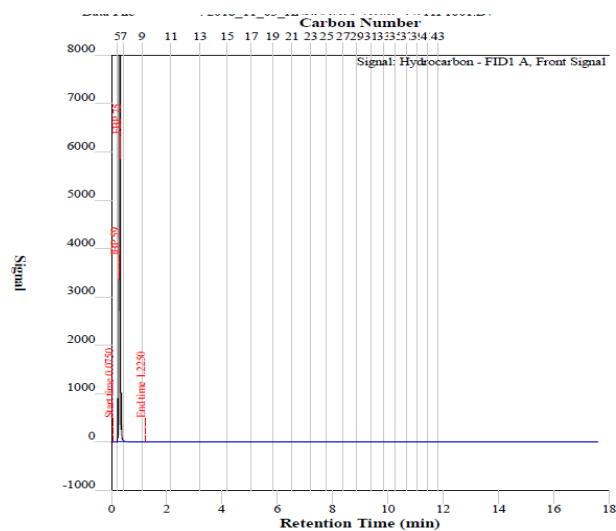


Figure D.3 SIM-DIS result of the experiment: DSR, GHSV=10000 h<sup>-1</sup>, H<sub>2</sub>O/C=2.5, Ni@20CeO<sub>2</sub>@Al<sub>2</sub>O<sub>3</sub>

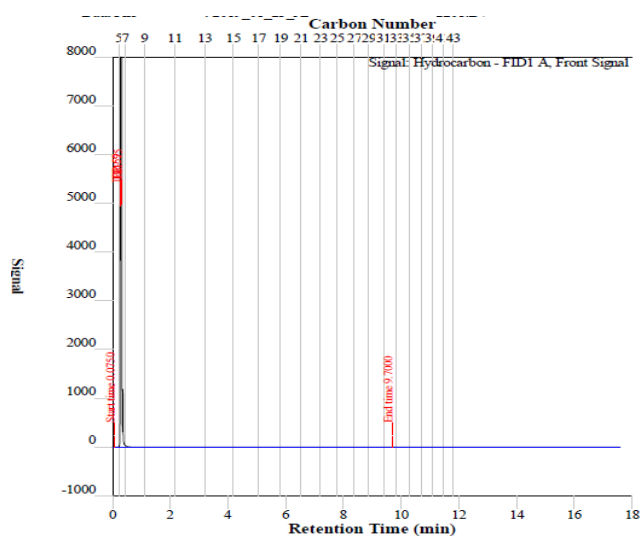


Figure D.4 SIM-DIS result of the experiment: DSR, GHSV=17000 h<sup>-1</sup>, H<sub>2</sub>O/C=2.5,  
Ni@20CeO<sub>2</sub>@Al<sub>2</sub>O<sub>3</sub>

Prior to the analysis at Tüpraş R&D Center laboratories, two of the samples collected after the diesel steam reforming experiments (Ni@20CeO<sub>2</sub>@Al<sub>2</sub>O<sub>3</sub> catalyst, at: 800°C, GHSV=25000 h<sup>-1</sup> and H<sub>2</sub>O/C=2.5) & (Ni@20CeO<sub>2</sub>@Al<sub>2</sub>O<sub>3</sub> catalyst, at: 800°C, GHSV=7500 h<sup>-1</sup> and H<sub>2</sub>O/C=2.5) were analyzed by METU Petroleum Analysis Laboratory to validate the used EPA-1664 method for the separation of water rich phase from the hydrocarbon phase of the collected sample. Results obtained from METU-PAL through the analysis of water rich samples and hexane rich samples separated using EPA-1664 method are presented below. Quantitative GC analysis results of the hexane rich sample of the experiment performed with the Ni@20CeO<sub>2</sub>@Al<sub>2</sub>O<sub>3</sub> catalyst at a temperature of 800°C, a GHSV value of 7500 h<sup>-1</sup> and a H<sub>2</sub>O/C ratio of 2.5 did not show any hydrocarbon compounds, similar to the result obtained through SIM-DIS analysis (Figure D.2). This means that complete conversion was achieved at the selected optimum operating conditions. Qualitative GC-MS analysis results of water rich phase of the same sample is given on Figure D.5. Presence of some aromatic components were observed in the water sample such as; phenol, benzaldehyde, acetophenon etc. Quantitative GC analysis results of the hexane rich sample of the experiment performed with Ni@20CeO<sub>2</sub>@Al<sub>2</sub>O<sub>3</sub> catalyst at a temperature of 800°C, a GHSV value of 25000 h<sup>-1</sup> and a H<sub>2</sub>O/C ratio of 2.5 are

presented in Figure-D.6 and Table D.1. The analysis of hydrocarbons that have carbon numbers less than 10 could not be performed by PAL. Content of hexane was assumed to consist of only alkanes. The analysis results of the sample did not show the presence of hydrocarbons that have higher carbon number than 21. Total molar amount of hydrocarbons in the hexane rich sample was calculated and presented on Table D.1, using PAL GC results. Total molar amount of diesel used for six hours of reaction time is 0.0318 mol. However total molar amount of hydrocarbons in hexane sample is  $2.74 \times 10^{-5}$  mol which consists of about 0.09% of used diesel. Analysis results qualitative GC-MS analysis result of water rich sample of the same experiment is given in Figure D.7. The most common component in the water sample was naphthalene and naphthalene compounds. The presence of naphthalene was expected due to the smell of the liquid products. Rest of the sample, other than water, was composed of majorly aromatic compounds, similar to the previous sample results.

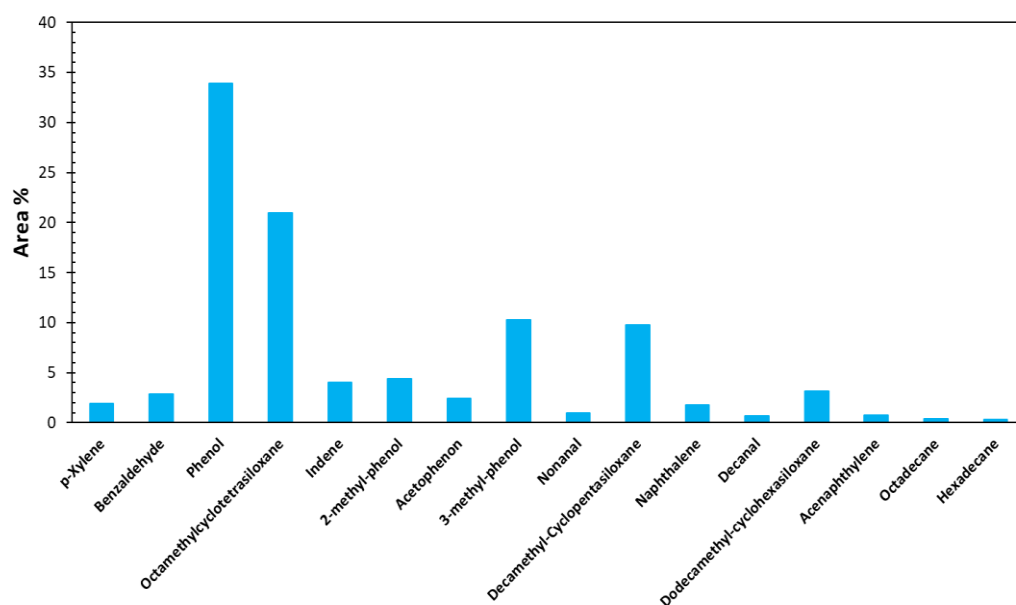


Figure D.5 GC-MS analysis results of water rich sample of the experiment performed with Ni@20CeO<sub>2</sub>@Al<sub>2</sub>O<sub>3</sub> catalyst, at: 800°C, GHSV=7500 h<sup>-1</sup> and H<sub>2</sub>O/C=2.5.

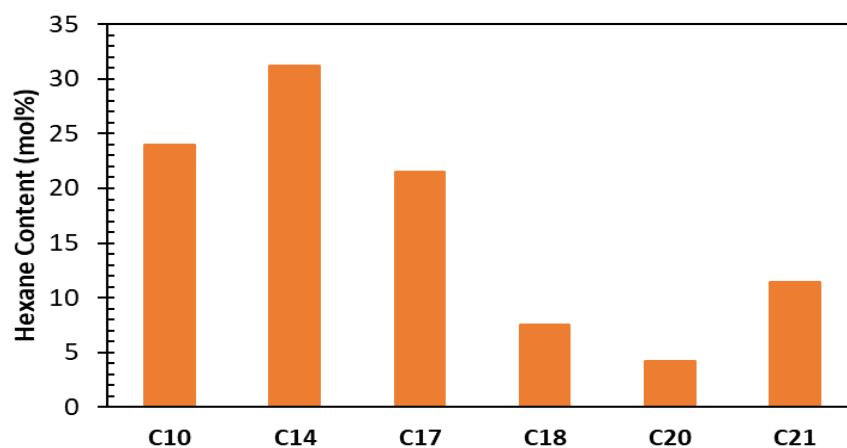


Figure D.6 GC analysis results of hexane rich sample of the experiment performed with Ni@20CeO<sub>2</sub>@Al<sub>2</sub>O<sub>3</sub> catalyst, at: 800°C, GHSV=25000 h<sup>-1</sup> and H<sub>2</sub>O/C=2.5.

Table D.1 Amount of hydrocarbons in the collected liquid sample according to GC analysis results (Ni@20CeO<sub>2</sub>@Al<sub>2</sub>O<sub>3</sub>, 800°C, GHSV=25000 h<sup>-1</sup> and H<sub>2</sub>O/C=2.5)

Component	Collected Total Amount (mol)
C10	$6.59 \times 10^{-6}$
C14	$8.57 \times 10^{-6}$
C17	$5.89 \times 10^{-6}$
C18	$2.08 \times 10^{-6}$
C20	$1.17 \times 10^{-6}$
C21	$3.13 \times 10^{-6}$

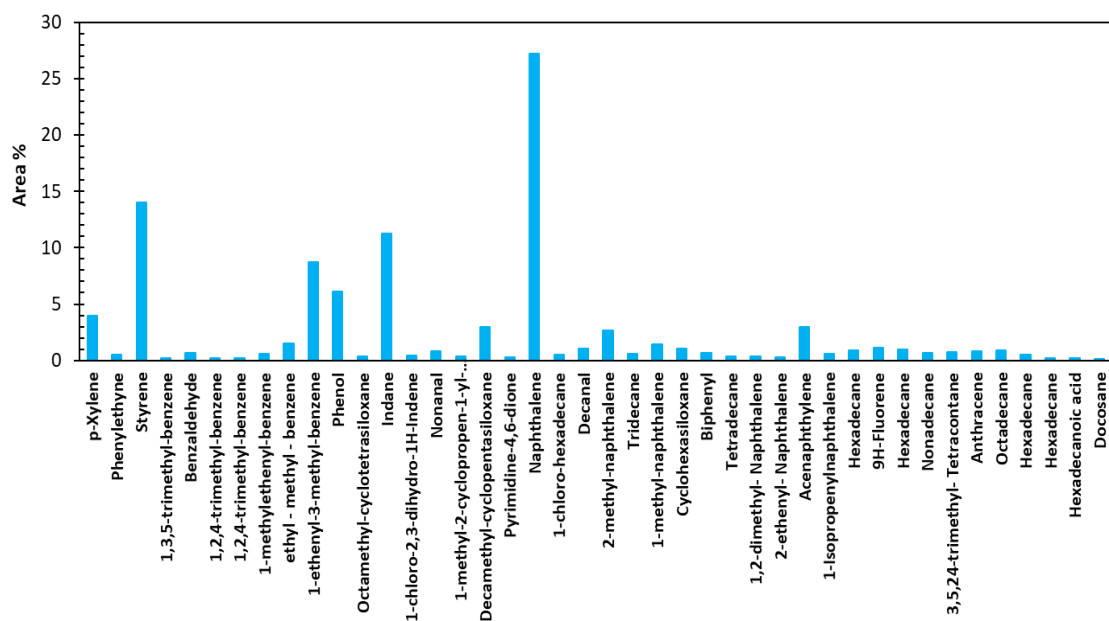


Figure D.7 GC-MS analysis results of water rich sample of the experiment performed with Ni@20CeO<sub>2</sub>@Al<sub>2</sub>O<sub>3</sub> catalyst, at: 800°C, GHSV=25000 h<sup>-1</sup> and H<sub>2</sub>O/C=2.5.

Figures D.8 and D.9 show SIM-DIS results of the hexane rich samples of the experiments conducted by using a H<sub>2</sub>O/C ratio of 2.0 and 1.5. Similarly, there were only trace amount of hydrocarbons present in the liquid samples. Figures through D.10 to D.14 show the SIM-DIS results of the hexane rich samples of the GHSV optimization experiments of ATR reaction. Experiments performed with GHSV values of 5000, 7500, 10000, 17000 and 25000 h<sup>-1</sup> showed no hydrocarbon presence on the SIM-DIS results given in Figures D.10, D.11, D.12, D.13 and D.14.

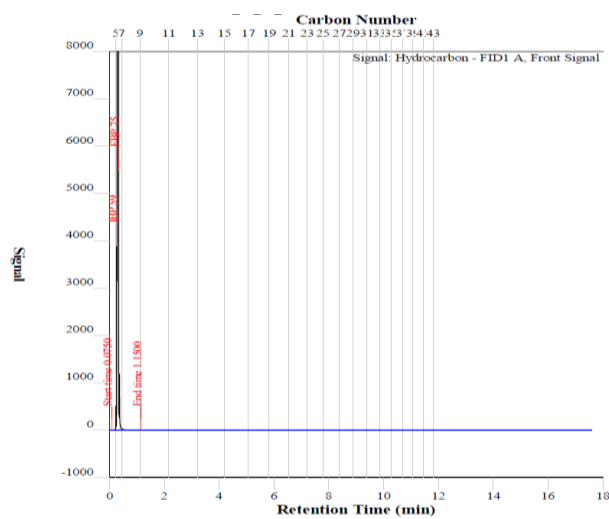


Figure D.8 SIM-DIS result of the experiment: DSR, GHSV=7500 h<sup>-1</sup>, H<sub>2</sub>O/C=2.0, Ni@20CeO<sub>2</sub>@Al<sub>2</sub>O<sub>3</sub>

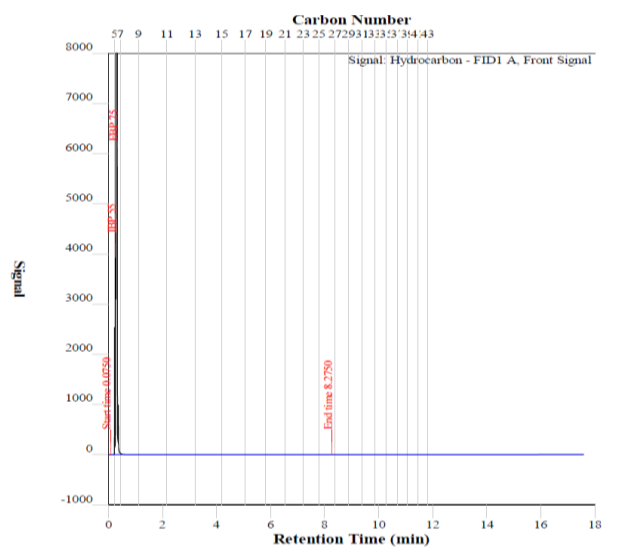


Figure D.9 SIM-DIS result of the experiment: DSR, GHSV=7500 h<sup>-1</sup>, H<sub>2</sub>O/C=1.5, Ni@20CeO<sub>2</sub>@Al<sub>2</sub>O<sub>3</sub>

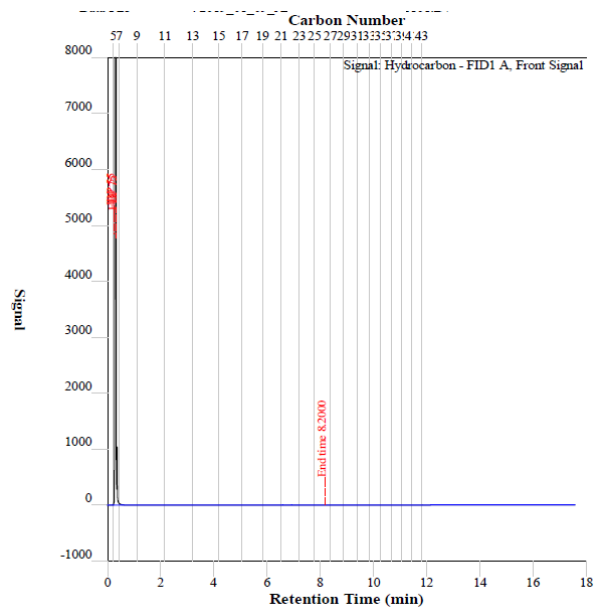


Figure D.10 SIM-DIS result of the experiment: ATR, GHSV=5000 h<sup>-1</sup>, H<sub>2</sub>O/C=2.5, O<sub>2</sub>/C=0.5, Ni@20CeO<sub>2</sub>@Al<sub>2</sub>O<sub>3</sub>

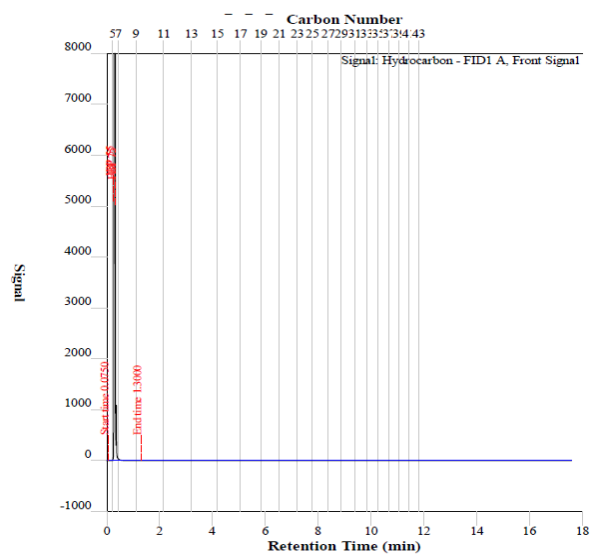


Figure D.11 SIM-DIS result of the experiment: ATR, GHSV=7500 h<sup>-1</sup>, H<sub>2</sub>O/C=2.5, O<sub>2</sub>/C=0.5, Ni@20CeO<sub>2</sub>@Al<sub>2</sub>O<sub>3</sub>

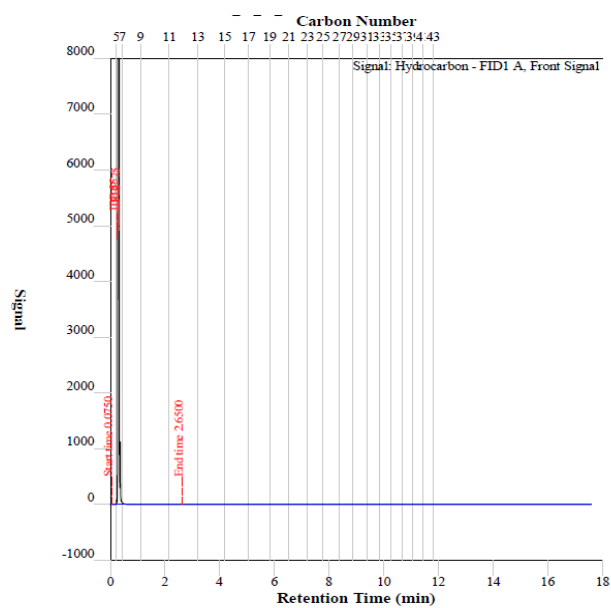


Figure D.12 SIM-DIS result of the experiment: ATR, GHSV=10000 h<sup>-1</sup>, H<sub>2</sub>O/C=2.5, O<sub>2</sub>/C=0.5, Ni@20CeO<sub>2</sub>@Al<sub>2</sub>O<sub>3</sub>

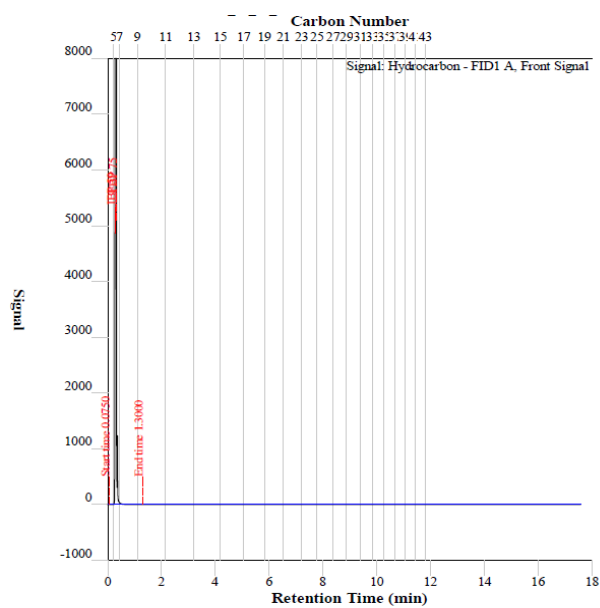


Figure D.13 SIM-DIS result of the experiment: ATR, GHSV=17000 h<sup>-1</sup>, H<sub>2</sub>O/C=2.5, O<sub>2</sub>/C=0.5, Ni@20CeO<sub>2</sub>@Al<sub>2</sub>O<sub>3</sub>

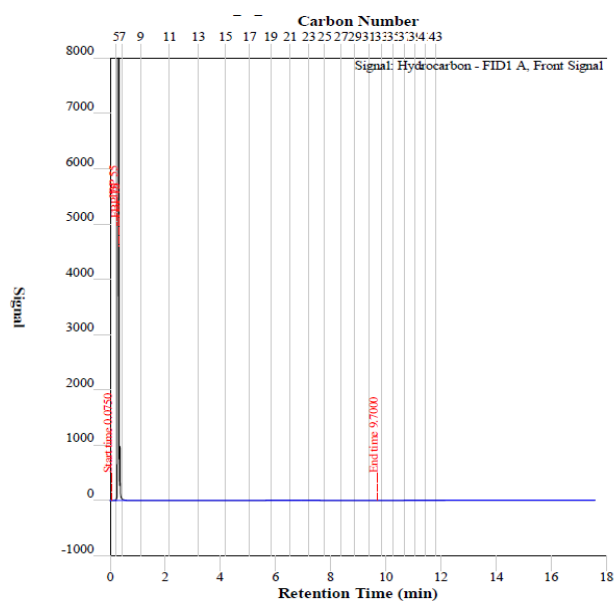


Figure D.14 SIM-DIS result of the experiment: ATR, GHSV=25000 h<sup>-1</sup>, H<sub>2</sub>O/C=2.5, O<sub>2</sub>/C=0.5, Ni@20CeO<sub>2</sub>@Al<sub>2</sub>O<sub>3</sub>

Figures through D.15 and D.25 show the SIM-DIS results of the hexane rich sample of the DSR experiments conducted with commercial alumina supported catalysts; namely Ni@Al<sub>2</sub>O<sub>3</sub>, Ni@10CeO<sub>2</sub>@Al<sub>2</sub>O<sub>3</sub>, Ni@20CeO<sub>2</sub>@Al<sub>2</sub>O<sub>3</sub>, Ni@10W-10CeO<sub>2</sub>@Al<sub>2</sub>O<sub>3</sub>, Ni@20W@Al<sub>2</sub>O<sub>3</sub>, Ni@0.5Ru@Al<sub>2</sub>O<sub>3</sub>, Ni@1.0Ru@Al<sub>2</sub>O<sub>3</sub>, Ni@1.5Ru@Al<sub>2</sub>O<sub>3</sub>, Ni@1.5Ru@10CeO<sub>2</sub>@Al<sub>2</sub>O<sub>3</sub>, 1.5Ru@10CeO<sub>2</sub>@Al<sub>2</sub>O<sub>3</sub>, and Ni@1.5Ru@20CeO<sub>2</sub>@Al<sub>2</sub>O<sub>3</sub>. Similarly, the analysis results showed only trace amounts of hydrocarbons.

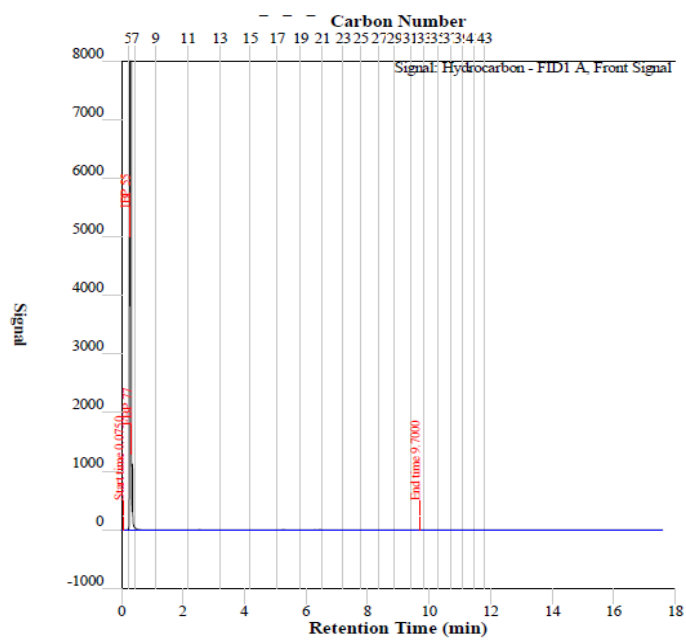


Figure D.15 SIM-DIS result of the experiment: DSR, GHSV=7500 h<sup>-1</sup>, H<sub>2</sub>O/C=2.5, Ni@Al<sub>2</sub>O<sub>3</sub>

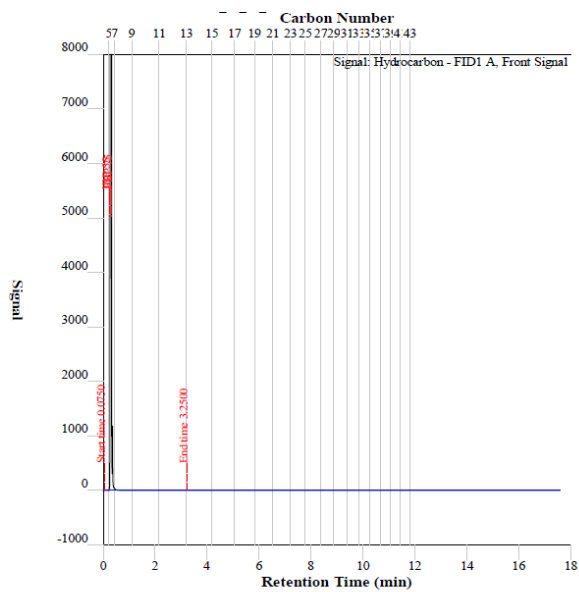


Figure D.16 SIM-DIS result of the experiment: DSR, GHSV=7500 h<sup>-1</sup>, H<sub>2</sub>O/C=2.5, Ni@10CeO<sub>2</sub>@Al<sub>2</sub>O<sub>3</sub>

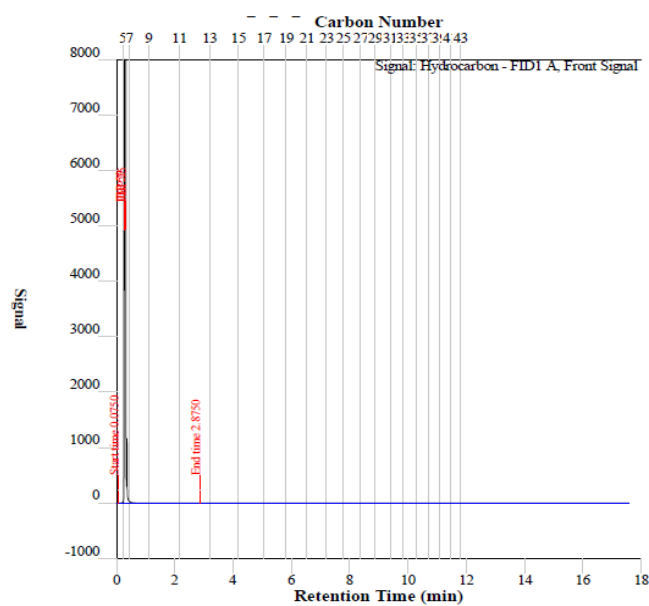


Figure D.17 SIM-DIS result of the experiment: DSR, GHSV=7500 h<sup>-1</sup>, H<sub>2</sub>O/C=2.5, Ni@20CeO<sub>2</sub>@Al<sub>2</sub>O<sub>3</sub>

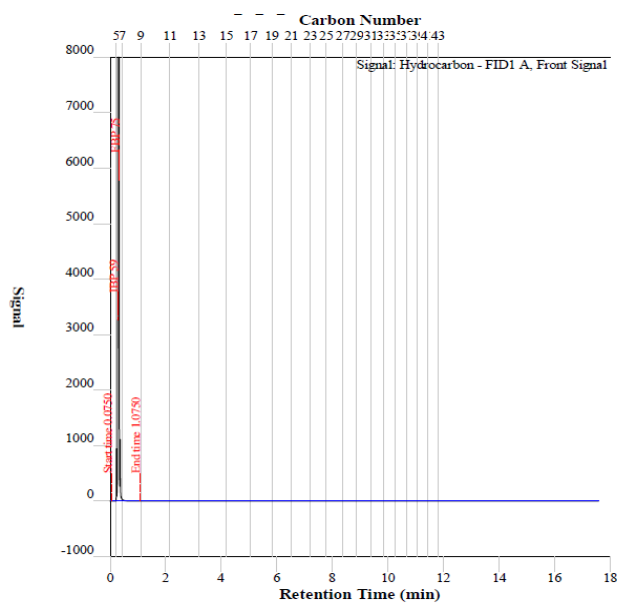


Figure D.18 SIM-DIS result of the experiment: DSR, GHSV=7500 h<sup>-1</sup>, H<sub>2</sub>O/C=2.5, Ni@10W-10CeO<sub>2</sub>@Al<sub>2</sub>O<sub>3</sub>

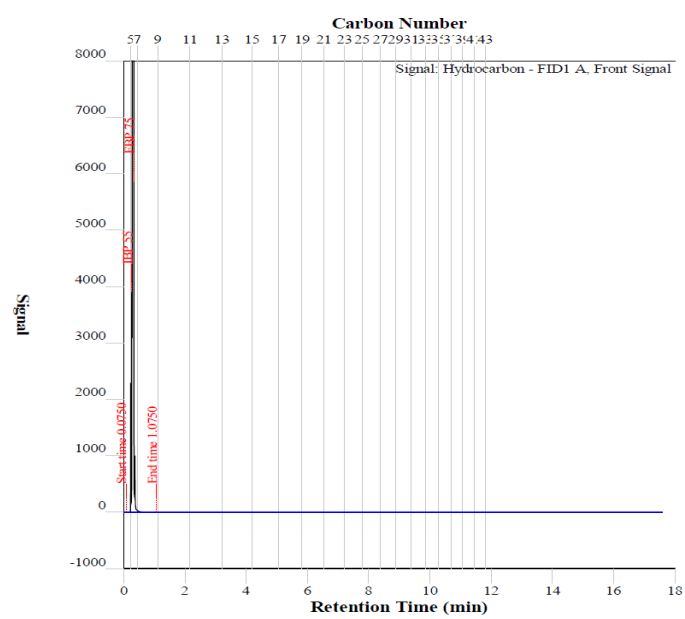


Figure D.19 SIM-DIS result of the experiment: DSR, GHSV=7500 h<sup>-1</sup>, H<sub>2</sub>O/C=2.5, Ni@20W@Al<sub>2</sub>O<sub>3</sub>

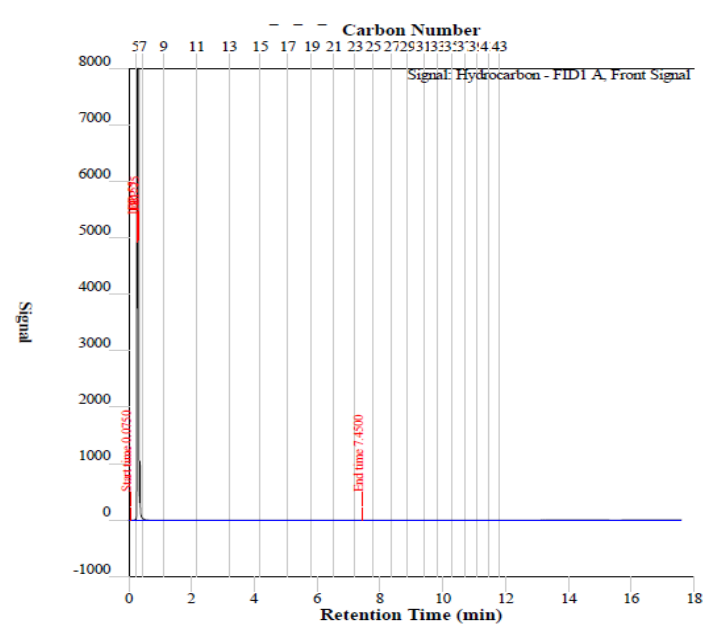


Figure D.20 SIM-DIS result of the experiment: DSR, GHSV=7500 h<sup>-1</sup>, H<sub>2</sub>O/C=2.5, Ni@0.5Ru@Al<sub>2</sub>O<sub>3</sub>

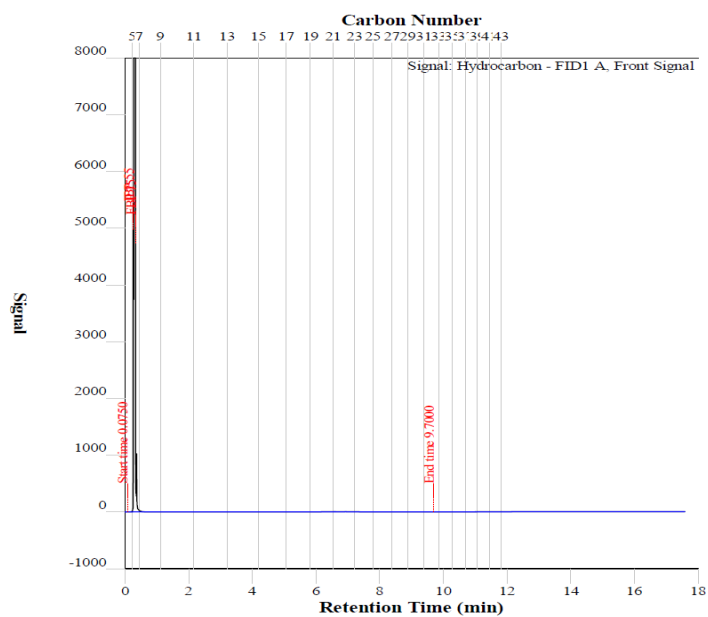


Figure D.21 SIM-DIS result of the experiment: DSR, GHSV=7500 h<sup>-1</sup>, H<sub>2</sub>O/C=2.5, Ni@1.0Ru@Al<sub>2</sub>O<sub>3</sub>

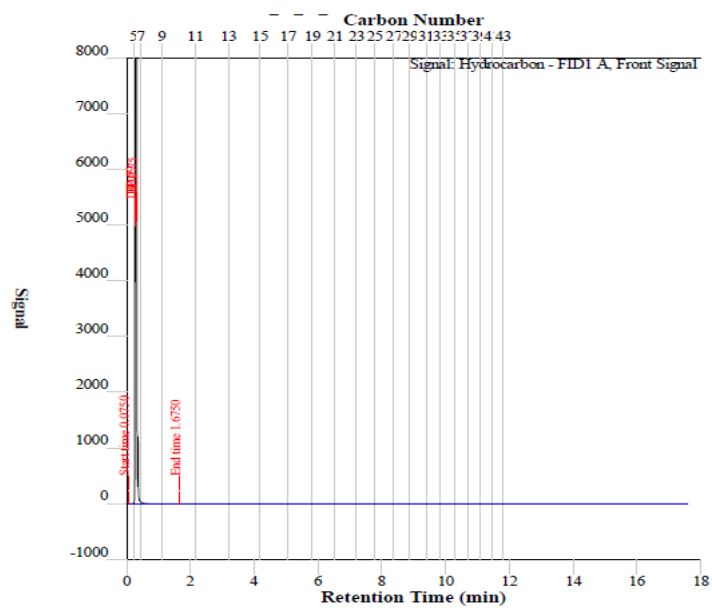


Figure D.22 SIM-DIS result of the experiment: DSR, GHSV=7500 h<sup>-1</sup>, H<sub>2</sub>O/C=2.5, Ni@1.5Ru@Al<sub>2</sub>O<sub>3</sub>

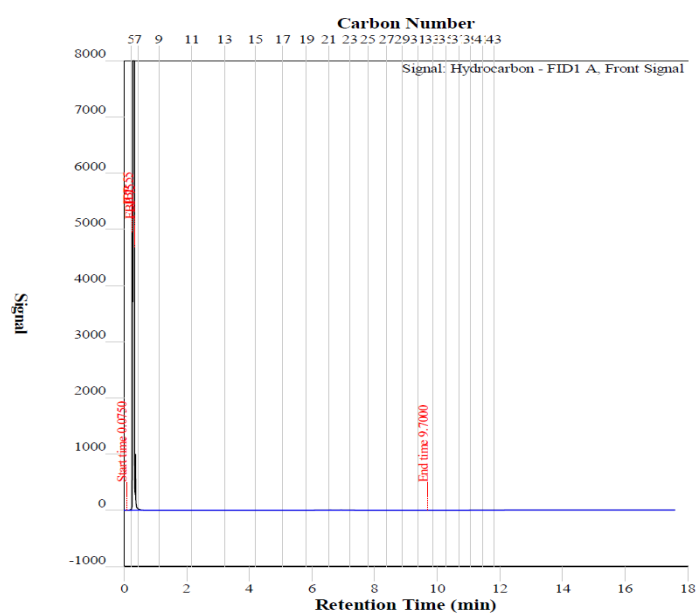


Figure D.23 SIM-DIS result of the experiment: DSR, GHSV=7500 h<sup>-1</sup>, H<sub>2</sub>O/C=2.5, Ni@1.5Ru@10CeO<sub>2</sub>@Al<sub>2</sub>O<sub>3</sub>

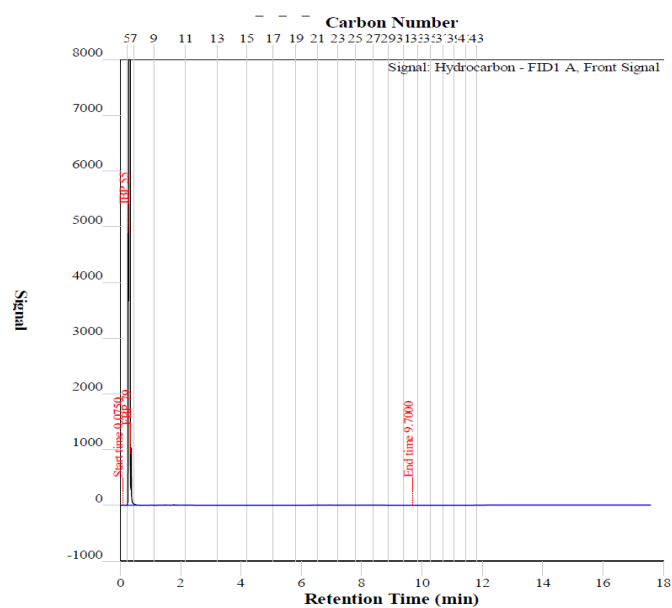


Figure D.24 SIM-DIS result of the experiment: DSR, GHSV=7500 h<sup>-1</sup>, H<sub>2</sub>O/C=2.5, 1.5Ru@20CeO<sub>2</sub>@Al<sub>2</sub>O<sub>3</sub>

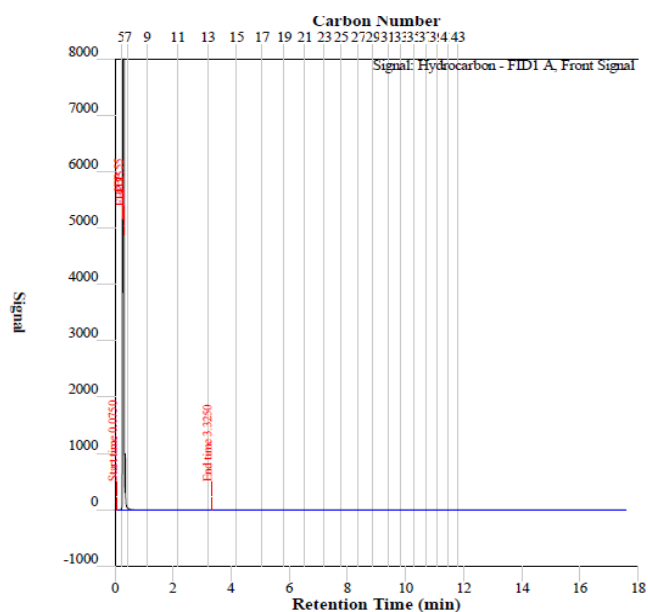


Figure D.25 SIM-DIS result of the experiment: DSR, GHSV=7500 h<sup>-1</sup>, H<sub>2</sub>O/C=2.5, Ni@1.5Ru@20CeO<sub>2</sub>@Al<sub>2</sub>O<sub>3</sub>

Figures through D.26 to D.31 show the SIM-DIS results of the hexane rich sample of the ATR experiments conducted with commercial alumina supported catalysts; namely; Ni@Al<sub>2</sub>O<sub>3</sub>, Ni@10CeO<sub>2</sub>@Al<sub>2</sub>O<sub>3</sub>, Ni@20CeO<sub>2</sub>@Al<sub>2</sub>O<sub>3</sub>, Ni@0.5Ru@Al<sub>2</sub>O<sub>3</sub>, Ni@1.5Ru@Al<sub>2</sub>O<sub>3</sub>, and Ni@1.5Ru@20CeO<sub>2</sub>@Al<sub>2</sub>O<sub>3</sub>. Figure D.32 shows the SIM-DIS result of the long term experiment performed with the Ni@0.5Ru@Al<sub>2</sub>O<sub>3</sub> catalyst. Similarly, analysis results showed trace amounts of hydrocarbons which suggests complete conversion of diesel.

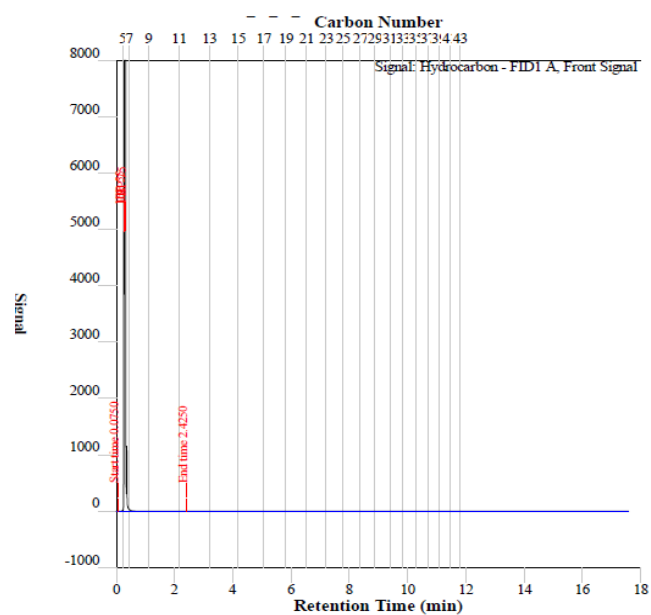


Figure D.26 SIM-DIS result of the experiment: ATR, GHSV=7500 h<sup>-1</sup>, H<sub>2</sub>O/C=2.5, O<sub>2</sub>/C=0.5, Ni@Al<sub>2</sub>O<sub>3</sub>

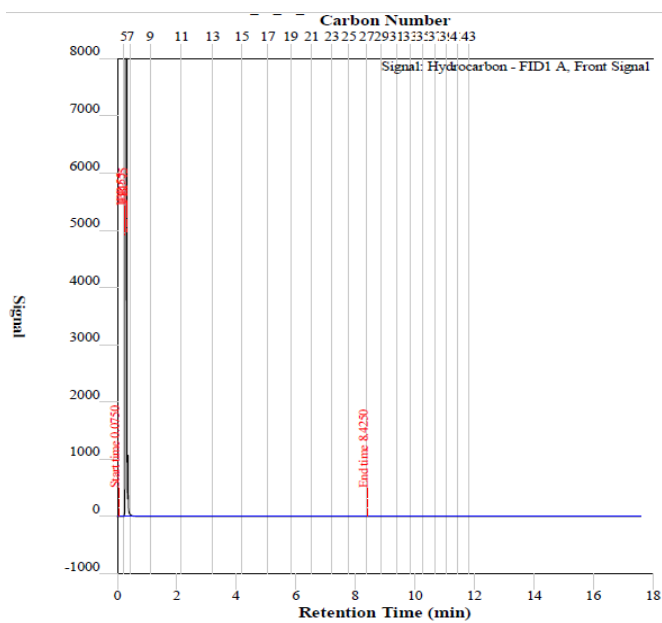


Figure D.27 SIM-DIS result of the experiment: ATR, GHSV=7500 h<sup>-1</sup>, H<sub>2</sub>O/C=2.5, O<sub>2</sub>/C=0.5, Ni@10CeO<sub>2</sub>@Al<sub>2</sub>O<sub>3</sub>

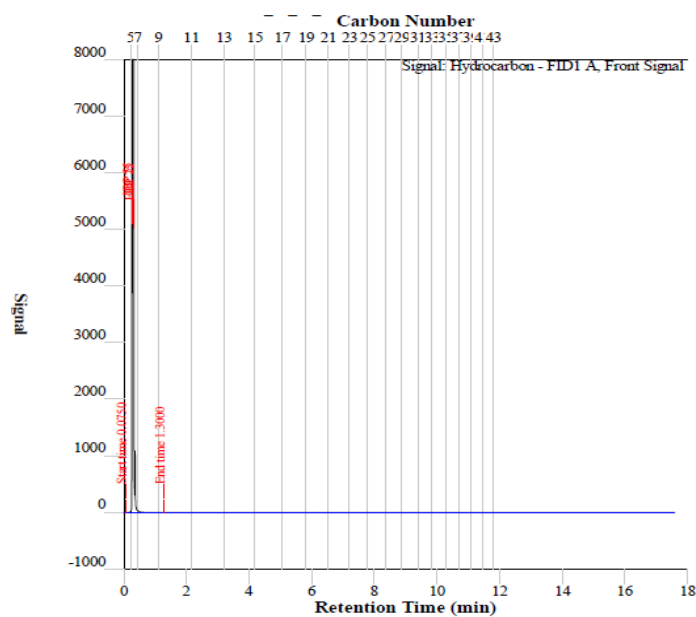


Figure D.28 SIM-DIS result of the experiment: ATR, GHSV=7500 h<sup>-1</sup>, H<sub>2</sub>O/C=2.5, O<sub>2</sub>/C=0.5, Ni@20CeO<sub>2</sub>@Al<sub>2</sub>O<sub>3</sub>

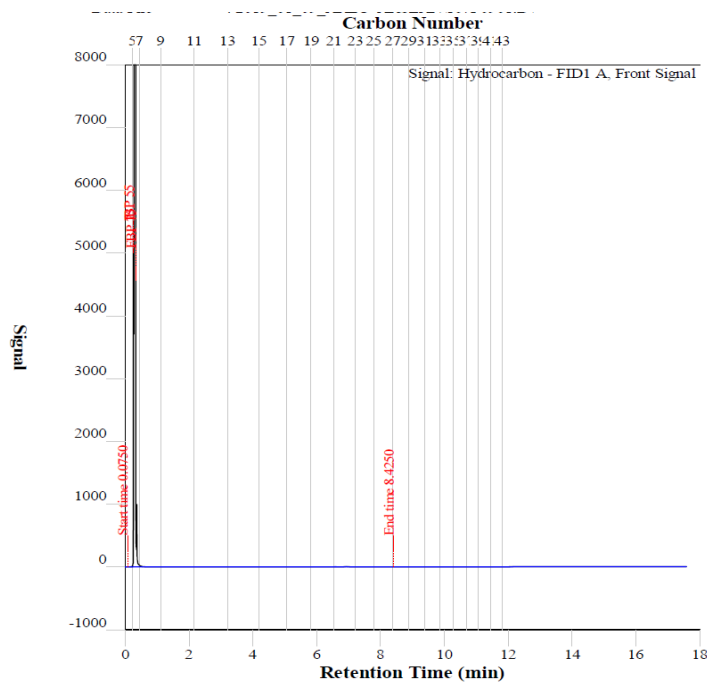


Figure D.29 SIM-DIS result of the experiment: ATR, GHSV=7500 h<sup>-1</sup>, H<sub>2</sub>O/C=2.5, O<sub>2</sub>/C=0.5, Ni@0.5Ru@Al<sub>2</sub>O<sub>3</sub>

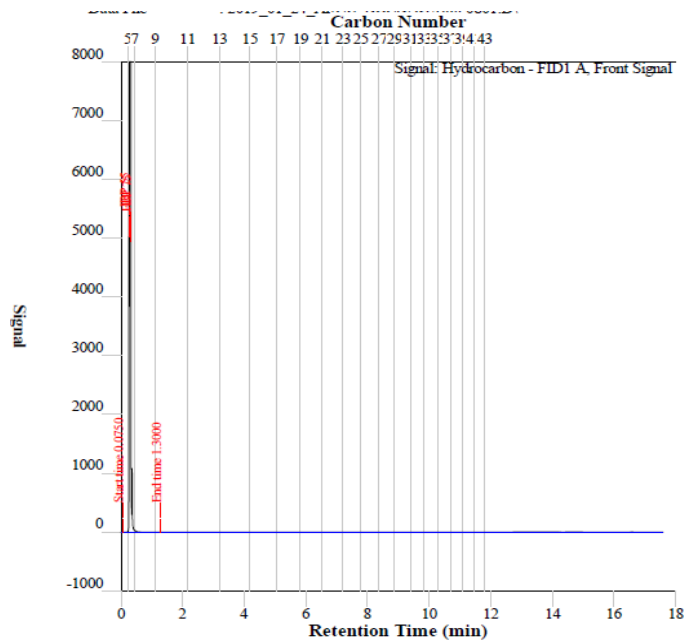


Figure D.30 SIM-DIS result of the experiment: ATR, GHSV=7500 h<sup>-1</sup>, H<sub>2</sub>O/C=2.5, O<sub>2</sub>/C=0.5, Ni@1.5Ru@Al<sub>2</sub>O<sub>3</sub>

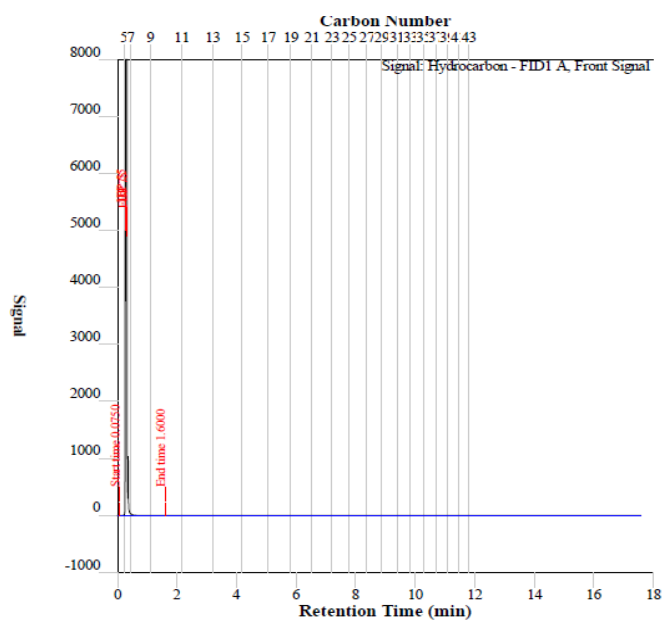


Figure D.31 SIM-DIS result of the experiment: ATR, GHSV=7500 h<sup>-1</sup>, H<sub>2</sub>O/C=2.5, O<sub>2</sub>/C=0.5, Ni@1.5Ru@20CeO<sub>2</sub>@Al<sub>2</sub>O<sub>3</sub>

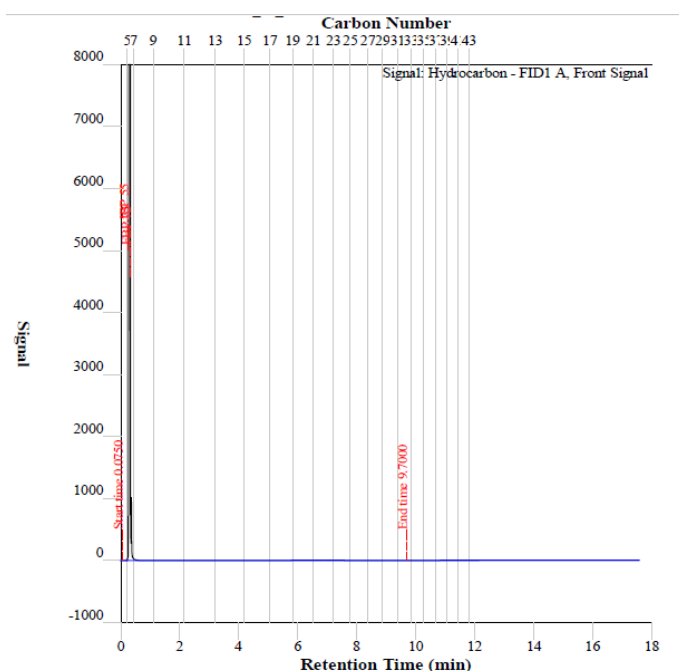


Figure D.32 SIM-DIS result of the long term experiment: DSR, GHSV=7500 h<sup>-1</sup>, H<sub>2</sub>O/C=2.5, Ni@0.5Ru@Al<sub>2</sub>O<sub>3</sub>

The SIM-DIS analysis results of liquid samples collected after experiments of DSR catalyst investigation performed with Ni@Al<sub>2</sub>O<sub>3</sub>-EISA, Ni@10CeO<sub>2</sub>-Al<sub>2</sub>O<sub>3</sub>-EISA, Ni@20CeO<sub>2</sub>-Al<sub>2</sub>O<sub>3</sub>-EISA, Ni@20CeO<sub>2</sub>@Al<sub>2</sub>O<sub>3</sub>-EISA, and Ni@8CeO<sub>2</sub>-2ZrO<sub>2</sub>-Al<sub>2</sub>O<sub>3</sub>@EISA were presented in Figures D.33-D.37. The SIM-DIS analysis result of the ATR experiments performed with Ni@8CeO<sub>2</sub>-2ZrO<sub>2</sub>-Al<sub>2</sub>O<sub>3</sub>-EISA and Ni@10CeO<sub>2</sub>-Al<sub>2</sub>O<sub>3</sub>-EISA are given in Figures D.38 and D.39. The SIM-DIS analysis result of the DSR experiments performed with Ni@8CeO<sub>2</sub>-2ZrO<sub>2</sub>-Al<sub>2</sub>O<sub>3</sub>-EISA and Ni@10CeO<sub>2</sub>-Al<sub>2</sub>O<sub>3</sub>-EISA at the harsh operating conditions (GHSV= 17000 h<sup>-1</sup>, H<sub>2</sub>O/C= 1.5) are given in Figures D.40 and D.41. Figure D.42 gives the SIM-DIS result of the long term experiment performed with the Ni@10CeO<sub>2</sub>-Al<sub>2</sub>O<sub>3</sub>-EISA catalyst. Presence of hydrocarbon was not observed in any of these results indicating complete conversion for all performed experiment with ceria incorporated EISA catalysts.

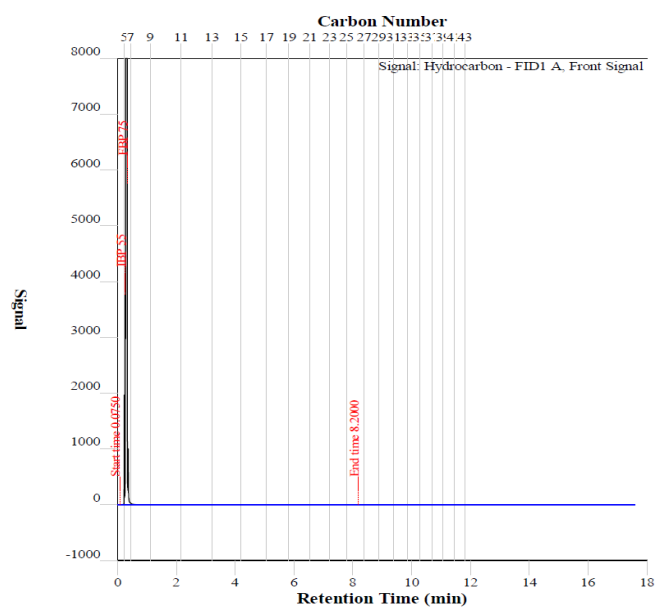


Figure D.33 SIM-DIS result of the experiment: DSR, GHSV=7500 h<sup>-1</sup>, H<sub>2</sub>O/C=2.5, Ni@Al<sub>2</sub>O<sub>3</sub>-EISA

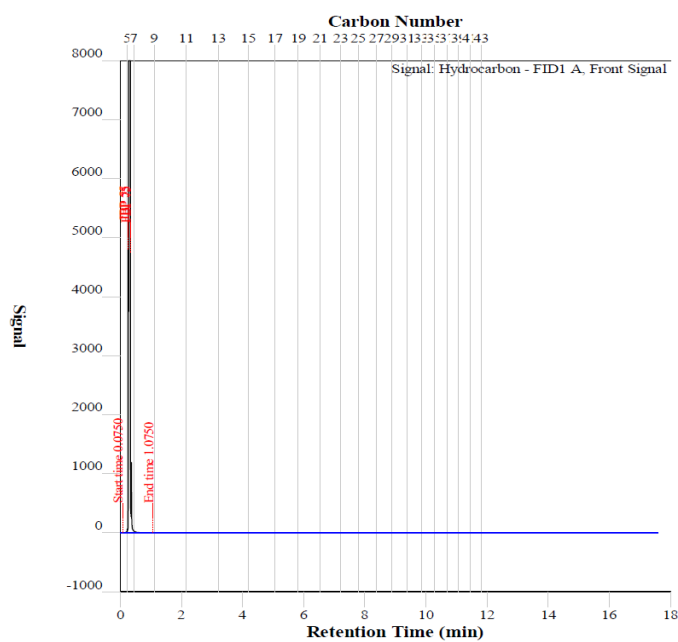


Figure D.34 SIM-DIS result of the experiment: DSR, GHSV=7500 h<sup>-1</sup>, H<sub>2</sub>O/C=2.5, Ni@10CeO<sub>2</sub>-Al<sub>2</sub>O<sub>3</sub>-EISA

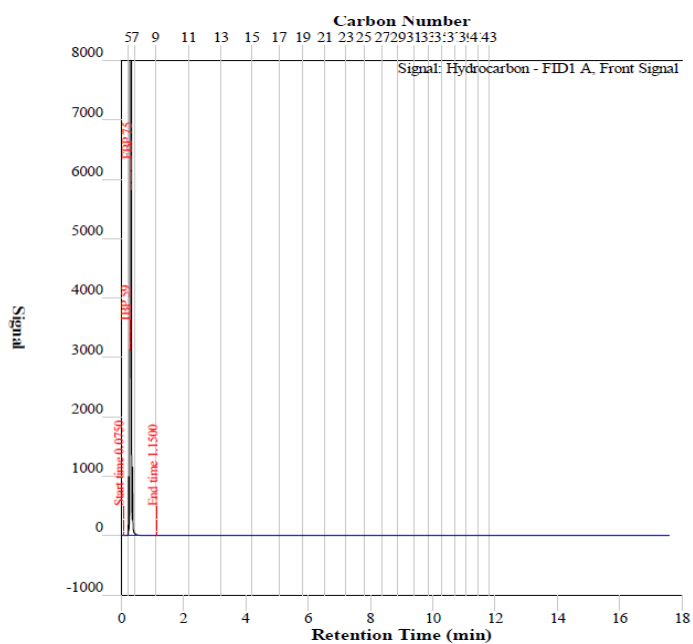


Figure D.35 SIM-DIS result of the experiment: DSR, GHSV=7500 h<sup>-1</sup>, H<sub>2</sub>O/C=2.5, Ni@20CeO<sub>2</sub>-Al<sub>2</sub>O<sub>3</sub>-EISA

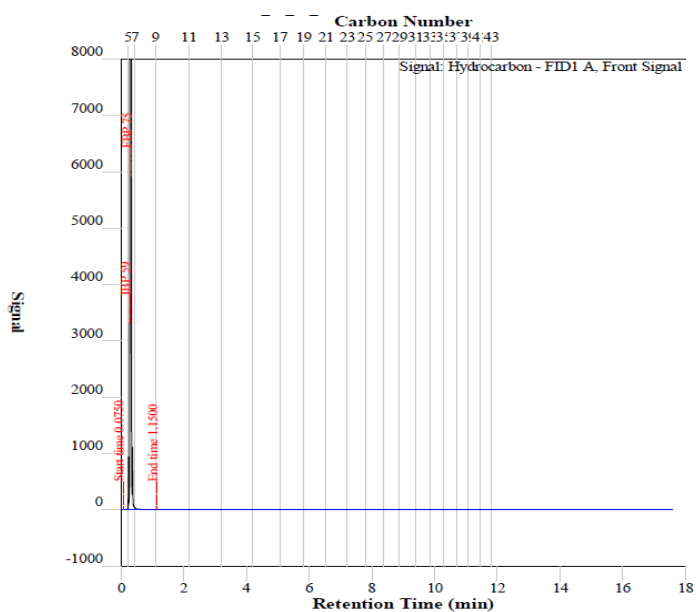


Figure D.36 SIM-DIS result of the experiment: DSR, GHSV=7500 h<sup>-1</sup>, H<sub>2</sub>O/C=2.5, Ni@20CeO<sub>2</sub>@Al<sub>2</sub>O<sub>3</sub>-EISA

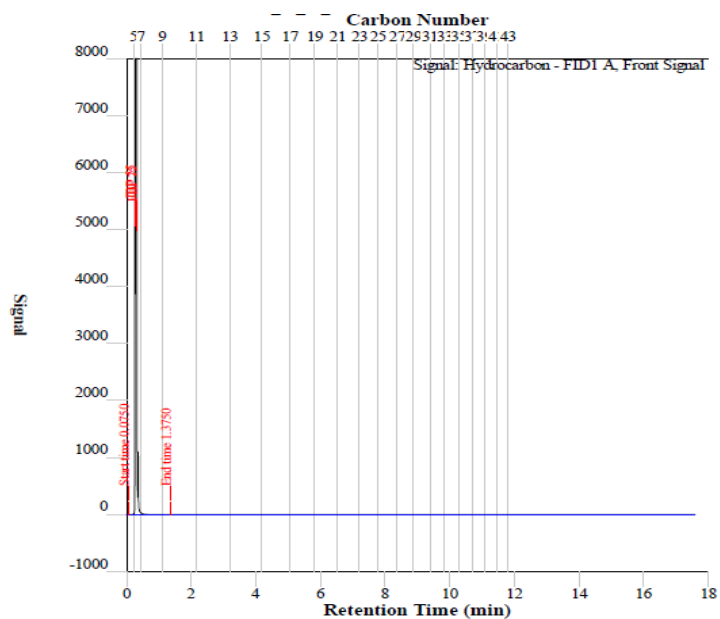


Figure D.37 SIM-DIS result of the experiment: DSR, GHSV=7500 h<sup>-1</sup>, H<sub>2</sub>O/C=2.5, O<sub>2</sub>/C=0.5, Ni@8CeO<sub>2</sub>-2ZrO<sub>2</sub>@Al<sub>2</sub>O<sub>3</sub>-EISA

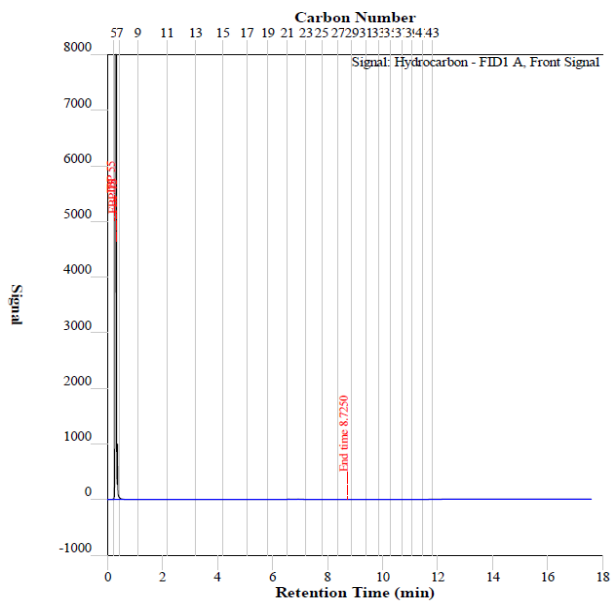


Figure D.38 SIM-DIS result of the experiment: ATR, GHSV=7500 h<sup>-1</sup>, H<sub>2</sub>O/C=2.5, O<sub>2</sub>/C=0.5, Ni@8CeO<sub>2</sub>-2ZrO<sub>2</sub>@Al<sub>2</sub>O<sub>3</sub>-EISA

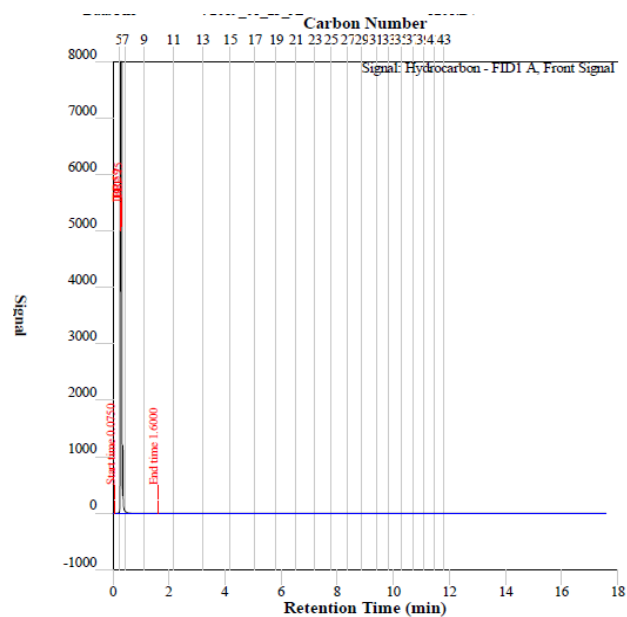


Figure D.39 SIM-DIS result of the experiment: ATR, GHSV=7500 h<sup>-1</sup>, H<sub>2</sub>O/C=2.5, O<sub>2</sub>/C=0.5, Ni@10CeO<sub>2</sub>-Al<sub>2</sub>O<sub>3</sub>-EISA

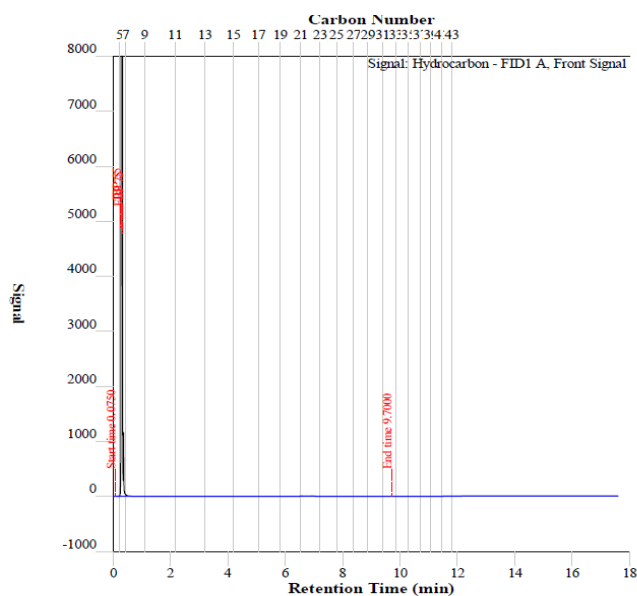


Figure D.40 SIM-DIS result of the experiment: DSR, GHSV=17000 h<sup>-1</sup>, H<sub>2</sub>O/C=1.5, Ni@Al<sub>2</sub>O<sub>3</sub>-EISA

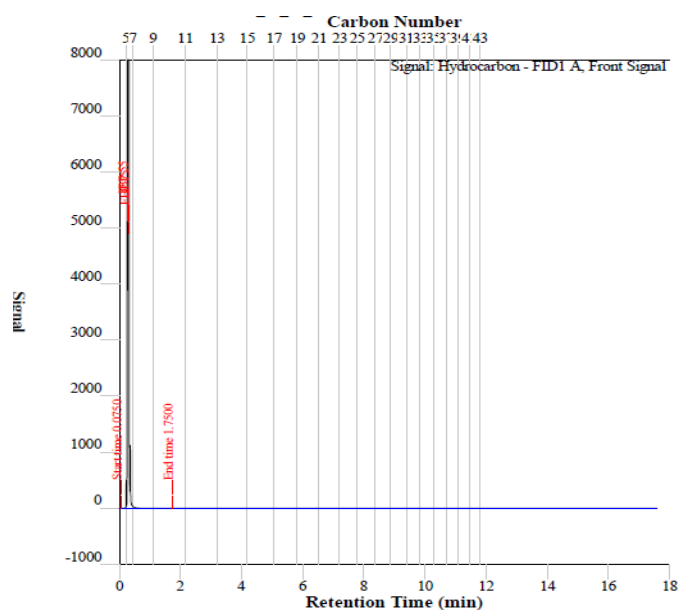


Figure D.41 SIM-DIS result of the experiment: DSR, GHSV=17000 h<sup>-1</sup>, H<sub>2</sub>O/C=1.5, Ni@10CeO<sub>2</sub>-Al<sub>2</sub>O<sub>3</sub>-EISA

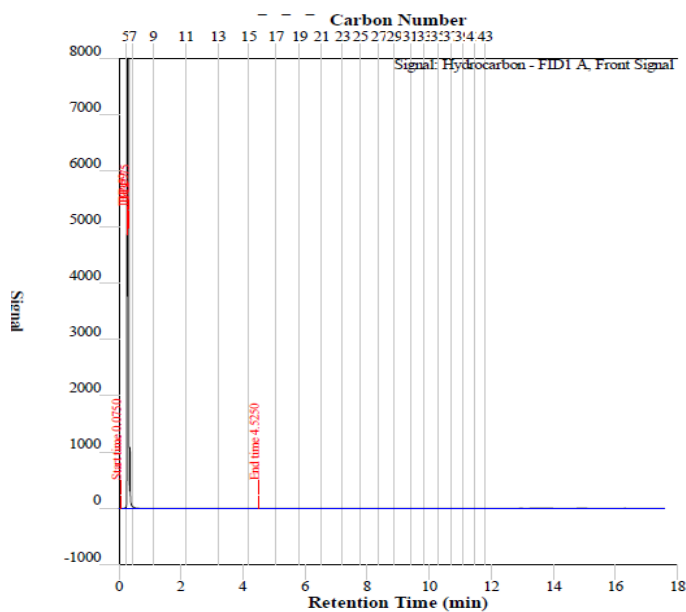


Figure D.42 SIM-DIS result of the experiment: Long-Term DSR, GHSV=7500 h<sup>-1</sup>, H<sub>2</sub>O/C=2.5, Ni@10CeO<sub>2</sub>-Al<sub>2</sub>O<sub>3</sub>-EISA

The SIM-DIS analysis results of liquid samples collected after experiments of DSR catalyst investigation performed with Ni@10Mg-Al<sub>2</sub>O<sub>3</sub>-EISA, Ni@10W-10CeO<sub>2</sub>-Al<sub>2</sub>O<sub>3</sub>-EISA, Ni@10W-Al<sub>2</sub>O<sub>3</sub>-EISA and Ni@20W-Al<sub>2</sub>O<sub>3</sub>-EISA were presented in Figures D.43-D.46. The SIM-DIS analysis result of the ATR experiments performed

with Ni@10Mg-Al<sub>2</sub>O<sub>3</sub>-EISA and Ni@10W-10CeO<sub>2</sub>-Al<sub>2</sub>O<sub>3</sub>-EISA are given in Figures D.47 and D.48. Figure D.49 gives the SIM-DIS result of the long-term experiment performed with the Ni@10Mg-Al<sub>2</sub>O<sub>3</sub>-EISA catalyst. Presence of hydrocarbons was not observed on any of these results indicating complete conversion for all performed experiment with tungsten/magnesium incorporated EISA catalysts.

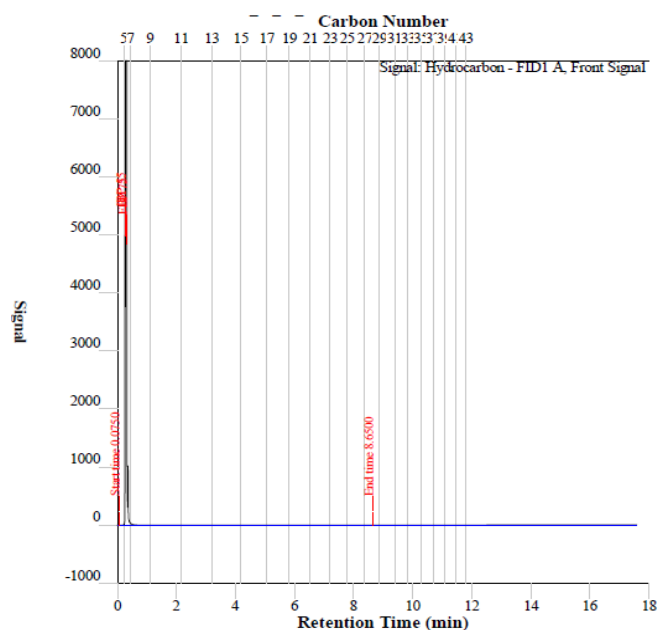


Figure D.43 SIM-DIS result of experiment: DSR, GHSV=7500 h<sup>-1</sup>, H<sub>2</sub>O/C=2.5, Ni@10Mg-Al<sub>2</sub>O<sub>3</sub>-EISA

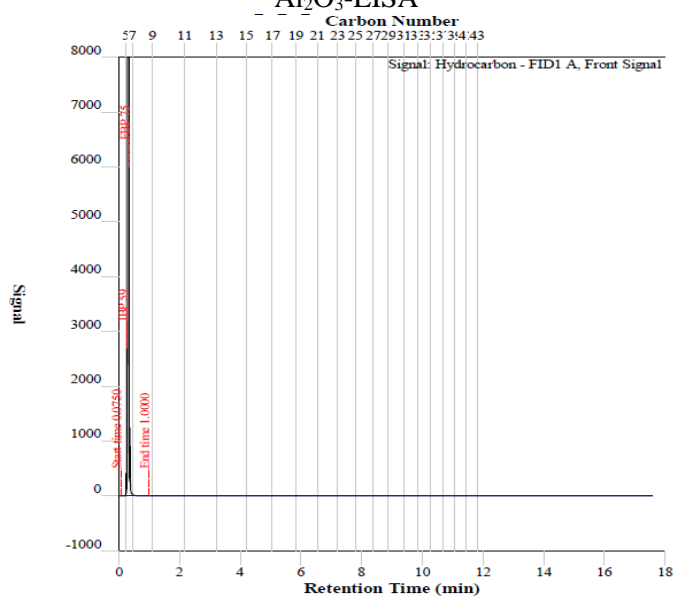


Figure D.44 SIM-DIS result of experiment: DSR, GHSV=7500 h<sup>-1</sup>, H<sub>2</sub>O/C=2.5, Ni@10W-10CeO<sub>2</sub>-Al<sub>2</sub>O<sub>3</sub>-EISA

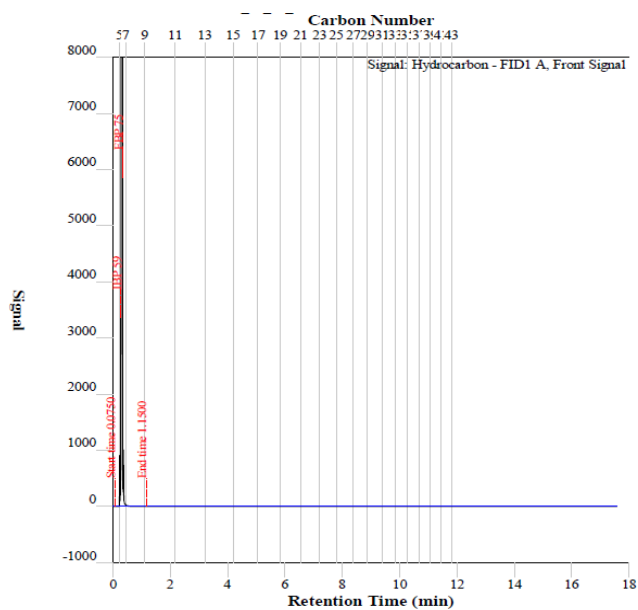


Figure D.45 SIM-DIS result of experiment: DSR, GHSV=7500 h<sup>-1</sup>, H<sub>2</sub>O/C=2.5, Ni@10W-Al<sub>2</sub>O<sub>3</sub>-EISA

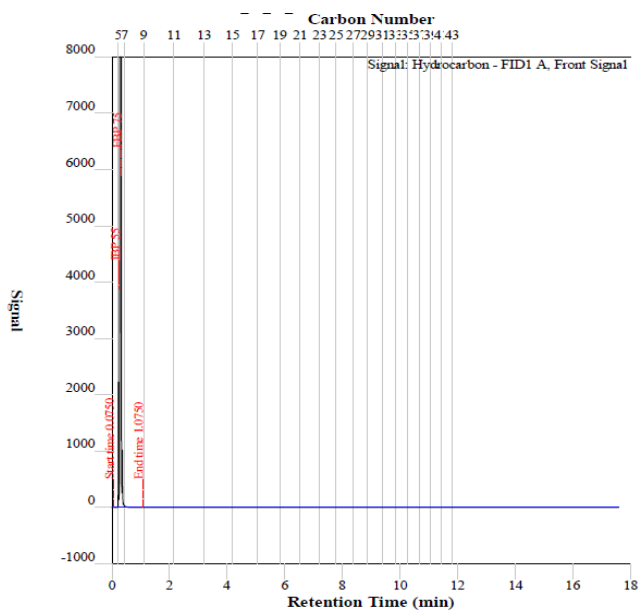


Figure D.46 SIM-DIS result of experiment: DSR, GHSV=7500 h<sup>-1</sup>, H<sub>2</sub>O/C=2.5, Ni@20W-Al<sub>2</sub>O<sub>3</sub>-EISA

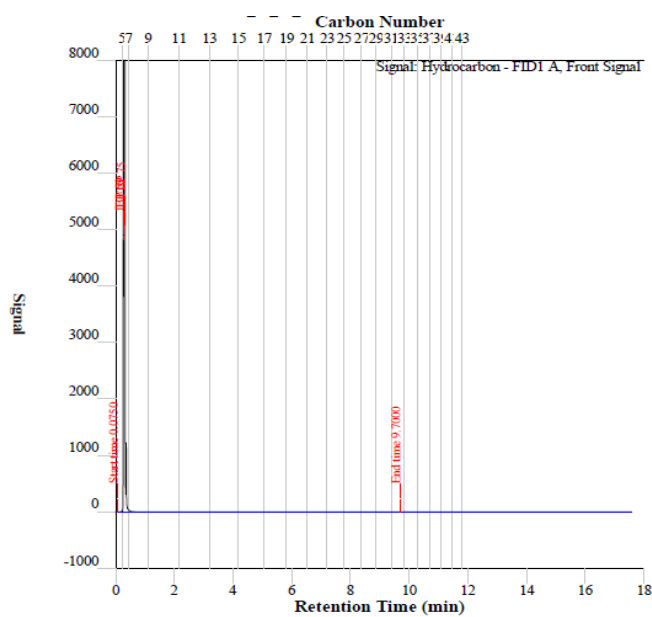


Figure D.47 SIM-DIS result of experiment: ATR, GHSV=7500 h<sup>-1</sup>, H<sub>2</sub>O/C=2.5, Ni@10W-10CeO<sub>2</sub>-Al<sub>2</sub>O<sub>3</sub>-EISA

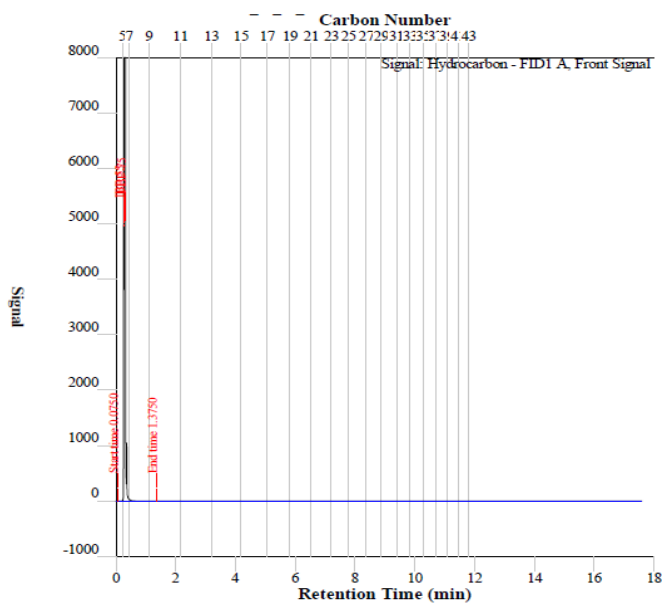


Figure D.48 SIM-DIS result of experiment: ATR, GHSV=7500 h<sup>-1</sup>, H<sub>2</sub>O/C=2.5, Ni@10Mg-Al<sub>2</sub>O<sub>3</sub>-EISA

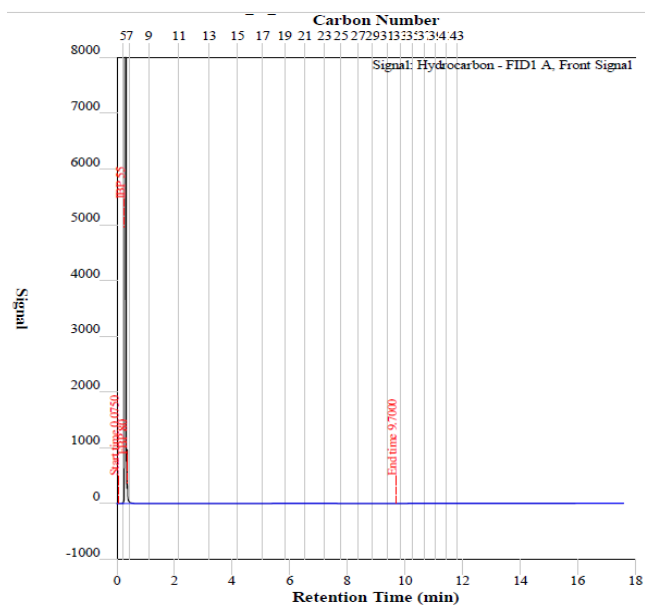


Figure D.49 SIM-DIS result of the long-term experiment (54 h): DSR, GHSV=7500 h<sup>-1</sup>, H<sub>2</sub>O/C=2.5, Ni@10Mg-Al<sub>2</sub>O<sub>3</sub>-EISA

Analyses of all samples with simulated-distillation analysis (SIM-DIS, ASTM D7169.23648) with a high temperature gas chromatography were performed to determine the range of hydrocarbons present in the sample. This analysis showed presence of hydrocarbons qualitatively. Following this analysis, selected samples were analyzed quantitatively with high-resolution gas chromatography (DHA, ASTM D6730-01), in detail. The reason of selection of a secondary analysis method was the long time requirement of this analysis that cannot be applied for all samples. By examining the results obtained from SIM-DIS method, samples that were suspected to contain some hydrocarbons in trace amounts were selected and analyzed with a high-resolution gas chromatography. Since the liquid samples were separated by using hexane as solvent, firstly hexane was analyzed and the resulting impurities in hexane was deduced from the results of liquid samples.

The summary of the selected samples and the overall hydrocarbon content of the corresponding sample is presented in Table D.2 in terms of the hydrocarbon amount corresponding to the total diesel feed in molar ratios. The data given in Table D.2 was

corrected since besides hydrocarbons coming from the reaction itself, it contained the impurities coming from the solvent, hexane. The raw data obtained from the analysis is also presented in Table D.3 together with the results of hexane for comparison.

As it can be seen from Table D.2, the presence of the highest hydrocarbon amount was observed in the samples gathered after the experiment with the lowest hydrogen productivity-activity such as Ni@20W@Al<sub>2</sub>O<sub>3</sub> and Ni@20W-Al<sub>2</sub>O<sub>3</sub>-EISA. However, even the highest hydrocarbon amount found in the samples only corresponds to 0.35% of the total diesel fed to the system during the six hours of experiment. Following the definitive results obtained with detailed hydrocarbon analysis, it is safe to conclude that the amount of hydrocarbon found in the liquid samples is negligible and all DSR and ATR experiments performed in the scope of this study reached complete conversion.

Table D.2 Reaction, operating conditions, catalysts of selected samples and corresponding overall analysis result of high-resolution gas chromatography (DHA, ASTM D6730-01

#	Rxn	T	GHSV	H <sub>2</sub> O/C	O <sub>2</sub> /C	Catalyst	Hydrocarbon in product sample / Diesel feed (%)
1	DSR	800	10000	2.5	0	Ni@20CeO <sub>2</sub> @Al <sub>2</sub> O <sub>3</sub>	0.11
2	DSR	800	7500	2.5	0	Ni@Al <sub>2</sub> O <sub>3</sub>	0.01
3	DSR	800	7500	2.5	0	Ni@Al <sub>2</sub> O <sub>3</sub> -EISA	0.27
4	DSR	800	7500	2.5	0	Ni@20W@Al <sub>2</sub> O <sub>3</sub>	0.35
5	DSR	800	7500	2.5	0	Ni@10W-Al <sub>2</sub> O <sub>3</sub> -EISA	0.15
6	DSR	800	7500	2.5	0	Ni@20W-Al <sub>2</sub> O <sub>3</sub> -EISA	0.34
7	ATR	800	7500	2.5	0.25	Ni@20CeO <sub>2</sub> @Al <sub>2</sub> O <sub>3</sub>	0.00
8	DSR	800	7500	2.5	0	1.5Ru@20CeO <sub>2</sub> @Al <sub>2</sub> O <sub>3</sub>	0.00
9	DSR	800	17000	1.5	0	Ni@Al <sub>2</sub> O <sub>3</sub> -EISA	0.00
10	DSR	800	17000	1.5	0	Ni@10CeO <sub>2</sub> -Al <sub>2</sub> O <sub>3</sub> -EISA	0.01
11	DSR	800	7500	2.5	0	Ni@10Mg-Al <sub>2</sub> O <sub>3</sub> -EISA - LT	0.00
12	DSR	800	7500	2.5	0	Ni@0.5Ru@Al <sub>2</sub> O <sub>3</sub> -LT	0.00
13	DSR	800	7500	2.5	0	Al <sub>2</sub> O <sub>3</sub>	0.00
14	DSR	800	7500	2.5	0	Ni@10CeO <sub>2</sub> -Al <sub>2</sub> O <sub>3</sub> -EISA-LT	0.00

Table D.3 Results of high-resolution gas chromatography (DHA, ASTM D6730-01) of selected samples in wt.% and hexane solvent prior to the correction of results due to impurities in hexane.

Component	ATR, 7500h <sup>-1</sup> , H <sub>2</sub> O/C =2.5 O <sub>2</sub> /C=0.25	DSR, Ni@0.5Ru@Al <sub>2</sub> O <sub>3</sub> -LT	DSR, Ni@10Mg-Al <sub>2</sub> O <sub>3</sub> -EISA-LT	DSR, 1.5Ru@2.0CeO <sub>2</sub> @Al <sub>2</sub> O <sub>3</sub>	DSR, Ni@Al <sub>2</sub> O <sub>3</sub> -EISA	DSR, Ni@Al <sub>2</sub> O <sub>3</sub>	DSR, Ni@10W-Al <sub>2</sub> O <sub>3</sub> -EISA	DSR, Ni@20W@Al <sub>2</sub> O <sub>3</sub>	DSR, Ni@20W-Al <sub>2</sub> O <sub>3</sub> -EISA	DSR, Ni@Al <sub>2</sub> O <sub>3</sub> -EISA	DSR, 10000h <sup>-1</sup> , H <sub>2</sub> O/C =2.5	DSR, Ni@10CeO <sub>2</sub> -Al <sub>2</sub> O <sub>3</sub> -EISA	DSR, Ni@10CeO <sub>2</sub> -Al <sub>2</sub> O <sub>3</sub> -EISA-LT	Hexane
i-pentane	0.00	0.00	0.00	0.00	0.00	0.00	0.00	0.01	0.01	0.00	0.00	0.00	0.00	0.00
n-pentane	0.00	0.00	0.00	0.00	0.00	0.00	0.12	0.28	0.28	0.24	0	0.02	0.00	0.00
2,2-dimethylbutane	0.01	0.01	0.01	0.01	0.01	0.01	0.02	0.04	0.03	0.03	0.01	0.01	0.01	0.01
cyclopentane	0.05	0.05	0.05	0.05	0.05	0.05	0.01	0.02	0.02	0.02	0.05	0.06	0.05	0.05
2,3-dimethylbutane	0.10	0.10	0.10	0.10	0.10	0.10	0.06	0.07	0.07	0.07	0.10	0.10	0.10	0.10
2-methylpentane	0.61	0.61	0.60	0.60	0.60	0.60	0.45	0.51	0.51	0.50	0.60	0.61	0.59	0.60
3-methylpentane	0.54	0.54	0.54	0.54	0.54	0.54	0.40	0.43	0.43	0.43	0.54	0.55	0.53	0.54
n-hexane	98.11	98.1	98.09	98.1	98.1	98.1	98.2	97.9	97.9	98.0	98.1	98.0	98.1	98.1
2,2-dimethylpentane	0.01	0.01	0.01	0.00	0.01	0.00	0.00	0.00	0.00	0.00	0.00	0.00	0.01	0.00
methylcyclopentane	0.40	0.40	0.40	0.40	0.40	0.40	0.56	0.55	0.55	0.55	0.40	0.40	0.40	0.40
2,4-dimethylpentane	0.00	0.00	0.00	0.00	0.01	0.00	0.01	0.01	0.01	0.00	0.00	0.00	0.00	0.00
cyclohexane	0.17	0.18	0.20	0.17	0.18	0.18	0.16	0.15	0.15	0.14	0.18	0.19	0.19	0.17
Naphthalene	0.00	0.00	0.00	0.00	0.00	0.01	0.00	0.00	0.00	0.00	0.00	0.00	0.00	0.00



## E. XRD Data

XRD data of  $\text{Al}_2\text{O}_3$ , Ni,  $\text{NiAl}_2\text{O}_4$ , W,  $\text{Ni}_4\text{W}$ ,  $\text{CeAlO}_3$ ,  $\text{CeO}_2$ , Ru,  $\text{RuO}_2$ , C,  $(\text{Mg}_{0.782}\text{Al}_{0.218})(\text{Al}_{1.782}\text{Mg}_{0.218})\text{O}_4$  are given in Tables E.1-E.11.

Table E.1 XRD data of  $\text{Al}_2\text{O}_3$

Compound Name: Alumina gamma		
Chemical Formula: $\text{Al}_2\text{O}_3$		
PDF Card No.: 01-074-4629		
Radiation: $\text{CuK}\alpha_1$		
Wavelength: 1.5405 Å		
Crystal System: Tetragonal		
2Theta	d-Value	Intensity
19.32	4.591	18.0
31.63	2.826	18.9
31.89	2.804	35.8
37.33	2.407	35.5
37.77	2.380	20.8
39.21	2.295	9.5
45.35	1.998	100.0
46.09	1.968	47.3
50.07	1.820	4.2
56.50	1.627	8.7
56.98	1.615	4.3
60.14	1.537	9.7
60.44	1.530	2.3
61.05	1.516	4.0
66.07	1.413	40.8
66.65	1.402	78.0
69.55	1.350	0.4
69.84	1.346	0.3
70.40	1.336	0.6
75.10	1.264	1.3
78.69	1.215	2.1
79.23	1.208	0.8
80.69	1.190	0.1
84.31	1.148	11.4
87.01	1.119	0.5

Table E.2 XRD data of Ni

Compound Name: Nickel		
Chemical Formula: Ni		
PDF Card No.: 01-071-4653		
Radiation: CuK $\alpha$ 1		
Wavelength: 1.5405 Å		
Crystal System: Cubic		
2Theta	d-Value	Intensity
44.28	2.044	100.0
51.59	1.770	41.9
75.97	1.252	16.3
92.39	1.067	14.5
97.84	1.022	3.9
121.00	0.885	1.7
143.05	0.812	5.3

Table E.3 XRD data of NiAl<sub>2</sub>O<sub>4</sub>

Compound Name: Nickel Aluminum Oxide		
Chemical Formula: NiAl <sub>2</sub> O <sub>4</sub>		
PDF Card No.: 01-010-0339		
Radiation: CuK $\alpha$ 1		
Wavelength: 1.5405 Å		
Crystal System: Cubic		
2Theta	d-Value	Intensity
19.07	4.650	20.0
31.41	2.846	20.0
37.01	2.427	100.0
45.00	2.013	65.0
55.97	1.641	8.0
59.66	1.548	30.0
65.54	1.423	60.0
68.99	1.360	1.0
74.41	1.274	1.0
77.74	1.227	10.0
78.81	1.213	1.0
83.10	1.161	8.0
91.51	1.075	4.0
94.66	1.048	12.0
99.92	1.006	8.0
112.00	0.929	8.0
117.75	0.900	8.0
139.36	0.821	16.0

Table E.4 XRD data of W

Compound Name: Tungsten		
Chemical Formula: W		
PDF Card No.: 01-089-3728		
Radiation: CuK $\alpha$ 1		
Wavelength: 1.5405 Å		
Crystal System: Cubic		
2Theta	d-Value	Intensity
40.26	2.238	100.0
58.25	1.583	14.0
73.18	1.292	23.4
86.99	1.119	6.3

Table E.5 XRD data of Ni<sub>4</sub>W

Compound Name: Nickel Tungsten		
Chemical Formula: Ni <sub>4</sub> W		
PDF Card No.: 01-072-2650		
Radiation: CuK $\alpha$ 1		
Wavelength: 1.5405 Å		
Crystal System: Tetragonal		
2Theta	d-Value	Intensity
21.92	4.052	26.9
29.56	3.020	24.0
31.19	2.865	10.2
43.51	2.078	100.0
44.70	2.026	3.6
50.31	1.812	29.5
51.39	1.776	12.6
54.50	1.682	3.7
56.52	1.627	3.2
61.35	1.510	2.4
64.14	1.451	4.1
65.06	1.433	1.0
69.55	1.351	0.8
70.44	1.336	1.5
73.05	1.294	2.6
73.91	1.281	6.5
74.78	1.269	1.269
83.23	1.160	0.8
86.54	1.124	0.7
89.86	1.091	11.6
91.53	1.075	6.4
95.67	1.039	5.0
98.17	1.019	1.1
99.86	1.007	0.5
103.23	0.983	0.5
108.40	0.950	1.7

Table E.5 (cont'd) XRD data of Ni<sub>4</sub>W

Compound Name: Nickel Tungsten		
Chemical Formula: Ni <sub>4</sub> W		
PDF Card No.: 01-072-2650		
Radiation: CuK $\alpha$ 1		
Wavelength: 1.5405 Å		
Crystal System: Tetragonal		
116.47	0.906	1.6
125.19	0.868	1.0
138.55	0.824	4.6

Table E.6 XRD data of CeAlO<sub>3</sub>

Compound Name: Cerium Aluminum Oxide		
Chemical Formula: CeAlO <sub>3</sub>		
PDF Card No.: 01-081-1185		
Radiation: CuK $\alpha$ 1		
Wavelength: 1.5405 Å		
Crystal System: Tetragonal		
2Theta	d-Value	Intensity
23.41	3.797	27.2
23.6	3.767	53.3
33.48	2.674	100
33.62	2.664	77.8
41.37	2.181	55.7
47.88	1.898	16.7
48.28	1.883	30.5
54.05	1.695	9.6
54.33	1.687	11.4
54.42	1.685	11.5
59.77	1.546	17.6
60.03	1.54	34.9
70.35	1.337	15.4
70.67	1.332	8.2
74.98	1.266	0.9
75.37	1.26	6.1
75.6	1.257	6.9
79.89	1.2	6.1
80.5	1.192	7.6
80.58	1.191	8.2
84.73	1.143	4.3
85.33	1.137	7.8
89.9	1.09	6.5

Table E.7 XRD data of CeO<sub>2</sub>

Compound Name: Cerium Oxide		
Chemical Formula: CeO <sub>2</sub>		
PDF Card No.: 00-004-0593		
Radiation: CuK $\alpha$ 1		
Wavelength: 1.5405 Å		
Crystal System: Cubic		
2Theta	d-Value	Intensity
28.55	3.12	100.00
33.08	2.71	29.00
47.49	1.91	51.00
56.33	1.63	44.00
59.09	1.56	55.00
69.40	1.35	15.00
76.73	1.24	6.00
79.08	1.21	100.00

Table E.8 XRD data of Ru

Compound Name: Ruthenium		
Chemical Formula: Ru		
PDF Card No.: 01-071-4656		
Radiation: CuK $\alpha$ 1		
Wavelength: 1.5405 Å		
Crystal System: Hexagonal		
2Theta	d-Value	Intensity
38.6	2.33	26.4
42.1	2.145	26.4
44.19	2.048	100
58.43	1.578	12.1
69.85	1.345	12.2
78.41	1.219	11.9
82.76	1.165	1.6
85.04	1.14	11.8
86.47	1.124	8.3
91.84	1.072	1.5
97.59	1.024	2
104.51	0.974	1.7
117.04	0.903	4.2
121.97	0.881	1.3
126.44	0.863	7.7
133.44	0.839	4.9
141.95	0.815	2.4
146.22	0.805	3.5

Table E.9 XRD data of RuO<sub>2</sub>

Compound Name: Ruthenium (IV) Oxide		
Chemical Formula: RuO <sub>2</sub>		
PDF Card No.: 00-004-0593		
Radiation: CuK $\alpha$ 1		
Wavelength: 1.5405 Å		
Crystal System: Cubic		
2Theta	d-Value	Intensity
28.27	3.154	100
35.21	2.547	40.8
35.35	2.537	49.2
40.17	2.243	9.8
40.66	2.217	9.1
40.83	2.208	6.3
45.26	2.002	0.8
45.6	1.988	0.6
54.56	1.681	27.2
54.85	1.672	28.2
58.48	1.577	12.3
59.74	1.547	7.1
65.85	1.417	5.2
66.55	1.404	5.1
67.38	1.389	12.2
69.79	1.346	7.4
70.55	1.334	6.8
73.44	1.288	0.1
74.1	1.278	0.2
74.45	1.273	2.9
74.78	1.269	2.8
76.82	1.24	0.1
77.22	1.234	0.1
78.01	1.224	0.2
78.25	1.221	0.2
84.03	1.151	3.8
84.43	1.146	4.2
86.75	1.122	1.3
88.02	1.109	1.4
88.47	1.104	6.2

Table E.10 XRD data of C

Compound Name: Graphite		
Chemical Formula: C		
PDF Card No.: 00-056-0159		
Radiation: CuK $\alpha$ 1		
Wavelength: 1.5405 Å		
Crystal System: Hexagonal		
2Theta	d-Value	Intensity
26.54	3.36	100.00
42.36	2.13	7.00
44.56	2.03	6.00
50.70	1.80	1.00
54.66	1.68	7.00
59.89	1.54	1.00
77.49	1.23	12.00
83.61	1.16	5.00
87.05	1.12	1.00
94.06	1.05	1.00
101.82	0.99	2.00

Table E.11 XRD data of (Mg<sub>0.782</sub>Al<sub>0.218</sub>)(Al<sub>1.782</sub>Mg<sub>0.218</sub>)O<sub>4</sub>

Compound Name: Spinel		
Chemical Formula:		
(Mg <sub>0.782</sub> Al <sub>0.218</sub> )(Al <sub>1.782</sub> Mg <sub>0.218</sub> )O <sub>4</sub>		
PDF Card No.: 01-070-6013		
Radiation: CuK $\alpha$ 1		
Wavelength: 1.5405 Å		
Crystal System: Cubic		
2Theta	d-Value	Intensity
19	4.667	34.2
31.27	2.858	33.6
36.85	2.437	100
38.55	2.334	1
44.81	2.021	52.8
49.08	1.855	0.1
55.66	1.65	8.7
59.36	1.556	41.4
65.24	1.429	63
68.63	1.366	2.5
69.74	1.347	0.1
74.12	1.278	2.6
77.34	1.233	8.5
78.41	1.219	0.8
82.63	1.167	5.4
85.77	1.132	2

The transformation sequence of  $\text{Al}(\text{OH})_3$  to different phases of  $\text{Al}_2\text{O}_3$  is presented in Figure E.1. X-Ray diffraction data of transition alumina phases are given in Figure E.2

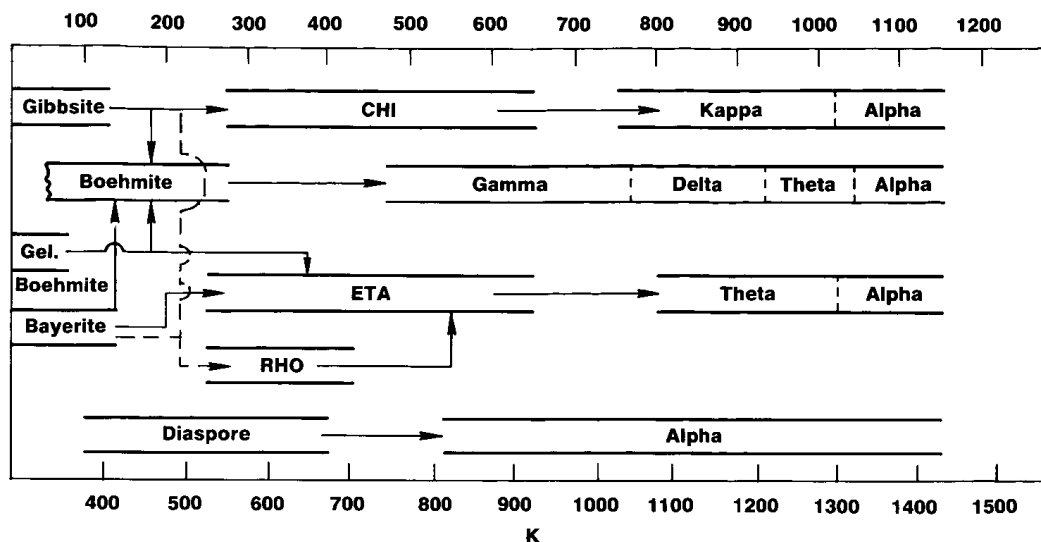


Figure E.1 Transformation sequence of  $\text{Al}(\text{OH})_3$  to different phases of  $\text{Al}_2\text{O}_3$ <sup>91</sup>.

Chi			Eta			Gamma			Kappa		Theta			Delta		
d Å	$l/l_1$	hkl	d Å	$l/l_1$	hkl	d Å	$l/l_1$	hkl	d Å	$l/l_1$	d Å	$l/l_1$	hkl	d Å	$l/l_1$	hkl
2.40	40	311	4.6	40	111	4.56	40	111	6.2	30	5.70	2	200	7.6	4	101
2.27	20	222	2.8	20	220	2.80	20	220	4.5	20	5.45	10	001	6.4	4	102, 004
2.11	30	321	2.40	60	311	2.39	80	311	4.2	10	4.54	18	201	5.53	4	111
1.98	20	400	2.27	30	222	2.28	50	222	3.04	40	2.837	80	400,401	5.10	8	112
1.53	10	311, 333	1.97	80	400	1.977	100	400	2.79	60	2.730	65	202,002	4.57	12	113
1.39	100	440	1.52	20	333	1.520	30	511	2.70	20	2.566	14	111	4.07	12	114, 105
			1.40	100	440	1.395	100	440	2.57	80	2.444	60	111	3.61	4	115
			1.21	10	533	1.140	20	444	2.41	30	2.315	45	401,310	3.23	4	116
			1.14	20	444	1.027	10	731	2.32	40	2.257	35	402,202	3.05	4	107, 214
			1.03	10	553	0.989	10	800	2.26	10	2.019	45	311,112	2.881	8	117
					.884	10	840	2.16	10	1.9544	8	601	2.728	30	222	
					.806	20	844	2.11	80	1.9094	30	600,312	2.601	25	302, 118	
								2.06	30	1.7998	14	510	2.460	60	312	
								1.99	40	1.7765	6	602,402	2.402	16	313	
								1.95	20	1.7376	4	403	2.315	8	314, 305	
								1.87	60	1.6807	2	601	2.279	40	226	
								1.82	30	1.6216	6	203,511	2.160	4	1.1.10	
								1.74	20	1.5715	2	113	1.986	75	400	
								1.64	60	1.5426	25	313	1.953	40	0.0.12	
								1.54	10	1.5120	6	603	1.914	12	318	
								1.49	30	1.4883	25	113,801	1.827	4	319, 2.2.10	
								1.45	30	1.4526	25	020	1.810	8	426, 3.1.11	
								1.43	80	1.4264	10	800,710	1.628	8	1.1.14	
								1.39	100	1.3883	100	712,512	1.604	4	513	
								1.34	30				1.538	8	1.1.15	
								1.12	10				1.517	16	523, 516	
								1.06	10				1.456	8	440	
								1.04	5				1.407	50	4.0.12	
								1.02	5				1.396	100		
								1.01	40							
								0.994	20							

Figure E.2 X-Ray diffraction data of transition aluminas<sup>91</sup>.

## F. Crystal size calculation through Scherrer Equation

Scherrer equation was used to calculate the crystal size of metals from the X-ray diffraction pattern. Peak location and the size of the full width at half max of the peak were required for the application of Scherrer Equation.

$$t_{\text{particle}} = \frac{C \times \lambda}{B \times \cos(\theta)}$$

C : crystal shape factor (0.89)

$\lambda$  : Wavelength (0.154 nm)

B : Full width at half max

$2\theta$  : Peak angle



### G. The effect of calcination temperature on Al<sub>2</sub>O<sub>3</sub>-EISA materials

X-Ray diffraction patterns of Al<sub>2</sub>O<sub>3</sub>-EISA support calcined at different temperatures to observe the temperature at which the structure of the material changes from amorphous to crystalline were presented in Figure G.1. According to XRD patterns of the materials, structural change was observed at a temperature range of 700 and 800 °C. The material can be identified as amorphous at calcination temperatures below 700 °C. However, material is crystalline when calcined above 800 °C.

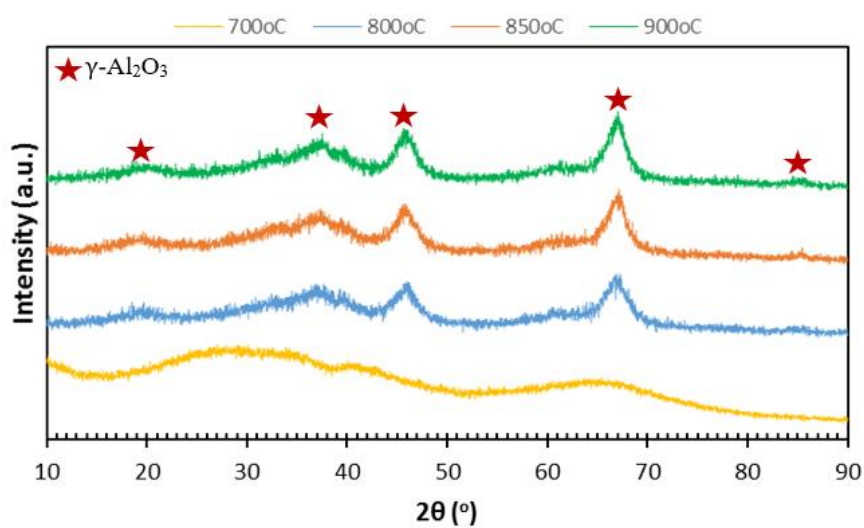


Figure G.1. XRD patterns of Al<sub>2</sub>O<sub>3</sub>-EISA materials calcined at different temperatures.



## CURRICULUM VITAE

### PERSONAL INFORMATION

Surname, Name : Arslan Bozdağ, Arzu  
Nationality : Turkish (TC)  
Date and Place of Birth : 3 April 1989, Gerede  
Phone : +90 533 475 2765  
E-mail : e162337@metu.edu.tr (arslanarzu@outlook.com)

### EDUCATION

Degree	Institution	Year of Graduation
MS	METU Chemical Engineering	2014
BS	METU Chemical Engineering	2012
High School	Ulubatlı Hasan Anadolu High School, Bursa	2007

### WORK EXPERIENCE

Year	Place	Enrollment
2018-Present	Tüpraş R&D Center	Engineer
2013-2018	METU Chemical Engineering	Teaching Assistant

### FOREIGN LANGUAGES

Advanced English

### PUBLICATIONS

- 1- Arslan Bozdag, A., Deniz Kaynar, A.D., Dogu, T., Sezgi, N.A., *Development of ceria and tungsten promoted nickel/alumina catalysts for steam reforming of diesel*, Chemical Engineering Journal, 377, 120274, 2013.
- 2- Sariyer, M., Arslan Bozdag, A., Sezgi, N.A., Dogu, T., *Performance comparison of microwave and conventionally heated reactors for sorption enhanced reforming of ethanol over Ni impregnated SBA-15*, Chemical Engineering Journal, 377, 120138, 2019.

- 3- Arslan, A., Dogu, T., *Effect of Calcination/Reduction Temperature of Ni Impregnated CeO<sub>2</sub>-ZrO<sub>2</sub> Catalysts on Hydrogen Yield and Coke Minimization in Low Temperature Reforming of Ethanol*. International Journal of Hydrogen Energy 41 (38): 16752-16761, 2016.
- 4- Arslan, A., Gunduz, S., Dogu, T., *Steam Reforming of Ethanol with Zirconia Incorporated Mesoporous Silicate Supported Catalysts*, International Journal of Hydrogen Energy 39 (32): 18264-18272, 2014.
- 5- Arslan, A., Bayat, A., Çelik, G., Dogu, T., *From Synthesis Gas to a Clean Transportation Fuel Dimethyl Ether: New Nanocomposite Bifunctional Catalyst Pairs*, Nanotech 1: 460-462, 2013.

## CONFERENCES

- 1- National Chemical Engineering Congress, TURKEY (June, 2012) Poster Presentation  
*Title: Direct Synthesis of DME from Synthesis Gas*
- 2- 10<sup>th</sup> Hypothesis Conference, SCOTLAND (JUNE, 2013) Poster Submission (Not attended)  
*Title: Steam Reforming of Ethanol over Ni Incorporated Ceria/Zirconia Based Catalysts*
- 3- International Porous Powder Materials Symposium & Exhibition, TURKEY (Sept, 2013) Poster Presentation  
*Title: Silicotungstic Acid Incorporated SBA-15 Catalysts for Dehydration of Alcohols*
- 4- 5<sup>th</sup> National Catalyst Congress, TURKEY (April, 2014) Poster Presentation  
*Title: Ethanol Steam Reforming with Ceria and Zirconia Supported Catalysts*
- 5- 20<sup>th</sup> World Hydrogen Energy Conference, KOREA (June, 2014) Oral Presentation  
*Title: Steam Reforming of Ethanol with Zirconia Incorporated Mesoporous Silicate Supported Catalysts*
- 6- National Chemical Engineering Congress, TURKEY (September, 2014) Poster Presentation  
*Title: Effect of H<sub>2</sub>O/EtOH ratio on coke formation in ethanol steam reforming reaction*
- 7- Turkish – German Conference on Energy Technologies, TURKEY (October, 2014) Poster Presentation  
*Title: Ethanol Steam Reforming with CeO<sub>2</sub>-ZrO<sub>2</sub> Supported Nickel Catalysts*
- 8- International Porous Powder Materials Symposium & Exhibition, TURKEY (Sept, 2015)  
*Title: Effect of Metal Incorporation on the Structural Properties of SBA-15 (Oral*

- Presentation)*  
*Title: Effects of Synthesis Conditions on the Structure of Ni Impregnated Ceria-Zirconia Supported Mesoporous Materials (Poster Presentation)*
- 9- European Symposium on Chemical Reaction Engineering, GERMANY (October, 2015) Poster Presentation  
*Title: Hydrogen Production through Low Temperature Ethanol Steam Reforming over Ni Impregnated CeO<sub>2</sub>-ZrO<sub>2</sub> with Coke Minimization*
- 10- 6<sup>th</sup> National Catalyst Congress, TURKEY (April, 2016) Poster Presentation  
*Title: Ceria Incorporated Alumina Supported Nickel Catalysts for Diesel Steam Reforming Reaction*
- 11- 21<sup>th</sup> World Hydrogen Energy Conference, SPAIN (June, 2016) Oral Presentation  
*Title: Development of Ceria-Alumina Supported Nickel Catalysts for Steam Reforming of Diesel*
- 12- 2<sup>nd</sup> International Hydrogen Technologies Congress, TURKEY (March, 2017) Poster Presentation  
*Title: Development of Tungsten or Ceria Incorporated Mesoporous Alumina Supported Nickel Catalysts for Hydrogen Production through Diesel Steam Reforming Reaction*
- 13- HYPOTHESIS XII Hydrogen Power Theoretical and Engineering Solutions International Symposium, Syracuse, ITALY (June, 2017) Oral Presentation  
*Title: Hydrogen Production through Diesel Steam Reforming Reaction over CeO<sub>2</sub> or W incorporated Al<sub>2</sub>O<sub>3</sub> Supported Ni Catalysts*
- 14- 4<sup>th</sup> Anatolian School of Catalysis, İzmir, TURKEY (September, 2017) Poster Presentation  
*Title: Effect of Tungsten or Ceria Incorporation into Ni/Al<sub>2</sub>O<sub>3</sub> Catalysts on Hydrogen Production Through Diesel Steam Reforming Reaction*
- 15- ISCRE25 The 25th International Symposium on Chemical Reaction Engineering (June, 2018) Poster Presentation  
*Title: CeO<sub>2</sub> and W Modified Mesoporous Ni/Al<sub>2</sub>O<sub>3</sub> Catalysts for Hydrogen Production by Steam Reforming of Diesel Fuel*

## HONOURS

- Dr. Haluk Sanver Scholarship (METU, Chemical Eng. Dept., March, 2017)
- Prof. Dr. Hasan Orbey Research Award (METU, Chemical Eng. Dept., November, 2016)
- 2012-2013 Academic Year METU Graduate Courses Academic Performance Award
- 5th National Catalysis Congress, 23-26 April 2014, Adana/Turkey. (Best Poster Award)